Doctoral theses at NTNU, 2013:211

Mark William Kennedy

Removal of Inclusions from Liquid Aluminium using Electromagnetically Modified Filtration

Doctoral Thesis

Mark William Kennedy

ISBN 978-82-471-4537-1 (printed version)
ISBN 978-82-471-4538-8 (electronic version)
ISSN 1503-8181

NTNU – Trondheim
Norwegian University of
Science and Technology

NTNU
Norwegian University of Science and Technology
Thesis for the degree of Philosophiae Doctor
Faculty of Natural Sciences and Technology
Department of Materials Science and Engineering

Doctoral theses at NTNU, 2013:211

NTNU

NTNU – Trondheim
Norwegian University of
Science and Technology

Mark William Kennedy

Removal of Inclusions from Liquid Aluminium using Electromagnetically Modified Filtration

Thesis for the degree of Philosophiae Doctor

Trondheim, August 2013

Norwegian University of Science and Technology
Faculty of Engineering Science and Technology
Department of Materials Science and Engineering

NTNU – Trondheim
Norwegian University of
Science and Technology

NTNU
Norwegian University of Science and Technology

Thesis for the degree of Philosophiae Doctor

Faculty of Engineering Science and Technology
Department of Materials Science and Engineering

ISBN 978-82-471-4537-1 (printed version)
ISBN 978-82-471-4538-8 (electronic version)
ISSN 1503-8181

IMT-Report 2013:178

Doctoral theses at NTNU, 2013:211

Printed by Skipnes Kommunikasjon as

PREFACE

This thesis entitled "Removal of Inclusions from Liquid Aluminium using Electromagnetically Modified Filtration," is submitted to the Norwegian University of Science and Technology (NTNU) in partial fulfilment of the requirements for the academic degree of Philosophiae Doctor. This doctoral thesis is the result of 3 years of work carried out at NTNU from January 2010 until November 2012, on the topic of filtration of liquid aluminium using Ceramic Foam Filters (CFFs) with the simultaneous application of electromagnetic fields. The experimental program was carried out through the Department of Materials Science and Engineering, at the laboratory of SINTEF Materials and Chemistry in Trondheim.

This work was conducted and funded as part of the RIRA (Remelting and Inclusion Refining of Aluminium) project funded by the Norwegian Research Council (NRC) - BIP Project No. 179947/I40. The industrial partners involved in the project were: Hydro Aluminium AS, SAPA Heat Transfer AB, Alcoa Norway ANS, Norwegian University of Science and Technology (NTNU) and SINTEF Materials and Chemistry. The funding granted by the industrial partners and the NRC is gratefully acknowledged.

Professor Ragnhild E. Aune at the Department of Materials Science and Engineering was the principle supervisor for the work. Prof. EM Jon Arne Bakken was the co-supervisor. Dr. Shahid Ahktar has also made a significant contribution to the direction of this work.

Results have been reported via presentations, conference and journal articles published or submitted as the work progressed. A US patent application for equipment and methods related to the electromagnetic priming of CFFs was also filed. These documents are included in the body of this thesis in either the form in which they were submitted or published.

This thesis consists of four main parts:

Part I: *Electromagnetic Phenomena*

The factors determining the magnetic flux density of a short coil containing a 'work piece' will be explored. The analytical solution for the electromagnetic Lorentz forces experienced by a cylindrical 'work piece' will be derived. The equations governing the *Leenov-Kolin effect* (electromagnetophoresis) will be reviewed with respect to spherical particles. Basic inductance and heating equations will be presented for completeness.

Part II: *Ceramic foam filters, characterization and hydrodynamics*

The ceramic foam filters used in this study are characterized with respect to physical, electrical and hydrodynamic criteria. Porosity, tortuosity and effective resistvity of 30, 40, 50 and 80 PPI ceramic foam filters are presented. Pore (cell), web and window diameters are determined and presented. Comparison is made to similar materials in the literature.

Part III: *Electromagnetically modified filtration, including gravity reference experiments, and priming*

Part III constitutes the 'heart' of the thesis. Filtration mechanisms are presented and discussed by way of dimensionless modelling parameters, and empirical models. Appropriate physical properties for use with analytical and numerical modelling are given. 2D axial symmetric flow fields are calculated. Results from early meniscus, batch and flow experiments are presented. The focus is on the obtained quantitative results for both gravity reference and electromagnetic filtration. The impact of electromagnetic priming is described in detail.

Part IV: A collection of the 8 main thesis articles, which are further divided into three main topics:

i. Electromagnetic phenomena including experimental, analytical and numerical modelling (2 articles).
ii. Filter morphology and liquid permeability, including experimental, analytical and numerical modelling (2 articles).
iii. Filtration of SiC particulates from liquid A356 aluminium under gravity (reference cases) and under the influence of electromagnetic Lorentz forces. The influence of Lorentz forces on the priming and subsequent filtration using gravity will also be discussed (4 articles).

“Progress is impossible without change, and those who cannot change their minds cannot change anything.”

-George Bernard Shaw (1856 - 1950),
“Everybody’s Political What’s What”, (1944).

ACKNOWLEDGMENTS

I would like to thank my primary supervisor, Prof. Ragnhild E. Aune for the opportunity to return to university to renew my education and increase my technical skills after many years in industry. The improvements gained in my article writing and new technical skills, such as numerical methods, will prove critical to my success in the remainder of my career.

I am deeply grateful for the technical reviews, electrical and mathematical guidance provided by my secondary supervisor, Prof. E.M. Jon Arne Bakken.

The moral support of Dr. Shahid Akhtar was crucial in surviving the transition from industry to academia. His skills in the casting laboratory and metallographic work have also been of vital importance to the outcome of this work.

The assistance of Dr. David Knight in the study of electromagnetic phenomena is also acknowledged. I am also thankful for the proof reading of the various manuscripts contained in this thesis by Dr. Allan MacRae, of MacRae Tech. Inc.

I wish to express gratitude to Egil Torsetnes at NTNU for helping with the design and construction of the experimental apparatus. Sincere gratitude is also due to Kurt Sandaunet and Arne Nordmark at SINTEF for their support and help, as well as for the use of the SINTEF laboratory.

I am indebted to a number of Master's students and researchers who have assisted me at various times, particularly to Robert Fritzsch, Kexu Zhang, and Behzad Mirzaei.

I would also like to thank my wife Elisabeth Stokker for accepting the disruption to our lives, taking care of our 3 children and allowing me the opportunity to apply myself to this task.

The funding and support through the RIRA project by the Norwegian Research Council (NRC) - BIP Project No. 179947/I40 and industrial partners: Hydro Aluminium AS, SAPA Heat Transfer AB, Alcoa Norway ANS, and SINTEF Materials and Chemistry are again acknowledged.

Mark William Kennedy
Trondheim, December 2012

SUMMARY

Solid inclusions can have serious detrimental effects to the quality of aluminium metal and the final properties of products produced from this metal. This research was conducted as part of the RIRA project, which had as an objective to removal all inclusions of >10μm. The intent of this portion of the research was to determine if it were possible to achieve greater efficiency of filtration using Ceramic Foam Filters (CFFs) *in combination with electromagnetic fields*.

It was known previously that electromagnetic fields applied to aluminium combined with electric current would produce Lorentz forces ($\vec{J}\times\vec{B}$), that could cause non-conducting solids (e.g. SiC and Al_2O_3) to migrate counter to these forces (*Leenov-Kolin effect*) and achieve particle collection at the walls of laboratory scale crucibles or flow channels. However, electromagnetic separation has not proven sufficiently practical for application within the aluminium industry. It was hoped that the combination of Lorentz forces with CFFs, would allow improved separation using practical equipment designs. CFFs could potentially benefit from Lorentz forces, either due to magneto-hydro-dynamic (MHD) recirculation of the metal for multiple filtration passes or via the *Leenov-Kolin effect* (electromagnetophoresis).

Electromagnetic phenomena were studied in detail, to allow the construction of appropriate coil designs, producing sufficient magnetic flux density. It was found during this review that errors of ~10-30% in flux density would result from assuming an infinitely long coil, depending on the coil and work piece geometry, and electromagnetic penetration depths. Review of the pertinent electromagnetic theory lead to the discovery of a little known means of analytically solving for the magnetic flux density of a short coil accounting for both coil shortness and the effect of a conducting work piece (e.g. a crucible full of liquid metal), published by Vaughan and Williamson in 1945. Use of this correlation would result in errors varying considerably with frequency from about 10% at low frequency to 1% at very high frequency, e.g. 100 kHz.

The frequency modified short coil correction factor proved key during this work, to the development for the first time of an accurate analytical solution to the time averaged value of the Lorentz forces in non-infinite coils. The final analytical equation was verified using the 2D axial symmetric FEM models and found to agree within about 30% over a range of about 9 orders of magnitude change in force. The use of a long coil assumption would have resulted in errors close to a factor of 2. This subsequently led to the creation of a new dimensionless *Leenov-Kolin number* to asses the relative impact of the

electromagnetic reaction force on spherical non-conductive particles in a conducting medium undergoing flow.

In order to execute the experimental program it was necessary to combine power supply and coil design, with new experimental, sampling and analytical procedures. Precision dimensioned coils were produced from mechanical grade copper tubing insulated with high temperature glass fibre. Filters were mounted in disposable 'filter bowls', constructed from standard materials used in the foundry industry. Metal was sampled using spectrographic disks which were machined, polished and photographed. Particles were counted using, macro-automated computer image analysis for particle counting. Used filters were sectioned using abrasive water jet cutting and mounted and polished for optical and SEM analysis.

Batch experiments were conducted (4) to determine the magnitude of the magnetic flux density, which could be safely applied to an aluminium melt, develop procedures and equipment (2), and study the effect of the magnetic field on the distribution of 2-30 μm SiC particles (16). An impact on the distribution of particles was clearly seen, cake formation over the filters was reduced ("disrupted") and particles were strongly biased towards the outer wall in the filters used (mainly 30 PPI). Evidence for bulk metal recirculation from below the filter and towards the walls of the crucible was observed during sectioning of used filters. Filtration efficiency could not be determined during the batch processing.

It was discovered (and subsequently a US patent application filed) during this phase of the work that *the magnetic field had a profound effect on the priming height of metal required for CFFs*, particularly for 'tight' 50 and 80 PPI filters. Filters were primed with as little as 100 mm without pre-heating, instead of requiring both preheating and metal heads of up to 400 mm. Special hot liquid metal experiments (2) were conducted to prove that the 50 and 80 PPI filters could not be primed with 150 mm of metal head in the absence of an electromagnetic field.

It was found that gas could be removed from these filters with near 100% efficiency after between 3 and 10 minutes of electromagnetic agitation or electromagnetic 'priming' using a magnetic flux density between 0.1 and 0.2 T. Wetting of the filter element by the aluminium was greatly improved with time. Higher casting rates (increased productivity) were subsequently found for well primed filters using standard metal casting heads.

Electrical properties (effective resistivity or conductivity) of 30, 40, 50 and 80 PPI CFFs were studied in detail during hot metal experiments (5) and subsequent cold analysis, in order to numerically model Lorentz forces produced within the CFFs using 2D axial symmetric FEM. A by-product of this effort was relatively accurate determination of filter tortuosity using novel electromagnetic induction methods. Filter tortuosity (from 1.3 to 3.2) and effective resistivity (from 1.5 to 3.7) were found to increase strongly with filter PPI from 30-80 PPI, having major significance for fluid flow, filtration efficiency and the Lorentz forces developed for a given flux density.

In order to numerically model the induced MHD mixing in the CFFs (a porous media), it was necessary to determine both the magnitude of the Lorentz driving forces and the inertial and viscous loss terms of the Navier-Stokes equation. Due to the higher than normal velocities induced by the MHD, it was necessary to determine both the first and second order terms for the Forchheimer equation. High precision measurements (70) were made with water of pressure gradient versus flow for about 8-10 flow rates (from 0.015 to 0.77 m/s), using 50 mm thick CFFs of 30, 40, 50 and 80 PPI, using long and short inlet lengths and with two different filter diameters (49 mm and 101 mm). Results were numerically modelled using 2D axial symmetric FEM to ensure that flow by-passing was not occurring with the 49 mm filters and to numerically arrive at the 101 mm filter's equivalent flow field diameter. Use of the 101 mm filters permitted independent confirmation of the 49 mm filter permeability results.

Additional permeability work was supervised, as part of a Masters thesis, "Liquid Permeability of Ceramic Foam Filters" (not reported here) to examine the statistical variability of CFF permeability between filters and within a single filter.

The morphology of CFFs was studied in detail as part of this work, determining the mean and standard deviation of the cell (pore), window and strut diameters, as well as filter total porosity. Both the first and second order Forchheimer coefficients were found to correlate best with the average measured window area for each filter type.

The measured pressure gradients could also be 'predicted' with reasonable precision using the best of the previously published correlations (±50%). Modified equations (originally by Dietrich and by Ergun) were developed which correlated the current data set with higher accuracy (±30%) and may help to achieve better generalized correlations for pressure drop in porous media.

Hot metal 'flow tests' (3 preliminary and 12 final) were conducted using 30, 50 and 80 PPI filters. It was again found that the magnitude of the magnetic field altered both the wetting, and particle distributions. It was further found that collection efficiency was reduced for the 50 and 80 PPI filters relative to the 30 PPI, when compared against appropriate gravity benchmark experiments. This is the reverse of the trend found in gravity filtration. The high effective resistivity and lower permeability of the 50 and 80 PPI filters appears to have reduced recirculation, as well as the effectiveness of the electromagnetic separation. According to the newly defined *Leenov-Kolin number,* electromagnetic separation should only be a significant mechanism for 30 PPI filters (and below). The 30 PPI filter achieved 47% overall filtration efficiency, while the 50 PPI only achieved 13% and the 80 PPI 29%.

2D axial symmetric MHD FEM modelling was performed using the measured permeabilties, and effective electrical conductivities for the filter. The resulting flow fields were found to corroborate the observed experimental phenomena. Greatly increased Lorentz forces and much higher recirculation were present within the 30 PPI filters, compared with the 50 or 80 PPI.

It was also found that the coarser particles were collected with lower efficiency than finer particles during electromagnetic filtration, again a reversal of the norm. The high velocity caused by MHD mixing appeared to be the cause. More particles were pushed through the filter due to the high velocity field. Once under the filter, coarser particles have a larger terminal settling velocity (*higher Gravitational number*) and tended to settle, due to gravity sedimentation, and did not recirculate for second or third passes.

For normal gravity filtration, correlations in accordance with previous literature (for well wet particulates) were found for the efficiency of filtration against velocity for the 30 PPI filters. Data was too limited for the 50 and 80 PPI filters to make firm conclusions.

New equations for calculating the interstitial velocity, single 'event' or cell efficiency, incorporating the tortuosity were identified. Comparison was made between traditional exponential filter empirical models (effectively assuming isotropic filter properties) and alternate methods based on independent statistical events, showing equivalence with the previous mathematics if a constant efficiency were assumed. The new equation does not require an assumption of isotropic filter properties and may permit improved models with variable efficiency by filter depth to be developed in the future.

Due to the very high particle loadings used in this research effort, equivalent metal masses many times the norm were filtered. It could, therefore, be concluded that it is possible to utilize CFF filters much longer than is the current industrial practice. If for example, four times the standard area of filters were used for any given casting rate, but for four times as long, the same number of filters would be used, and dramatically improved particle collection efficiency would likely be obtained.

In relation to the RIRA project objective of removing all particles >10μm, the following results were obtained:

i. >98% of particles larger than 10 μm were removed at low filtration velocity (~1 mm/s) using 80 PPI filters, which had been electromagnetically primed, and
ii. >94% of particles larger than 10 μm were removed at low filtration velocity (~2 mm/s) under gravity filtration using 30 PPI filters.

Future work:

In the continuation of this line of research, the following options may be worth further consideration:

i. A stack of 2 or 3, 50 mm thick filters (e.g. 30 or 50 PPI) will achieve much higher efficiency according to the accepted empirical filtration models, and can be primed using electromagnetic priming.
ii. Homogeneous magnetic fields can be produced using coils of non-constant pitch in order to eliminate MHD mixing and maximize the *Leenov-Kolin effect*. Such coils can be accurately designed by the validated 2D FEM models produced during this research.
iii. Lower PPI filters (10 or 20 PPI) can also be used to achieve increased benefit from the *Leenov-Kolin effect*.
iv. Lower casting velocity (<1 cm/s and probably between 2 and 5 mm/s), could be used to dramatically improve the efficiency of standard 30 or 50 PPI filters under gravity casting conditions. This would require increased filter area to maintain the productivity.
v. Alternate frequencies should be explored, e.g. lower for deeper penetration in large filters or higher to enhance the *Leenov-Kolin effect* at the walls.
vi. Or some combination of the above.

*Keywords***:** Electromagnetic, Lorentz, Filtration, CFF, Aluminium

SUPPLEMENTS

The present thesis includes the following supplements:

Part I: *Electromagnetic phenomena*

Supplement 1: "Review of Classical Design Methods as Applied to Aluminum Billet Heating with Induction Coils," M.W. Kennedy, S. Akhtar, J.A. Bakken, R.E. Aune, *EPD Congress 2011*: John Wiley & Sons, ISBN 978-1-1180-3652-5, (2011), 707-722.

Supplement 2: "Analytical and Experimental Validation of Electromagnetic Simulations Using COMSOL®, re Inductance, Induction Heating and Magnetic Fields," M.W. Kennedy, S. Akhtar, J.A. Bakken, R.E. Aune, *COMSOL Conference 2011 - Proceedings CD*: COMSOL, Burlington, MA, USA, ISBN 978-0-9839688-0-1, (2011), 1-9.

Part II: *Ceramic foam filters, characterization and hydrodynamics*

Supplement 3: "Characterization of Ceramic Foam Filters used for Liquid Metal Filtration," M.W. Kennedy, K. Zhang, R. Fritzsch, S. Akhtar, J.A. Bakken, and R.E. Aune*, Metallurgical and Material Transactions B, DOI 10.1007/s11663-013-9799-7,* ISSN 1073-5615, Published On-line*,* (2013), 1-20.

Supplement 4: "Determination and Verification of the Forchheimer Coefficients for Ceramic Foam Filters Using COMSOL CFD Modelling," M.W. Kennedy, K. Zhang, J.A. Bakken, and R.E. Aune, *COMSOL Conference 2012 - Proceedings CD*: COMSOL, Burlington, MA, USA, ISBN 978-0-9839688-0-1 (2012), 1-7.

Part III: *Electromagnetically modified filtration, including gravity reference experiments, and priming*

Supplement 5: "Electromagnetically Enhanced Filtration of Aluminum Melts.," M.W. Kennedy, S. Akhtar, J.A. Bakken, and R.E. Aune, *Light Metals 2011*: Wiley-Blackwell, ISBN 9781118029350, (2011), 763-768.

Supplement 6: "Electromagnetically Modified Filtration of Liquid Aluminium with a Ceramic Foam Filter," R. Fritzsch, M.W. Kennedy, S. Akhtar, J.A. Bakken, and R.E. Aune, Accepted for publication by *Journal of Iron and Steel Research, International*, (2012), 1-4.

Supplement 7: "Electromagnetically Modified Filtration of Aluminum Melts Part I: Electromagnetic Theory and 30 PPI Ceramic Foam Filter Experimental Results," M.W. Kennedy, S. Akhtar, J.A. Bakken, and R.E. Aune, *Metallurgical and Material Transactions B, DOI 10.1007/s11663-013-9798-8,* ISSN 1073-5615, Published On-line, (2013), 1-15.

Supplement 8: "Electromagnetically Modified Filtration of Aluminum Melts Part II: Filtration Theory and Experimental Filtration Efficiency with and without Electromagnetic Priming for 30, 50 and 80 PPI Ceramic Foam Filters," M.W. Kennedy, R. Fritzsch, S. Akhtar, J.A. Bakken, and R.E. Aune, Submitted to *Metallurgical Transactions B*, (2012), 1-69.

PRESENTATIONS

Mark William Kennedy, Shahid Akhtar, Jon Arne Bakken, Ragnhild Elisabeth Aune, "Review of Classical Design Methods as Applied To Aluminum Billet Heating with Induction Coils," *EPD Congress 2011*, San Diego, 27 February – 3 March, (2011).

Mark William Kennedy, Shahid Akhtar, Jon Arne Bakken, Ragnhild Elisabeth Aune, "Electromagnetically Enhanced Filtration of Aluminum Melts," *TMS Light Metals 2011*, San Diego, 27 February – 3 March, (2011).

Mark William Kennedy, Shahid Akhtar, Jon Arne Bakken, Ragnhild Elisabeth Aune, "Analytical and Experimental Validation of Electromagnetic Simulations Using COMSOL®, re Inductance, Induction Heating and Magnetic Fields," *COMSOL Conference 2011*, Stuttgart Germany, 26-28 October, (2011).

Mark William Kennedy, Robert Fritzsch, Shahid Akhtar, Jon Arne Bakken and Ragnhild Elisabeth Aune, "Effect of Electromagnetic Force on the Distribution of Inclusions Removed from Liquid Aluminium by a Ceramic Foam Filter," *Euromat 2011*, Montpellier, France, 12-15 September, (2011).

Mark William Kennedy, Kexu Zhang, Shahid Akhtar, Jon Arne Bakken, and Ragnhild Elisabeth Aune , "Determination and Verification of the Forchheimer Coefficients for Ceramic Foam Filters Using COMSOL CFD Modelling," *COMSOL Conference 2012,* Milan, Italy, 10-12 October, (2012).

Robert Fritzsch, Mark William Kennedy, Shahid Akhtar, Jon Arne Bakken, and Ragnhild Elisabeth Aune, "Electromagnetically Modified Filtration of Liquid Aluminium with a Ceramic Foam Filter," *Electromagnetic Processing of Materials Conference*, Beijing, China, 22-24 October, (2012).

PATENT APPLICATIONS

M. W. Kennedy, R. Fritzsch, S. Akhtar, J. A. Bakken, and R. E. Aune, "Apparatus and Method for Priming a Molten Metal Filter," *U.S. Provisional Patent Application*, 61/639,196, (2012), 1-26. See Appendix 1.

PAPERS AS SECOND/THIRD AUTHOR

R. Fritzsch, M.W. Kennedy, S. Akhtar, J.A. Bakken, and R.E. Aune, "Electromagnetic Priming of Ceramic Foam Filters (CFF) for Liquid Aluminium Filtration," Accepted for *TMS Light Metals 2013*, 3-7 March, (2013), San Antonio, Texas.

R. Fritzsch, B. Mirzaei, M.W. Kennedy, and R.E. Aune, "Automated Quantification of SiC-particles in Solidified A356 Aluminium Using Image Pro-Plus 7.0," Accepted for *TMS Light Metals 2013*, 3-7 March, (2013), San Antonio, Texas.

CONTENTS

Chapter 1

INTRODUCTION

Inclusions are both indigenous and exogenous particulates that are present in commercial metals such as aluminium. If large individual or large numbers of inclusions are present, they can have a significant negative impact on the appearance, mechanical and chemical behaviour of products produced from the metal. Aluminium is known to contain large numbers of both indigenous and exogenous inclusions ≤ 50 μm in size, e.g. typically <1 ppm by volume or <100,000 inclusions of >20 μm per kg of metal as detectable using a Liquid Metal Cleanliness Analyzer, LiMCA [1]. Depending on the final application of the aluminium, inclusions can render the metal 'not fit for purpose', and result in serious economic consequences to metal producers.

According to Groteke [2], solid inclusions can have negative effects on the machinability, static and dynamic mechanical properties, as well as leading to increased gas porosity and shrinkage of the metal during casting. Inclusions can be highly detrimental to a number of high value products such as in automotive and aeronautic applications [3], foil and lithographic sheet [4], can body stock and computer disks [5], sheet ingot and wire rod production [6]. Inclusions also decrease the corrosion resistance [7] and can have detrimental effects on the surface finish of the end product [8].

It is not surprising that the aluminium industry has developed a number of treatment processes to improve metal cleanliness, given the large number of high value products whose quality can be adversely affected by inclusions. These treatment processes include: settling, flotation, degassing, and liquid metal filtration using Particle Deep Bed Filters (PDBFs) [9], Bonded Particle Filters (BPFs) [10], and Ceramic Foam Filters (CFFs) [5, 11]. CFFs are the most commonly applied filtration process and have been used to filter >50% of the world production of aluminium since the 1990's [5].

Inclusions in aluminium may be particles, bifilms [12] or clusters of: oxides (Al_2O_3, SiO_2), spinels ($MgO{\cdot}Al_2O_3$), carbides (SiC, Al_4C_3), nitrides (AlN),

borides (TiB_2), sulfides, phosphides and intermetallics [2], with a higher melting point and typically with a significantly higher hardness than the host metal. Some of the inclusions found in aluminium are summarized in Table 1.1 [13].

Table 1.1 Typical Inclusions in Aluminium [13]

Inclusion Type		Form	Specific Gravity (g/cm^3)	Physical Dimensions (μm)
Oxides	Al_2O_3	p, (s)	4.0	0.2-30 (10-5000)
	MgO	p	3.6	0.2-30
	$MgO{\cdot}Al_2O_3$	p	3.6	0.2-30
	SiO_2	p	2.6	0.2-30
Chlorides	NaCl	p	2.2	0.1-5
	KCl	p	2.0	0.1-5
Carbides	Al4C3	p	2.4	0.5-25
	SiC	p	3.2	0.5-25
Nitrides	AlN	p	3.2	10-50
Borides	TiB_2	p, (c)	4.5	1-10 (30)
	AlB_2	p	3.2	0.1-3
p=particles, s=skins, c=clusters				

It can be clearly seen from Table 1.1, that many inclusions are larger than 10 μm and below 20 μm. These inclusions are problematic, in that they are difficult (or impossible) to quantify via LiMCA, but still large enough to potentially have catastrophic impacts on products, particularly thin products like: foils, heat exchange tubing and beverage cans, and for surface critical products like lithographic plate. Filtration efficiency data in this size range of particulates is almost non-existent, but extrapolation from larger sizes would lead one to conclude efficiencies would be in the range of 50-70%, depending on filtration velocity [14].

The filtration efficiency of CFFs can easily be improved by operating at lower velocity [15], or using thicker or tighter filters [14]; however, these options have the drawbacks of either lower productivity or requiring high priming or operational 'heads' to produce the required gravity pressure driving forces. The motivation of this work was, therefore, to determine if it were possible to overcome these inherent challenges by applying electromagnetic forces to the normal gravity filtration process using CFFs, to achieve increased filtration efficiency for particulates of >10 μm, at filtration velocities acceptable to industry.

1.1 RIRA Project - Thesis Objectives and Methods

This research was conducted as part of the RIRA project, which had as an objective to removal all inclusions of >10 μm. The RIRA project had a secondary objective to develop new methods of inclusion separation, e.g. electromagnetic separation. The intent of this part of the research effort was to find ways to combine electromagnetic fields with Ceramic Foam Filters (CFFs), to determine if it were possible to achieve greater efficiency of filtration for liquid aluminium.

The main objectives of this research included:

1. How high a magnetic flux density can be safely applied to liquid aluminium (meniscus experiments)?
2. How do the coil, work piece geometry, current and temperature affect the magnetic flux density (billet experiments, Analytical/COMSOL modelling)?
3. How do the filter types, time and coil magnetic flux density, affect the particle distribution within and over the filters (batch experiments)?
4. What are the hydrodynamic/magnetohydrodynamic (MHD) properties within the filter media (permeability, pore/cell size, effective resistivity, CFD modelling)?
5. How does the filter type, with and without a magnetic field affect the final obtained filtration efficiency as a function of both velocity and particle size (flow tests)?

The phenomena involved in these experiments included, but were of course not limited to:

- Induction (using helical induction coils)
- Electromagnetic fields
- Lorentz forces (MHD)
- *Leenov-Kolin effect* reaction forces
- Porous media fluid mechanics (permeability)
- Fundamental filtration mechanisms

The phenomena listed above were investigated via a combination of the following study methods:

- Literature and theory
- Analytical solutions
- Empirical measurements
- Empirical modelling
- Finite element modelling

Thus, the present work is intended to trace the following flow diagram:

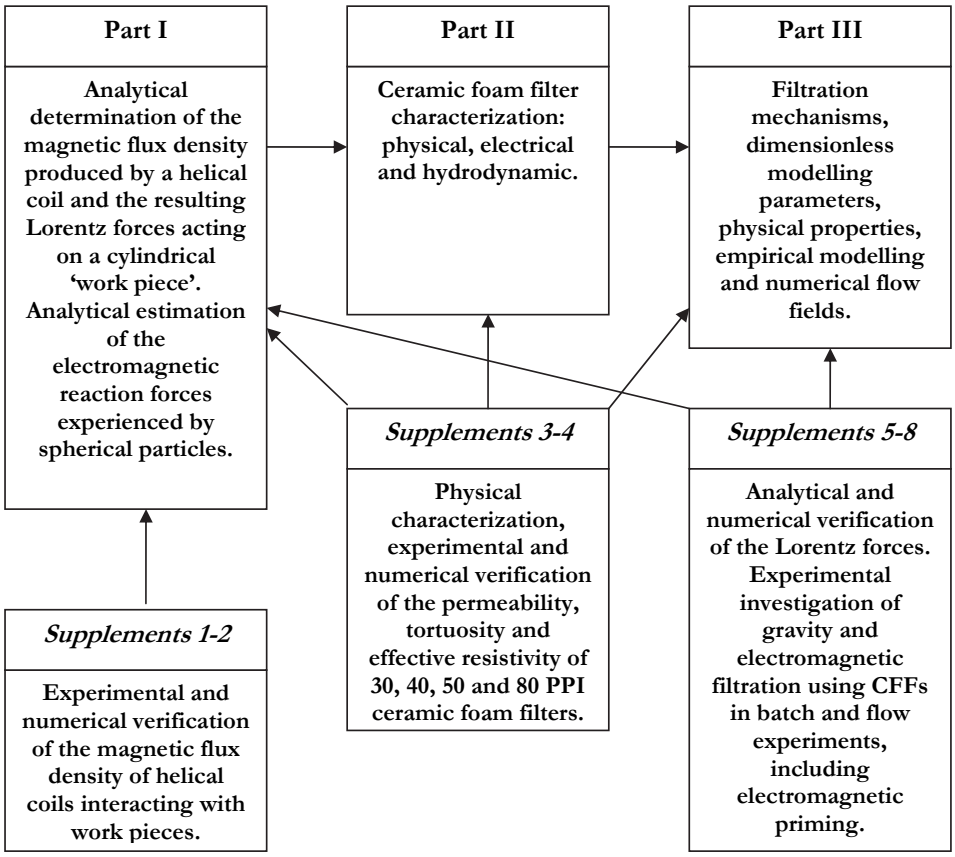

Figure 1.1− Schematic outline of the thesis and *Supplements*.

This thesis includes the following *Supplements*:

Part I:

Supplement 1 describes the investigation of classical induction heating literature, which was required in order to construct the induction coils used in the experimental program. It was found that the magnetic flux density of short coils was determined not only by the current and coil turns per unit length, but also by a complex interaction of the coil geometry (diameter to length ratio) with that of the 'work piece' or liquid metal, and with the applied frequency and the electrical conductivities. The 1945 correction factor of Vaughan and Williamson [16] was found to be the most accurate design method, when compared against rudimentary

induction heating experiments on 'raw' billet sections. Vaughan and Williamson's equation was not known to the induction industry prior to this publication, but the figure produced by Tudbury in 1960 was [17]. It was not understood that the graph of "work piece shortness correction factor" produced by Tudbury, was in fact the square of Vaughan and Williamson's equation, as Tudbury had failed to reference his sources. Identifying the original and more fundamentally useful equation, thus represents a significant, if simple contribution to the theory in this field.

In *Supplement 2*, a 2 D axial symmetric finite element model is described in some detail. The exact analytical solution to a current sheet inductor was used to determine the required size of the 'magnetic domain' and achieve inductance agreement of 1 part in 10000. The model was validated against power, magnetic flux density and inductance measurements made at 50 Hz. Mesh spacing and coil domain type for high frequency were determined by comparison of numerical and analytical heating and resistance estimates. A frequency correction to Vaughan and Williamson's equation, utilizing the electromagnetic penetration depth was proposed. The new equation was shown to significantly improve analytical estimates for low frequency, in comparison to the numerical results.

Part II:

In *Supplement 3*, the ceramic foam filters (CFFs) used in this study of 30, 40, 50 and 80 PPI are characterized. Measurements of porosity, tortuosity, effective electrical resistivity, cell (pore), web and window diameters are determined. The main focus is on the first and second order, Darcy and non-Darcy coefficients for use with the Forchheimer equation. Results are measured using two different filter types, with long and short inlet lengths at 8-10 different flowrates, and moving between laminar and turbulent inlet conditions. Experimental results are compared against analytical model results and 2D axial symmetric FEM modelling showing agreement with less than 7% error. Both first and second order Forchheimer coefficients were found to correlate with the measured CFF window area. Comparisons are made with previously published correlations and improved correlations are presented.

Supplement 4 is similar in content to *Supplement 3*, but with focus on only the permeability data and the use and development of the 2D axial symmetric finite element model using COMSOL® 4.2a.

Part III:

Results from the early stages of the theoretical review and process experiments, including meniscus and batch filtration results are presented in *Supplement 5*. Development of the coil design from a long, low flux density coil, to a short multi-layer coil, with a corresponding 100% increase in peak flux density is illustrated.

Very large electromagnetic menisci were produced using the new coil configuration, leading to powerful metal agitation and oxidation. Changes were required to the equipment design to allow a substantial metal height over the top of the coil, in order to prevent the formation of a meniscus and attendant oxidation.

The preliminary batch filtration experiments showed evidence of strong metal recirculation from below the filter, pushing casting sand into the bottom of the filter and requiring further modifications to the design of the equipment to prevent contamination (ceramic plate on the bottom).

Supplement 6 reviews the impact of Lorentz forces and more particularly the curl in the obtained Lorentz forces caused by the higher effective filter electrical resistivity. Using a 2D axial symmetric FEM model, accurate estimates were made of the Lorentz forces using the measured filter electrical resistivities, combined with measured filter liquid permeabilities, to predict the fluid flow fields. The results were in good agreement with the experimental observations reported in *Supplement 5*.

The impact of the electromagnetic flux density on priming is discussed and data provided, showing that priming should not be possible for 50 and 80 PPI filters in the absence of the induced Lorentz forces.

Photographic and SEM evidence from more recent batch experiments is presented, showing the progressive removal of gas and improvement of wetting achieved with the application of electromagnetic priming. Batch test results indicated a redistribution of particulates towards the outer wall of the crucible, in accordance with the predicted flow fields and the *Leenov-Kolin effect*.

In *Supplement 7* the analytical solution for the Lorentz forces in a short coil is presented. Previously published metallurgical literature contained equations, which confounded the real and imaginary parts of the equation for the 'real' or time averaged (RMS) forces produced in an 'infinite' coil and could not be used for any practical purpose. The frequency modified short coil correction factor, which was developed during the current research effort, was found to apply also to the strength of the Lorentz forces produced by short coils. The new analytical equation allowed for accurate comparison to be made with the estimates produced using 2D axial symmetric FEM modelling. Agreement was within about 30% over a range covering 9 orders of magnitude change in force.

The *Leenov-Kolin* formulae are presented to relate the Lorentz forces, to the reaction forces experienced by conductive and non-conductive spherical particles.

Preliminary flow experimental results are presented that show that the changes in filter wetting and particle distribution observed during the batch experiments also apply to the flow experiments. Filtration using an electromagnetic field is shown to have reduced the filtration efficiency and to have reversed the normally expected trend between particle size and filtration efficiency (now decreasing for larger sized particles). Empirical filtration modelling is introduced, indicating that the source of the lower overall filtration efficiency for the electromagnetic experiments, might have been the high induced interstitial liquid velocity.

Particle agglomeration is suggested to play a role in the observed 'flat' efficiency versus size relationship for the gravity filtration reference experiment, based on observations of few individual particles and many agglomerates over, in and under the filter elements.

Supplement 8 represents the culmination of the research effort into electromagnetically modified filtration. The physics and physical processes involved in gravity and electromagnetic filtration are reviewed in some detail and the relative effectiveness of different mechanisms explored by examining the magnitudes of various dimensionless force ratios. A new *Leenov-Kolin number* is proposed to define the relative impact of electromagnetic separation on spherical particles in a flowing metal.

New equations are developed, using the measured tortuosity, with regards to the interstitial melt velocity and filtration efficiency. An alternate means of empirically modelling CFF filtration efficiency is proposed, which uses discrete event probabilities and avoids the need to assume that the filters are isotropic media.

The filtration efficiency as a function of velocity under gravity filtration conditions, both overall and as functions of particle size ranges, is presented for 30, 50 and 80 PPI CFFs. Sufficient results were available for the 30 PPI CFFs to conclusively show that the overall efficiency decreases with increased superficial filtration velocity, in agreement with previous literature.

Results for electromagnetic filtration are also presented and found to 'counter-intuitively' reverse the normal trend both for efficiency vs. PPI and for efficiency vs. particle size (in accordance with the results from *Supplement 7*). Results from 2D axial symmetric MHD modelling using FEM, are shown to agree with the experimental results, indicating that the 30 PPI filters experience both greater Lorentz forces and higher rates of fluid recirculation. 30 PPI filters therefore benefit more from the *Leenov-Kolin effect* and have a larger portion of particulates recirculate for multiple filtration passes. For the 30 PPI filters, it was shown that the Lorentz forces

could cause sufficiently powerful fluid flows, to result in physical damage to the filter elements.

During SEM examination of used filter sections from gravity filtration, evidence was found supporting both the role of impaction/interception for 'web-like' 30 PPI filters and for greater levels of gravity settling in the more 'pore-like' 80 PPI filters. Many indications were found during optical and SEM analysis of both filter sections and metal samples, to suggest that clustering or agglomeration played a major role in determining the obtained experimental filtration efficiencies under gravity. Few single particles were present in any of the samples and many bridges often in combination with bifilms were observed. Bifilms were observed many times decorated with particles, either unfurled or wrapped into more spherical shapes.

A new macro-automated computerized particle counting procedure was applied to the 'fast cooled' spectrographic disks and was shown by comparison with a manually controlled count to give excellent results (~3% bias in efficiency). The new counting method represents a significant advance, in that it was not practical to determine the efficiency as a function of size for particles in the size range <20 μm previously, due to the time required to perform the analysis work or the fact that LiMCA could not measure such particles 'on-line'. The variability of results from disk to disk on starting samples, suggested that additional samples are required in the future, to quantify and reduce this source of experimental variance. Operation with lower particle concentrations over longer durations is now possible, due to the optimized analytical procedure; hence, improved statistical reliability can be obtained in future work by the use of greater number of starting and time/weight based samples.

Concrete recommendations were made for future work, using different possible coil designs, filter configurations and process parameters (e.g. frequency or velocity).

Chapter 2

PART I – THEORY AND VERIFICATION

ELECTROMAGNETIC PHENOMENA

2.1 ***Leenov-Kolin Effect, Electromagnetophoresis*** [see *Supplement 7*]

The principle of electromagnetic separation by reaction to Lorentz forces ($\vec{J} \times \vec{B}$) was described mathematically in 1954 by Leenov and Kolin [18]. A schematic representation of the Lorentz forces and the reaction forces acting on a non-conducting particle, in a curl free magnetic field is presented in Figure 2.1.

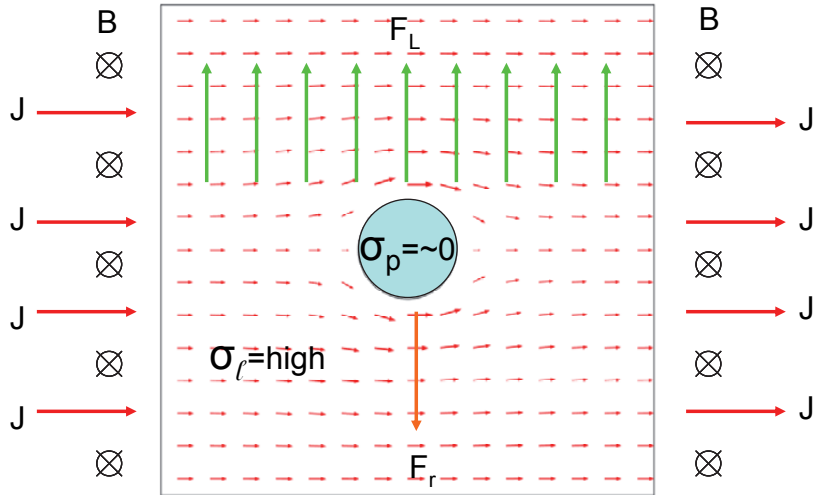

Figure 2.1–The Lorentz forces (F_L) and the reaction forces (F_r) acting on a non-conducting particle in a curl free magnetic field. Note the impact of the particulate on the current distribution. (J = current density [A/m^2]; B = magnetic flux density [T]; σ_l = liquid phase electrical conductivity [S/m]; σ_p = particulate electrical conductivity [S/m]), [*Supplement 7*].

In the concept shown in Figure 2.1, non-conductive particles migrate through the melt in a direction opposite to the Lorentz forces produced by the cross product of a homogeneous magnetic field ($\vec{B}$) and a uniform current distribution ($\vec{J}$), i.e. ($\vec{J} \times \vec{B}$). The non-conductive particles present in the fluid will experience a pressure gradient created by the Lorentz forces, but not the Lorentz forces themselves. The particles are 'pinched' experiencing a reaction force, which causes them to migrate in a direction counter to the Lorentz forces. An early example of the application of this technique was reported in 1968 by Vilinskas and Schiltz [19], i.e. the removal of zirconium oxide spheres from liquid sodium. Various methods of applying this principle in metallurgical processing were patented by Conti et al. in 1989 [20]. More serious efforts to develop this technology began in the 1990's [21-24] and have continued up to date [25-49].

There are several studies reported in the literature illustrating the migration of oxide and SiC inclusions under the influence of electromagnetic fields [21, 24, 36, 50, 51]. It has previously been shown by Takahashi *et al*. [36] that 1.1 mass % of SiC particles of 20.5 μm in liquid aluminium at 1073 K, will migrate in response to an applied electromagnetic field from an induction coil as shown in Figure 2.2.

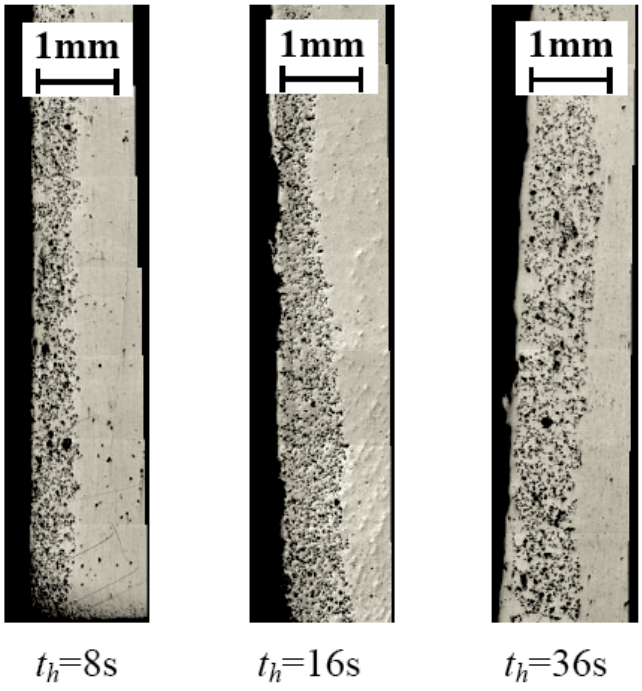

Figure 2.2−Migration of 20.5 μm SiC particles in liquid aluminium at 1073K, contained in a 94 mm diameter crucible in response to 163 A applied to a 15 turn induction coil at 30 kHz [36].

The results shown in Figure 2.2, indicate that the SiC particles are quickly collected into a depth roughly corresponding to both the hydrodynamic boundary layer and the electromagnetic penetration depth, δ_p, which in the case shown in Figure 2.2 is ~1.5 mm. The confluence of these two layers might be called the '*electromagnetic boundary layer*'. Similar results have recently been presented for 30-100 μm alumina particles in commercially pure aluminium at 993 K, with a 0.04 T field applied to a small 10 mm crucible, at 20 kHz as shown in Figure 2.3 [52].

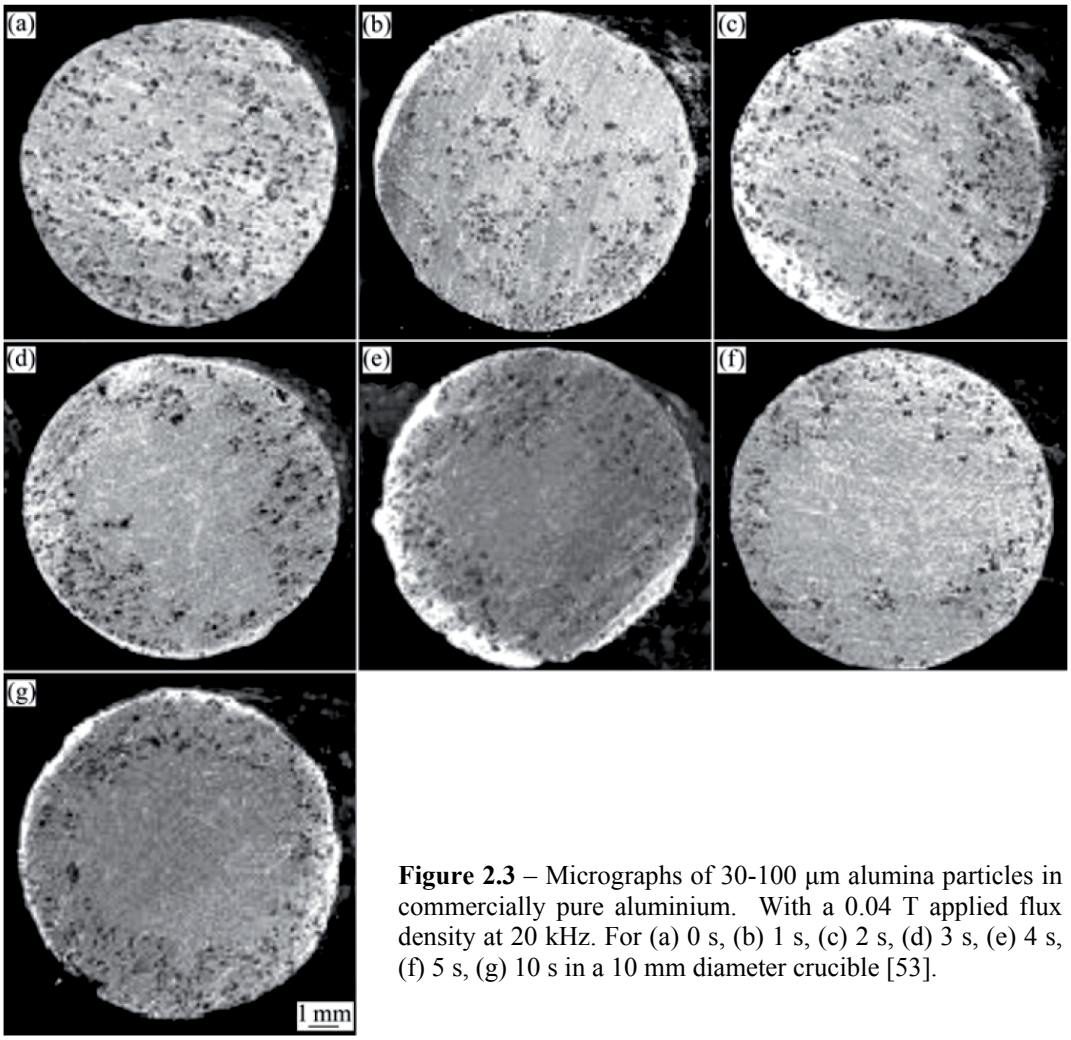

Figure 2.3 – Micrographs of 30-100 μm alumina particles in commercially pure aluminium. With a 0.04 T applied flux density at 20 kHz. For (a) 0 s, (b) 1 s, (c) 2 s, (d) 3 s, (e) 4 s, (f) 5 s, (g) 10 s in a 10 mm diameter crucible [53].

While the potential of this innovative method has been demonstrated in small batch tests, its implementation in the aluminium industrial for continuous flow conditions has not been reported. A significant problem is that powerful and curl free Lorentz forces, as shown previously in Figure 2.1 are not possible to achieve industrially using standard helical induction coils, due to so-called coil

'*end effects*'. If a curl exists in the Lorentz force field, it will produce electromagnetic or Magneto-Hydro-Dynamic (MHD) stirring. This is referred to as the "secondary mixing effect", as observed by several investigators [22, 34]. These mixing effects result in particles being rapidly transported from the bulk of the melt to the crucible walls (in small scale batch experiments), where the stagnant hydrodynamic boundary layers exist, as shown in Figures 2.2 and 2.3. This results in rapid and effective removal of particulates in small crucibles, but is not a practical alternative for industrial scale equipment. The available volume in which to 'store' collected particulates is very small and the depth and therefore volume of influence of high frequency induction fields is limited. Risk of re-entrainment of collected particles is also significant.

In 1990 El-Kaddah *et al.* [22, 53] presented the concept of combining electromagnetic separation with filtration and baffles to control secondary mixing effects, and to enhance the inclusion removal efficiency as shown in Figure 2.4 (a). Sufficient experimental verification of this concept was, however, not provided at that time. A more recent patent application on the use of flow modifying devices of high collection area has been filed by other researchers, and is presented in Figure 2.4 (b) [54].

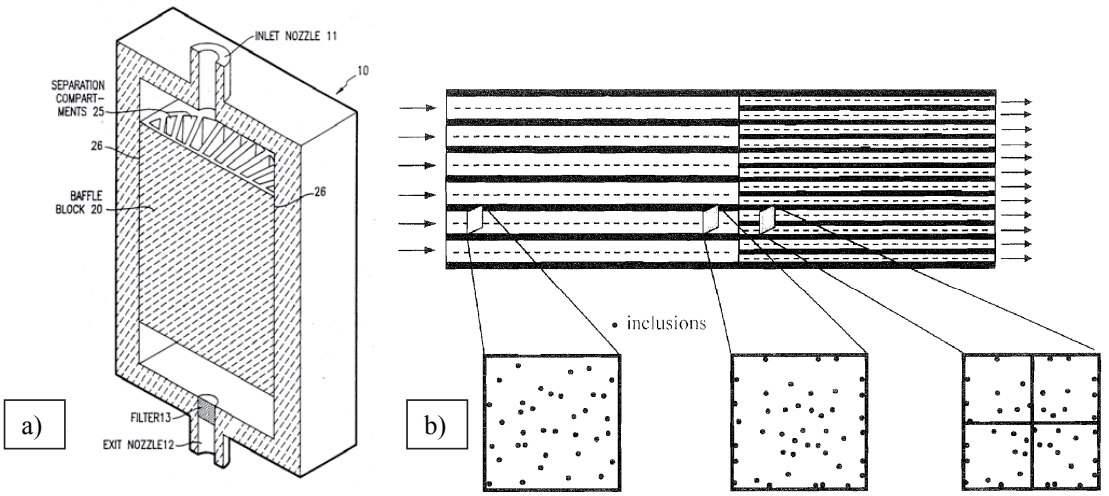

Figure 2.4–Advanced designs for electromagnetic separation of particulates from aluminium, incorporating flow control devices to *reduce secondary mixing effects* and provide maximum stagnant boundary layers for collection (a) El-Kaddah [53], (b) Shu *et al.* [54].

The application of CFFs with a helical induction coil as in the current research, is somewhat similar in concept to that shown in Figure 2.4, with the added possibility that the so called 'secondary mixing effects', i.e. MHD stirring can also result in back mixing of particulates for multiple filtration possibilities and the filter itself should continue to function as an effective phase separation medium for the overall gravity driven bulk fluid flow.

Leenov and Kolin [18] derived the following equation describing the reaction force acting on a low conductivity particle present in a high conductivity fluid, when subjected to a curl free Lorentz force field:

$$\vec{F}_r = -\frac{3}{2}\frac{\sigma_l - \sigma_p}{2\sigma_l + \sigma_p}\frac{\pi d_p^3}{6}\vec{F}_L \qquad [1]$$

where $\vec{F}_r$ is the reaction force experienced by a particulate [N], $\vec{F}_L$ is the Lorentz force acting on the fluid [N/m^3], σ_l the electrical conductivity of the liquid phase [S/m], σ_p the particle electrical conductivity [S/m], and d_p the particle diameter [m]. For non-conducting particles Eq. [1] can be reduced to the following:

$$\vec{F}_r = -\frac{\pi d_p^3}{8}\vec{F}_L \qquad [2]$$

where

$$\vec{F}_L = \vec{J} \times \vec{B} \qquad [3]$$

and assuming that

$$\nabla \times \vec{F}_L = 0 \qquad [4]$$

The particles can then be collected into the boundary layers through the reaction force presented in Equations [1] or [2]. A limited volume, however, exists within which to accumulate particles and the ability of the particles to resist re-entrainment can be questioned.

2.2 Analytical Solution for the Time Averaged (RMS) Lorentz Forces Produced by an Induction Coil

To apply Equations [1] or [2], one must be able to quantify analytically the magnitude of the Lorentz forces ($\vec{J} \times \vec{B}$) applied to the fluid containing the particulates. In the case of a short induction coil, one must quantify the:

i. time averaged surface z-component of the magnetic flux density (B_z) produced by the induction coil,
ii. magnitude of the induced current $\vec{J}(r)$, local magnetic flux density $\vec{B}(r)$ and the phase shift between them at each radial position, *(r)* in the metal, and
iii. the applied frequency and work piece electrical conductivity,

in order to obtain the required analytical solution.

2.2.1 Magnetic Flux Density of Real Coils with Work Pieces [*Supplements 1-2*]

Estimates for magnetic flux densities and related inductance or induction calculations are frequently made using the so called 'long coil assumption'. The magnetic field of a very 'long' coil can be found using Ampère's original law [55] ignoring the displacement current [56]:

$$\oint_C \vec{B} \bullet \delta\vec{l} = \mu_0 \mu_r \iint_s \vec{J} \bullet \delta\vec{s} = \mu_0 \mu_r I_{enclosed} \qquad [5]$$

where $\vec{B}$ [T] is the magnetic flux density parallel to the an infinitesimal vector length $\delta\vec{l}$ and tangent to the closed curve *C*, μ_0 is the permeability of free space (4π x10^{-7} [H/m]), μ_r is the relative magnetic permeability (with recommended values of 1.0000 for air, copper and aluminium [unitless]), $\vec{J}$ [A/m^2] is the current density normal to closed curve *C*, [m^2], $\delta\vec{s}$ is an infinitesimal vector area of surface S normal to $\vec{J}$ and $I_{enclosed}$ [A] is the total enclosed current or $\vec{J} \cdot S$. The orientation of $\vec{B}$ relative to $\vec{J}$ is given by the right hand rule, and both are vector quantities. When written as *B* and *J* in this text, Root Mean Square (RMS) magnitudes are implied.

In Figure 2.5, Equation [5] is applied to a finite section of an infinite solenoidal coil. The total current enclosed by the closed path, whose sides are length l_c is clearly $N_c \cdot I_c$. Current is passing out of the page at the top and into the page at the bottom. The flux density within the coil is B_∞, which has a direction from left to right in accordance with the right hand rule. As the coil extends from and to infinity, the flux lines are parallel to l_c, having only a z-component. Thus it can be immediately concluded that there is no magnetic flux external to the coil and $B \cdot -l_c = 0$. On both of the sides of the box, the magnetic flux is perpendicular to the length and thus there is no parallel component and $\vec{B} \bullet \delta\vec{l} = 0$. Integrating around the closed path, it is then immediately seen that Equation [5] yields $B_\infty \cdot l_c = \mu_0 \mu_r N_c \cdot I_c$. Solving for B_∞ results in Equation [6] [56].

$$B_\infty = \frac{\mu_0 \mu_r N_c \cdot I_c}{l_c} \qquad [6]$$

where B_∞ is the flux density [T] of a finite length l_c [m] of a very 'long' or infinite coil, N_c is the number of turns of the coil and I_c is the current per turn [A RMS].

Equation [6] is however, not strictly valid for a coil with any length less than 'infinity'. In a short coil the flux is not homogenously distributed and is not parallel with the coil axis, having both a z-component and an r-component. The magnetic flux density external to the coil is also non-zero.

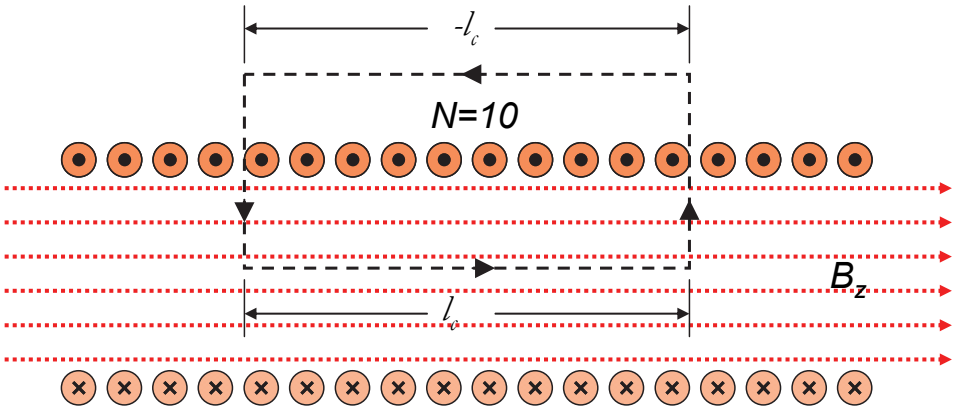

Figure 2.5 - Magnetic field produced by 10 turns of an infinite solenoid, indicating a magnetic field present only on the interior of the coil and in the z-direction [56].

The inductance of a 'real', i.e. non-infinite coil, is determined by the number of flux linkages per unit current [*Supplement1*]:

$$L_c = \frac{A_c N_c B_z}{I_c} \qquad [7]$$

where L_c is the inductance of the coil [H], A_c is the area of the coil [m^2], and B_z is now the z-component of the magnetic flux density [T]. B_z being the z-component of the magnetic flux density, clearly links all the coil turns N. The radial component B_r will be symmetrical around the central axis, and integrating in polar coordinates will result in zero net contribution to inductance.

In 1879 Lorenz [57] published a formula to solve for the inductance of a current sheet inductor of finite length, such as the one shown in Figure 2.6. Lorenz' formula required the solution to elliptical integrals of both the first and second kinds. In 1909, Nagaoka [58] reformulated Lorenz' formula using the shape factor (D_{cs}/l_c), where D_{cs} is defined as the current sheet diameter [m]. Nagaoka tabulated the results for his short coil correction factor k_N to 6 decimal places, for discrete intervals of the shape factor (D_{cs}/l_c). Weaver has now written software to numerically solve the same equation to double precision [59], and this software was used in the preparation of this thesis [60]. Equation [7] can be re-written using the Nagaoka coefficient [*Supplement 1*]:

$$L_c = k_N \frac{A_c N_c B_\infty}{I_c} \qquad [8]$$

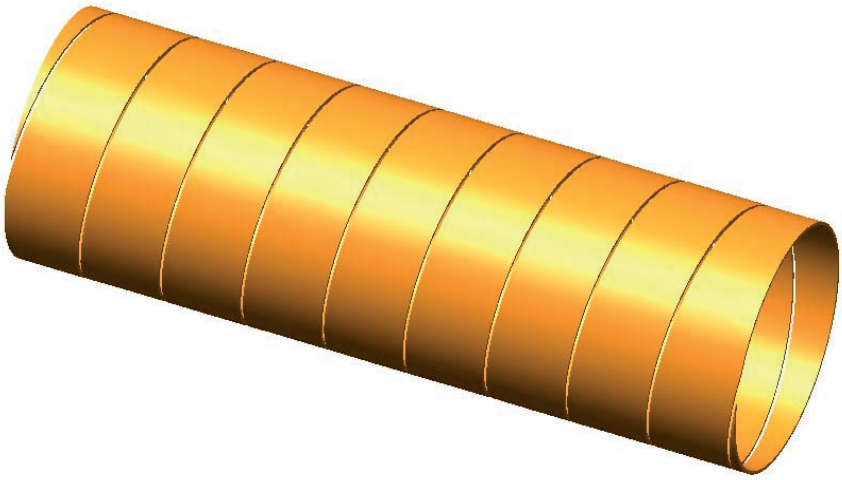

Figure 2.6 - 10 turn helical 'current sheet' coil or solenoid, created by making infinitesimally thin cuts in a 'sheet' of negligible thickness, [*Supplement 1*].

It can be seen from inspection of Equations [7] and [8] that B_z is equal to $k_N \cdot B_\infty$ or:

$$B_z = \frac{k_N \mu_0 \mu_r N_c \cdot I_c}{l_c} \qquad [9]$$

In 1928 Wheeler published an empirical formula for the inductance of real short coils with *finite* wire thickness and coil length [61], as shown in Equation [10] in both the original form, and with SI units [56].

$$L_{\mu H} = \frac{r_i^2 N_c^2}{9r_i + 10l_i} = \frac{r_{cs}^2 N_c^2}{0.2286 r_{cs} + 0.254 l_c} \qquad [10]$$

where $L_{\mu H}$ is the inductance of the real short coil [μH], r_i is the coil radius measured on the wire centre-line [inches], which is taken as equivalent to the current sheet radius r_{cs} [m], and l_i is the coil length measured end-to-end [inches].

Knight [62] recently reformulated Equation [10] in SI units, to directly solve for the Nagaoka coefficient, k_N, accurate to approximately 3 significant figures [*Supplement 1*]:

$$k_N = \frac{1}{1 + 0.4502 \left(\frac{D_c + \delta_c}{l_c} \right)} \qquad [11]$$

where D_c is defined as the coil inner diameter [m] and δ_c is the electromagnetic penetration depth into the coil [m] given by:

$$\delta = \sqrt{\frac{\rho}{\pi \mu_o \mu_r f}} \qquad [12]$$

where ρ is the electrical resistivity [Ω·m], and f is the frequency of the applied coil current [Hz]. Equation [12] can also be used to solve for either the electromagnetic penetration depth into a coil or a conductive work piece, by substituting the appropriate resistivity and effective magnetic permeability.

The electrical resistivity is the inverse of the electrical conductivity:

$$\rho = \frac{1}{\sigma} \qquad [13]$$

where σ is the electrical conductivity [S/m]. For 100% International Annealed Copper Standard (IACS) copper, the recommended conductivity is 58.0 MS/m at 293 K [63]. For chemically pure solid aluminium, the recommended electrical conductivity is 65% IACS or 37.7 MS/m [64]. For the liquid alloy A356, as used in the current experiments, the electrical resistivity as a function of temperature is given in *Supplements 7* and *8*, using the data of Brandt *et al.* for metal containing 7 wt. % Si and 0.6 wt. % Mg [65]:

$$\rho_l = \rho_o \left(1 + \alpha_{894}\left[T - 894K\right]\right) \qquad [14]$$

where ρ_o is the resistivity of the liquid metal at the reference temperature T [Ω·m], α_{894} the temperature coefficient of resistivity [K^{-1}], and T the reference temperature (894 [K]). The following values are recommended: ρ_o = 2.883 x10^{-7} Ω·m, α_{894} = 5.59 x10^{-4} K^{-1}.

Electromagnetic penetration depths have been calculated for solid 100% IACS copper and chemically pure aluminium at 293 K, and for liquid A356 at 973 K in Figure 2.7, as a function of the applied frequency, using Equation [12]. The current experimental program was conducted using 50 Hz, AC. At this low frequency the electromagnetic penetration depth for liquid A356 at 973 K is 39.1 mm, which could be compared to solid copper at 293 K, where the depth is only 9.3 mm, due to its much higher electrical conductivity. At 10000 Hz, it can be seen that for chemically pure solid aluminium at 293 K, that the electromagnetic penetration depth has been reduced from 11.6 mm at 50 Hz, to only 0.8 mm.

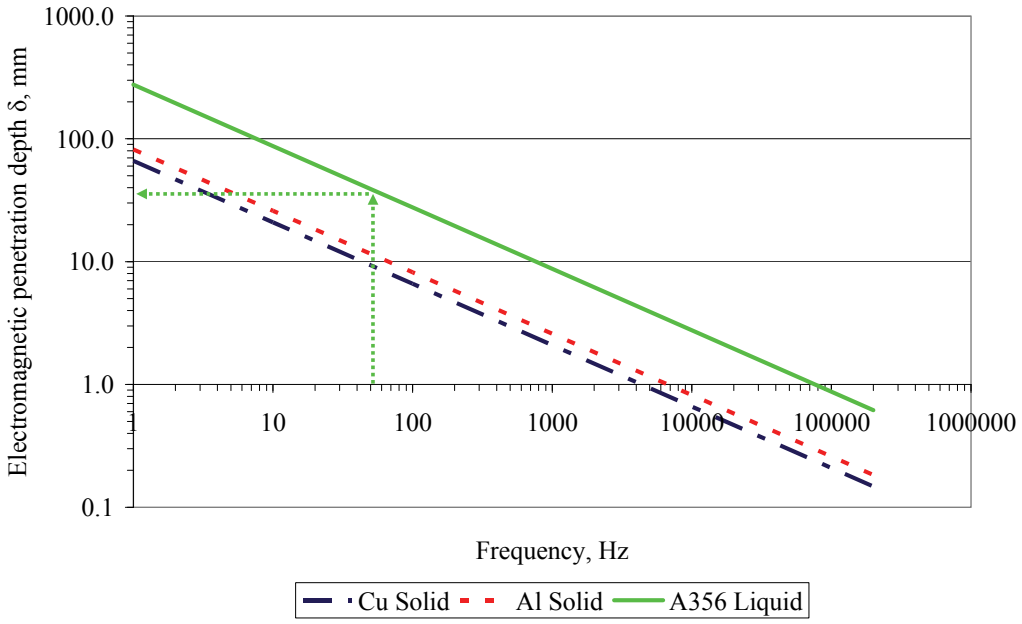

Figure 2.7 – Electromagnetic penetrations depth versus frequency for solid 100% IACS copper and chemically pure aluminium at 293 K, and for liquid A356 aluminium alloy at 973 K. An electromagnetic penetration depth of 39.1 mm is indicated by the dotted line for A356 at 50 Hz.

The use of Equation [11] does not add any significant error in the calculation of induction coil magnetic flux densities, given that state of the art Hall Effect Gauss meters have a typical uncertainty on the order of 0.5 to 1% for AC magnetic fields.

For a typical induction coil with a shape factor of 1, Equation [11] indicates that the coil will have only 69% of the z-component magnetic flux density of the equivalent 'long coil'. To have 95% of the long coil magnetic flux density, the coil would need to have a shape factor of 0.122, and to have 98%, it would need to have a shape factor of 0.048. It is therefore concluded that all typical induction coils are 'short' and that Equation [6] can not be accurately applied, i.e. Equation [6] will always result in an empirically measureable error.

For coils constructed of round wire, it has been empirically found at 50 Hz, that $(D_c + \delta_c)/l_c$ in Equation [11], can be equated to the average coil diameter measured from the centre-to-centre of the conductors of the coil, in accordance with classical inductance calculations, i.e. the equivalent current sheet diameter (D_{cs}) should be used.

It is clear from Equation [11] that the magnetic flux density varies strongly with shape factor, as can also be seen using the *Biot-Savart law* [66]. It is relatively easy to solve *the Biot-Savart law*, Equation [15], along the centre-line of a solenoidal coil.

$$\delta\vec{B} = \frac{\mu_o I_c}{4\pi}\frac{\delta\vec{l}\times\hat{r}}{r^2} \qquad [15]$$

where $\delta\vec{B}$ is the incremental flux density [T] measured at a point, which is distance of r [m] away from a current carrying conductor, $\delta\vec{l}$ is an incremental distance along the conductor [m] and $\hat{r}$ is a unit vector pointing from $\delta\vec{l}$ toward the measuring point.

Solving Equation [15] along the centre-line of a 'current sheet' solenoid yields [67]:

$$B_0 = \frac{\mu_0 N_c I_c}{2l_c}\left(\frac{xl_c}{\sqrt{(xl_c)^2 + r_{cs}^2}} + \frac{(1-x)l_c}{\sqrt{((1-x)l_c)^2 + r_{cs}^2}}\right) \qquad [16]$$

where B_0 is the z-component of the flux density [T] along the central axis of a solenoidal coil of length l_c, [m], with current sheet radius r_{cs} [m] and where x is the dimensionless coil length. For $l_c >> r_{cs}$, Equation [16] simplifies to Equation [6].

Dividing Equation [16] by Equation [6] yields a dimensionless centre-line flux density, which is independent of current and the number of coil turns, and somewhat analogous to the Nagaoka coefficient [67].

$$\frac{B_0}{B_\infty} = \frac{1}{2}\left(\frac{xl_c}{\sqrt{(xl_c)^2 + r_{cs}^2}} + \frac{(1-x)l_c}{\sqrt{((1-x)l_c)^2 + r_{cs}^2}}\right) \qquad [17]$$

Equation [17] has been plotted as a function of coil shape factor in Figure 2.7.

The coil '*end effects*' can clearly be seen in Figure 2.8, particularly for long coils, e.g. (D_{cs}/l_c) of 0.1. The longitudinal variation of the magnetic flux density, gives rise to a similar variation in the induced currents and hence a powerful variation along the length of the coil in terms of the induced Lorentz forces. The resulting curl in the Lorentz forces typically produce strong MHD stirring, or the "secondary mixing effects" reported by previous investigators [22, 34].

The estimation of the surface magnetic flux density is further complicated by the fact that the presence of the work piece, alters both the magnitude and distribution of the electromagnetic field, as shown in Figure 2.9 for the results of 2D axially symmetric FEM models, solved using COMSOL® 4.2a [67]. Figure 2.9 clearly shows that there is negligible electromagnetic penetration into a high conductivity work piece in accordance with Equation [12], and as shown previously in Figure 2.7.

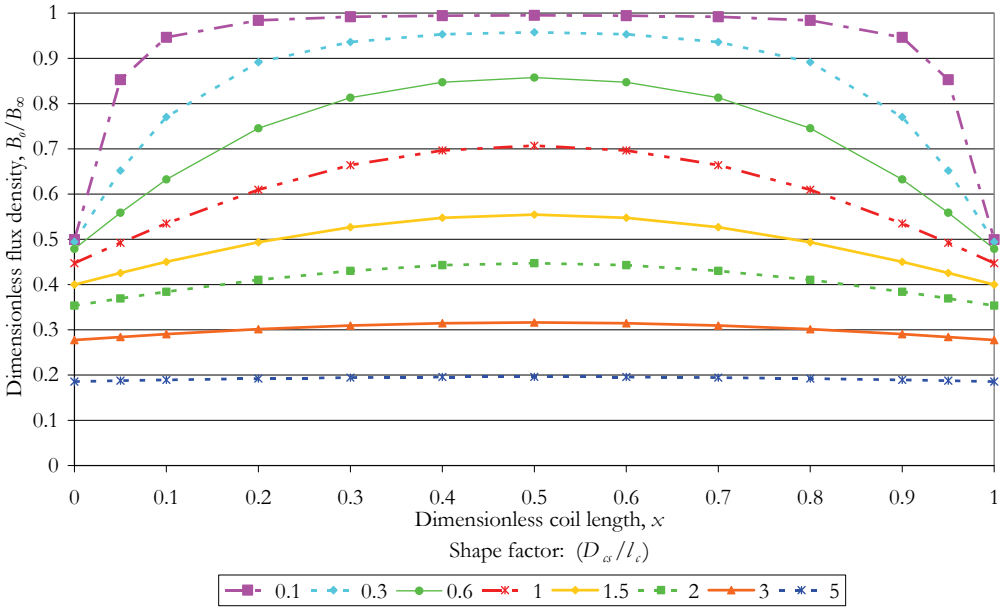

Figure 2.8 - Dimensionless coil centre-line flux density (B_0/B_∞) as a function of coil shape factor (D_{cs}/l_c) and dimensionless coil length (x), [*Supplement 5*].

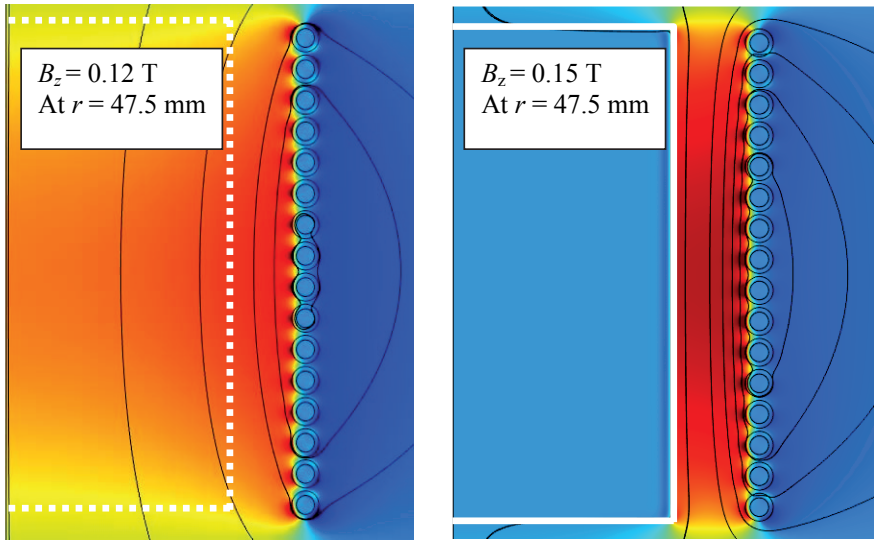

Figure 2.9 - A 16 turn copper coil, 131.5 mm diameter by 105.75 mm high (D_c/l_c = 1.243), with a 95 mm diameter by 105.75 mm high work piece, of high purity solid aluminum (65% IACS electrical conductivity) at 10 kHz, and 1000 A RMS applied current. Showing a 25% increase in magnetic flux density (z-component) at the surface of the work piece, when compared to the 'air-core' coil alone. Work piece length is exactly equal to coil length as per classical analytical solutions [67].

In 1945 Vaughan and Williamson proposed the use of an empirically modified Nagaoka short coil correction factor [16], as shown in Equation [18] based on their experiments conducted with high conductivity work pieces at 10 kHz. This correction factor accounted for the influence of the geometry of the coil and of the work piece on the magnetic flux density, as shown in Figure 2.9. This factor was subsequently 'squared' and republished without reference by Tudbury, as his "Workpiece Shortness Correction Factor" in 1960 [17], as revealed for the first time in *Supplement 1*.

$$k_N{}^* = k_N\left(1-\left(\frac{D_w}{D_c}\right)^2\right)+\left(\frac{D_w}{D_c}\right)^2 \qquad [18]$$

where $k_N{}^*$ is a modified Nagaoka short coil correction factor [unitless] and D_w is the outer diameter of the work piece [m].

Equation [18] implies that the coil produces a fixed number of electromagnetic flux lines Φ [Wb] at any given current. As flux lines are excluded from the coil and work piece at high frequency and correspondingly low electromagnetic penetration depth, they become proportionately concentrated into the air gap, which exists between the coil and work piece. This is shown numerically in Figure 2.9, where the presence of the work piece has resulted in a 25% increase in the air gap magnetic flux density for a fixed applied current and frequency.

In *Supplement 1* it was shown that the virtually unknown method of Vaughan and Williamson was in fact the most accurate method available to estimate the heating rate of a work piece in an induction coil with errors of <10%. This accuracy implied that the combination of Equations [9], [11] and [18] could estimate the average surface electromagnetic flux density with an error of ~3-4% (square root of the error in the power estimate).

In *Supplement 2* it was postulated based on the observed behaviour of the 2D axial symmetric FEM model with frequency, that Equation [18] could be improved by the application of frequency adjustment using the electromagnetic penetration depth Equation [12], and shown in Equation [19].

$$k_N{}^* = k_N\left(1-\left(\frac{D_w-\delta_w}{D_c+\delta_c}\right)^2\right)+\left(\frac{D_w-\delta_w}{D_c+\delta_c}\right)^2 \qquad [19]$$

where δ_w is the electromagnetic penetration depth [m] into the work piece, which can be found substituting the work piece electrical resistivity into Equation [12].

Equation [19] was subsequently validated using reactive or 'imaginary' power measurements in [56], and is empirically shown to predict the flux density in the air gap with an accuracy of ~1%.

Experimental verification of the accuracy of the analytical models presented in this section for the magnitude of the magnetic flux density of short coils and the impact of a work piece, i.e. Equation [18] is available in *Supplements 1-2*. Typical differences between estimated values, using both 2D axial symmetric FEM and analytical models such as Equations [9] with [19] and Equation [17], are on the order of ±1-2% on average when compared against experimental measurements made using Hall Effect Probes [56].

Great care was taken to develop the basic 2D axial symmetric FEM model to ensure that the magnetic domain was sufficiently large, as to avoid influencing the estimation of the magnetic flux density, and to ensure that the mesh was sufficiently dense, to give accurate estimates of total power and hence local current density. The differential equations used in the FEM model, the development and model experimental validation, are thoroughly discussed in *Supplement 2*.

2.2.2 Estimation of Lorentz Forces as a Function of Radius in the Work Piece

[See *Supplement 7*]

The eddy current density $\vec{J}$ is related to the curl of the magnetic field intensity ($\nabla \times \vec{H}$) and the magnetic flux density $\vec{B}$, as presented in the following equation:

$$\vec{J} = \nabla \times \vec{H} = \frac{\nabla \times \vec{B}}{\mu} \qquad [20]$$

where $\vec{J}$ is the eddy current density [A/m^2], $\vec{H}$ is the magnetic field intensity [A(-turns)/m], $\vec{B}$ is the magnetic flux density [T] and μ the electromagnetic permeability of the conductive fluid ($\mu = \mu_0 \mu_r$), which is equal to 4π x10^{-7} [H/m] for aluminium. In accordance with the mathematical definition of the curl in Equation [20], it is the time varying value of the local magnetic field intensity in the z-direction, which induces the current in the liquid metal, in the phi-direction.

It is important to point out that in Eq. [20], $\vec{J}$ and $\vec{B}$ are both vectors and phasors (time varying functions), that can be represented by *complex vector quantities*, i.e. by $\underline{\vec{J}}$ and $\underline{\vec{B}}$. Both the magnitude and the phase shift between $\underline{\vec{J}}$ and $\underline{\vec{B}}$ changes with the penetration depth into the work piece, making the solution for the Lorentz forces challenging. The following formula is proposed for the time averaged values, i.e. the

real part of $\underline{\vec{J}} \times \underline{\vec{B}}$, which will have a unique solution at each radial position in the work piece.

$$\left|\vec{F}_L\right| = \mathrm{Re}\left\{\underline{\vec{J}}^* \times \underline{\vec{B}}\right\} \qquad [21]$$

where $\underline{\vec{J}}^*$ is the complex conjugate of the Root Mean Square (RMS) current density in the phi direction [scalar values of A/m^2] and $\underline{\vec{B}}$ the RMS complex magnetic flux density in the z-direction [scalar values of T]. From the definition of the vector cross product and the right hand rule, the time average force is known to be in the negative r-direction. The Lorentz component in the z-direction is in the present study assumed to be negligible, (i.e. the radial component of $\vec{B}$ is negligible compared to the axial).

If all of the phase angles are referenced to the magnetic flux density (and hence also the magnetic field intensity) at the surface of the work piece, then the magnitude of the magnetic flux density/field intensity in the z-direction at the surface have only a real component and can be found directly from Equations [9] and [20].

$$H_z = \frac{k_N^* N_c I_c}{l_c} \qquad [22]$$

The solution to the local magnetic field intensity as a function of depth can be found by applying the solution to a modified zero order Kelvin Bessel of the first kind [68]:

$$\underline{H}_z(r) = \frac{ber\xi_r + jbei\xi_r}{ber\xi_R + jbei\xi_R} H_z \qquad [23]$$

The derivation of Equation [23] requires the application of both Faraday's [69] and Ampere's laws [55] and the solution to differential equations involving time varying complex vector quantities. The reader is therefore directed to the complete mathematical development in the following reference by Kennedy [56].

ξ_r and ξ_R can be defined as:

$$\xi_r = \frac{\sqrt{2}r}{\delta_w} \text{ and } \xi_R = \frac{\sqrt{2}R}{\delta_w} \qquad [24]$$

where R is the outer radius of the work piece [m] and r is the radius [m] at which the magnetic field intensity and ultimately the Lorentz forces, are to be evaluated. ξ_R can be considered as a type of dimensionless electromagnetic penetration depth and is found many places in the literature.

From Equations [20] and [23] it is clear that:

$$\underline{B}_z(r) = \mu \frac{ber\xi_r + jbei\xi_r}{ber\xi_R + jbei\xi_R} H_z \qquad [25]$$

The induced current at depth *r* can be found by applying Equation [20] to Equation [23]:

$$\underline{J}_\Phi(r) = -\frac{\partial}{\partial r}\left(\frac{ber\xi_r + jbei\xi_r}{ber\xi_R + jbei\xi_R}\right) H_z \qquad [26]$$

Performing the required differentiation on Equation [26] yields:

$$\underline{J}_\Phi(r) = -\frac{ber'\xi_r + jbei'\xi_r}{ber\xi_R + jbei\xi_R} \frac{\sqrt{2}}{\delta_w} H_z \qquad [27]$$

where *ber'* and *bei'* are the derivatives of *ber* and *bei*, which are the real and 'imaginary' parts of the modified zero order Kelvin Bessel function and their derivatives, and can be found using look up tables [70] or using numerical solvers [60]. Numerical solvers accurate to double precision have been used in the analysis of the current work.

Performing the complex division in Equation [27], and evaluating the complex conjugate required for use in Equation [21], results in:

$$\underline{J}^*_\Phi(r) = -\frac{ber'\xi_r - jbei'\xi_r}{ber\xi_R - jbei\xi_R} \frac{\sqrt{2}}{\delta_w} H_z \qquad [28]$$

Substituting Equations [25] and [28] into [21] and performing the required vectorial multiplication results in:

$$F_L = -\mu \frac{\sqrt{2}}{\delta_w} H_z^2 \left(\frac{ber\xi_r + jbei\xi_r}{ber\xi_R + jbei\xi_R}\right)\left(\frac{ber'\xi_r - jbei'\xi_r}{ber\xi_R - jbei\xi_R}\right) \qquad [29]$$

Performing the complex multiplication and taking only the real portion of Equation [29], results in:

$$F_L = \mathrm{Re}\left\{\vec{J}^* \times \vec{B}\right\} = -\mu \frac{\sqrt{2}}{\delta_w} H_z^2 \left(\frac{ber\xi_r ber'\xi_r + bei\xi_r bei'\xi_r}{ber^2\xi_R + bei^2\xi_R}\right) \qquad [30]$$

Defining:

$$\varphi(R,r) = \frac{\sqrt{2}(ber\xi_r ber'\xi_r + bei\xi_r bei'\xi_r)}{ber^2\xi_R + bei^2\xi_R} \qquad [31]$$

and substituting Equation [22] into [30] then yields:

$$F_L = -\frac{\mu_r \mu_o}{\delta_w}\left(\frac{k_N^* N_c I_c}{l_c}\right)^2 \varphi(R,r) \qquad [32]$$

as also found as Equation [7] in *Supplement 7*.

Equations [31] and [32] are similar to the equations previously published by Korovin [71, 72]; however, in the English translations of Korovin's work [71, 72], the real and imaginary parts of his equations were apparently confounded by the accidental omission of the √-1 and the resulting equation can not be used for any practical purpose. Korovin's solutions have also been modified to include the frequency adjusted 'short' coil correction factor Equation [19], without which it is not possible to analytically estimate the Lorentz forces with less than about a factor of two error.

In Figure 2.10 the correction factor, φ, calculated from Equation [31], is plotted as a function of the dimensionless radial position, r/R, for different values of the dimensionless outer (reference) radius, ξ_R. As can be seen from the figure, at larger values of ξ_R a higher value is obtained for the correction factor, φ at the surface ($r=R$).

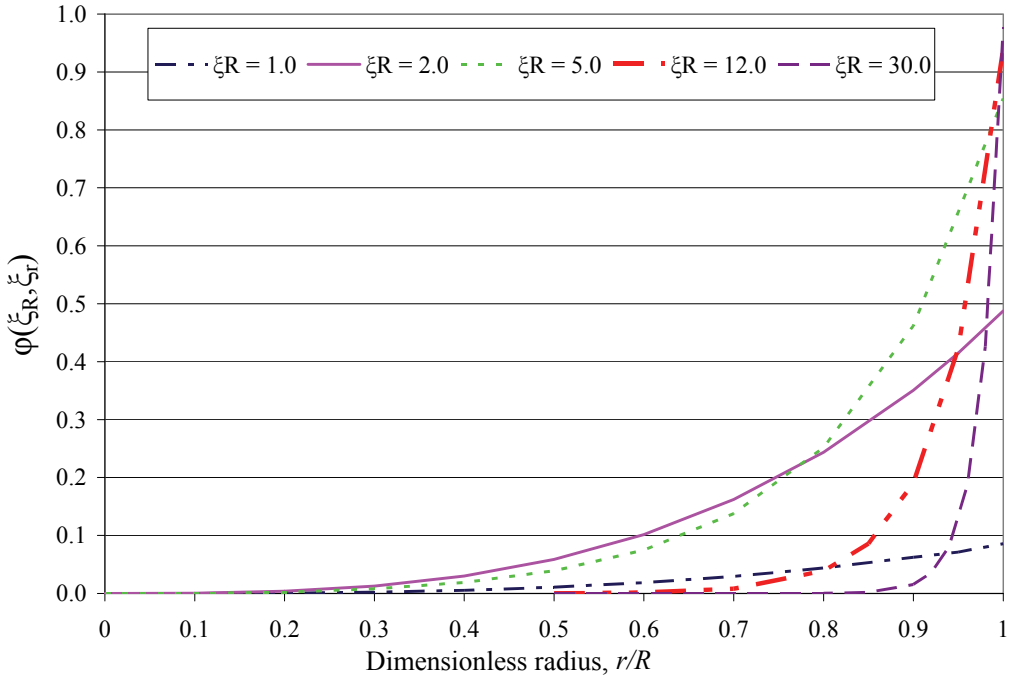

Figure 2.10 - The correction factor φ given by Equation [31] as a function of the dimensionless radius (r/R) for different values of the dimensionless outer (reference) radius (ξ_R).

For a fixed outer radius, R, a large dimensionless reference radius, ξ_R, corresponds to a low electromagnetic penetration depth, δ_w, and thus a high frequency, f, in accordance with Equation [12] and Figure 2.7. At high frequencies the magnitude of Equation [32] becomes very large at the surface, due to the low electromagnetic penetration depth obtained in the denominator, as well as the high value of the correction factor, φ. The obtained electromagnetic force becomes very powerful, but confined to a thin layer, i.e. the *electromagnetic boundary layer*. This effect is clearly seen in Figure 2.11, where the time average Lorentz forces, F_L, are plotted against the dimensionless radius, r/R, for different values of the dimensionless reference radius at the surface, ξ_R, equivalent to frequencies from 16 Hz to 14.4 kHz.

Results from Equation [32] are plotted against the numerical results of a 2D axial symmetric FEM model, showing excellent agreement over a range of more than 9 orders of magnitude. Some of the discrepancy in Figure 2.11 is due to the use of experimental data from a coil containing a ½ turn, which can never be perfectly modelled using axial symmetry. The agreement between the FEM model and the analytical solution was taken as mutual confirmation of the analytical and the FEM model accuracies. It was concluded that experiments were therefore not required to validate the magnitude of the induced Lorentz forces, even though such experiments are possible to conceive.

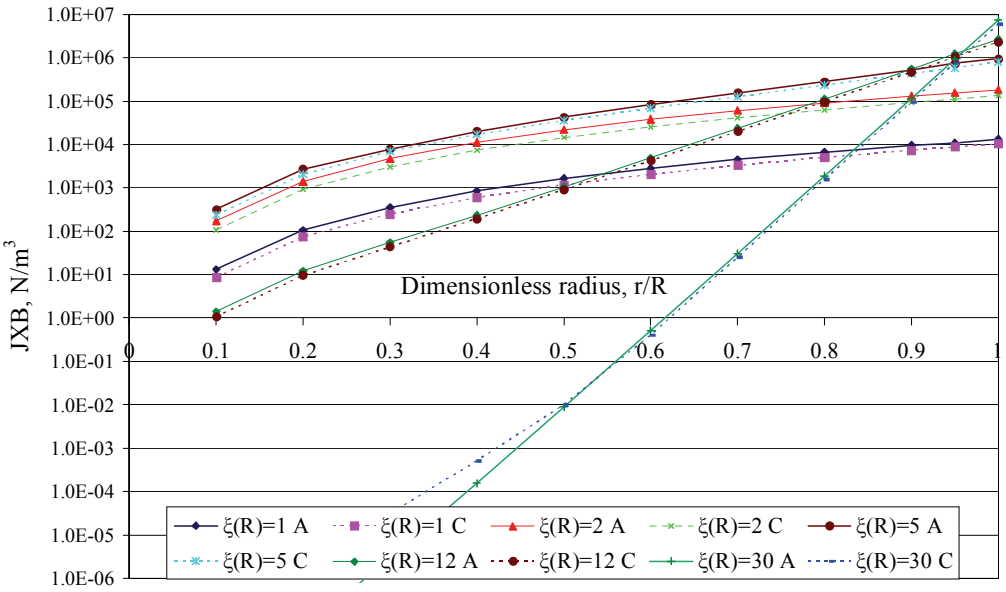

Figure 2.11 − Comparison of the time averaged Lorentz force estimates from Equation [32], and from COMSOL® 4.2. The calculations were performed for 100 mm in diameter of liquid A356 alloy (with 4% non-conductive solids) at 980 K, using 932 A in a 'short' coil, D_{cs}=132 mm, l_c = 111 mm, N_c=16.5, B_z = 0.126 T from Equation [9], [*Supplement 7*]. A=analytical, C=COMSOL.

Examining Figure 2.11 or applying Equation [32] to a 100 mm diameter sample of liquid aluminium at 50 Hz, it can be found that the Lorentz forces will exceed those of gravity by approximately 1 order of magnitude for the actual coils and conditions used in the present work. If the applied magnetic field is not homogenous (as clearly indicated in Figures 2.8 and 2.9), i.e. if there is a curl, then it is not surprising that powerful MHD stirring will result, dominate the hydrodynamic flow fields, and cause robust recirculation. The investigation of the curl in the Lorentz forces, the permeability of the filters to flow and the resulting recirculation of the melt, is therefore one of the main topics of study in this work.

2.3 Effective Conductivity of a Ceramic Foam Filter [see *Supplement 3*]

In order to develop validated Lorentz force models and subsequently flow field calculations, it was necessary to determine the influence of the CFFs on the electrical behaviour of the system. Experiments were therefore conducted as indicated in Figure 2.12.

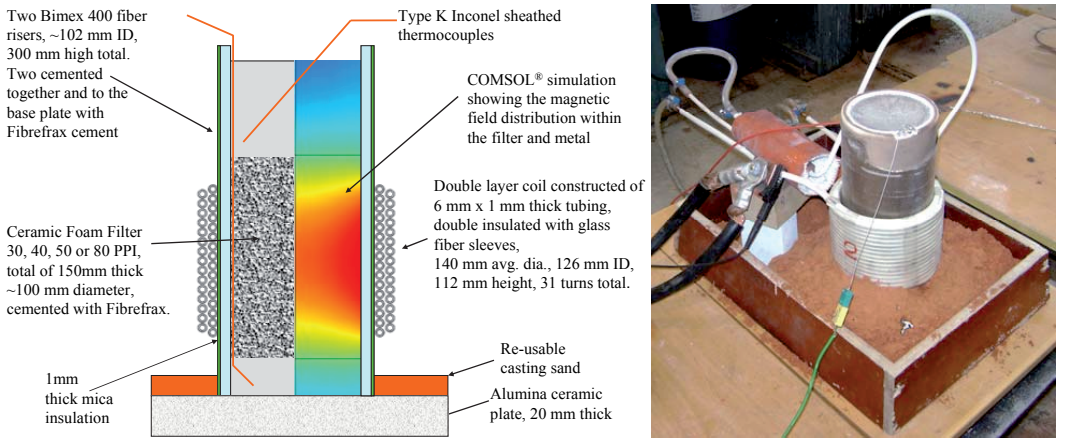

Figure 2.12 – Schematic of the filter effective electrical conductivity apparatus (a) and photograph (b), showing a 2 layer, 31 turn (total) induction coil, operated at 371-734 A, using line frequency 50 Hz AC power, [*Supplement 3*].

A series of experiments were conducted on 30, 40, 50 and 80 PPI filter elements as described in *Supplement 3*. Power induced in the stack of 3 filters as shown in Figure 2.12, was determined electrically by subtracting the measured power of a coil running empty, from the power of the coil operating filled with CFFs and impregnated with commercial grade liquid aluminium. See *Supplements 1-3* for experimental details on power measurements.

Power induced by induction coils can be determined by an equation very similar in form to Equation [32], e.g. as shown as Equation [14] in [56] and reproduced below:

$$P_w = -\sqrt{2}\pi l \left(\frac{k_N^* I_c N_c}{l_c} \right)^2 \frac{1}{\sigma_w} \xi_R \varphi(\xi_R) \qquad [33]$$

where l is either the length of the work piece or coil, whichever is shorter [m] and σ_w is the electrical conductivity of the work piece [S/m].

In the case of the system shown in Figure 2.12, l is the length of the coil (112 mm) and σ_w is the unknown effective electrical conductivity of the metal impregnated filter. The effective electrical conductivity of the filter is reduced by the longer path length forced on the current by the tortuosity, τ and by the reduction in conducting area due to a porosity, ε of less than 1. The combined impact of tortuosity and porosity can be determined if the electrical conductivity of the liquid metal σ_m is known.

$$\frac{\sigma_m}{\sigma_w} = \frac{\sigma_m}{\sigma_f} = \frac{\tau}{\varepsilon} \qquad [34]$$

where σ_f is the effective electrical conductivity of the different filter media [S/m].

An average liquid metal temperature measured using 2 Type K thermocouples (one over and one under the filter elements) was used to estimate the liquid metal conductivity within the filter elements, starting with literature conductivity data for ultra pure metal, and correcting for the actual measured room temperature conductivity of the clean metal after experimentation [64]:

$$\sigma_m = \frac{IACS_m^{293K}}{24.77\ 10^{-8}\ (1 + 0.000571\ [T_m - 933.2])\ 65} \qquad [35]$$

where $IACS_m^{293K}$ is the average room temperature conductivity of the solidified metal used during the experiment [% IACS] and T_m is the temperature of the liquid alloy under experimental conditions [K].

From the measured power induced in the work piece (i.e. the filters and liquid metal), and the metal conductivity estimated by Equation [35], it was possible to determine the effective filter electrical conductivity using either Equation [33] or with the 2D axial symmetric FEM model. Good agreement was found between these two methods; however, the FEM results were used for consistency with further modelling. The ratios of the metal to the effective filter conductivity, are also plotted in Figure 2.13 against filter type, for 30-80 PPI filters.

Due to the novelty of the induction method combined with CFFs, further confirmation was attempted using cold readings, on solidified and sectioned filters. Vertical sections and Horizontal sections were both tested using a high frequency (60 kHz) conductivity probe as described in *Supplement 3*. Results were in general agreement except for the 80 PPI CFF, which had lower readings cold, than hot, as also plotted in Figure 2.13. This effect might have been due to the low electromagnetic penetration depth with cold metal at 60 kHz, or due to anisotropic filter effective conductivity. Vertical cuts resulted in currents being measured on the r-z plane, while Horizontal cuts were on the r-phi plane. The hot metal experiments were readings purely in the phi direction.

No systematic bias was observed between the Vertical and Horizontal cuts. The observed variations may the result of the random location of the sections through the pore structure of the filter elements and the low electromagnetic penetration depth of the high frequency cold method, which is less than one cell diameter. It is assumed that the low readings for the 80 PPI filters at room temperature, are therefore due to the low electromagnetic penetration depth (<1 mm at 60 kHz, vs. >50 mm at 50 Hz).

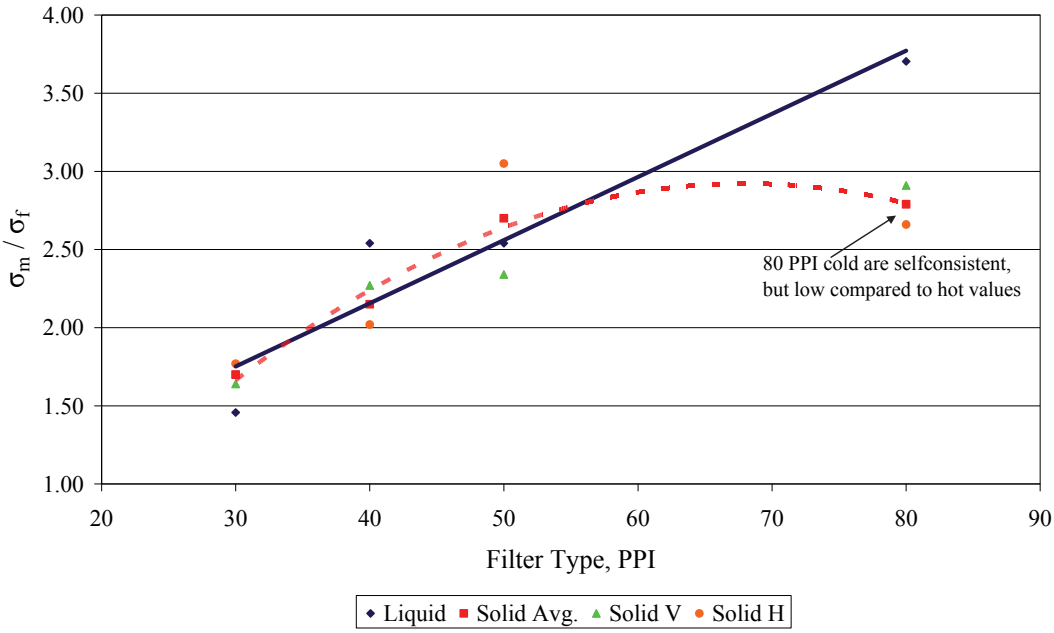

Figure 2.13 – Conductivity ratio of metal (σ_m) and metal impregnated filter (σ_f) versus filter type in PPI. Comparison is shown between liquid metal values fitted to experimental data using FEM and average, vertical, and horizontally cut solid filter sections (cold readings). Accuracty for hot measurements is estimated to be ±20%, [*Supplement 3*].

All hot and cold results are summarized in Table 2.1.

Table 2.1 Ratio of Metal Conductivity to Filter Conductivity for both Hot Metal and Cold Inductance Measurement, [*Supplement 3*]

Filter Type (PPI)	**FEM Estimate of Conductivity Ratio (σ_m/σ_f)**	**Cold Average Conductivity Ratio (σ_m/σ_f)**	**Cold Vertical Conductivity Ratio (σ_m/σ_f)**	**Cold Horizontal Conductivity Ratio (σ_m/σ_f)**
30	1.46±0.06	1.70	1.64	1.77
40	2.54±0.18	2.15	2.27	2.02
50	2.54±0.12	2.70	2.34	3.05
80	3.70±0.06	2.79	2.91	2.66

In order to correlate results to physical parameters more significant than PPI, it is necessary to examine the filter morphology in more detail. In the next section both the filter morphology and hydraulic behaviour are examined. Filter permeability to liquid flow is necessary, as the next step to estimating accurate Magneto-Hydro-Dynamic flow fields using finite element modelling.

Chapter 3

PART II– THEORY AND VERIFICATION

CERAMIC FOAM FILTERS, CHARACTERIZATION AND HYDRODYNAMICS

In order to create realistic filtration models and produce accurate estimates of the induced flow fields using finite element models, additional data were required for the 30-80 PPI filters used in the current study. Available hydrodynamic data showed significant scatter, accuracies of correlations were poor or simply unknown, and not all required data were available for the type (commercial supplier) and sizes (PPIs) of CFFs used. It was therefore decided to conduct a systematic investigation into the physical morphology and hydraulic properties of the types of CFFs used in the hot metal experiments. 40 PPI filters were included in order to add intermediate data points to the obtained correlations. Results have been published mainly in *Supplements 3* and *4* and key results are summarized in the following sections.

3.1 CFF Basic Morphology

Commercial filters of 30, 40, 50 and 80 PPI where examined by a combination of light microscopy, optical scanning and scanning electron microscope (SEM) to determine cell, d_c window, d_w and strut, d_s dimensions. Optical images for the 30-80 PPI CFFs, are shown in Figures 3.1 (a) through (d). It can be observed that the 30 PPI filters are more 'web-like' and that progressively more of the cell windows become blocked at higher PPI levels, resulting in a more 'pore-like' structure. This apparently has profound impacts on both the permeability and tortuosity, as will be shown in later sections.

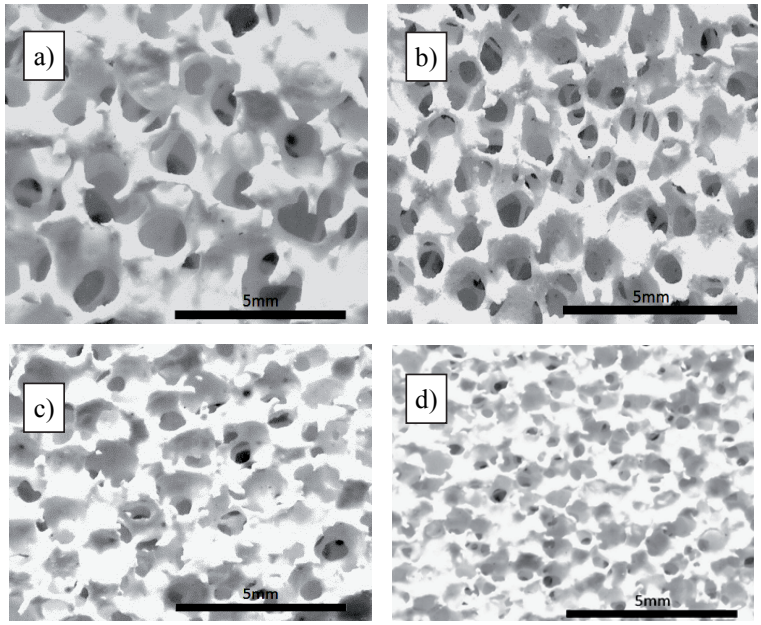

Figure 3.1 –Optical scans of CFFs (a) 30 PPI, (b) 40 PPI, (c) 50 PPI, (d) 80 PPI, showing less 'web-like' and more 'pore-like' structure (blocked openings) with higher PPI levels, [*Supplement 8*].

SEM images of the 30-80 PPI filters are given in Figures 3.2 and 3.3. The figures also show the definitions of cell, d_c window, d_w and strut, d_s dimensions. It should be noted that these parameter names are now relatively standard in the CFF literature and have not been selected at random.

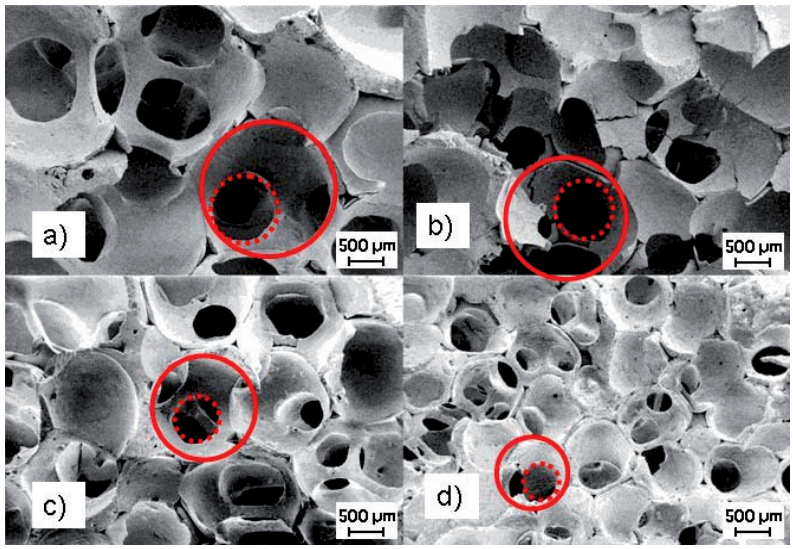

Figure 3.2 –Representative SEM micrographs of 30 (a), 40 (b), 50 (c) and 80 (d) PPI commercial alumina ceramic foam filters. Cell or pore sizes, d_c are indicated by solid circles and window sizes, d_w, are indicated by dotted circles, [*Supplement 3*].

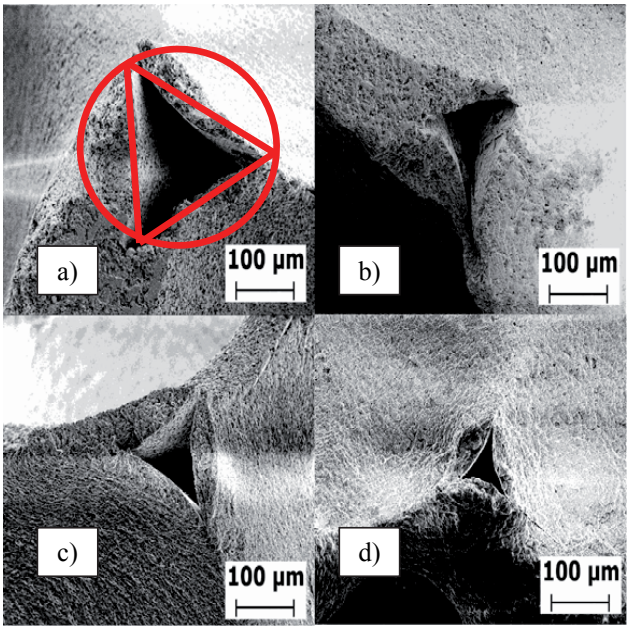

Figure 3.3 – Representative SEM micrographs of 30 (a), 40 (b), 50 (c) and 80 (d) PPI commercial alumina ceramic foam filters. Cell strut diameter, d_s, is indicated for the 30 PPI filter as the solid circle and is measured at the thinnest point. The internal porosity left by the removal of the substrate is indicated as a triangle, [*Supplement 3*].

Measurements of cell and window diameter were made on the original, uncut surface of the 50 mm thick alumina CFF's. 200 counts were made each for cell and window determination, and 40 counts for strut dimensions. Strut dimensions were measured at their thinnest point. Histograms of the results can be found in *Supplement 3*.

Mean cell sizes have been plotted against window sizes for each filter type, and compared with previously published data for similar commercial filters [73] in Figure 3.4, showing excellent agreement. The obtained results correlated according to the following empirical equation:

$$d_c = 1.79 d_w,\ R^2 = 0.988 \qquad [36]$$

The linear relationship between cell and window diameters implies a simple geometric relationship, likely originating with the original substrate used during the filter fabrication process.

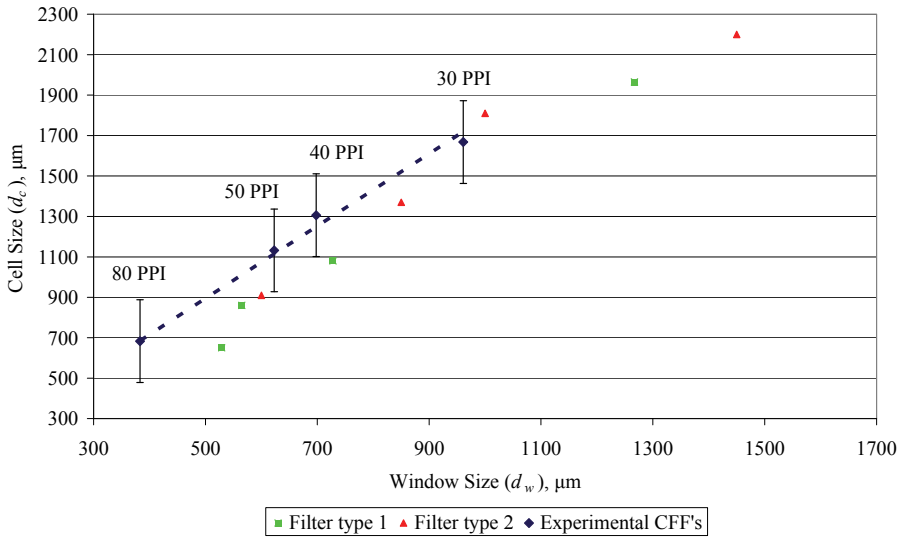

Figure 3.4 – Commercial ceramic foam filter cell size, d_c, versus window size, d_w [µm] and comparison with literature [73]. One 'standard error' is indicated by the error bars, [*Supplement 3*].

Total porosity, ε [unitless] can be determined using the true particle density, ρ_p [kg/m^3] found using pycnometry, and the measured filter mass, m_f [kg], for a known filter volume, V_f [m^3]:

$$\varepsilon = 1 - \frac{m_f}{\rho_p V_f} = 1 - \frac{\rho_f}{\rho_p} \qquad [37]$$

Densities of the 101 mm filter sections used in these experiments were determined by using precise measurement of the filter dimensions, calculation of the total volume, and weighing on an analytical balance. Sample porosity was then calculated using Equation [37], and a measured particle density of 3.48±0.02 g/cm3 (average of 3 readings). Overall precision was estimated to be ~±0.2% porosity. The obtained results are given in Table 3.1. 'Full filter porosity' indicated in Table 3.1, is the average of 2-4 readings on industrial 20" or 23" filters, showing excellent agreement with the used filter sections.

Table 3.1. Summary of Basic Filter Physical Properties, [*Supplement 3*]

Filter Type (PPI)	Filter Porosity Eq. [37]	Full Filter Porosity Eq. [37]	Cell Diameter, d_c (µm)	Window Diameter, d_w (µm)	Strut Diameter, d_s (µm)
30	0.892	0.890±0.0002	1668±417	961±190	185±41
40	0.900	N/A	1306±251	698±151	211±46
50	0.863	0.864±0.004	1132±130	623±120	190±36
80	0.865	0.860±0.004	683±87	383±87	119±20

One standard deviation is indicated by the ranges.

3.2 CFF Tortuosity

Tortuosity, τ [unitless] is here defined as the ratio between the actual length traversed by the liquid flow, L_a [m] and the linear thickness of the filter, L [m]:

$$\tau = \frac{L_a}{L} \qquad [38]$$

Tortuosity can be determined from electromagnetic induction experiments using alloys of known electrical conductivity, σ_m [S/m]. Inside of the filter, the available conducting area is reduced by the presence of non-conducting obstructions (e.g. trapped gas or solid and filter media), and the conducting path length is increased due to the tortuosity. Assuming that the filter media is the only significant obstruction, the tortuosity can be estimated from the measured filter effective conductivity, σ_f , and filter porosity, ε as follows:

$$\tau = \varepsilon \frac{\sigma_m}{\sigma_f} \qquad [39]$$

Filter tortuosity has been determined for metal impregnated 30, 40, 50 and 80 PPI filters. Measurements have been obtained with the metal in both liquid and solid states as described in the previous chapter and found in *Supplement 3*. The hot metal experiments were conducted using the apparatus already shown in Figure 2.12. Detailed results can be found in Appendix Table I of *Supplement 3*.

Hot liquid metal (FEM estimate), filter porosity and calculated tortuosity results (using the hot metal data) are summarized in Table 3.2, for all four filter types.

Table 3.2 Summary of Key Tortuosity Experimental Results, [*Supplement 3*]

Filter Type (PPI)	FEM Estimate of Conductivity Ratio (σ_m/σ_f)	Filter Porosity Eq. [37]	Filter Tortuosity Eq. [39]
30	1.46±0.06	0.892	1.30
40	2.54±0.18	0.900	2.29
50	2.54±0.12	0.863	2.19
80	3.70±0.06	0.865	3.20

Relatively few measured values have been published previously for ceramic foam tortuosities. Moreia *et al*. measured tortuosity values using an ionic conduction method equivalent to the induction method described here. Their values for ceramic foams of 8, 20 and 45 PPI were 1.68, 1.71 and 1.84

respectively [74]. Diedericks *et al.* have theoretically studied tortuosity in some detail, proposing a value of ~1.45 at ε=0.88, for 'foam like' materials [75]. Methods using water and ionic solutes, will likely underestimate the true filter tortuosity, due to penetration of the water and ions into the micro and nano-porosity of the filter structure itself. Liquid metal poorly wets the surface of the ceramic and in the absence of intense pressure (e.g. 4000 Bar for mercury) will not penetrate the micro porosity.

The conductivity ratios shown in Table 3.2 have been correlated with the measured window diameters from Table 3.1 by the following equation [*Supplement 3*]:

$$\frac{\sigma_m}{\sigma_f} = 5.10 - 3.8\ 10^3 d_w,\ R^2 = 0.981 \qquad [40]$$

3.3 Filter Permeability - Theory

Permeability is an important parameter for the characterization of CFFs, since it is required to predict the flow rate obtainable for an imposed pressure gradient (e.g. the casting rate for a given metal head and filter area) or to be able to predict the pressure drop (and therefore the required head or elevation change) necessary to achieve a specific flow rate for a fixed filter area (as in the design of a casting line and filter bowl).

The transition of pressure drop from first to second order behaviour for 65 and 80 PPI CFFs using water, has been reported to be in the range from 0.01 to 0.015 m/s and to be beyond 0.015 m/s for 40 and 50 PPI filters [76]. In order to more accurately model MHD phenomena using finite element modelling (FEM) at high liquid velocity, it was necessary to obtain both first order (Darcy) and second order (Non-Darcy) terms for use with the Forchheimer equation [77]:

$$\frac{\Delta P}{L} = \frac{\mu}{k_1} u_s + \frac{\rho}{k_2} u_s^2 \qquad [41]$$

where ΔP is pressure drop [Pa], L is the filter thickness [m], u_s is the fluid superficial velocity [m/s], μ is the fluid dynamic viscosity [Pa·s], ρ is the fluid density [kg/m^3], k_1 [m^2] and k_2 [m] are empirical constants called the Darcian and non-Darcian permeability coefficients respectively.

Equation [41] represents the sum of viscous (first term) and kinetic energy losses (second term). It is implicit in Equation [41] that flow exists only on a

single axis, i.e. in the direction of L. For a given volumetric flow in axial symmetric geometry, there must therefore exist a single 'flow field diameter', which defines the superficial velocity, u_s.

The correlation between flow and pressure drop can be obtained empirically by fitting experimental data as per Equation [41] or by theoretical prediction using 'easily' measured physical properties such as porosity, ε, characteristic porous media dimensions, and the known liquid properties. The Ergun equation is often applied to predict the pressure drop in beds of solids [78]:

$$\frac{\Delta P}{L} = 150\frac{(1-\varepsilon)^2}{\varepsilon^3}\frac{\mu V_s}{d_p^2} + 1.75\frac{(1-\varepsilon)}{\varepsilon^3}\frac{\rho V_s^2}{d_p} \qquad [42]$$

where d_p is the 'equivalent' spherical particle diameter [m]. Even 'improved' versions of Equation [42] are known to have deviations in the range of ± 50%, relative to packed bed pressure drops [79].

Given that a porous solid is not a packed bed and has no clearly definable particle diameter, d_p, it is possible to apply the Ergun formula using alternately: the cell, d_c window, d_w or strut, d_s diameters. These diameters are indicated in Figures 3.2 and 3.3 (a) through (d), for the 30-80 PPI filters used in this study. One would expect that the estimation errors would exceed the ± 50% typical of the Ergun equation, unless an appropriate 'diameter' for correlation could be defined.

Ergun defined the 'equivalent' particle diameter of a non-spherical solid, d_p as the diameter of the sphere having the same 'outer' specific surface area per unit solid volume, S_v of the actual material in question (internal porosity, and small projections or cavities were ignored) [m^2/m^3] [78]:

$$d_p = \frac{6}{S_v} \qquad [43]$$

In Equation [43] the nomenclature of Ergun is maintained. Some confusion may ensue when referring to recent literature, where S_v is sometimes used to represent the surface area of solid per unit bed volume (i.e. S_B). Equation [42] can be re-written using Equation [43] as:

$$\frac{\Delta P}{L} = \alpha\frac{S_v^2(1-\varepsilon)^2\mu V_s}{\varepsilon^3} + \beta\frac{S_v(1-\varepsilon)\rho V_s^2}{\varepsilon^3} \qquad [44]$$

where α and β are empirical constants found by Ergun to be approximately 4.17 and 0.292 respectively [80].

Richardson *et al.* [80] explored the relationship between S_v and d_w for porous ceramics, and suggested applying the hydraulic diameter d_h concept. They equated the hydraulic diameter to the measured window diameter, i.e.:

$$d_w = d_h = 4\frac{\text{wetted area}}{\text{wetted perimeter}} \qquad [45]$$

Assuming idealized regular pores, i.e. all with the same hydraulic diameter, a simple geometric analysis yields:

$$S_v = \frac{4\varepsilon}{d_w(1-\varepsilon)} \qquad [46]$$

Substituting Equation [46] into Equation [44] yields:

$$\frac{\Delta P}{L} = 66.7\frac{\mu V_s}{\varepsilon d_w^2} + 1.17\frac{\rho V_s^2}{\varepsilon^2 d_w} \qquad [47]$$

Recently Dietrich *et al.* [81, 82] proposed the following equation after correlating 2500 separate experimental values from 20 authors:

$$\frac{\Delta P}{L} = 110\frac{\mu V_s}{\varepsilon d_h^2} + 1.45\frac{\rho V_s^2}{\varepsilon^2 d_h} \qquad [48]$$

The similarity between Equations [47] and [48] is obvious. If the hydraulic diameter is assumed equal to the window diameter in Equation [48], then Equation [48] will yield 40-50% higher pressure drops than Equation [47] [81]. As both empirical constants in Equation [48] are larger than those in Equation [47], it will yield higher estimated pressure drops for any velocity. Equation [48] has recently been independently shown to give excellent results using an optically determined hydraulic diameter, i.e. the equivalent circular window diameter, d_w [83]. The optically determined window diameters for the CFFs used in this study have been previously presented in Table 3.1.

It should be noted that the total, ε and open porosity, ε_o are of very similar magnitude, as illustrated in Figure 3 of *Supplement 3*, for an electromagnetically primed [84], 50 PPI filter filled with an A356 aluminium alloy. Some small areas of closed porosity are created by the substrate used in the filter fabrication process. Grosse *et al.* have described the morphological

characterization of CFFs in detail, including the steps required to correctly determine total and open porosity (e.g. using mercury at up to 4000 Bar) [85, 86]. Grosse *et al.* found that the difference between the total and the open porosity is <5% of the measured value. The convention of Dietrich, i.e. equality between the total and open porosities, has therefore been followed in this work.

3.4 Filter Permeability - Experimental

Permeability experiments were conducted using water with commercial alumina CFFs of 30, 40, 50 and 80 PPI and two filter diameters (49 mm 'straight through' and 101 mm 'expanding flow field' diameter) as shown in Figure 3.5 (a) and (b) [*Supplements 3* and *4*]. Water in a temperature range from 5-8 ^{o}C was used, typical ρ_w=999.9 kg/m^3, and μ_w=1.3775 10^{-3} Pa·s.

Mass flows from about 0.05 to 2 kg/s of water were circulated through 46.4 mm ID smooth plastic piping, representing Reynolds numbers from ~1200-39000 and moving from laminar flow, into transitional and partially turbulent pipe flow in the inlet pipe [87]. Eight to ten different experimental velocities were used to measure pressure drop for each filter. Long and short inlet lengths were tested on one 101 mm diameter, 50 PPI CFF, to determine if the development of the inlet flow profile, had any impact on the obtained pressure gradients. Inlet length did not have a measureable impact on the obtained results.

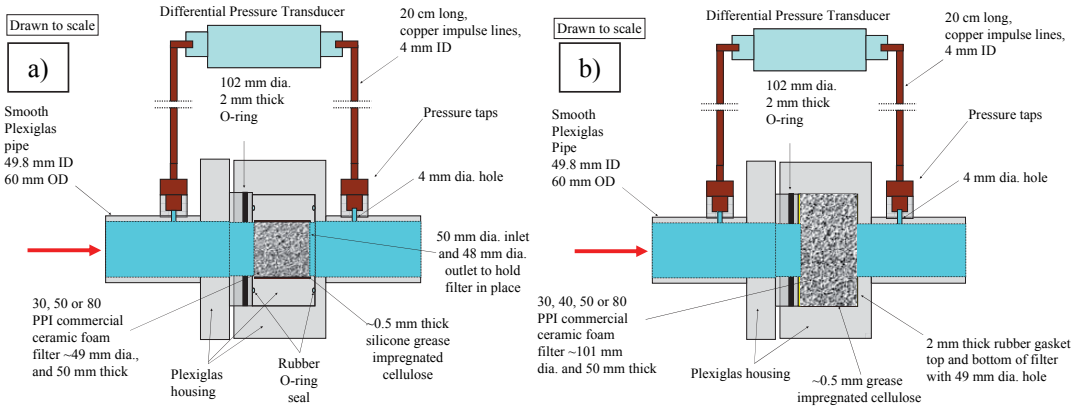

Figure 3.5 – (a) the experimental setup used for the 50 mm thick 49 mm diameter 'straight through', and (b) the 101 mm diameter 'expanding flow field' filter experiments (both drawn approximately to scale). The flow is from left to right. For further equipment details, see *Supplement 3*.

101 mm nominal diameter elements were cut from the full size (20" or 23" square) commercial filters using diamond bores. The 49 mm diameter filter elements were cut from the centre of the 101 mm filter elements after completion of the 101 mm experiments. The true diameter and thickness of each filter element were measured using a micrometer, and the averages of 6 readings were used in the subsequent experimental analysis.

Two Plexiglas® apparatus designs where used, one for the 49 mm diameter filters is shown in Figure 3.5 (a) and the second for 101 mm filters is shown in Figure 3.5 (b). The use of a transparent housing ensured that all air was correctly eliminated from the system prior to recording any pressure readings. The sealing arrangements were of critical importance in the design of the filter housings. In order to prevent wall effects from significantly affecting the results, it is of paramount importance to prevent the flow from bypassing the filter and moving along the walls. Therefore in the final experimental procedure, high viscosity silicone grease was used to smooth the outer surface of each filter (fill the outer-most broken or cut cells), which were then wrapped in paper and pressed tightly into the holder. Upon contact with water, swelling of the cellulose fibres provided a seal of negligible permeability. It is necessary to seal the entire side surface of the filter, as normal O-rings are unable to stop the flow from bypassing along the wall. Development and experimental validation of the sealing procedures are discussed further in *Supplement 3*.

The pressure transducer used was a DF-2 (AEP transducers, Italy), 0-1 Bar measuring range, equipped with a 4-20 mA output. The transducer was factory calibrated and certified to an error of ±0.04% of reading, over the full scale from 0-1 Bar, using a 6 point calibration. During the experiments the current produced by the transducer at zero liquid flow velocity was determined manually using a FLUKE 26 III, True RMS Multimeter (Fluke, USA) to a precision of 0.001 mA (6.25 Pa), using the lowest available current scale. Current during the flow measuring periods were computer data logged at 100 ms intervals by conversion to a 0-5 V signal, with a resolution of 0.001V or 0.004 mA (i.e. 25 Pa resolution or a gradient uncertainty of ~±625 Pa/m depending on the sample). At higher than 4.1 mA, no bias could be detected between the manual and automated current readings, at the available 0.01 mA resolution (the FLUKE switched to a lower resolution at greater than 4.099 mA). The length between the pressure taps was 160 mm (varying ~±1mm). One tap was located 1.5 L/D's up-stream and the other 0.75 L/D's down-stream of the filter element as shown approximately to scale in Figure 3.5.

The water flow rate was determined by accumulating mass over the measuring period in a 100 L tank, located on a digital balance, equipped with a 4-20 mA

output. The scale had a resolution of 10 g and a maximum reading of 100 kg. The zero and span of the scale were verified accurate at the 10 g resolution using test weights to 50% of full scale prior to use. The rate of mass gain of the measuring tank was computer data logged at 100 ms intervals. Depending on the required mass flow, from 10 to 50 kg of water were accumulated. 'Sloshing' of the water in the tank (mainly at very high flows) produced noise on the weight signal that was smoothed by taking a 1 second rolling average (rolling average of 10 readings), which resulted in a maximum flow rate uncertainty of ~±0.5% of reading. The flow rate was found from the slope of the accumulation of mass with time and determined using least squares regression over the whole measuring period (typical R^2=0.9985). Temperatures were measured using a 1 mm diameter Inconel sheathed Type K thermocouple located in the holding tank and the temperature data were also computer logged.

3.5 Filter Permeability – Results

The obtained experimental results for the 101 mm diameter filters are presented in Figure 3.6. Further results can be found in Figure 10 of *Supplement 3* for the 49 mm diameter filter sections.

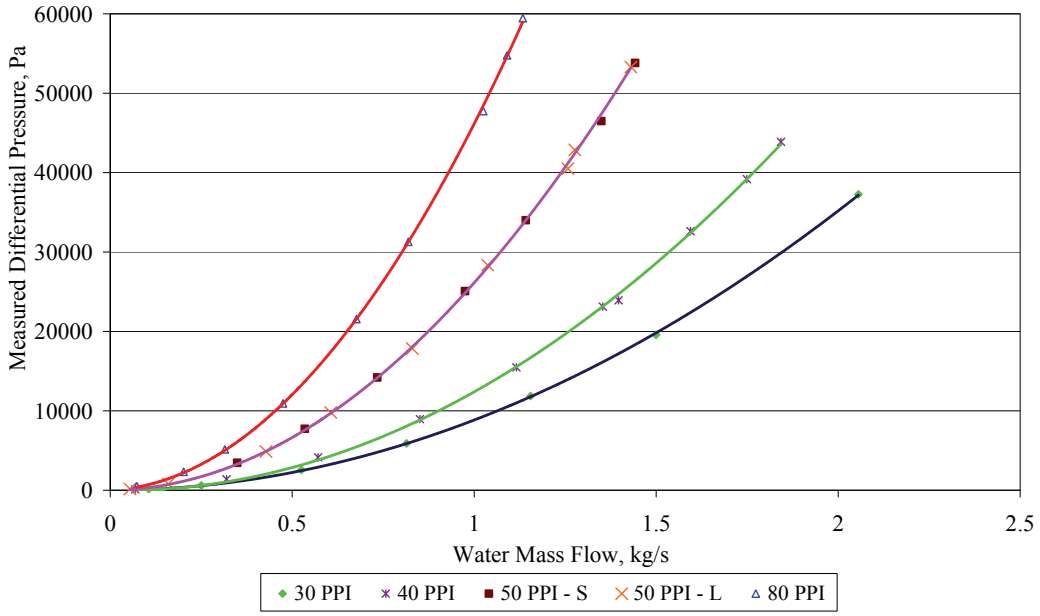

Figure 3.6 – Experimentally measured pressure gradients for the 101 mm 'expanding flow field' design, S indicates a short (1 m) inlet length, and L indicates a long (3 m) inlet length [*Supplement 3*].

Equation [41] was used with the measured pressure gradients and superficial velocities as shown in Figure 3.6, to determine the Forchheimer terms k_1 and k_2. Each estimate used the appropriate water temperature, and therefore density and viscosity, representative of the individual mass flow reading. Superficial velocity was determined using the actual measured filter diameter for the '49' mm filter elements or using the 'effective' flow field diameter for the '101' mm filter elements, as determined using the procedure presented in Figure 3.7. In the 101 mm diameter design the impact of 'wall effects' are essentially eliminated by allowing the flow field to expand within the filter element and making the outer wall a 'stagnant' region. FEM is then required in order to elucidate the flow field and calculate an 'effective' flow diameter for use with Equation [41], which assumes a single representative diameter.

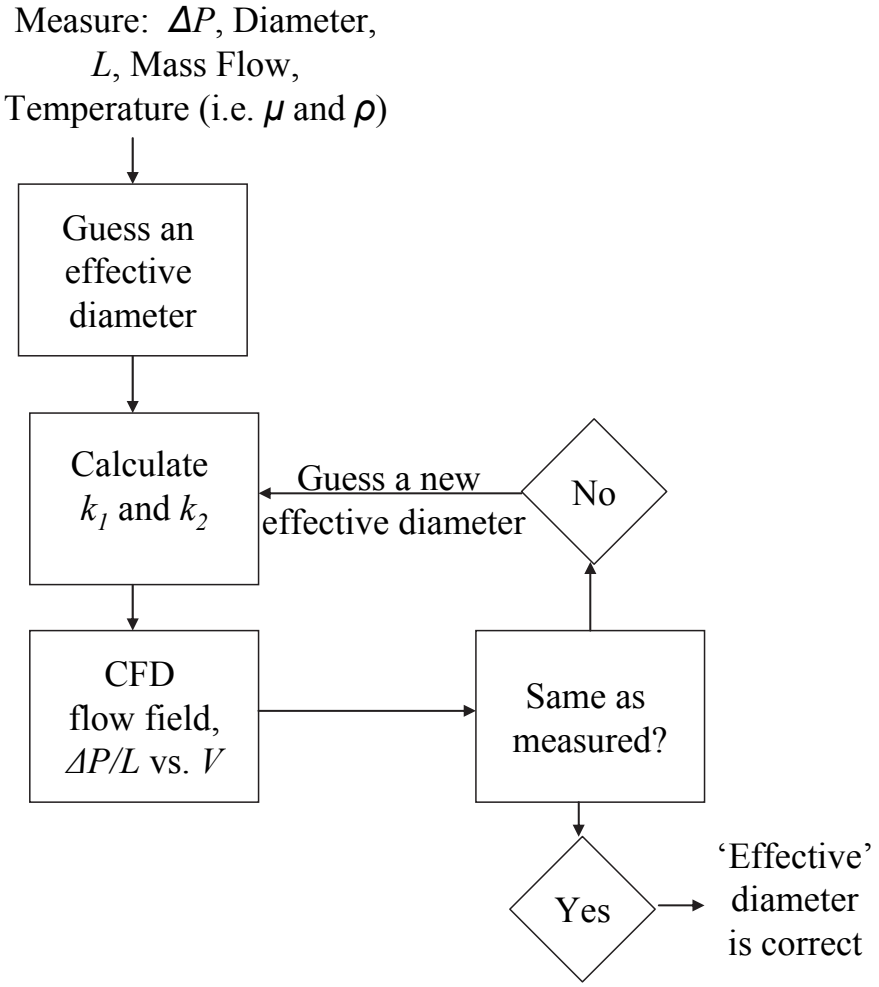

Figure 3.7 – The FEM CFD procedure applied to the 101 mm experimental results to determine the Forchheimer parameters k_1 and k_2, [*Supplement 3*].

Final k_1 and k_2 values are the arithmetic average of the 8-10 values determined for each filter element and are summarized in Table 3.3 for the 49 and 101 mm filters, including short and long inlet lengths for the 50 PPI 101mm diameter.

Table 3.3 Empirically Calculated (49 mm) and Numerically Derived (101 mm) Forchheimer Coefficients for Equation [41], [*Supplement 4*]

Filter Type (PPI)	Actual Filter Diameter (m)	FEM Effective Flow Field Diameter (m)	Eq. [41] Forchheimer k_1 (m^2)	Eq. [41] Forchheimer k_2 (m)	Inlet Length (m)
30	48.7	N/A	5.08E-08	5.46E-04	1.0
30	101	65.5	5.57E-08	5.25E-04	1.0
40	101	66.0	3.10E-08	3.38E-04	1.0
50	49.2	N/A	1.57E-08	1.66E-04	1.0
50	101	66.1	1.71E-08	1.69E-04	1.0
50	101	66.1	1.52E-08	1.71E-04	3.0
80	49.1	N/A	6.52E-09	1.15E-04	1.0
80	101	66.5	5.44E-09	9.96E-05	1.0

It is worth noting, that all deviations in the experiments resulted in lower measured pressure gradients, i.e. the highest measured pressure drop and lowest permeability value for a given filter are most probably the correct values. Recently Innocentini *et al.* [88] discussed the impact of bypassing and flow field expansion on measured pressure drops in metal foam. Examination of the change in pressure drop with filter thickness indicated that wall bypassing reduced the pressure drop and that the measured pressure drop did not increase linearly with increased thickness. The flow field expansion in Innocentini's alternate apparatus design was not analyzed using CFD and in both cases no sealing was indicated at the walls [88]. Inadequate sealing or no-description of the sealing arrangements or failure to account for flow field expansion appeared to be a common feature of many previous articles.

In order to derive the Forchheimer coefficients in Table 3.3, three different mathematical procedures were explored:

1 An 'automated' second order regression, with a zero intercept, using Excel 2003/2010.
2 Ergun *et al.*'s procedure of dividing Equation [41] by the velocity and performing a linear regression [89].
3 An iterative procedure to first guess k_1, subtract the first order component from the total, and then correlate the remainder for k_2, using an exponential regression.

These procedures are discussed in detail in *Supplement 3*. Procedure 1 gave physically meaningless results for k_1 values in particular. Procedure 2 gave greatly improved results. Procedure 3 gave the best results, and hence was used to derive the data presented in Table 3.3. In procedure 3, the first order coefficient was first guessed and subtracted from the total measured pressure gradient. The remainder was correlated using an exponential regression with Excel. The procedure was repeated until an exponent of 2.00000, was obtained. This procedure appeared to prevent experimental uncertainty from being concentrated into the first order Forchheimer term, which when using Procedure 1 became virtually random 'noise'.

3.6 Filter Permeability – Discussion

The obtained Forchheimer k_1 and k_2 parameters were found to correlate well with the measured window area, $\frac{\pi d_w^2}{4}$ as shown in Figure 3.8. Results for both the 101 and 49 mm filter elements could be treated as a single data set.

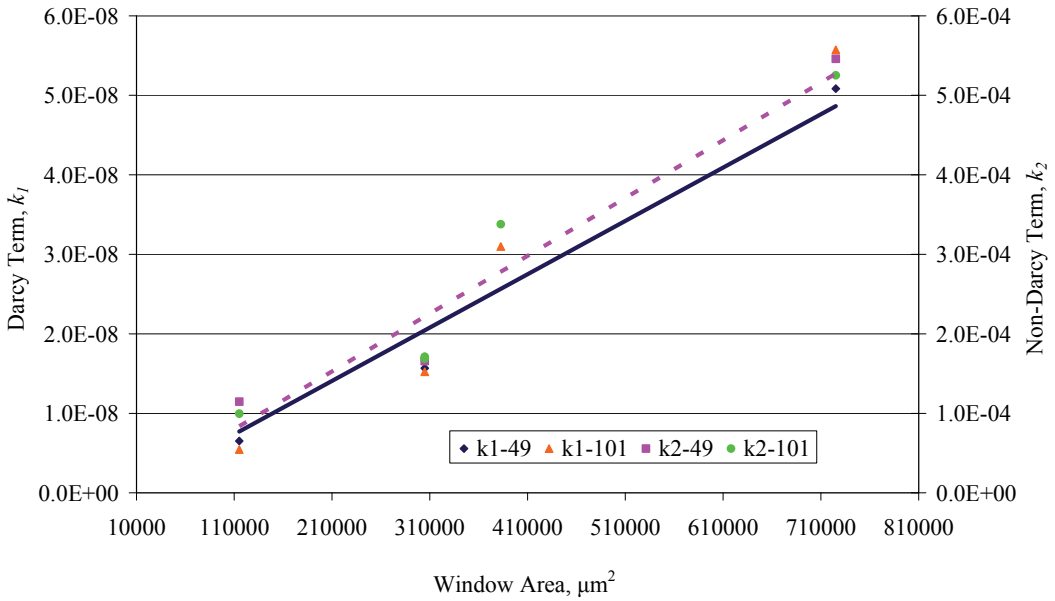

Figure 3.8 – Correlation of Darcy term, k_1 [m^2] and Non-Darcy term, k_2 [m] with window area $\frac{\pi d_w^2}{4}$, [*Supplement 3*].

Empirical correlations have been developed for k_1 [m^2] and k_2 [m], as functions of the window diameter, d_w [m]:

$$k_1 = \frac{6.71\times10^{-2}\pi d_w^2}{4},\ R^2 = 0.974 \quad [49]$$

$$k_2 = \frac{7.27\times10^{2}\pi d_w^2}{4},\ R^2 = 0.960 \quad [50]$$

From Figure 3.8 and Equations [49] and [50], it is concluded that the 30-80 PPI filters tested in these experiments behave much more like a series of 'orifices', than they do a series of struts as is assumed in simple cubic cell [90, 91] or more complex dodecahedron [92] and tetrakaidecahedron [80, 93, 94] models. An examination of Figures 3.1 and 3.2 would seem to support the concept of 'orifices', given the high percentage of closed windows, particularly at higher PPIs. A simple strut model would not appear to be valid for the ceramic foam filters used in this study.

Extensive efforts have been made to correlate the obtained results and compare with previously published general equations. Of the previously published equations, only the equation of Dietrich, Equation [48], was found to adequately describe the data. This comparison is made for the 30, 50 and 80 PPI, 'straight through' 49 mm results in Figure 3.9. Agreement is considered adequate being typically within ±50% (except at low velocity), i.e. it achieves a similar accuracy for foams, as the original Ergun equation achieves for packed beds.

Other equations were found to dramatically underestimate the measured pressure drops obtained using the final and 'well sealed' experimental procedure. Most previously published equations did describe the obtained results for the 'straight through' experiments in the absence of a wall seal or the 'expanding flow field' results in the absence of area correction. No firm conclusions can be drawn from these facts, as details on the sealing arrangements and analysis techniques used in previous studies are generally lacking.

The best empirical correlation obtained was with a slightly modified version of Ergun's equation [78].

$$\frac{\Delta P}{L} = 8.385\left(150\frac{(1-\varepsilon)^2}{\varepsilon^3}\frac{\mu V}{D_w^2} + 1.75\frac{(1-\varepsilon)}{\varepsilon^3}\frac{\rho V^2}{D_w}\right),\ R^2=0.95 \quad [51]$$

Equation [51] is plotted in Figure 3.10, along with +30% and -30% lines.

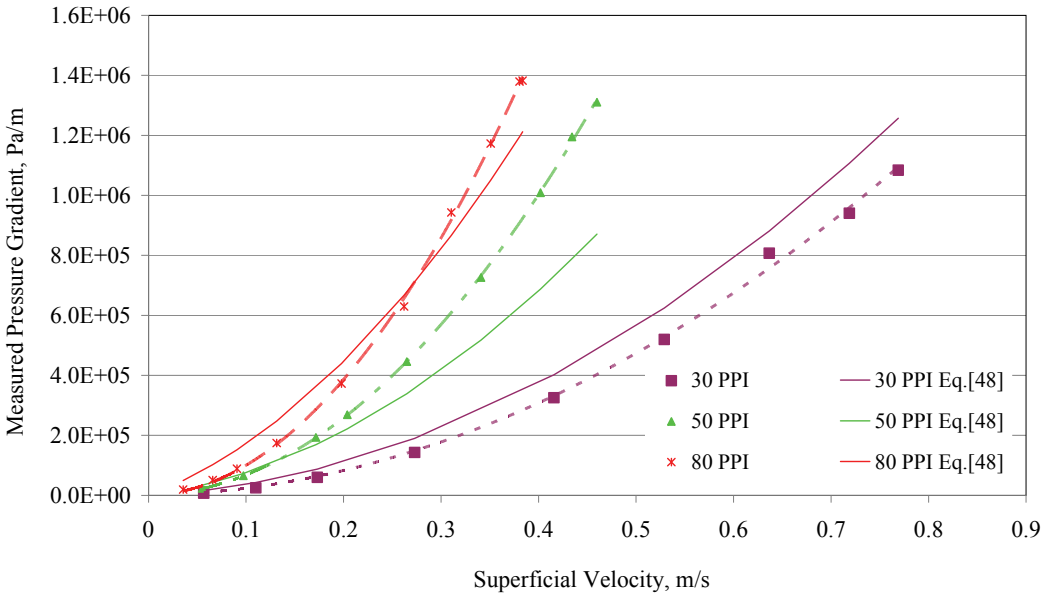

Figure 3.9 – Comparison between Dietrich's Equation [48] [81, 82] and measured data for the 49 mm diameter 'straight through' 30, 50 and 80 PPI measured data. Experimental data are plotted with dotted lines and symbols, Dietrich's predictions are plotted as solid lines, [*Supplement 3*].

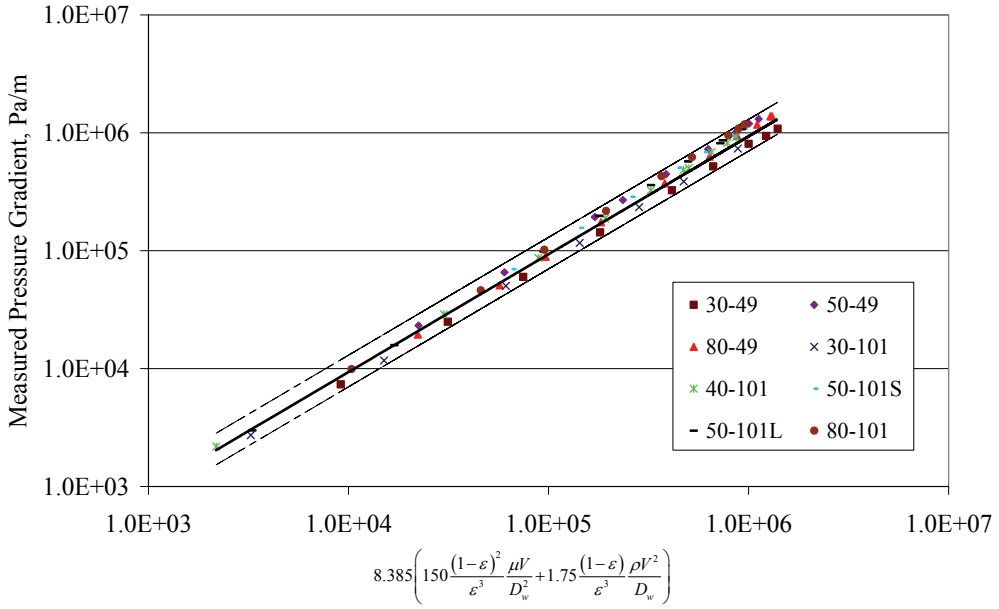

Figure 3.10 – Overall correlation Equation [51], comparison to the measured pressure gradients for 30-80 PPI filter elements. 49 mm diameter measurements were not available for the 40 PPI filters, as the filter exhibited poor mechanical properties and disintegrated on cutting. Dotted lines in the figure indicate a range of ±30%, [*Supplement 3*].

Equation [51] is equivalent to using 23.4 and 2.00 (based on an average ε = 0.88), as the empirical constants, instead of the values 110 and 1.45 in Dietrich's Equation [48] or the Ergun equivalent values of 66.7 and 1.17 from Equation [47]:

$$\frac{\Delta P}{L} = 23.4\frac{\mu V_s}{\varepsilon d_h^2} + 2.00\frac{\rho V_s^2}{\varepsilon^2 d_h} \qquad [52]$$

Applying Equation [52] to the obtained data indicates a significant reduction in error compared with the original Equation [48], particularly at low velocity and pressure and an overall reduction in average error from ~40% to ~30%. Equation [52] is plotted against the 30, 50 and 80 PPI, 'straight through' 49 mm results in Figure 3.11.

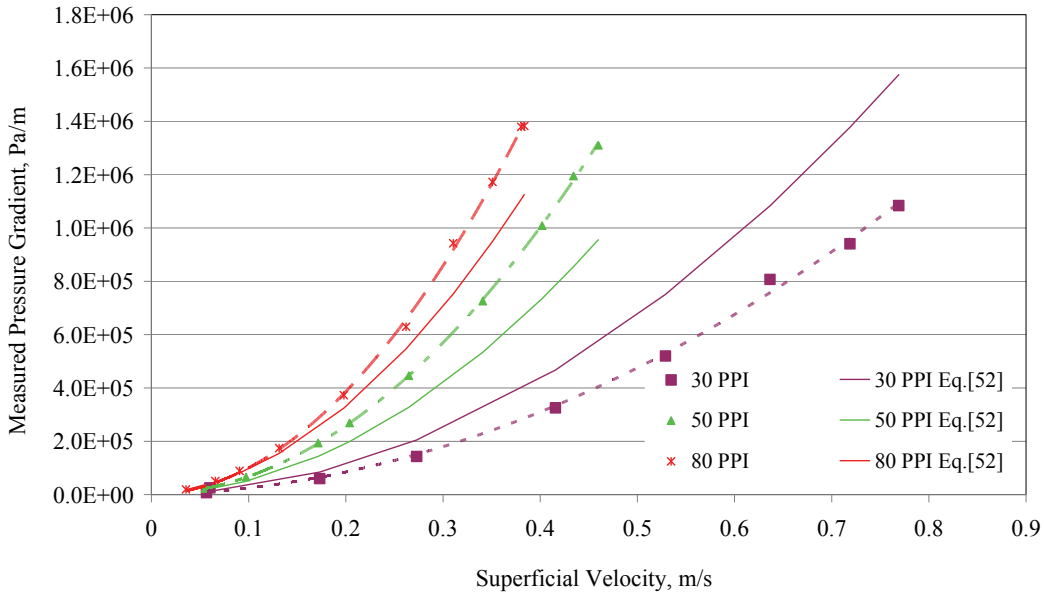

Figure 3.11 – Comparison of the modified Dietrich Equation [52] with experimental data for the 49 mm diameter 'straight through' experimental results from the 30, 50 and 80 PPI filters.

Attempts were made to use cell diameter, d_c, strut diameter, d_s and tortuosity, τ in various correlations; however, no improvement could be made over the accuracy of Equations [52], [51] or [48].

3.7 Filter Permeability –CFD FEM modelling

The CFD models are discussed in detail in *Supplement 4*. 2D axial symmetric models were produced using COMSOL® 4.2a. The geometry of the main filter apparatus, shown previously in Figures 3.5 (a) and (b), were reproduced with an accuracy of about ±0.1 mm, including minor step changes produced during the fabrication process.

Model results are compared for both the 'straight through' 49 mm and 'expanding flow field' 101 mm results in Figure 3.12, showing excellent agreement with the measured pressure gradients. No individual differences exceeded 7%. Results with both the 49 and 101 mm have been modelled with similar accuracy, including both the long and short inlet lengths.

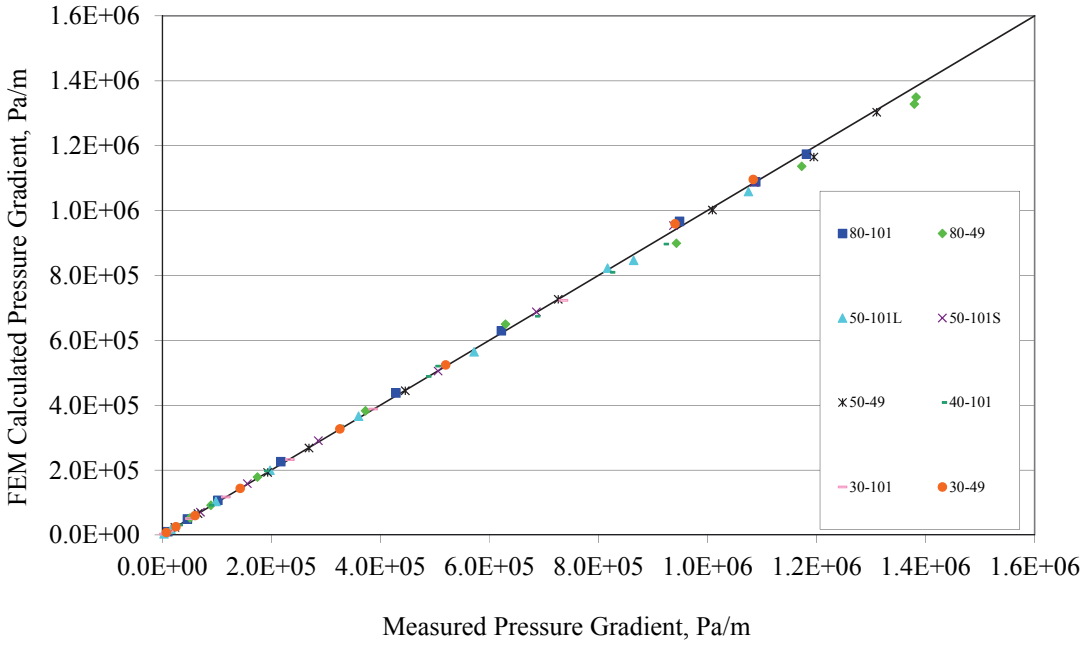

Figure 3.12 – Comparison of FEM calculated and measured pressure gradients, indicating typical errors of <4% for each filter type. The 1:1 line is drawn for reference. S is for a short inlet (1 m) and L is for a long inlet (3 m), as shown previously in Table 3.3.

Some pertinent points to achieving adequate agreement between FEM, analytical models and measured values were:

- Iteration between high quality measurements and FEM to ensure validity of assumptions and accuracy of final models.
- Correct and validated boundary conditions, e.g.: no-slip walls, contiguous velocity fields between liquid and porous media domains, and validation of the assumed inlet velocity profile.
- Use of the low Reynolds number k-ε, Reynolds-Averaged Navier-Stokes (RANS) model for turbulence (k_0 = 0.005 m^2/s^2 and ε_0 = 0.005 m^2/s^3), to adequately cover the difficult range of velocities in the inlet region.
- Use of dense meshes in regions of high velocity gradients (e.g. boundary mesh at the 'no-slip' walls). Failure to use boundary meshes would have resulted in an error of up to 18% in the model estimates [*Supplement 4*].
- Precise measurement and exact geometric reproduction of the actual apparatus.

A sample calculation at 0.5 m/s inlet velocity has been performed using both the FEM models for the 101 mm and 49 mm diameter filter elements and the results are shown in Figures 3.13 (a) and (b). The effect of the expansion of the flow on the velocity field for the 101 mm filter element is clearly indicated in Figure 3.13 (a). The resulting decrease in velocity reduced the pressure gradient for the 101 mm filter element to 501 kPa/m, when compared with the 49 mm filter element with 1612 kPa/m, both at an inlet velocity of 0.5 m/s.

The use of boundary meshes proved critical to achieve an acceptable agreement between model and experimental data, particularly for the 'straight through' 49 mm diameter experimental apparatus. For example, if the results shown in Figure 3.13 are recalculated without boundary meshes, an error of -18% is obtained for the 49 mm diameter experimental apparatus, and -8.2% for the 101 mm case. Smaller errors of ~±1% can be generated by using inappropriate slip wall boundary criteria, or by using significantly biased inlet flow conditions, rather than the assumed uniform inlet velocity.

Discrepancies between the k_1 and k_2 derived with the help of numerical methods (expanding flow field), and those directly determined experimentally (straight through), were on average within 5%, with no individual difference exceeding 17%. Deviations were such that they were compensated, i.e. a high k_1 value was compensated by a lower k_2 value, resulting in nearly identical total pressure drop for each superficial velocity.

It is important to note, that if significant bypassing had occurred during these experiments, it would not have been possible to achieve agreement between the CFD model and the experimental data for the 49 mm filter design. The agreement between the CFD results and the 49 mm and subsequently the 49 mm with the 101 mm designs, is taken as confirmation that the wall sealing arrangements were in fact of negligible permeability.

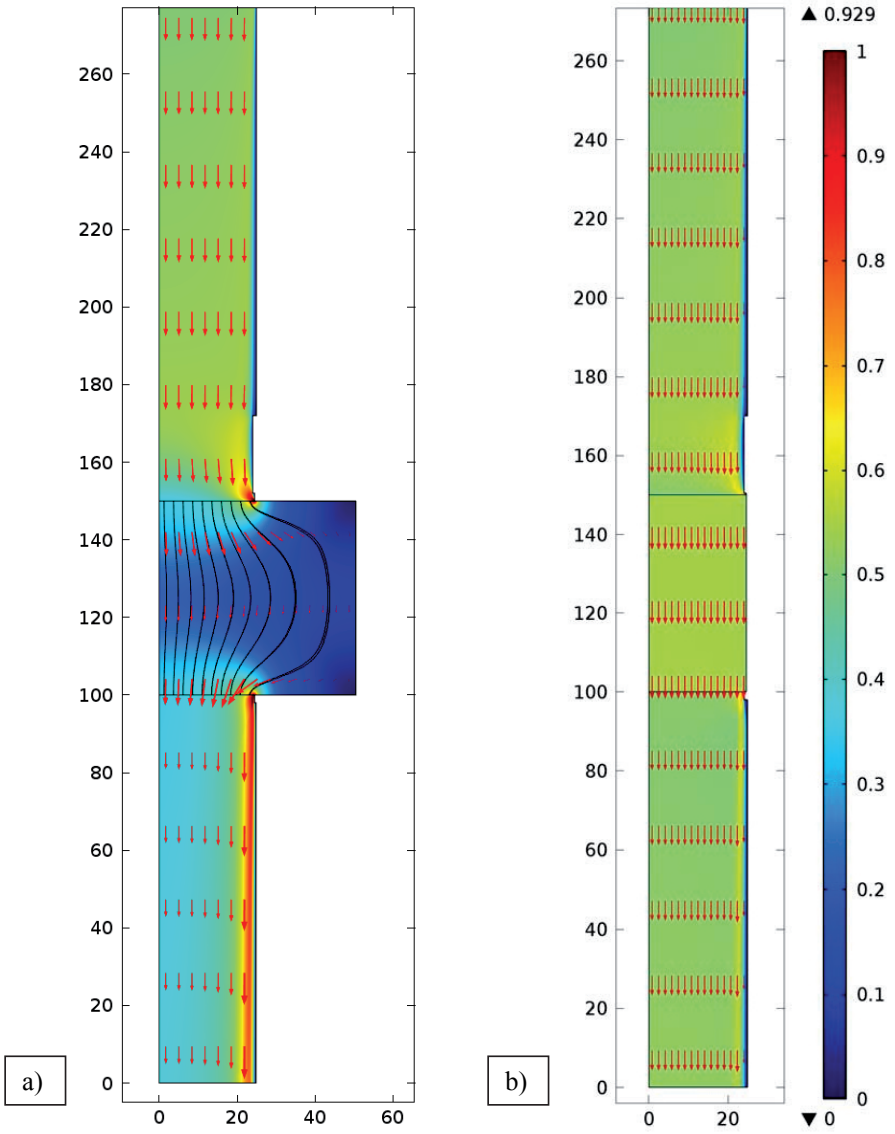

Figure 3.13 – Comparison of calculated flow fields for 50 PPI CFF, i.e. for (a) the 101 mm 'expanding flow field' and (b) the 49 mm 'straight through' designs, both at a 0.5 m/s uniform inlet velocity and for 280 K water temperature.
The results are shown with a common 0-1 m/s colour scale. [*Supplement 4*]

Chapter 4

PART III– THEORY AND VERIFICATION

ELECTROMAGNETICALLY MODIFIED FILTRATION, INCLUDING GRAVITY REFERENCE EXPERIMENTS, AND PRIMING

The objective of the experimental study reported in this thesis, was to apply electromagnetic fields, in order to determine if improved separation could be achieved for particles at sizes down to 10 μm. In order to quantify an improvement, benchmarking of the system under gravity is necessary. Unfortunately filtration efficiency is highly depended on the filter morphology as described in the previous chapter, and this in turn is dependent on the manufacturing process. In order to have adequate benchmark information, not only would results for efficiency in the range from 10-30 μm be required, but it would necessarily need to be for the same filter PPIs and ideally from the same supplier, in order to be assured of the complete relevance. Furthermore, industry standard analytical equipment, is not able to count particles in the range of 10-20 μm with any effectiveness, and there is a resulting paucity of available data in the literature. It was therefore required to execute an experimental program with extensive testing, both using gravity filtration alone, and with electromagnetic fields.

In order to understand the influence of the electromagnetic field on the obtained results, a firm grasp of filtration theory using Ceramic Foam Filters is first required.

4.1 Filtration with CFFs– Introduction and Background

Ceramic Foam Filters as presented in Chapter 3 are applied in the aluminium industry using 'filter bowls', as shown in Figure 4.1. Filters are normally preheated prior to use to prevent metal freezing, reduce thermal shock and to ensure priming of the filters with metal during filling. Priming and filtration are both accomplished using a gravity head of metal, i.e. the inlet to the 'filter bowl' is higher than the outlet as shown in Figure 4.1. During priming, liquid metal fills the pores of the filter and most of the interstitial gas is expelled.

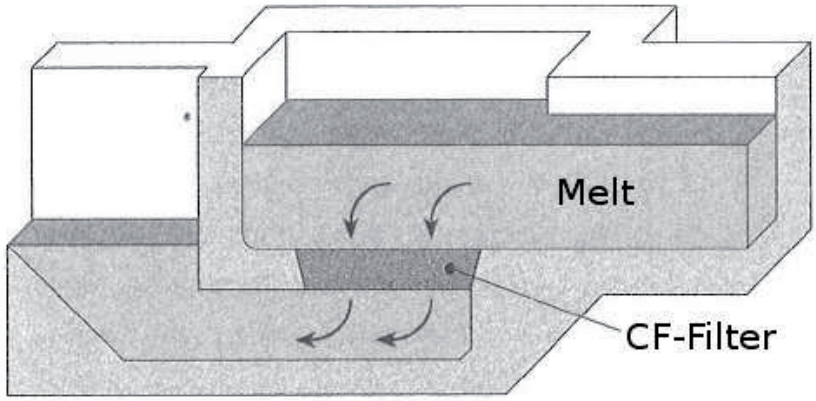

Figure 4.1 – Schematic of a CFF installed in a 'filter bowl' [95].

CFFs are available in different pore sizes, as has been discussed in Chapter 3. Different applications have different recommended casting velocities and pore sizes, based on the required filtration efficiencies [14].

Table 4.1 Supplier Recommended Filter Sizes and Casting Rates [14].

Type of Casting	Superficial Velocity mm/s	Metal Flux kg/s/m^2	Typical Pore Range
Billett	8-15	19-36	30-40
Slag	7-12	17-29	40-65
Continuous	2.5-8	6-19	20-50

Typical industrially obtained filtration efficiency data are presented in Figures 4.2 [11] and 4.3 [14]. Efficiency varies by filter type as indicated in both Figures 4.2 and 4.3, and according to particle size as indicated in

Figure 4.3. The wide ranges of efficiency in Figure 4.1 are partly due to the impact of both different inlet loadings and different casting velocities. Efficiency is generally acknowledged to decrease with increasing velocity [14].

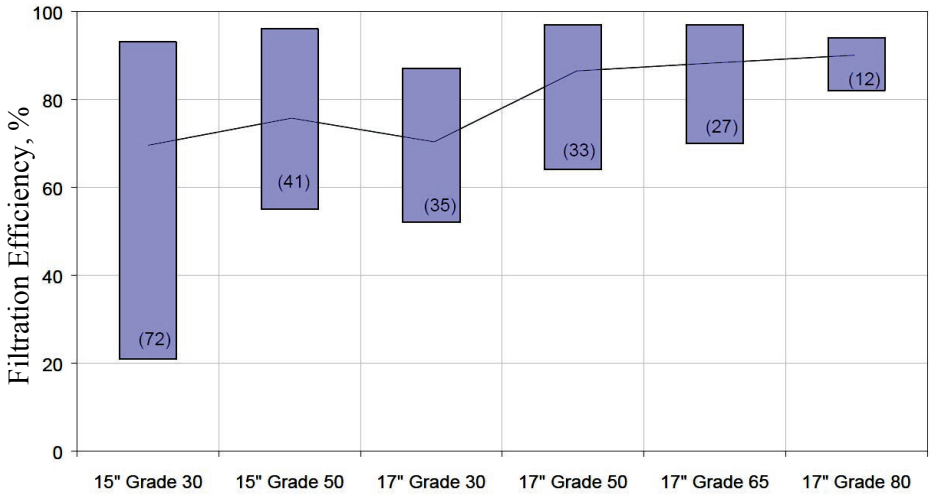

Figure 4.2 – Industrial LiMCA measured filtration efficiency by filter type. Bars indictate ranges of typical efficiency, (brackets) give the range, and the solid line shows the mean values [11].

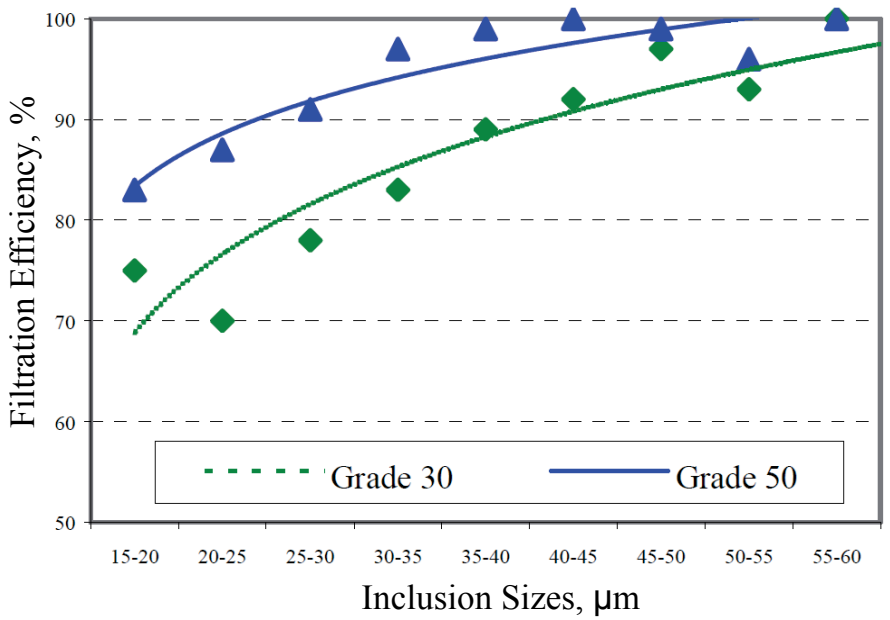

Figure 4.3 – Industrial removal efficiency for 30 and 50 PPI filters as a function of inclusion size for commercial CFF operation, measurements taken using LiMCA [14].

4.2 Filtration – Theory [*Supplements 7-8*]

The removal of solid inclusions from liquid metal is a complex process involving the interaction of many competing collection mechanisms, with physical properties, chemical phenomena, and geometric factors. Many of these factors are summarized in Table 4.2, with reference to various dimensionless numbers commonly applied to filtration phenomena for modelling purposes. Details on these dimensionless groups, the physical properties required to evaluate them, and their relative magnitudes, are given in the Theory section of *Supplement 8*. See Tables III-V.

Additional factors relating to the influence of electromagnetic effects have been added to the traditional factors in Table 4.2, to cover some of the added issues related to the present work. It is possible to define a new dimensionless number to relate the electromagnetic '*pinch*' or *Leenov-Kolin effect* [18] that is experienced by non-conductive particles in a conductive fluid, in the presence of current and a crossed magnetic field [*Supplement 8*]:

$$N_{L-K} = \frac{\pi d_p^3}{8}\left|F_L\right|\frac{1}{3\pi d_p \mu u_i} = \frac{d_p^2\left|F_L\right|}{24\mu u_i} \qquad [53]$$

where $|F_L|$ is magnitude of the Lorentz forces experienced by the conductive fluid [N/m^3] as defined previously in Equation [32] and u_i is the interstitial fluid velocity inside the CFF [m/s].

Equation [53] represents a force ratio between the electromagnetically induced reaction force and the viscous (Stokes) drag force acting on a particle. Equation [53] indicates that electromagnetic separation will be most effective for coarse particles, e.g. >100 μm (>10 μm in the case of the 30 PPI CFFs), and at low filtration velocities, e.g. < 1 cm/s, as shown in Table IV and V of *Supplement 8*.

Equation [53] is only strictly true in the limit of zero interstitial velocity, which is approximately true in hydrodynamic boundary layers. The electromagnetic force decreases from the outer surface of the filter due to electromagnetic penetration effects as shown in Chapter 2 and *Supplement 7*. It will therefore be most effective in the 'stagnant' layer immediately at the outer surface of the filter, in what has been referred to in this document as an '*electromagnetic boundary layer*'.

Table 4.2 Mechanisms, Properties and Phenomena Important to Ceramic Foam Filter Performance with Liquid Aluminum, Including ElectroMagnetic (EM) Effects in Deep Mode Filtration [*Supplement 8*]

	Mechanisms	Most Important Dimensionless Group	Most Significant With
1.	interception	N_R	A web-like series of 'fine' collectors.
2.	impaction	N_{Stk}	High velocity and tortuosity.
3.	sieving	N_S	For bifilms, large particles and agglomerates.
4.	sedimentation	N_G	Large, dense particles at low velocity, horizontal flow, 'porous' collector.
5.	Brownian motion	N_{Pe}^{-1}	Fine, e.g. 1 μm particles, and collector with large internal surface at high turbulence.
6.	attachment (collection)	N_{London}, N_ε, N_{Re}	Small particles, rough collectors, strong surface forces and low velocity.
	Physical properties and phenomena		
i.	gravity fluid flow velocity (fluid density and viscosity, head and filter permeability)		
ii.	Lorentz forces via magneto-hydro-dynamic (MHD) mixing or through a Leenov-Kolin 'pinch' effect (electrical conductivities, magnetic field strength and frequency)		
iii.	surface forces (e.g. wettability and surface chemistry), particle concentration and morphology causing agglomeration, bridging or surface adhesion		
iv.	drag forces, fluid pressure or mechanical vibration, causing particle re-entrainment		
	Geometric factors		
a.	filter morphology (e.g. particle-like, web-like, or pore/window-like)		
b.	internal surface area to volume ratio		
c.	surface roughness		
d.	porosity		
e.	tortuosity		
f.	filter effective resistivity (if current or electromagnetic fields are applied)		
g.	cell, window and strut sizes		
h.	filter thickness		
i.	particle morphology (e.g. rods, needles, spheroids, bifilms)		
j.	equipment arrangement (e.g. down, up or cross flow, arrangement of filter and coil in EM separation, etc.)		

4.3 Filtration – Mechanisms

Filters can operate in two modes of filtration: deep or cake mode [96]. In cake mode filtration, the particles are trapped on the surface of the filter, either by the fine porosity of the filter media (the pores being smaller than the particles) or on other particles which have built up at the entrance of the pores reducing their aperture to less than that of the newly arriving particles. In cake mode filtration the thickness of the cake builds up with time and even for a constant cake pressure gradient, this leads to an increased total pressure drop with time. An increasing total pressure drop and a fixed available head (as in the gravity filtration of liquid aluminium), leads to reduced flow and hence productivity with time. It is therefore generally preferred in the case of the aluminium industry, to operate the filters in deep mode [97].

In deep mode filtration, a pressure gradient forces particles and liquid into the filter, the particles remain within the body of the filter, while the filtrate exits on the 'clean' side. In deep mode filtration particles can be collected by a number of mechanisms including:

a) Interception
b) Impaction
c) Gravity settling
d) Brownian motion
e) Sieving

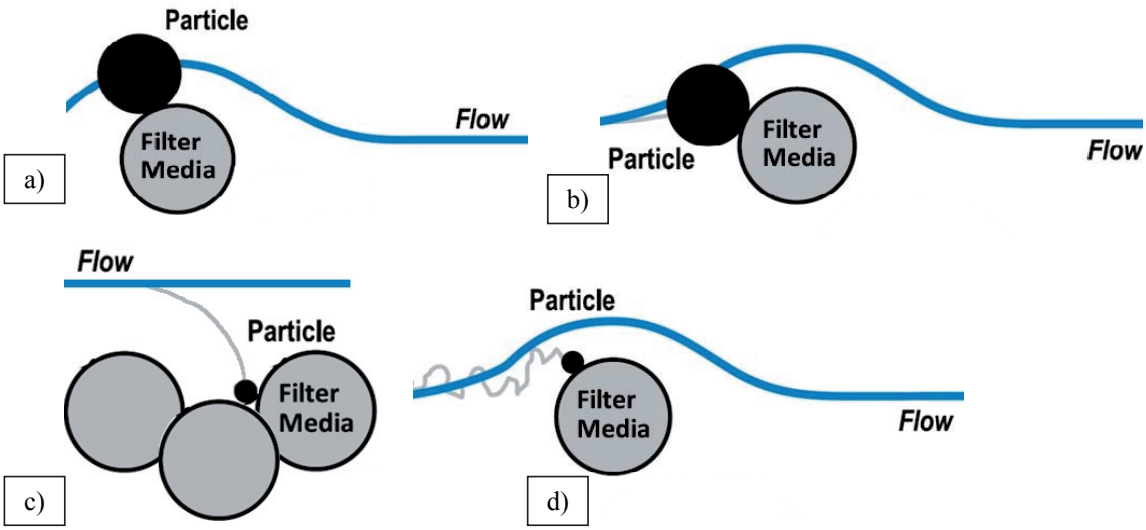

Figure 4.4 – Illustrations of inclusion removal mechanisms (a) Interception, (b) Impaction, (c) Gravity Settling, and (d) Brownian Motion [95].

Researchers trying to identify the controlling mechanism in deep CFF filtration tend to believe gravity sedimentation [98], interception [99] or both [3, 100] are the most significant collection mechanisms. Brownian motion is generally assumed to not play a role in determining collection efficiency in liquid systems.

Numerous analytical solutions for single collector efficiency exist for potential, viscous or inertial flow, which while providing indicative information, are not capable of estimating the overall filtration efficiency. Examples of full theoretical models focused either on sedimentation [98] or interception [6, 99] or a combination (e.g. "limiting trajectory) [13] are available for CFFs.

Sieving or mechanical separation are generally ignored as a mechanism in deep filtration, as it is assumed to play a role only in surface filtration; however, a great deal of evidence exists to indicate that it is a valid mechanism in deep bed filtration. Figure 4.5 (a) through (c) illustrate examples where interception or particle agglomeration appears to have reduced the aperture of a window to where 'bridge-building' or sieving is occurring.

Particle agglomeration within a re-melt furnace, e.g. due to the feeding of surface oxidized scrap, or occurring within the pores of the filter may also make deep filtration a significant mechanism. Particle shape could also play a role, where particles have radically different aspect ratios (e.g. rods and needles) or particles can fold and un-fold (bi-films) or otherwise change dimensions. Figure 4.6 shows a similar image to Figure 4.5 (b) and (c) [4], however the close up image clearly shows particles interacting with bifilms [12]. On cooling the bifilms have been opened by hydrogen gas expansion, as shown in the close up view 4.6 (b). The mechanism of bifilm formation is shown in Figure 4.7, where the oxide layer on the surface of the aluminium metal has been folded onto itself via turbulence.

Particle agglomeration is likely to increase the role of sieving, and increase the efficiency of interception as well as gravity settling. The role of agglomeration in the enhancement of settling beyond that predicted by Stokes law in quiescent systems, has been reported for both TiB_2 in aluminium [101] and SiC in A356 aluminium alloy [102]. The rate of settling in casting furnaces has previously been modelled as a function of not only Stokes law, but of particle concentration [103], which fits with the assumption that particle-particle interactions lead to the formation of agglomerates which may settle, intercept or be sieved with higher than expected efficiency. Clearly any analysis based on single particle efficiency, will fail if particle-particle interactions play a significant role in determining the overall collection efficiency.

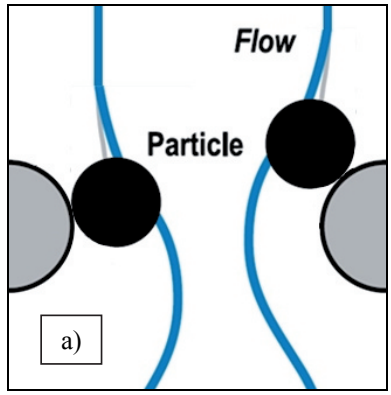

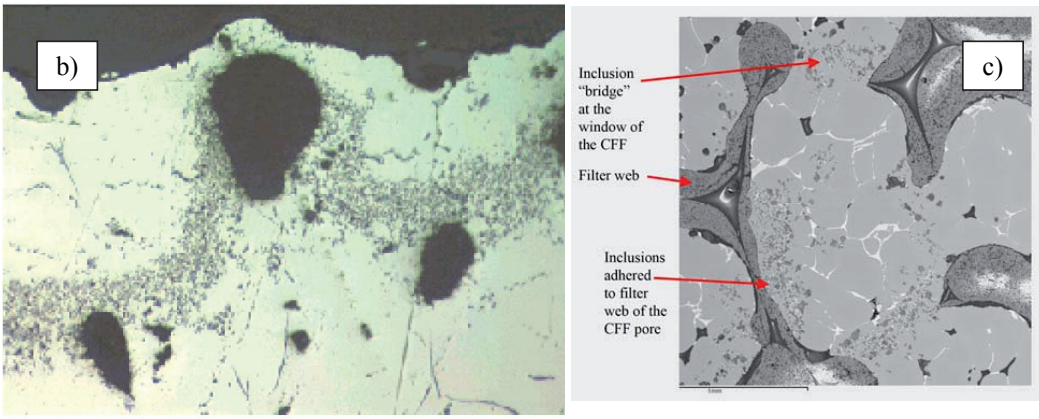

Figure 4.5 – (a) Mechanism of bridge building by interception [95], followed by Sieving mechanism, as shown in micrographs (b) [73] and (c) [14].

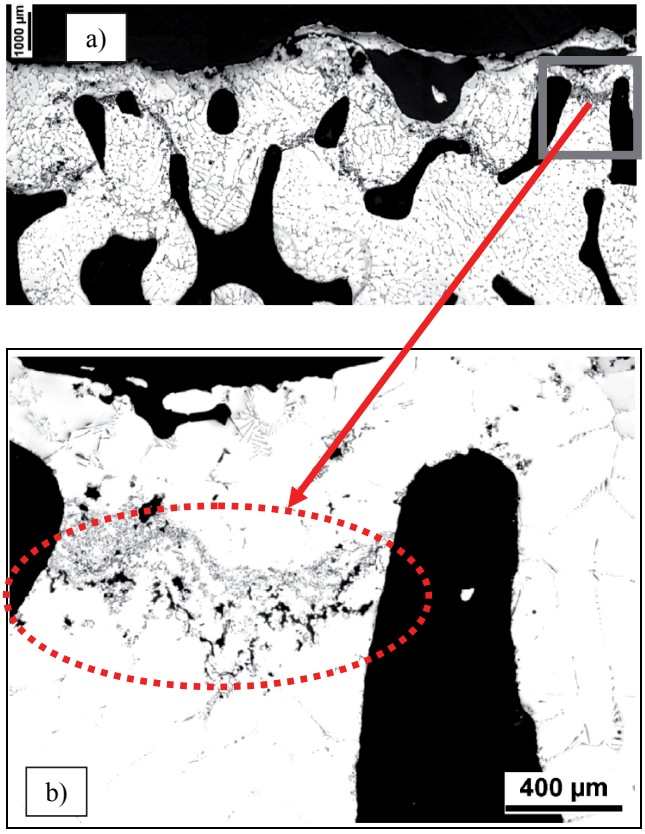

Figure 4.6 – (a) Bridges formed at the top of a 30 PPI CFF, (b) Close-up of a bridge formed by bifilms, shown in the dotted red circle. Bifilms have opened after solidification due to the evolution of hydrogen gas [4].

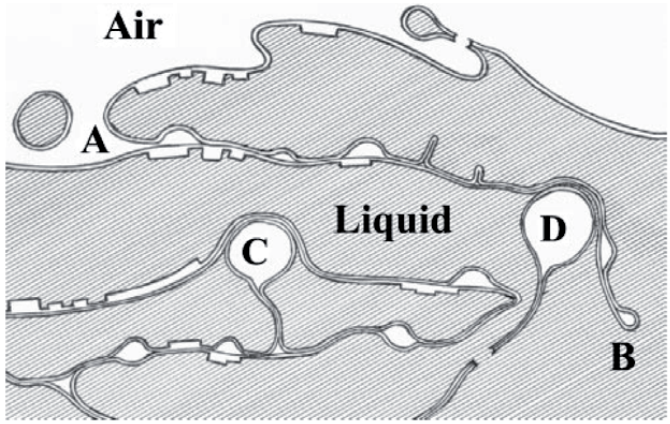

Figure 4.7 – Mechanism of Bifilm formation due to surface turbulence in a liquid metal-gas system and resulting folding of the oxidized surface layer [12].

4.4 Filtration – Empirical Modelling

Analytical modelling is discussed in some detail in *Supplement 8*. Due to the large number of simplifying assumptions required, the utility of mechanistic analytical models must be questioned, particularly if they fail to account for particle-particle interactions or particle re-entrainment. Given the number of assumptions required to arrive at an 'analytical' solution, one must admit that these models are in fact semi-empirical in nature and their utility can only be demonstrated by comparison with experimental data.

A logical alternative to analytical modelling, is purely empirical modelling, which has a long history beginning with Iwasaki in 1937 [104]:

$$E = 1 - \exp^{-\lambda L} \qquad [54]$$

where E is the efficiency of collection [unitless], λ is the filter coefficient [1/m] and L is the physical filter thickness [m]. Iwasaki suggested that the filter coefficient would evolve with time as particulates were collected, beginning from an initial coefficient λ_0, such that the initial filtration efficiency would be defined as:

$$E_0 = 1 - \exp^{-\lambda_0 L} \qquad [55]$$

This type of empirical modelling has proven highly successful for both PDBFs [15, 105] and CFFs [1, 3, 14, 15]. A slightly modified version of Equation [55] was adopted by Apelian *et al.* [105] for the modelling of aluminium filtration, accounting explicitly for superficial velocity:

$$E_0 = 1 - \exp^{-\frac{K_0 L}{u_s}} \qquad [56]$$

Here E_0 is the initial filtration efficiency, i.e. before a significant number of particles have filled the pores, K_0 was defined by Apelian as the initial 'kinetic' parameter [1/s] and u_s is the superficial filtration velocity [m/s].

Apelian found that while K_0 increased with velocity, the overall filtration efficiency decreased with increasing velocity in accordance with the observation in Section 4.1 [14]. The observation of reduced filtration efficiency with velocity had been corroborated in subsequent investigations for both PDBFs [8] and CFFs [3, 13, 14].

Equation [56] is consistent with the assumption that the rate of particle collection is proportionate to the local concentration of particles and that the probability of collection for an individual particle is the same in each unit length throughout a filter. These assumptions immediately lead to the conclusion that the concentration of particles should be an exponentially decaying function of filter depth, which has been verified experimentally on several occasions [3, 106-108].

Traditionally the superficial velocity u_s, is used to evaluate Equations such as [53] or [56]. This assumption is adequate to compare the performances within the same family of filters having similar morphology under various geometric and process operating conditions. It is not logical to use the superficial velocity in comparing the performance of PDBFs with low porosity, (and probably low dead volume and tortuosity), with CFFs having high porosity, dead volume and tortuosity [15]. It is also not logical to analytically model based on conditions, which are not indicative of the local conditions in the vicinity of the actual collector surfaces within the filter. The resulting dimensionless numbers (e.g. force ratios like Equation [53]) would in this case lose all physical significance. Therefore it should be more useful to model using the local internal velocity or *interstitial* velocity, u_i, which is defined here as:

$$u_i = \frac{u_s \tau v_f}{\varepsilon\left(v_f - v_d\right)} = \frac{u_s \tau}{\varepsilon\left(1 - f_d\right)} \qquad [63]$$

where u_s is the superficial velocity [m/s], τ is the tortuosity [unitless], v_f is the filter total volume [m^3], ε is the total porosity [unitless] and v_d is the filter dead volume [m^3] and f_d is the fraction dead volume of the total filter volume [unitless].

Dead volumes (i.e. the difference between total porosity and porosity available for flow) have been determined for CFFs by different investigators and found to be in the range of 30-40% of the total volume for 30-80 PPI CFFs [76] and 16-20% for 8-45 PPI CFFs [74]. 30% dead volume (f_d = 0.3), is therefore taken as representative of the filters used in this study. Total porosities, tortuosities and other morphological parameters of the CFFs were already reported in Chapter 3.

Remembering the definition of tortuosity given in Equation [38], it is possible to calculate the actual average length, which fluid must travel when moving through a filter:

$$L_a = \tau L \qquad [64]$$

From the discussion of CFF morphology in Chapter 3, it is clear that the CFF is made up of cells (or pores), separated by 'struts', which are shared by adjacent cells. The length of a single 'unit cell', L_c [m] would therefore be equal to:

$$L_c = d_c + d_s \qquad [65]$$

The number of cells, N_c [unitless] that any individual fluid element must traverse in the passage from the inlet to the outlet of the filter can be estimated from:

$$N_c = \frac{\tau L}{L_c} \qquad [66]$$

Using Equation [66], and assuming the filter thickness L is the standard 50 mm, the number of cells that the fluid must pass through can be estimated for a 30 PPI, 35 cells, a 50 PPI, 83 cells, and an 80 PPI, 200 cells.

As fluid passes through each cell, every individual particle has a finite probability to be collected. Each of these collection 'events' can be considered unrelated, and the total collection efficiency E is related to *the probability η of collection in one 'event'* [unitless]:

$$E = 1 - (1 - \eta)^{N_c} \qquad [67]$$

where in this probabilistic view, E must be defined based on particle counts, i.e. related to the number of individual particle collection possibilities:

$$E = \frac{N_i - N_o}{N_i} \qquad [68]$$

where N_i is the count of particles entering into the filter per unit time, and N_o is the count of particles out of the filter per unit time. In the current experiments, N_i and N_o have been determined by the number of particle counts per mm^2 of sample area, from rapidly frozen spectrographic disks, taken before and after filtration.

If it is further assumed that each particle has but one opportunity for collection during a passage through a cell, then the 'event' probability becomes equal to the 'cell' probability. Equation [67] assumes that each collection event has the same probability, but provides the flexibility that η can be assumed to also be a function of depth in the filter if so desired. For variable efficiency, Equation [67] must then be 'expanded' into its individual terms.

It is worth considering the differences between Equation [67], which is probabilistic in nature, based on a repeated series of unrelated events, and Equation [56], which assumes that the filter is a continuously differentiable isotropic material. Equation [67] can be approximately re-written:

$$E = 1-(1-\eta)^{N_c} \approx 1-\exp^{-\eta N_c} \qquad [69]$$

where η, which is the collection probability in one 'event' or 'per cell', is assumed very small: $\eta << 1$.

It is now possible to compare the results of Equation [67] with those predicted by Equation [69] for a given probability of collection per cell, e.g. $\eta = 0.05$ or $\eta = 0.5$, and as a function of the number of cells through which the fluid must flow, N_c, as plotted in Figure 4.8.

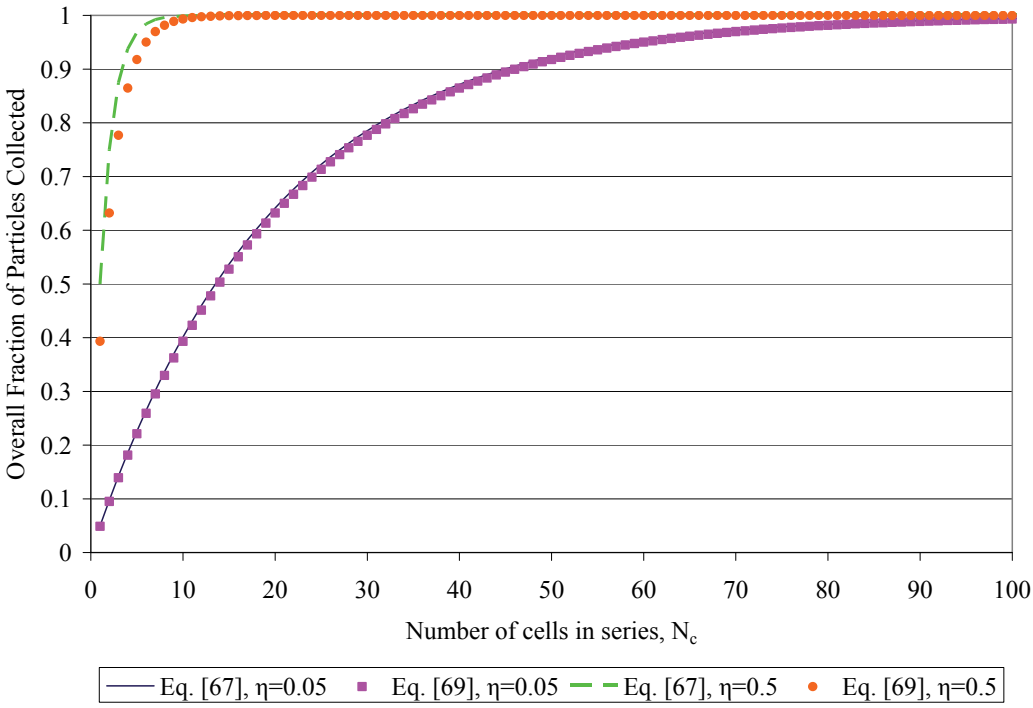

Figure 4.8 – Overall fraction of particles collected for a fixed probability of collection of $\eta = 0.05$ and $\eta = 0.5$, as a function of the number N_c of cells in series, using Equations [67] and [69], [*Supplement 8*].

It can be observed from Figure 4.8, that both Equations [67] and [69] give equivalent numerical results, with no more than a 2.5% difference in estimated values for $\eta = 0.05$ (a realistic single event probability). Larger errors,

e.g. 10%, can be experienced with very large η, e.g. 0.5, and small numbers of cells. This is not a serious issue, as such a theoretical filter would have an overall efficiency of ~100% for normal filter thicknesses, as also indicated in Figure 4.8. It can therefore be concluded that Equation [67] will also result in an exponential decay of the collected particulates versus depth in a filter, without the need to assume that the filter is a continuous isotropic material. As a filter actually consists of periodically alternating volumes of solid and liquid, Equation [67] is therefore more consistent with physical reality, and also provides the possibility of applying variable collection efficiency during modelling.

Comparing Equation [56] with the approximation Equation [69] it can be observed that:

$$\frac{K_0 L}{u_s} \approx \eta N_c \qquad [70]$$

where η is the total collection probability for each cell. K_0 must be calculated in the case of Equation [70], by using Equation [56].

4.5 Filtration - Experimental

The focus of the experimental and filtration results presented in the cover of this thesis will be on the 12 final flow filtration experiments reported in detail in *Supplements 7* and *8*. Older experiments are well documented in either the attached *Supplements 5* and *6*, or (for 13 out of 16 batch experiments) in the recent Masters thesis by Fritzsch [95]. Experiments related to the early equipment and procedural developments are discussed in *Supplement 6*. *Supplement 6* discusses some of the highlights from the batch experiments, including electromagnetic priming. Electromagnetic priming will be discussed as a separate topic after filtration. The recent provisional US Patent application [84] on this particular topic can be found in *Appendix 1*.

A series of 15 flow filtration experiments have been conducted to explore the relationships between filter PPI, filtration rate (i.e. superficial velocity), particle size, electromagnetic priming and induced magnetic fields on filtration efficiencies using CFFs. 3 preliminary experiments looking at the impact on filter wetting and two of the earliest experiments looking at filtration efficiency with 30 PPI filters with and without a magnetic field, are discussed in detail in *Supplement 7*. The final 12 experiments are the focus of *Supplement 8*. Highlights of these 12 experiments will be presented here, but the reader is recommended to read *Supplement 8* in its entirety.

The conditions for the final 12 flow experiments are outlined in Table 4.3. In these experiments, it was not practical to construct an apparatus of sufficient height to realize Gravity priming of 50 and 80 PPI filters in the absence of a magnetic field, and therefore no Gravity priming-Gravity filtration experiments were performed with these types of filters.

Table 4.3 Summary Final Quantitative Filtration Efficiency Experiments, [*Supplement 8*]

Experiment number	Filter Type, PPI	Discharge orifice size, mm	Electro-Magnetic or Gravity priming	Electro-Magnetic or Gravity filtration
1	30	3.2	G	G
2	30	3.2	G	G
3	30	3.2	EM	G
4	30	6	G	G
5	30	6	EM	G
6	50	3.2	EM	G
7	50	6	EM	G
8	80	3.2	EM	G
9	80	6	EM	G
10	30	3.2	EM	EM
11	50	6	EM	EM
12	80	6	EM	EM

A large batch of 150 kg of melt was produced for use with 4 experiments of up to 25 kg each on each day of testing. The melt was held in an agitated vessel with a graphite mixer to prevent settling of the SiC particulates. During the experiments, metal was continuously added to maintain ~125-150 mm of metal head (100 mm minimum) over the filter. In Figure 4.9, liquid metal is shown being continuously added by transfer ladles from the holding furnace (two ladles were used to maintain the transfer), flowing through the filter and passing out through the orifice indicated in the schematic, through a hole in the support table and falling into the fibre receiving crucible on the scale (where the filtration rate was measured).

Metal samples for filtration efficiency determination were taken directly from the holding furnace (i.e. before filtration) and 'in-flight' from the falling metal stream under the apparatus. Steady state filtration was continued until approximately 20 kg of metal had been filtered or cake filtration began, at which point feeding was stopped and the apparatus was allowed to empty.

975 K was typical of the average temperature during steady state filtration for all experiments. A typical set of computer data logged during one experiment is presented in Figure 4.10.

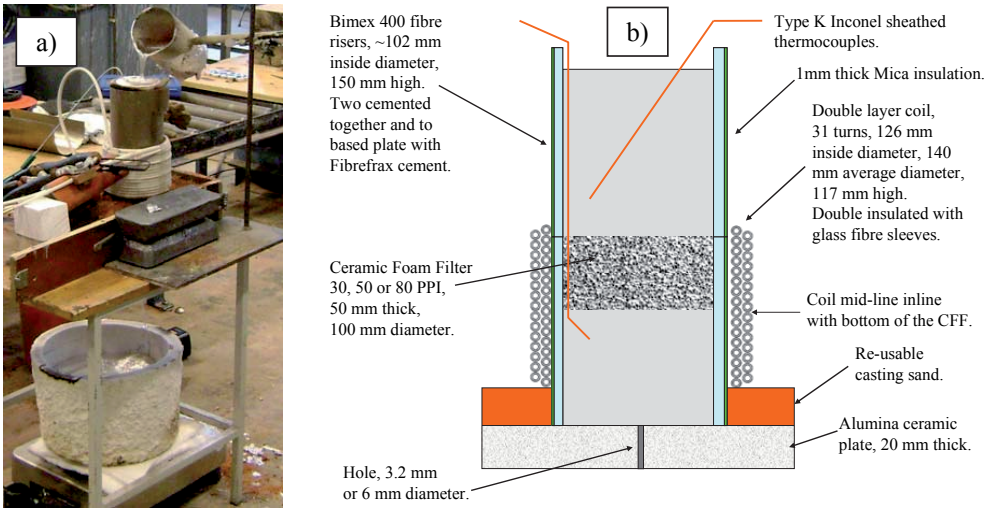

Figure 4.9 – (a) Photograph showing metal addition and discharge onto the weighing device during actual operation. The receiving fibre crucible volume limited runs to approximately 25 kg each. (b) Schematic of experimental apparatus used for filtration experiments. Note that the coil is placed such that the mid-line of the coil (and highest flux density) is inline with the bottom of the CFF, [*Supplement 8*].

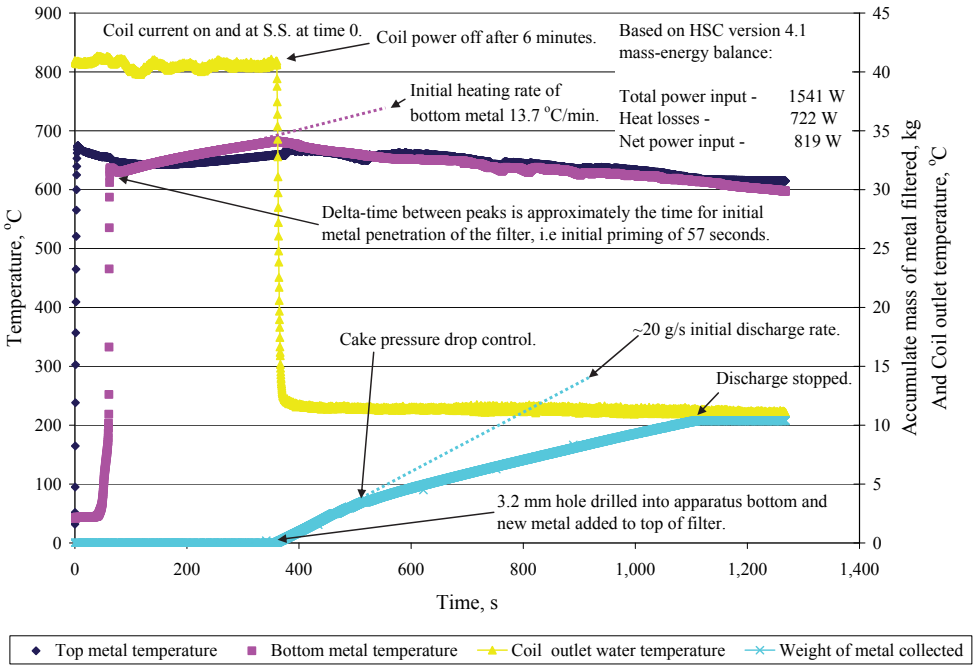

Figure 4.10 – Typical set of computer logged experimental data, annotated with comments. For an 80 PPI filter, EM primed for 6 minutes, and Gravity discharge during filtration. Period with coil power is indicated by coil cooling water outlet temperature. Coil applied current was 732 A at 50 Hz and total coil power input was 13.0 kW, [*Supplement 8*].

4.6 Material and Sample Analysis

A standard non-grain refined A356 alloy was used for all the filtration experiments (see *Supplements 5, 6 or 8*). For the flow filtration tests, a feed recipe was prepared containing 90% A356 alloy, and 10% composite SiC/A356 master alloy. The master alloy reportedly contained 15 wt.% SiC particles, with a size range of 13-23 μm. A representative image take of the Master alloy is shown in Figure 4.11.

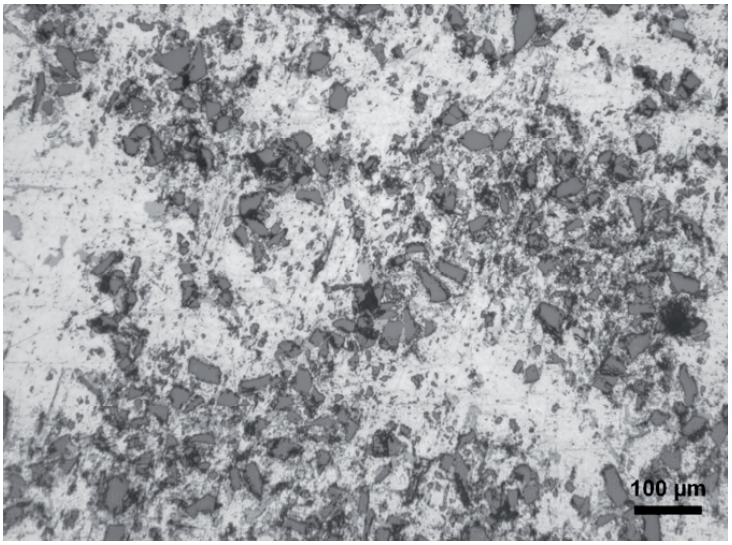

Figure 4.11 – Typical SiC containing master alloy light microscope image at 20 X magnification. One image out of 260 used for establishing a particle count and size distribution using Image-Pro® Plus Version 7.0 macro-automated image processing and analysis software, [*Supplement 8*].

The size distribution of the Master alloy (as determined using optical image analysis) is shown in Figure 4.12. The fraction >20 μm in Figure 4.12 is not more than 3.2%, and represent the only particles in the sample, which would normally be counted in a LiMCA [109] detector on the N_{20} channel. Comparing only >20 μm particles, and assuming 6.3% by weight particles as determined optically in the master alloy, each kg of 'recipe' represents ~4000 kg of 'normal' aluminium (with an N_{20} count of 30000/kg). Each kg of metal filtered, corresponds therefore to about 6 hours of industrial filtration at 1 cm/s superficial velocity, and was therefore significantly greater than what would normally be processed industrially in a single cast through one filter [4].

The overall quantitative filtration efficiency and efficiency by particle size, was determined using rapidly solidified spectrographic samples from before, and during the flow filtration trials. A series of 40 digital photographic images

taken at 10 X magnification from each of the rapidly solidified samples (typically 8 samples and 320 images per experiment) were analyzed using Image-Pro® Plus Version 7.0 macro-automated image processing and analysis software. See *Supplements 7* and *8* for details.

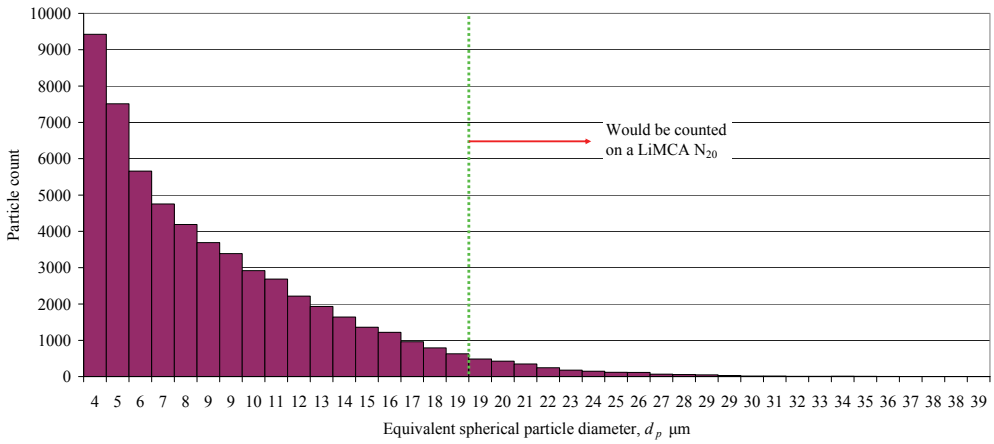

Figure 4.12 – Master alloy particle count for various measured particle diameters, d_p using 260 images at 20 X magnification. Mean master alloy particle size was 8.8 µm, median 7.5 µm, standard deviation 4.8 µm. Measured total particle fractional area was 5.4 area/volume % or about 6.3 wt. %. Particle counts and measured area do not include particles <2 µm, which could not be analyzed with sufficient reliability. Particles to the right of the dotted line represent the particles which would normally be counted by a LiMCA N_{20} count, or about 3.2% of the total, [*Supplement 8*].

Overall efficiency (E_{total}) could be determined by comparing the fraction of the area of the disk samples occupied by particles before and after filtration.

$$E_{total} = \frac{Fractional\ area_{particles\ in} - Fractional\ area_{particles\ out}}{Fractional\ area_{particles\ in}} \qquad [71]$$

This method is equivalent to using a volume or weight fraction, as correction factors apply equally to numerator and denominator and hence cancel. This method is comparable to the chemical methods used previously by Apelian *et al.* [105], but does not provide efficiency by size information.

Efficiency by size ($E_{size\ fraction\ x}$) was determined using the equivalent spherical particle diameters (corrected for stereoscopic effects) in the ranges from 2-5 µm, 5-10 µm, 10-15 µm, 15-20 µm, and 20-25 µm and comparing the particle counts before and after filtration, for identical photographic areas.

$$E_{size\ fraction\ x} = \frac{Normalized\ Count\ In_{size\ fraction\ x} - Normalized\ Count\ Out_{size\ fraction\ x}}{Normalized\ Count\ In_{size\ fraction\ x}} \quad [72]$$

Only steady state filtration results are presented in this thesis. This period was defined as the period after the initial priming metal had left the filter (for electromagnetic priming) and up until cake pressure drop became the controlling flow resistance in the system. During the steady state filtration phase, it was assumed that the efficiencies calculated using Equations [71] and [72] were equivalent to the 'initial' E_0 from Equation [56]. Given the very high particle loading used in this experimental program, this assumption may not have been accurate and future experiments could benefit from a lower particle loading and larger number of starting and time based samples.

4.7 Filtration - Results

Experiments were conducted with each type of filter on each of 4 days of testing, which should have reduced systematic biases due to uncontrolled variations. In Tables 4.4 and 4.5 the experiments have been arranged into comparable groupings, according to filter type and filtration conditions. Table 4.4 summarizes the power measurements for the electromagnetic priming and filtration experiments. The magnetic flux density remained approximately constant in all these experiments (~ 0.17 T).

Table 4.4 Electrical and Magnetic Conditions During the Priming and Electromagnetic Filtration Periods, [*Supplement 8*]
(N/A = not applicable for gravity filtration)

Experiment	Filter type, PPI	Discharge orifice size, mm	Current, A	Volts, W	Total coil input power, W	Net power induced in melt, W	Estimated field strength, T	Comments
1	30	3.2	N/A	N/A	N/A	N/A	N/A	Gravity
2	30	3.2	N/A	N/A	N/A	N/A	N/A	Gravity
3	30	3.2	730	28.59	12900	1644	0.18	EM priming
4	30	6	N/A	N/A	N/A	N/A	N/A	Gravity
5	30	6	730	28.7	13000	1668	0.18	EM priming
6	50	3.2	720	28.32	12600	1563	0.17	EM priming
7	50	6	727	28.59	12780	1547	0.17	EM priming
8	80	3.2	732	28.78	13000	1541	0.17	EM priming
9	80	6	725	28.51	12700	1475	0.17	EM priming
10	30	3.2	720	28.4	12660	1613	0.17	EM filtration
11	50	6	731	28.67	12820	1503	0.17	EM filtration
12	80	6	727	28.44	12630	1492	0.17	EM filtration

Table 4.5 summarizes the main filtration results including results from Equation [71] based on fractional area and Equation [68] based on particle counts per unit sample area.

Table 4.5 Summary of obtained Filtration Rates, Overall Filtration Efficiency based on Equations [68] and [71], and Filtration Efficiency per 'event', η, from Equations [67] and [69], for 150 mm Nominal Metal Head, [*Supplement 8*]

Experiment	Filter type, PPI	Discharge orifice size, mm	Average experiment temperature, K	Steady state filtration superficial velocity, cm/s	Average SS filtration eficiency based on area	Average SS filtration eficiency based on particle count	Efficiency per 'event' from Eq. [67]	Efficiency per 'event' from Eq. [69]	Comments
1	30	3.2	932	0.15	0.89	0.84	0.052	0.053	Gravity
2	30	3.2	969	0.22	0.75	0.62	0.027	0.027	Gravity
3	30	3.2	998	0.17	0.68	0.69	0.033	0.033	EM priming
4	30	6	988	0.54	0.50	0.50	0.020	0.020	Gravity
5	30	6	986	0.68	0.16	0.19	0.006	0.006	EM priming
6	50	3.2	924	0.13	0.81	0.73	0.016	0.016	EM priming
7	50	6	980	0.70	0.60	0.61	0.011	0.011	EM priming
8	80	3.2	927	0.08	0.93	0.90	0.011	0.011	EM priming
9	80	6	967	0.10	0.96	0.95	0.014	0.015	EM priming
10	30	3.2	946	0.18	0.37	0.47	N/A	N/A	EM filtration
11	50	6	980	0.73	0.33	0.13	N/A	N/A	EM filtration
12	80	6	969	0.59	0.16	0.29	N/A	N/A	EM filtration

Overall steady state filtration efficiency based on particle counts from Equation [68] has been plotted for each experiment in Figure 4.13, grouped according to filter type and filtration conditions. Figure 4.13 indicates a decrease in overall efficiency for the 50 and 80 PPI filters with EM filtration, while the 30 PPI filter, was significantly less impacted. EM priming did not have a significant impact on the obtained filtration efficiency for the 30 PPI filters, when compared to the wide standard deviation of 30 PPI filter results encountered under laboratory and industrial conditions as indicated in Figure 4.14.

The wide range of 'typical' performance for commercial 30 PPI CFFs are indicated in Figure 4.14 [11], along with the reduced ranges typical of 50 and 80 PPI CFFs (generally assumed to be due to the reduced variation in the cell/pore or window sizes indicated by the lines on the figure). Under similar conditions, the efficiency is found to decrease at higher superficial velocities in accordance with Equation [56], and as shown in Figure 4.15. The velocity effect explains most of the 'scatter' in Figure 4.14, without consideration of the variance in the cell or window sizes. Figures 4.15 and 4.16 show generally lower efficiency with EMF than using Gravity alone.

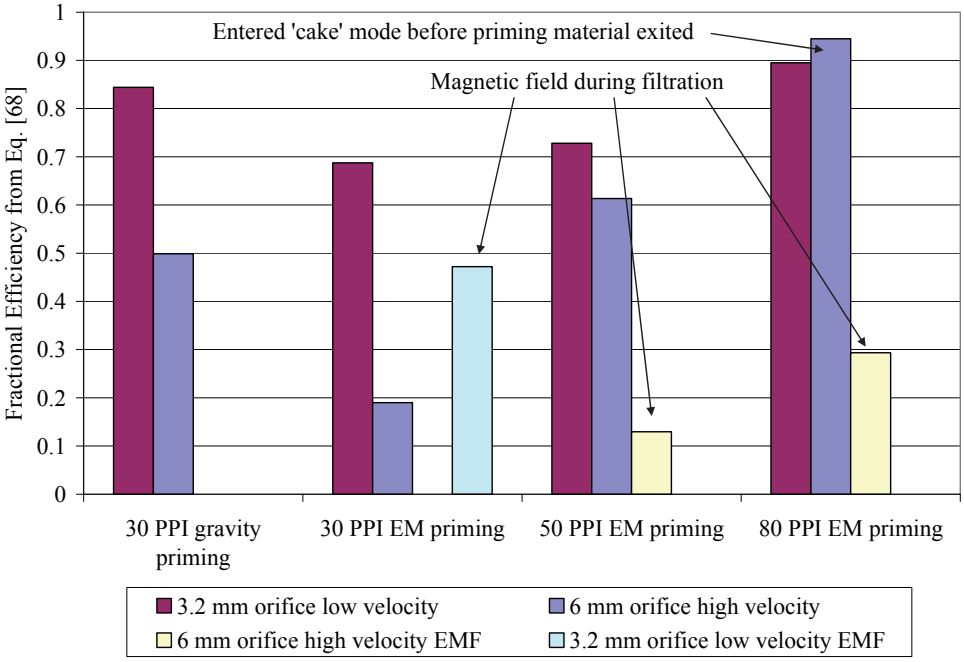

Figure 4.13 – Overall steady state filtration efficiency from Equation [68] by filter type and priming/filtration conditions. EMF indicates experiments with electromagnetic filtration, [*Supplement 8*].

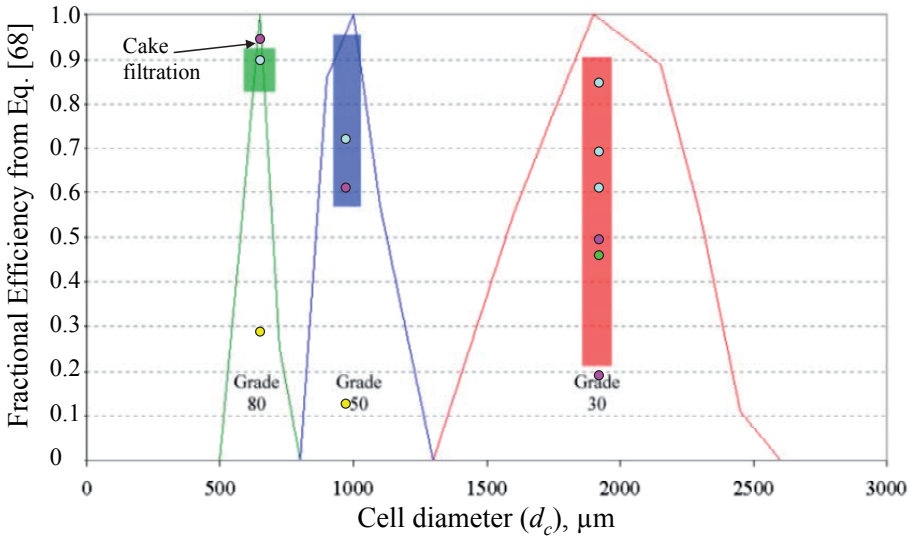

Figure 4.14 – Experimentally obtained overall fractional steady state filtration efficiency from Equation [68] plotted for different filter types (30, 50 and 80 PPI) against the typical cell diameter data for each filter type [11]. Filtration conditions are defined by the dot colour: blue - 3.2 mm orifice gravity, green - 3.2 mm orifice EM filtration, purple - 6 mm gravity, and yellow - 6 mm EM filtration. Gravity and electromagnetic priming are plotted as a single data set. Coloured bars indicate the range of normal commercial filtration efficiency and the lines indicate the relative frequency of different cell diameters, [*Supplement 8*].

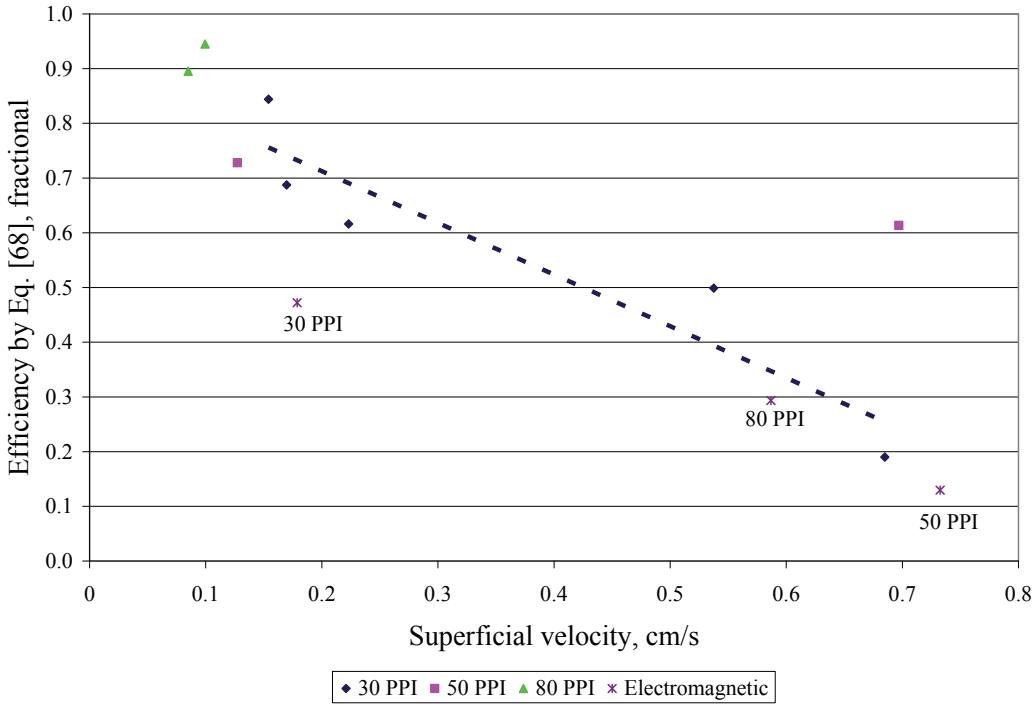

Figure 4.15 – Overall steady state gravity filtration efficiency by Equation [68] versus superficial velocity, u_s, for different filter types: 30, 50 and 80 PPI. Electromagnetic filtration data is also indicated for comparison purposes, [*Supplement 8*].

Insufficient data is available to develop correlations with velocity for the 50 or 80 PPI, but the following empirical correlation was found for the five 30 PPI filtration experiments (including data from both electromagnetic and gravity priming):

$$E_{30\,PPI} = 0.9014 - 0.9445\, u_s,\ R^2=0.87 \qquad [73]$$

where u_s is the superficial velocity [cm/s].

Equation [73] is presented using superficial velocity in accordance with tradition and to avoid the use of debatable assumptions (like dead volume). To compare the current data with other systems (e.g. with PDBFs) will therefore require compensation for changes in porosity, dead volume and tortuosity.

4.8 Electromagnetic Filtration after Electromagnetic Priming

Filtration with the simultaneous application of an electromagnetic field, results in fluid *recirculation* due to the curl in the Lorentz forces, which invalidates the theoretical basis of Equations [56] and [67], i.e. once through filtration. With the application of Lorentz forces, the liquid metal no longer makes only a single pass through the filter and no longer flows solely 'down' under the influence of gravity, i.e. it may flow sideways or even upwards and therefore comparable K_0 values to those of Apelian *et al.* [105] can not be calculated. Efficiency by size under electromagnetic conditions has been plotted for each of the filter types in Figure 4.16, along with various explanatory annotations.

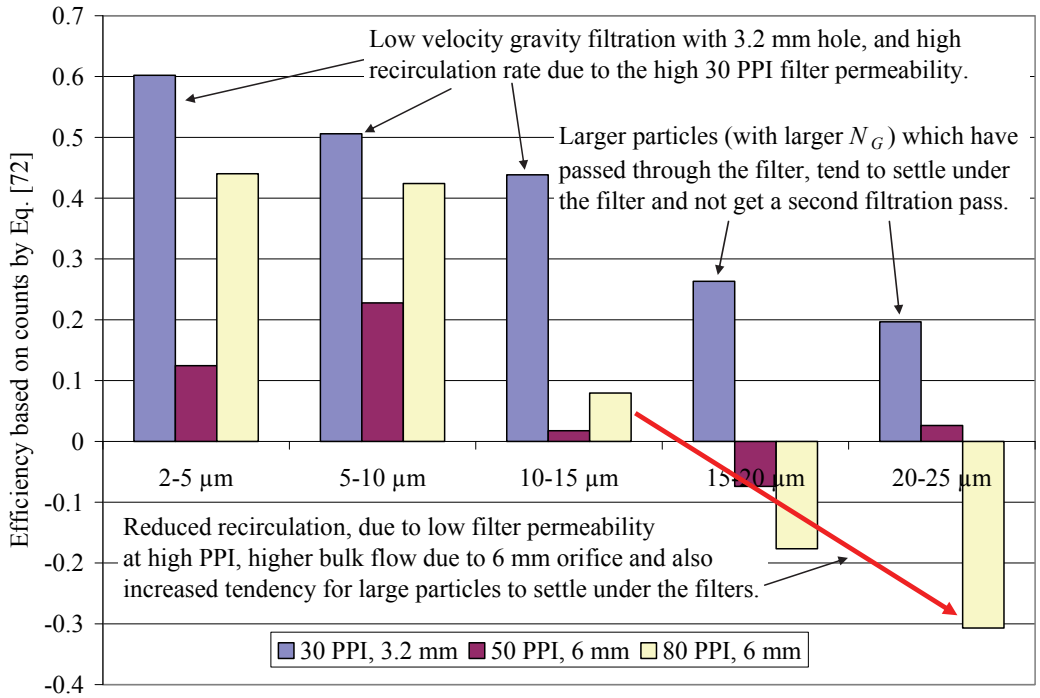

Figure 4.16 – Efficiency for size ranges 2-5 through 20-25 µm, for experiments 10 to 12 and operation using a standard 0.17 T electromagnetic field during filtration. Results show reduced filtration efficiency for higher PPI filters, for coarser particles and increased bulk flow rates. Negative efficiency for large particles indicates that previously collected particles from the EM priming stage were released during the EM flow filtration. The very small total number of coarse particles must also be considered, [*Supplement 8*].

Figure 4.16 indicates that under EM filtration conditions, the 30 PPI filter performs better than both 50 and 80 PPI filters. The 30 PPI filter will experience higher rates of metal recirculation, due to the higher filter permeability, as shown previously in Table 3.3 and has a higher $N_{L\text{-}K}$ number

(see *Supplement 8*, Tables IV and V) and will therefore benefit more from the *Leenov-Kolin effect*.

Figure 4.16 implies that the higher induced velocities 'push' particles through the filters, hence reducing the initial filter efficiency in agreement with gravity flow conditions, as shown in Figure 4.15. Overall efficiency can only be maintained, provided that the particles are recirculated into the filter for additional filtration possibilities, i.e. a second, third, etc. pass.

Fine particles in the metal under the filter will tend to remain 'in suspension' and follow the stream lines back into the filter. Coarser particles and agglomerates with a high gravitational number, N_G [see *Supplement 8*], that have been pushed through the filters, will have a greater tendency to settle, and thus remain uncollected, hence explaining the strong inverse relationship between efficiency and size shown in Figure 4.16.

The inverse relationship with filter PPI also shown in Figure 4.16, is due to the lower permeability and therefore reduced recirculation rate, as will be shown further by evaluation of the induced flow fields in the following section.

The negative efficiency for coarse particles (15-25 μm) for the 50 and 80 PPI filters is due to two factors, the very low number of such particles and the release of previously collected particles from the period of EM priming.

This analysis implies that 20 or even 10 PPI filters would benefit more from the application of electromagnetic filtration. These experiments have not examined changes in magnetic field distribution or flux density (except during the previous batch tests). It may be that better performance could be achieved by the use of specially engineered coils, e.g. a variable pitch coil located only in the region of the filter. Such a coil would reduce/eliminate the induced flow and enhance the *Leenov-Kolin effect*, which if combined by a 20 or 10 PPI filter (with low effective resistivity) would enhance particle collection on the first pass.

Additional valuable information could be obtained by performing residence time distribution tests, as these could explicitly determine the recirculation rate, as well as assist in better defining the system dead volume. For example a tracer 'pulse' input of a zinc containing aluminium alloy could be used.

4.9 FEM Model Flow Field Calculations

In order to better understand the impact of the EM fields on filtration, fluid flow fields induced by the curl in the Lorentz forces, i.e. Magneto-Hydro-Dynamic (MHD) mixing have been estimated at steady state for the various filters applied in this study, using 2D axial symmetric FEM, solved using the commercial COMSOL® 4.2a code.

Bulk flow due to gravity has been eliminated, as the magnitudes are small relative to the induced velocity and to provide a common basis for the three cases, showing only electromagnetically induced flow and induced recirculation from below the filters. The results are therefore highly representative of the induced flow during the EM priming periods.

Table 4.6 Summary of data used to solve for Flow Fields for 30, 50 and 80 PPI Filters, [*Supplement 8*]

Filter, PPI	Filter Total Porosity, ε	Filter Effective Resistivity, R_{filter}/R_{metal}	Forchheimer k_1, m^2	Forchheimer k_2, m	Current, A	Average experiment temperature, K	Metal Resistivity, ohm·m	Metal Viscosity, Pa·s	Metal Density, kg/m^3
30	0.892	1.5	5.08E-08	5.46E-04	720	946	2.97E-07	0.00111	2397
50	0.863	2.5	1.57E-08	1.66E-04	731	980	3.02E-07	0.00104	2348
80	0.865	3.7	6.52E-09	1.15E-04	727	969	3.00E-07	0.00106	2350

Results shown in Figure 4.17 indicate that the induced velocities are one to two orders of magnitude greater than the flow in and out of the apparatus during gravity filtration, clearly showing the dominance of the MHD recirculation on the overall flow field. The velocities and volumetric rate of recirculation are greatest for the 30 PPI filter, with flow returning at the centre of the filter and moving towards the wall where the $N_{L\text{-}K}$ value will be at a maximum. For any given velocity and particle size, the $N_{L\text{-}K}$ value is significantly higher for the 30 PPI filter, as shown in Tables IV and V of *Supplement 8*. The 30 PPI filter will have the most benefit from both MHD mixing and electromagnetic cleaning effects, to balance the detrimental effects of the higher interstitial velocity.

Results in Figure 4.17 also show a reduction of the peak velocity in the 80 PPI filter by 32% when compared with the 30 PPI (near the lower liquid metal interface) and a much reduced zone of high velocity due to the significantly lower permeability of the 80 PPI filters. The results indicate a significantly reduced volumetric recirculation rate of fluid from below the filter.

Additional FEM modelling should be performed to explore the impact of alternate coil geometries, higher and lower currents and different frequency of

induction on the magnitude of the Lorentz forces and induced metal velocities. Dynamic simulations could be performed to explore the mixing/residence time and determine the volumetric recirculation rate under various conditions. This work should be performed prior to further testing in order to optimize the design of the future test apparatus and procedures.

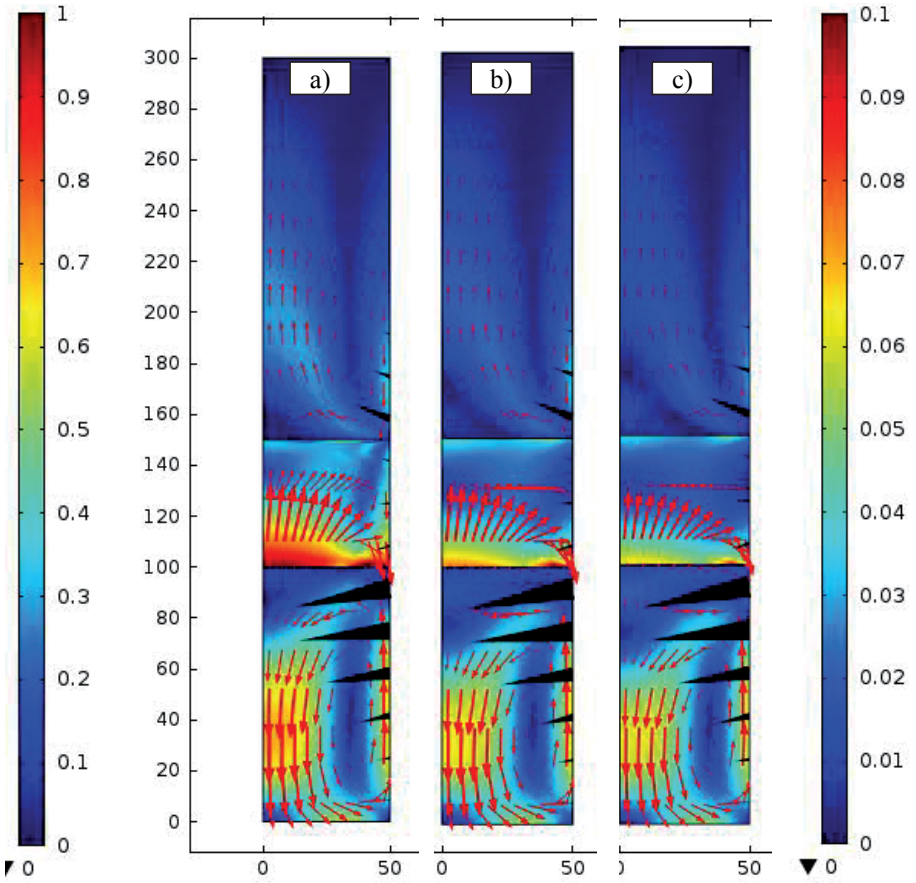

Figure 4.17 – Flow fields calculated for (a) 30, (b) 50 and (c) 80 PPI filters, velocities scales indicated in m/s, left-hand scale is for metal regions, and the right-hand scale is for porous media regions. Peak velocities in metal: 0.71, 0.64 and 0.64 m/s and in the filter: 0.19, 0.15 and 0.13 m/s, respectively. Conical arrows indicate relative time averaged Lorentz force strength (RMS). Regular arrows indicate direction and magnitude of fluid flow in metal and porous media regions, sizes are not comparable between regions. Coil position, relative to the filter is as indicated in Figure 4.9, [*Supplement 8*].

4.10 Electromagnetic Priming

Electromagnetic priming was accidently discovered during the batch testing phase of this work and is the subject of a recent provisional US patent application [84]. It was not initially appreciated how difficult it should be to prime 50 and 80 PPI filters, as indicated in Figure 4.18 using both commercial and experimental results. During the equipment and procedural development, it became apparent *that in the presence of the AC magnetic field the filters could be primed without preheating*, while using only 100-150 mm of metal head. It was observed that this was a simple and highly effective procedure, when sufficient magnetic flux density was applied.

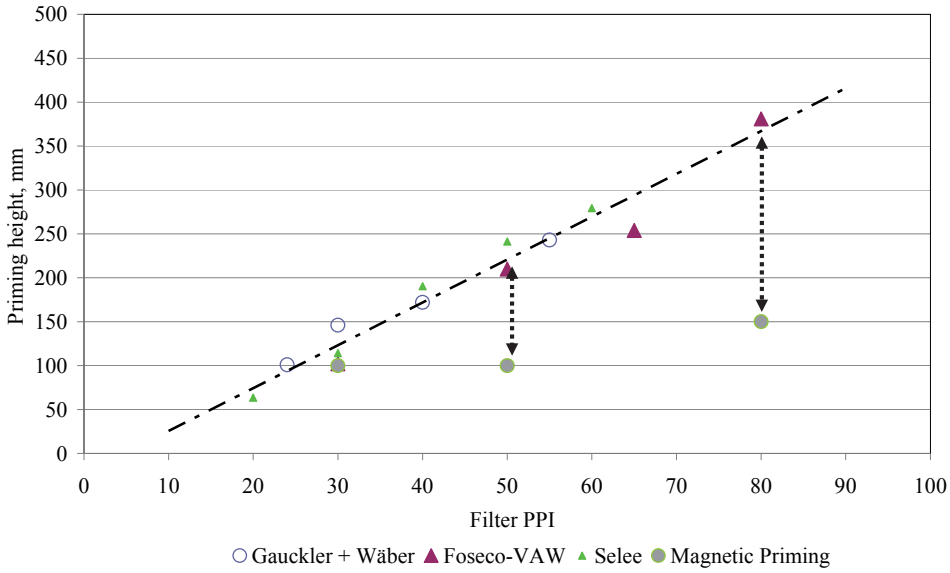

Figure 4.18 – Priming height vs. filter PPI from different producers compared with electromagnetic priming at ~0.17 T [11, 110], [*Supplement 8*]

Subsequent metallographic investigations showed both improved wetting [*Supplement 3, Supplement 6*] and increased gas removal with time, as indicated in Figure 4.19 [*Supplement 6*]. It was presumed that removing more of the gas would increase the area available for flow, and thus increase the metal throughput at constant metal head for a given filter type. Improved filter wetting might increase filtration efficiency for non-wetting inclusions (i.e. make it easier to approach the filter internal surfaces for collection). Figure 4.19 clearly indicates that when only 100-150 mm of metal head is used to attempt to prime a 50 or 80 PPI filter that they fail to prime, in full agreement with the industrial data presented in Figure 4.18.

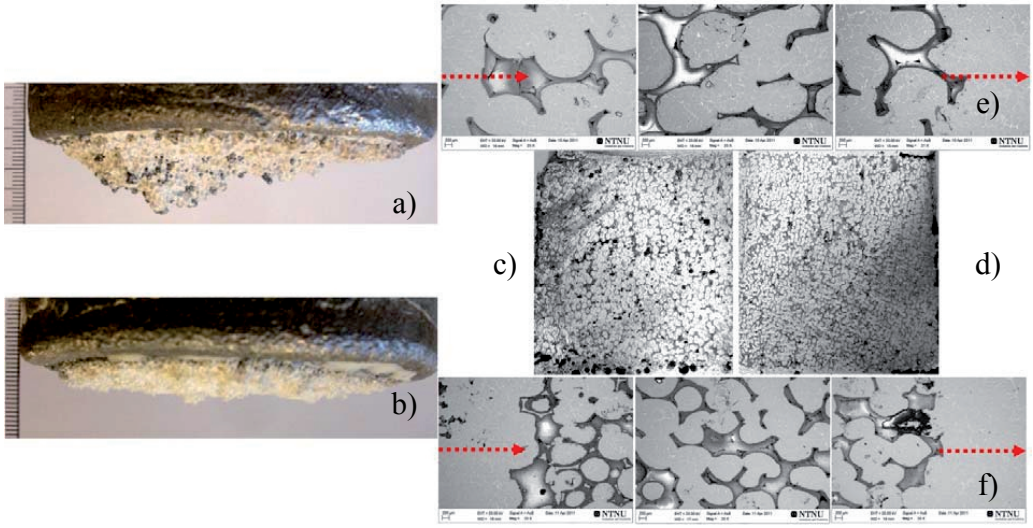

Figure 4.19 – 'Failed' gravity priming with 150 mm of head showing metal frozen over the filters, with: (a) <18 mm of metal penetration 50 PPI CFF and (b) <7 mm of metal penetration 80 PPI CFF. Fully primed and well wetted filters were obtained after 3 minutes of EM priming with 150 mm of metal head for (c) 50 PP CFF, and for (d) 80 PPI CFF, shown as half filter sections. Complete gas removal was obtained after 10 minutes of EM priming for 80 PPI CFFs. The arrows represent the flow direction of the melt during the initial filling [*Supplement 6*].

It was observed during the experiments that the productivity was enhanced after electromagnetic priming for a fixed metal head in accordance with expectations. Results were particularly pronounced for the 50 PPI filter, when compared with the 30 PPI gravity primed filter, as indicated in Figure 4.20. The 50 PPI filter with EM priming had the same initial discharge rate as the 30 PPI with EM priming and a 25% higher discharge rate than the 30 PPI with only gravity priming. It should be noted however, that the 50 PPI filter more quickly converted into 'cake' mode during gravity filtration.

When the electromagnetic field was used during filtration for the 50 and 80 PPI, the build up of cake was "*disrupted*" as reported previously for the 30 PPI filters [*Supplement 3*], and the filtration continued at a high rate similar to the 30 PPI; however, the filters performed with greatly reduced filtration efficiency, as previously indicated in Figures 4.13-4.16. This may indicate that 'cake' mode filtration or 'sieving' is a significant mechanism for the 50 and 80 PPI filters (either over or within the filters), at least for the high inlet particle loadings used during these experiments.

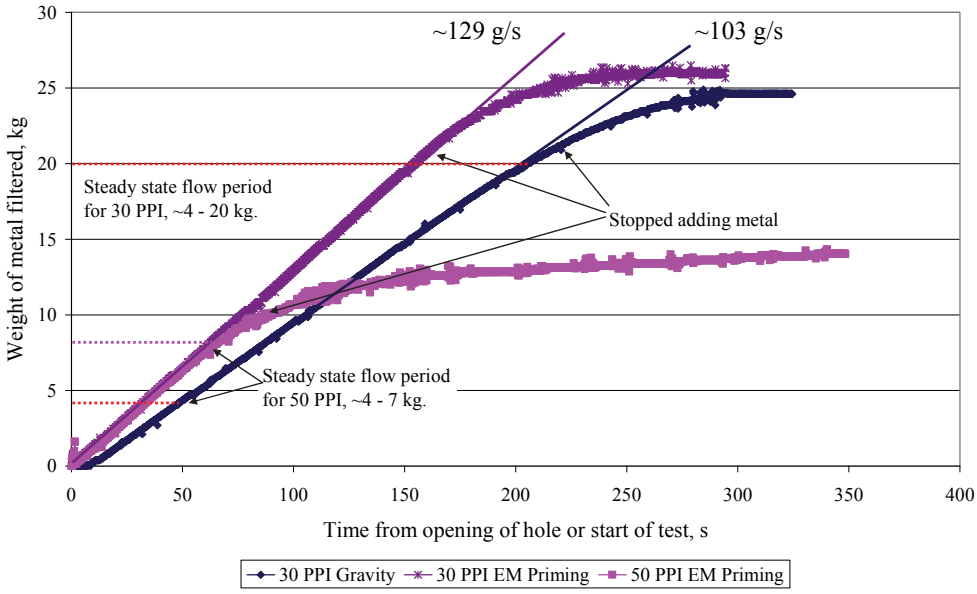

Figure 4.20 – Impact of electromagnetic priming on filter productivity with ~150 mm of metal head for 30 PPI filters with and without EM priming, and 50 PPI filter with EM priming. Note that the EM primed 50 PPI filter had the same initial flow rate as the 30 PPI EM primed and had a 25% greater discharge rate than the 30 PPI without EM priming, [*Supplement 8*].

Gravity filtration after EM priming appeared to behave more or less like conventional gravity filtration after gravity priming, once the increased superficial velocity is accounted for. Figure 4.15 clearly shows the detrimental effect of velocity on efficiency for both gravity and EM primed experiments. With EM priming, higher velocities were obtained, as indicated for the 30 PPI filter in Figure 4.20, and therefore lower filtration efficiencies resulted. Within the experimental scatter, it would appear that gravity or EM priming will achieve roughly the same filtration efficiency (at least for the 30 PPI) at the same superficial velocity, i.e. no benefit from increased filter 'wetting' was observed. This effect might also of course be dependent on the type of particles being used experimentally, i.e. wetted or non-wetted by liquid aluminium.

The low tortuosity of the 30 PPI filter, gives a lower effective resistivity as shown previously in Table 3.3, and this leads to higher forces as evidenced by the high $N_{L\text{-}K}$ numbers shown in Tables IV and V of *Supplement 8*. When combined with the high filter permeability of the 30 PPI filter and the curl in the Lorentz forces, these result in a high velocity upwards directed fluid stream in the centre of the filter, as shown in Figure 4.17. It was periodically observed after testing that the 30 PPI filters operating with an electromagnetic field either during priming or filtration, had experienced mechanical damage as reported in

Supplement 5, and pictured below for experiment 10. The thinning of the filter may have increased the filtration rate and/or reduced the filtration efficiency, both in accordance with Equation [56].

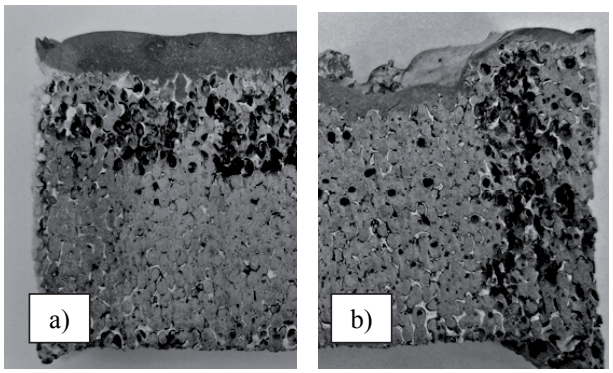

Figure 4.21 – Damage caused to the 30 PPI filters by electromagnetic forces. (a) Gravity primed and filtered 30 PPI from experiment 2, and (b) EM primed and EM filtered 30 PPI (6 minutes priming, and 12 minutes of filtration) experiment 10. Filter section (b) has been thinned by the upwards flowing metal at the centre of the filter. Filter sections are both originally 50 mm thick, with a 50 mm radius, [*Supplement 8*].

4.11 Filtration – Discussion: Impact of Particle Agglomeration, Bifilms and Analytical Methods on 'Perceived' Efficiency During Gravity Filtration

Based on the metallographic observations made during this work, the small 2-30 μm particles had a very high tendency to agglomerate in the master alloy, in the stirred holding furnace, i.e. the starting samples, and in the final 'clean' filtered samples, as can be seen in various sample images in *Supplement 8*. These agglomerates may be perceived by a LiMCA unit, as single larger sized particles, and may have produced bias in previously published literature results, if such agglomerates were present.

Bifilms being primarily composed of alumina will have a high affinity for the alumina structure of the CFF and low wetting tendency with the liquid aluminium [99] and therefore be captured with relatively ease. Bifilms have a strong tendency to become decorated with fine particles as mentioned previously and also to form 'scaffolds' helping to construct many of the filter 'bridges' observed in this study, as shown in the representative micrographs, Figures 4.22 and 4.23.

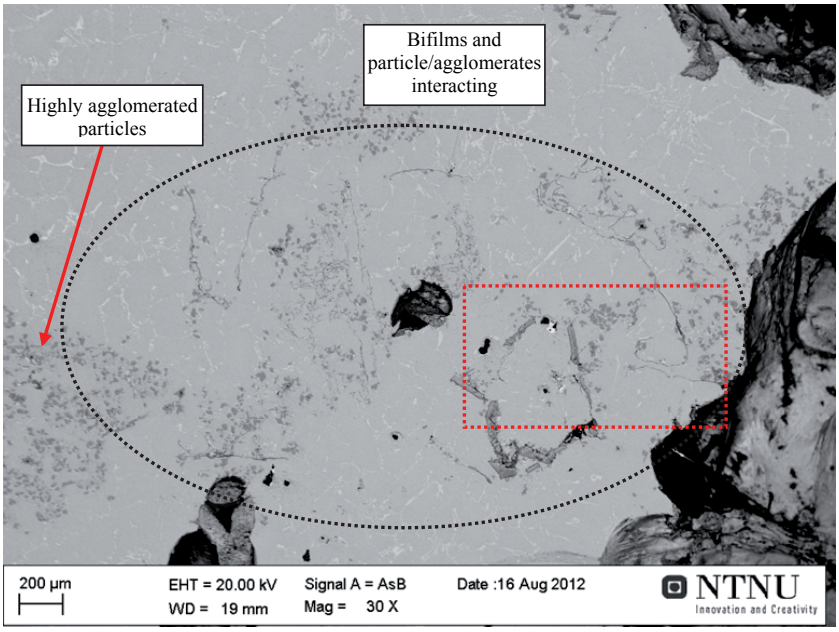

Figure 4.22 – SEM micrograph from experiment 4, showing bifilms attached to the pore wall, unfolded, holding back and collecting particles and agglomerates within a 30 PPI filter, shown in the dotted circle, [*Supplement 8*]. Section in dotted red is expanded in Figure 4.23.

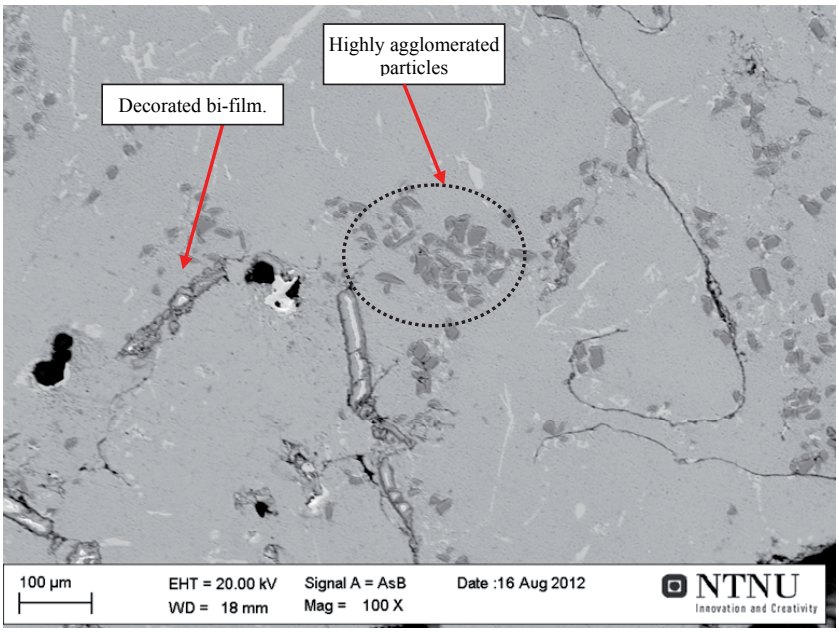

Figure 4.23 – Close-up SEM micrograph from experiment 4, showing highly agglomerated particles interacting with bifilms within the filter pores of a 30 PPI filter, [*Supplement 8*].

Bridges have been shown on many occasions as previously indicated in Figure 4.5 and 4.6 [3, 4, 14, 73, 106] and likely play a role in enhancing sieving both within and over the filter. It is therefore unlikely that any analytical model focusing on single particle collection efficiency will ever be adequate to predict overall filtration efficiency. Closer study of particle-particle interaction and particle-bifilm-CFF interaction during filtration is clearly warranted.

In the current work, the relative ratio of bifilms to 'real', i.e. artificially introduced exogenous SiC particles is small. It may therefore be a relative lack of bifilms as a percentage of total particles added, which produced the low observed filtration efficiency under gravity filtration conditions as can be seen in Figure 4.15. This may be a factor in the filtration of TiB_2 particles formed by the addition of grain refiners, which is well known to reduce the apparent filtration efficiency of CFFs measured using LiMCA, as shown in Figure 4.24 [111].

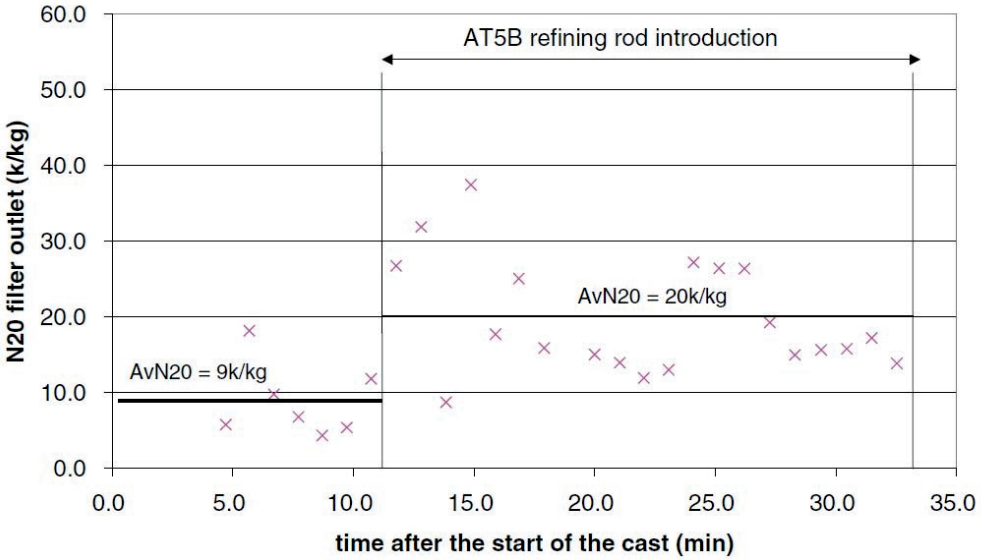

Figure 4.24 – Impact of the addition of AT5B grain refiner on the clean metal inclusion count measured using LiMCA [111] .

The only gravity filtration reference data found in the literature, which could be directly compared with the current experimental and analytical procedures, are the results of Mutharasan *et al.* [15] for the filtration of fine 1-30 μm TiB_2, using 7.5 cm diameter, 5 cm thick, commercial 30 PPI alumina CFFs, with 85% total porosity, at superficial velocities from 0.1-0.8 cm/s, and flow controlled via a discharge orifice. The similarity to the current experiments of both the equipment and the size range of particles filtered is remarkable.

The results of Mutharasan *et al.* were measured based on the chemical assay of TiB_2 in the metal in versus metal out (not particle counts using LiMCA) and are therefore proportionate to total weight or volumetric efficiency as presented previously in Table 4.5, which in the case of the recent study also showed a strong correlation with efficiency based on counts (see Table 4.5). Mutharasan *et al.* reported that the overall efficiency varied inversely with the superficial velocity from about 80% at 0.1 cm/s, to 40% at 0.8 cm/s in excellent agreement with the current 30 PPI gravity filtration results shown in Figure 4.15.

The excellent agreement between the current results and those of Mutharasan *et al.*, may indicate that SiC particles are 'well wet' by liquid A356 alloy, similar to TiB_2 and this may also result in lower collection efficiencies. Collection efficiencies of artificially introduced Al_2O_3 particles (i.e. not bifilms) have been reported to be 60-77% using LiMCA data, for similar 30/50 PPI CFFs and at much higher velocities from 1.3-1.8 cm/s [3], suggesting a strong role of particle wetting on collection efficiency, as recently reported [99].

4.12 Filtration – Discussion: Observed Filtration Mechanisms During Gravity Filtration

It should be noted that filters could only be sectioned after the completion of the experiments, where cake mode was always controlling and hence all show evidence of extensive cake mode filtration. The micrographs can therefore not be used to determine if cake filtration was occurring during the 'steady state' filtration period. Settling of particles over the filter after completion of an experiment ensured that a thick cake was always found on final sectioning.

Further experiments should be conducted where less dense mixtures of SiC particles are used and the experiments are interrupted during normal filtration, by closing the discharge hole. This should allow the filters to be 'frozen' as close to 'steady state' filtration conditions as possible (i.e. prior to cake mode filtration) and without any metal drainage from the filter, which makes metallographic examination difficult. In the final frozen filters, cake mode filtration or sieving was observed both over and inside of the filter as indicated in Figure 4.25.

Deep bridges of material as shown in Figure 4.25, may well act like a packed or 'fluidized bed'. Particle-particle interactions such as agglomeration and mechanical interference likely become significant. Particle-fluid interaction may greatly increase the effective fluid viscosity, further reducing fluidity in accordance with the Roscoe-Einstein equation [112]. Densely packed particles

may travel in a mean-free-path-like manner. Particles may be deemed to be collected, when in fact they are merely hindered from moving in any given direction by the presence of other nearby particles, much like the behaviour in a fluid bed in terms of particle elutriation [113]. Fine particles such as those used in these experiments are generally reported to be Geldart C, cohesive particles [114], difficult to fluidize with air and susceptible to building cohesive strength when in direct contact and bridging very large openings like silo outlets in materials handling applications [115]. The behaviour shown in Figure 4.25 appears somewhat similar.

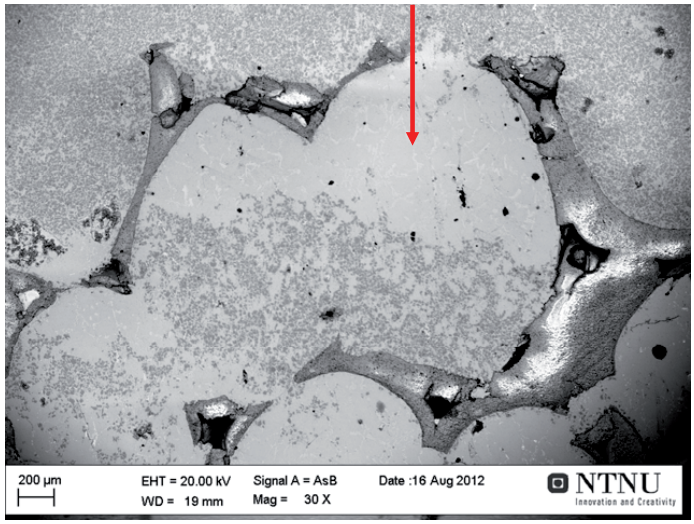

Figure 4.25 – Sieving or 'cake' mode filtration over and in the upper section of 50 PPI filter from experiment 7. Flow direction (and gravity) marked by the arrow, [*Supplement 8*].

The impact of fluid velocity on bridges, may be to build 'back pressure' until either the fluidizing velocity is reached or the bridge is collapsed due to the total applied force. A broken piece of a bridge in an upper section of the filter is highly likely to be recaptured prior to exiting the filter. Filter thickness and the number of opportunities for collection will therefore remain significant to overall filtration efficiency.

Deeper within the filters of all types, evidence was shown of both impaction/interception and settling. Impaction/interception appeared to be more common in the 30 PPI filters as shown by Figure 23 of *Supplement 8*. Gravity settling appeared to be more important for the 80 PPI filters due to the preponderance of particle collected in what appeared to be dead volumes and inclined pores in the direction of gravity, rather than the flow direction, as shown in Figure 24 of *Supplement 8*.

4.13 Filtration – Discussion: Analytical Method Accuracy and Bias

Figure 4.26 indicates a typical bias of ~ -10% for the Image-Pro® software when compared to a meticulously executed manually controlled count. Initial samples analyzed by Image-Pro® Plus were biased by -13.5% on average, while the lower particle count metal samples were biased by -6.3%. A detailed comparison of the impact of the bias on efficiency found that the Image-Pro® Plus data resulted in an underestimation of filtration efficiency by ~3%. All results presented in this article were calculated using the Image-Pro® Plus data, and so have a similar bias. It should be noted that the use of the macro-automated software saved more than a man year, at the expense of 3% filtration accuracy. A detailed review of the analytical technique is the subject of a new publication [116].

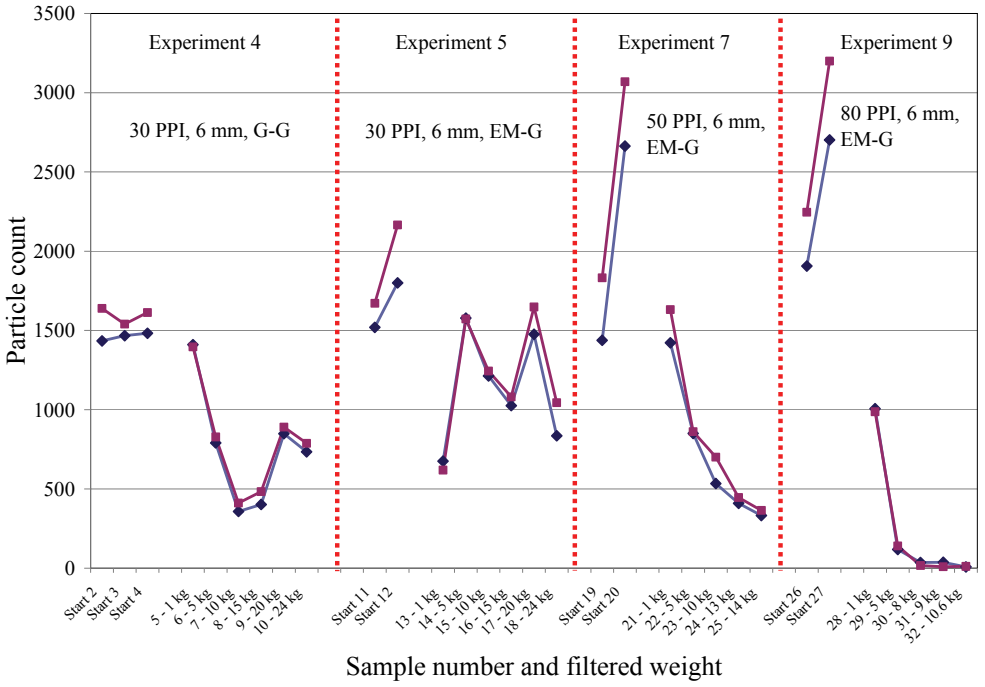

Figure 4.26 – Comparison of particle counts (20 images per point) produced by the manually controlled ImageAccess easyLab 6® and the macro-automated Image-Pro® Plus Version 7.0 software for starting samples and 'weight' samples taken during filtration for experiments 4, 5, 7 and 9, indicating a typical bias of ~ -10% for the Image-Pro® data, and resulting in a -3% bias in the estimated filtration efficiencies.

Sampling may also have produced random variation as would be evidenced by the redundant starting samples. Individual results typically varied by up to ±25 % from the mean, and therefore represent one of the larger experimental uncertainties.

Prior to the development and validation of the new automated methodology (a late development) only a limited number of samples could be analyzed manually.

Additional starting samples and longer runs with fewer SiC particles, would improve statistical accuracy in future work.

Chapter 5

FINAL DISCUSSION

The motivation of this research was to address two key objectives of the RIRA project to:

- Remove all inclusions of >10 μm in diameter, and
- Develop new methods of inclusion separation, e.g. electromagnetic separation.

The specific intent of this part of the research effort was to find ways to combine electromagnetic fields with Ceramic Foam Filters (CFFs), to determine if it were possible to achieve greater efficiency of filtration for liquid aluminium for particles exceeding 10 μm.

Objectives of this research included:

1. How high a magnetic flux density can be safely applied to liquid aluminium (meniscus experiments)?

   Up to 0.2 T, has been used without difficultly. See applied flux densities in *Supplements 5-8*. Higher flux densities can likely be used provided sufficient head is present over the coil to prevent the formation of a significant meniscus or apparatus designs producing reduced Lorentz force curl are developed.

2. How do the coil, work piece geometry, current and temperature affect the magnetic flux density (billet experiments, Analytical/COMSOL modelling)?

   See Equations [11], [12], [14], and [18]. See 2D axial symmetric FEM modelling in *Supplements 1-2* and Figure 2.9.

3. How do the filter types, time and coil magnetic flux density, affect the particle distribution within and over the filters (batch experiments)?

   Particles are concentrated near the top-centre and towards the outer wall of the crucible inside the filters. Entrained gas is removed and wetting improved

progressively with the application of higher magnetic fields and time. Higher PPI filters take more time to achieve complete gas removal. The filter cake is "disrupted", with application of a magnetic field. Less cake over and more particles are observed within the filter element itself. See *Supplements 4-5* and Masters thesis by R. Fritzsch [95].

4. What are the hydrodynamic/magnetohydrodynamic (MHD) properties within the filter media (permeability, pore/cell size, effective resistivity, CFD modelling)?

Higher filter PPIs result in lower liquid permeability and higher effective filter electrical resistance. The net effect on MHD can be observed by solving 2D axial symmetric models for the Lorentz forces and fluid flow, as shown in Section 4.9, and using data from *Supplements 3-4,* and *6-8*. Results show a reduced velocity and volumetric recirculation with higher filter PPIs for the same coil design and applied current.

5. How does the filter type, with and without a magnetic field affect the final obtained filtration efficiency as a function of both velocity and particle size (flow tests)?

In gravity filtration, higher filter PPIs and lower filtration velocity both result in higher efficiency, as shown in Figure 4.15. Filtration efficiency is normally assumed to increase with particle size as shown in Figure 4.3, although there is contradictory evidence in the literature [3]. The results presented in *Supplements 7* and *8*, appear to show that with large scale agglomeration and the presence of bi-films and extensive 'bridge-building', that particulate collection efficiency is not a strong function of particle size. 'Bridge-building' and particle agglomeration are shown in Figures 4.5, 4.6, 4.25 and discussed extensively in *Supplements 7* and *8*.

In electromagnetic filtration, counter-intuitively the normal behaviour obtained in gravity filtration is reversed. Filtration efficiency was found to be best for the lowest PPI filters used in this study, due to a powerful *Leenov-Kolin effect* and greatly increased aluminium recirculation into the filter. The filtration efficiency was seen to decrease with increasing particle sizes, due to the greater tendency of coarse particles to settle, if pushed through the filter by the higher MHD induced velocity and to not '*back-mix*' into the filter.

In relation to the primary RIRA project objective of removing all particles >10μm, the following results were obtained for 50 mm thick CFFs:

i. >98% of particles larger than 10 μm were removed at low filtration velocity (~1 mm/s) using 80 PPI filters, which had been electromagnetically primed, and
ii. >94% of particles larger than 10 μm were removed at low filtration velocity (~2 mm/s) under gravity filtration using 30 PPI filters.

In relation to the secondary objective of developing a new method of separation of inclusions, i.e. electromagnetic filtration, it can be concluded that while the theoretical ground work has now been established to allow the systematic design of such a process, that this objective has not been achieved, as evidenced by the lower obtained filtration efficiencies during electromagnetic filtration. However, a significant new invention has been achieved, i.e. electromagnetic priming, and this may allow for the substantial achievement of the primary objective (higher removal efficiency for >10 μm particles), by the use of thicker CFFs or stacks of standard CFFs.

5.1 Possible Improvements to Achieve Enhanced Electromagnetic Filtration

Timelines from idea to industrial realization for new technology are extremely long in metallurgy, due to the complexity of the processes, general risk aversion and conservatism of the industry. 15 years from conception to industrialization, is not atypical for a major new metallurgical process [117]. 5-10 years is reasonable for a 'small', but innovative technology such as studied in this thesis.

In 3 years, "Electromagnetically Enhanced Filtration," has progressed from a concept, to a level where proper engineering studies and design work is now possible. In 2010, even the answers to the simplest questions like: "What is the magnetic flux density of a short coil?", "What magnitude of Lorentz forces will be induced in liquid aluminium by this short coil?", "What pressure drop will a given aluminium flow rate produce moving through this ceramic foam filter?" could not be calculated with sufficient accuracy or certainty. These questions can now all be answered with reasonable certitude.

Using the data and correlations presented in this thesis, it is possible to extrapolate to obtain estimates of data for CFFs, which have not yet been tested, as shown in Table 5.1. It is then possible to take such data and apply it in the validated 2D axial symmetric finite element model, which has been built as part of the current effort, to produce estimates of Lorentz forces, fluid flow velocities, particle migration rates, magnetic flux densities, heating rates, and

so on. More targeted experimental designs and the equipment required to achieve them can now be created with relatively low uncertainty.

Table 5.1 Extrapolated Filter Data (Marked in Yellow) for 10, 15 and 20 PPI CFFs

Filter, PPI	Total Porosity, ε	Tortuosity, τ	Effective Resistivity, R_{filter}/R_{metal}	Window Diameter, d_w, µm	Strut Diameter, d_s, µm	Cell Diameter, d_c, µm	Forchheimer k_1, m^2	Forchheimer k_2, m
10	**0.905**	**1.0**	**1.1**	**1087**	**240**	**1945**	**6.22E-08**	**6.74E-04**
15	**0.902**	**1.1**	**1.2**	**1034**	**232**	**1851**	**5.63E-08**	**6.10E-04**
20	**0.899**	**1.2**	**1.4**	**981**	**224**	**1757**	**5.08E-08**	**5.50E-04**
30	0.892	1.3	1.5	961	185	1668	5.08E-08	5.46E-04
40	0.900	2.3	2.5	698	211	1306	3.10E-08	3.38E-04
50	0.863	2.2	2.5	623	190	1132	1.57E-08	1.66E-04
80	0.865	3.2	3.7	383	119	683	6.52E-09	1.15E-04

Using the developed tools, alternate equipment designs can be 'tested' in software, as shown in Figure 5.1. This figure shows a multi-layer helical coil, designed to achieve a homogenous flux density and produce a low curl, as evidenced by the greatly reduced bulk-liquid and porous-media velocities, when compared with Figure 4.17 (a). A coil of such a design could operate with higher current, magnetic flux density and Lorentz forces, i.e. a greater *Leenov-Kolin effect*, while simultaneously reducing the MHD mixing effects likely to reduce the 'standard' filtration efficiency.

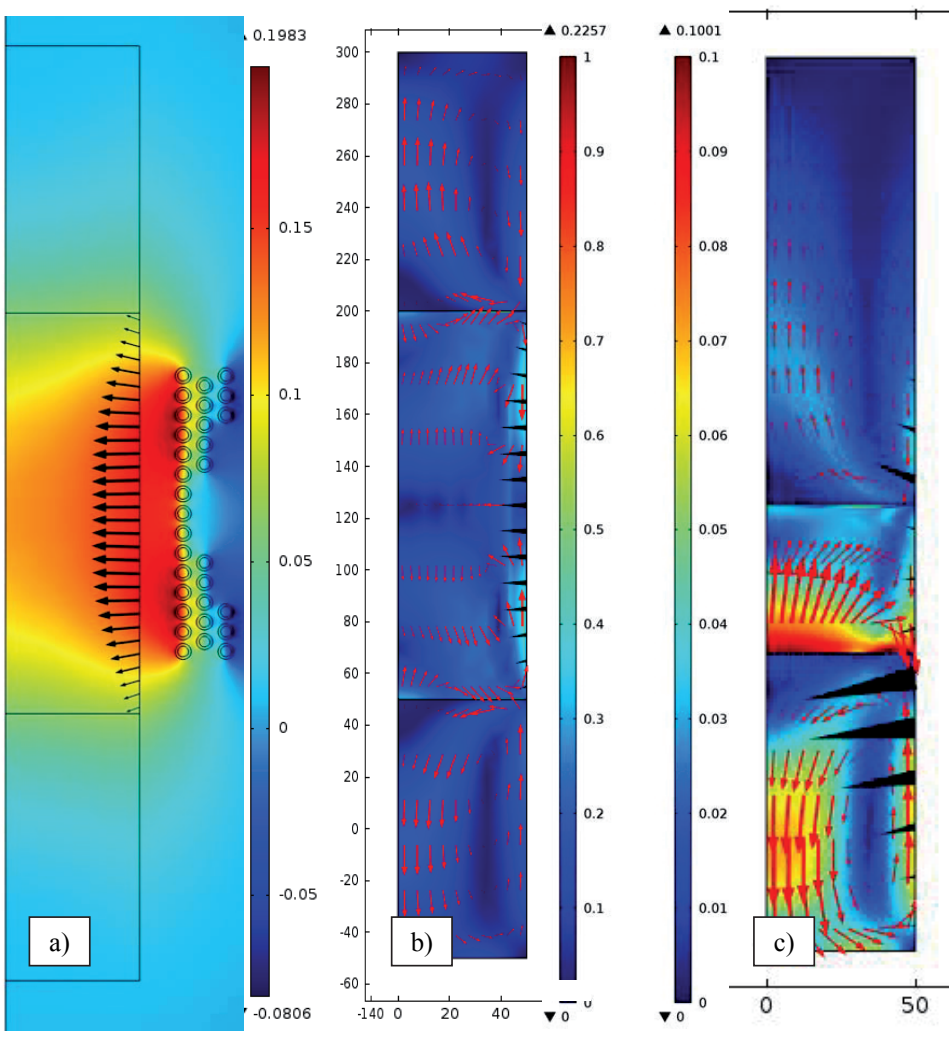

Figure 5.1 – (a) Magnetic flux density [T, RMS], colour indicating flux density and black arrows indicating relative strength and direction of the Lorentz forces and (b) Induced flow field for 150 mm thick, 30 PPI filter, with liquid A356 aluminium at 975 K for 31 turn multi-layer coil design operating at 720 A and 50 Hz, (c) Reproduction of Figure 4.17 (a) for direct comparison using a common colour scale in [m/s] for both bulk-liquid, red=1.0 m/s and porous-media, red=0.1 m/s.

Using Equation [56] and assuming gravity filtration with 30 PPI CFFs with an K_0 of 0.049 [s^{-1}], for particles sized 10-15 μm [*Supplement 8*], the impact of velocity and filter thickness on the obtained filtration efficiencies can be explored, as shown in Figure 5.2. The original objective of 100% removal of all particulates >10 μm, can of course be achieved at 0 cm/s superficial velocity, which is not an economically interesting operating point.

The objectives of the RIRA project should be restated in more realistic terms, i.e.: What efficiency, for which types of particles (See Table 1.1), of what sizes and for which product? A figure such as Figure 5.2, could then be used to determine the thickness of filter and superficial velocity and hence area of filter, that is required to process a given throughput of aluminium and produce a specified quality. Knowing the filter permeability, the required metal head could then be calculated with high accuracy and the required filter bowl appropriately designed.

Filter thicknesses of 10 or 15 cm are likely impractical in industry, without the application of electromagnetic priming, most particularly for high PPI filter types, such as 50 or 80 PPI. Electromagnetic priming therefore offers a realistic way of achieving improved gravity filtration efficiency at normal casting velocities, simply by the use of thicker filters, as indicated in Figure 5.2.

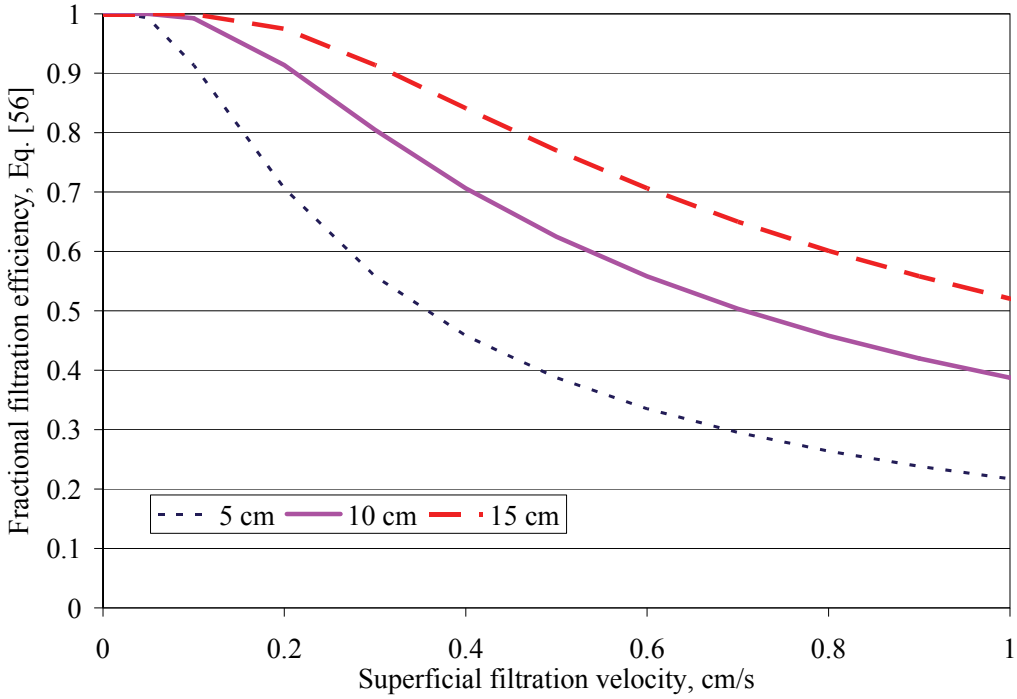

Figure 5.2 – Estimated fractional efficiency for gravity filtration with 30 PPI filters of 5, 10 and 15 cm thickness for particles of 10-15 μm in size, as a function of superficial velocity [cm/s]. Evaluated using Equation [56] and using a K_0 of 0.049 [s^{-1}].

The industrial implications of the current results are described in more detail in a new publication [118].

Chapter 6

CONCLUSIONS AND FUTURE WORK

6.1 Conclusions

Equipment designs, sampling procedures and analytical methods have been created and validated, which have allowed the impact of electromagnetic fields on filtration with Ceramic Foam Filters to be determined for particles as small as 2 μm, a significant improvement over industrial systems with limitations of 15-20 μm.

In agreement with previous literature, it has been found that filtration efficiency is inversely proportional to filtration velocity during gravity reference experiments. The coil designs used in the current experimental program were specifically designed to maximize magneto-hydro-dynamic mixing and specifically achieve a high level of back mixing from below the filter, in order to produce multiple filtration passes for the liquid aluminium. It was found in the current experimental program that the impact of the 'back-mixing' did not compensate for the high interstitial velocities induced by the curl in the electromagnetic Lorentz forces.

It was found that traditional 'truths' related to gravity filtration were no longer applicable in electromagnetic filtration. Higher PPI filters reduced filtration efficiency, due to reduced magnitudes of the *Leenov-Kolin effect* and reduced back-mixing, due to lower filter liquid permeability. Under the high induced velocity conditions, coarse particles that were pushed through the filters, tended to settle, which resulted in an efficiency by size relationship, opposite to the gravity norm.

The systematic study of the physics, analytical and numerical modelling, empirical measurement of filter properties and both gravity and electromagnetic filtration behaviour, has resulted in the creation of a 'tool-box' of know-how,

which can now be applied to achieve improved results for both gravity and electromagnetically modified filtration as discussed in Chapter 5. With thicker filters, alternate selections of filter PPI and greatly modified coil designs, it should be possible to achieve improved filtration efficiencies, when referenced against gravity benchmarks.

The concept of electromagnetic priming has been invented as part of this work, and this concept if applied to normal gravity filtration, will allow thicker CFFs to be used and greatly improved filtration efficiency to be realized.

Evidence was gathered in the course of this research, which challenges many of the historic notions of what determines gravity filtration efficiency. Extensive evidence of the role of agglomeration, particle-particle interaction and bifilms on the filtration behaviour has been observed, confirming many similar observations made in recent filtration literature.

The following equations represent contributions to electromagnetic and filtration theory, which may have a general utility to future researchers:

i. $$k_N{}^* = k_N\left(1-\left(\frac{D_w-\delta_w}{D_c+\delta_c}\right)^2\right)+\left(\frac{D_w-\delta_w}{D_c+\ \delta_c}\right)^2$$

ii. $$F_L = -\frac{\mu_r\mu_o\sqrt{2}}{\delta_w}\left(\frac{k_N^* N_c I_c}{l_c}\right)^2\left(\frac{ber\xi_r ber'\xi_r + bei\xi_r bei'\xi_r}{ber^2\xi_R + bei^2\xi_R}\right)$$

iii. $$\frac{B_0}{B_\infty} = \frac{1}{2}\left(\frac{xl_c}{\sqrt{(xl_c)^2 + r_{cs}{}^2}} + \frac{(1-x)l_c}{\sqrt{((1-x)l_c)^2 + r_{cs}{}^2}}\right)$$

iv. $$u_i = \frac{u_s\tau v_f}{\varepsilon\left(v_f - v_d\right)} = \frac{u_s\tau}{\varepsilon\left(1-f_d\right)}$$

v. $$E = 1-(1-\eta)^{N_c} \approx 1-\exp^{-\eta N_c}$$

vi. $$N_{L-K} = \frac{\pi d_p^3}{8}\left|F_L\right|\frac{1}{3\pi d_p\mu u_i} = \frac{d_p^2\left|F_L\right|}{24\mu u_i}$$

6.2 Future Work

Future work should explore the influence of alternate coil geometries, frequencies (other than 50 or 60 Hz AC) and electromagnetic field strengths on the obtained filtration efficiencies during electromagnetic filtration. In particular, the (vertical) position of the induction coil relative to the filter should be addressed. Thick filters of low PPI (e.g. 2 or 3 times 50 mm of 10-30 PPI), could be combined with variable pitch helical coils to produced larger *Leenov-Kolin* numbers, $N_{L\text{-}K}$ with lower MHD stirring. The 2D axial symmetric FEM model could be used to optimize the equipment and experimental design without the need for a large, expensive and time consuming development phase.

The practicality of applying electromagnetic priming with larger scale filters should be demonstrated by full scale commercial testing with larger, e.g. 17" square filters.

The role of particle wetting, particle concentration and bifilms should be studied using a variety of particles with different surface properties, at a range of lower concentrations than used in these experiments with and without bifilms. Extensive testing with frequent sampling over longer periods of time may help to elucidate the role that particle-particle, particle-fluid and particle-bifilm-filter interactions may play for filters, as they dynamically build up bridges and particulates in their interstitial spaces.

Residence time distribution (RTD) studies should be performed to examine the plug flow, back mixed and dead volume components of the RTD curves. Combined with tortuosity studies, these should improve the understanding of the magnitude of interstitial velocity within the filter structure of different PPI CFFs.

Additional filter tortuosity experiments should be performed to more accurately determine the filter tortuosity in the direction of flow (currently accurate to ~±20% and only known with accuracy in the phi-direction), e.g. filters could be turned 90 degrees and re-measured inductively to determine if the tortuosity is isotropic.

REFERENCES

[1] C. Dupuis, G. Béland, and J. Martin, "Filtration Efficiency of Ceramic Foam Filters for Production of High Quality Molten Aluminum Alloys," in *Proceedings of the 32nd Annual Conference of Metallurgists*, Quebec, Canada, 29 August - 2 September, (1992), 349-358.

[2] D. E. Groteke, "The Reduction of Inclusions in Aluminum by Filtration," *Modern Casting,* vol. 73, (1983), 25-27.

[3] H. Duval, C. Rivière, É. Laé, P. Le Brun, and J. Guillot, "Pilot-Scale Investigation of Liquid Aluminum Filtration through Ceramic Foam Filters: Comparison between Coulter Counter Measurements and Metallographic Analysis of Spent Filters," *Metallurgical and Materials Transactions B,* vol. 40, (2009), 233-246.

[4] S. Instone, M. Badowski, and W. Schneider, "Development of Molten Metal Filtration Technology for Aluminium," *Light Metals,* (2005), 933-938.

[5] K. Butcher and D. Rogers, "Update on the Filtration of Aluminum Alloys with Fine Pore Ceramic Foam," *Light Metals*, (1990), 797-803.

[6] A. Engelbrecht, "Removal of Solid Inclusions from Molten Aluminium through Ceramic Foam Filtration," *Light Metals*, (2010), 779-784.

[7] Z. Szklarska-Smialowska, "Pitting Corrosion of Aluminum," *Corrosion Science,* vol. 41, (1999), 1743-1767.

[8] F. Frisvold, "Filtration of Aluminium: Theory, Mechanisms, and Experiments," PhD. Thesis, Department of Materials Science and Engineering, NTH, Trondheim, Norway (1990).

[9] G. Le Roy, J. M. Chateau, and P. Charlier, "PDBF: Proven Filtration for High-End Applications," *Light Metals,* (2007), 651-655.

[10] D. Neff and E. Stankiewicz, "The Mulicast Filtration System," *Light Metals,* (1986), 821-828.

[11] N. Keegan and S. Ray, "An Evaluation of Industrial Filtration Systems," Alcastek, Mumbai, India, Edited by Dr Nilmanied, 2002, 1-10.

[12] J. Campbell, "Entrainment Defects," *Materials Science and Technology,* vol. 22, (2006), 127-145.

[13] C. Conti and P. Netter, "Deep Filtration of Liquid Metals: Application of a Simplified Model Based on the Limiting Trajectory Method," *Separations Technology,* vol. 2, (1992), 46-56.

[14] S. Ray, B. Milligan, and N. Keegan, "Measurement of Filtration Performance, Filtration Theory and Practical Applications of Ceramic Foam Filters," *Aluminium Cast House Technology*, (2005), 1-12.

[15] R. Mutharasan, D. Apelian, and C. Romanowski, "A Laboratory Investigation of Aluminum Filtration through Deep Bed and Ceramic Open-Pore Filters," *Journal of Metals,* vol. 33, (1981), 12-17.

[16] J. Vaughan and J. Williamson, "Design of Induction-Heating Coils for Cylindrical Nonmagnetic Loads," *American Institute of Electrical Engineers, Transactions of the,* vol. 64, (1945), 587-592.

[17] C. Tudbury, *Basics of Induction Heating, Vol. 1*. New York: John F. Rider, (1960).
[18] D. Leenov and A. Kolin, "Theory of Electromagnetophoresis. I. Magnetohydrodynamic Forces Experienced by Spherical and Symmetrically Oriented Cylindrical Particles," *The Journal of Chemical Physics,* vol. 22, (1954), 683-688.
[19] P. Vilinskas and R. Schiltz, "Separation Technique for Nonconducting Solids in Liquid Sodium," *Nucl. Appl.*, vol. 6, no. 2, (1969), 176-177.
[20] C. Conti, J. Meyer, J. Riquet, and P. Netter, "Separation by Filtration of Inclusions," *Patent Number EP 290360 A(00290360/EP-A),* (1988).
[21] S. Taniguchi and J. Brimacombe, "Application of Pinch Force to the Separation of Inclusion Particles from Liquid Steel," *ISIJ international,* vol. 34, (1994), 722-731.
[22] N. El-Kaddah, A. Patel, and T. Natarajan, "The Electromagnetic Filtration of Molten Aluminum Using an Induced-Current Separator," *Journal of Metals,* vol. 47, (1995), 46-46.
[23] J. Sheng, "A Numerical Model of MHD Separation of Inclusions from Molten Aluminum," Masters Thesis, University of Toronto, Canada, (1997).
[24] D. Shu, T. Li, B. Sun, J. Wang, and Y. Zhou, "Study of Electromagnetic Separation of Nometallic Inclusions from Aluminum Melt," *Metallurgical and Materials Transactions A,* vol. 30, (1999), 2979-2988.
[25] Z. Jiang, Z. Ren, and Y. Zhong, "Theoretical Model for Particle Behavior at Solidifying Front in Electromagnetic Force Field," *Journal of Shanghai University (English Edition),* vol. 4, (2000), 246-249.
[26] M. Li and R. Guthrie, "Numerical Studies of the Motion of Particles in Current-Carrying Liquid Metals Flowing in a Circular Pipe," *Metallurgical and Materials Transactions B,* vol. 31, (2000), 357-364.
[27] T. Li, Z. Xu, B. Sun, D. Shu, and Y. Zhou, "Remove Inclusions from Aluminum Melt in Electromagnetic Field," *Acta Metallurgica Sinica-English Letters-,* vol. 13, (2000), 1068-1074.
[28] D. Shu, T. Li, B. Sun, Y. Zhou, J. Wang, and Z. Xu, "Numerical Calculation of the Electromagnetic Expulsive Force Upon Nonmetallic Inclusions in an Aluminum Melt: Part II. Cylindrical Particles," *Metallurgical and Materials Transactions B,* vol. 31, (2000), 1535-1540.
[29] D. Shu, B. Sun, J. Wang, X. Zhang, and Y. Zhou "Magnetohydrodynamic Study of Electromagnetic Separation of Nonmetallic Inclusions from Aluminum Melt," *Science in China Series E: Technological Science*, vol. 45, no. 4, (2002), 417-425.
[30] N. El-Kaddah, "A Comprehensive Mathematical Model of Electromagnetic Separation of Inclusion in Molten Metals," *Industry Applications Society Annual Meeting*, 2-7 October, vol. 2, (1988), 1162-1167.
[31] K. Li, J. Wang, D. Shu, T. Li, B. Sun, and Y. Zhou, "Theoretical and Experimental Investigation of Aluminum Melt Cleaning Using Alternating Electromagnetic Field," *Materials Letters,* vol. 56, (2002), 215-220.
[32] A. Raichenko, A. Derevyanko, and V. Popov, "Redistribution of Extraneous Solid Particles Suspended in Molten Metal During Passage of an Electric Current," *Powder Metallurgy and Metal Ceramics,* vol. 41, (2002), 335-341.
[33] D. Shu, B. Sun, K. Li, T. Li, Z. Xu, and Y. Zhou, "Continuous Separation of Non-Metallic Inclusions from Aluminum Melt Using Alternating Magnetic Field," *Materials Letters,* vol. 55, (2002), 322-326.
[34] D. Shu, B. Sun, K. Li, J. Wang, and Y. Zhou, "Effects of Secondary Flow on the Electromagnetic Separation of Inclusions from Aluminum Melt in a Square Channel by a Solenoid," *ISIJ international,* vol. 42, (2002), 1241-1250.
[35] S. Da, S. Baode, L. Ke, W. Jun, and Z. Yaohe, "Continuous Separation of Inclusions from Aluminum Melt Flowing in a Circular Pipe Using a High Frequency Magnetic Field," *Journal of Materials Science and Technology - Shenyang-,* vol. 19, part 3, (2003), 221-225.

[36] K. Takahashi and S. Taniguchi, "Electromagnetic Separation of Nonmetallic Inclusion from Liquid Metal by Imposition of High Frequency Magnetic Field," *ISIJ international,* vol. 43, (2003), 820-827.

[37] T. Ogasawara, N. Yoshikawa, S. Taniguchi, and T. Asai, "Flow of Conducting Liquid around Two Nonconducting Particles in DC Electromagnetic Field and the Electromagnetic Migration Force," *Metallurgical and Materials Transactions B,* vol. 35, (2004), 847-855.

[38] B. Sun, W. Ding, D. Shu, and Y. Zhou, "Purification Technology of Molten Aluminum," *Journal of Central South University of Technology,* vol. 11, (2004), 134-141.

[39] Y. Guang-chun and L. Yi-han, "Dynamic Electromagnetic Separation of Iron-Rich Phase Inclusions from Al Alloy," *China Foundry*, vol. 3, no. 3, (2006), 200-203.

[40] C. Song, Z. Xu, G. Liang, and J. Li, "Study of in-Situ Al/Mg2Si Functionally Graded Materials by Electromagnetic Separation Method," *Materials Science and Engineering: A,* vol. 424, (2006), 6-16.

[41] B. Zhang, "Continuous Electromagnetic Separation of Inclusion from Aluminum Melt Using Alternating Current," *Transactions of Nonferrous Metals Society of China,* vol. 16, (2006), 33-38.

[42] M. Afshar, M. Aboutalebi, M. Isac, and R. Guthrie, "Mathematical Modeling of Electromagnetic Separation of Inclusions from Magnesium Melt in a Rectangular Channel," *Materials Letters,* vol. 61, (2007), 2045-2049.

[43] A. Warczok and G. Riveros, "Slag Cleaning in Crossed Electric and Magnetic Fields," *Minerals Engineering,* vol. 20, (2007), 34-43.

[44] Z. Xu, T. Li, and Y. Zhou, "Continuous Removal of Nonmetallic Inclusions from Aluminum Melts by Means of Stationary Electromagnetic Field and DC Current," *Metallurgical and Materials Transactions A,* vol. 38, (2007), 1104-1110.

[45] Z. Qing-tao, Y. Zhang, and J. Ting-ju, "Motion Behavior of Non-Metallic Particles under High Frequency Magnetic Field," *Transactions of Nonferrous Metals Society of China*, vol. 19, no. 3, (2009), 674–680.

[46] Z. Sun, M. Guo, J. Vleugels, O. Van der Biest, and B. Blanpain, "Numerical Calculations on Inclusion Removal from Liquid Metals under Strong Magnetic Fields," *Progress In Electromagnetics Research,* vol. 98, (2009), 359-373.

[47] Z. Zhang, "Motion Behavior of Non-Metallic Particles under High Frequency Magnetic Field," *Transactions of Nonferrous Metals Society of China,* vol. 19, (2009), 674-680.

[48] M. Reza Afshar, M. Reza Aboutalebi, R. Guthrie, and M. Isac, "Modeling of Electromagnetic Separation of Inclusions from Molten Metals," *International Journal of Mechanical Sciences,* vol. 52, (2010), 1107-1114.

[49] G. Zhi-qiang, Z. Ting-ju, and J. Chun-pyo, "Separation Efficiency of Alumina Particles in Al Melt under High Frequency Magnetic Field," *Transactions of Nonferrous Metals Society of China*, vol. 20, no. 1, (2010), 153–157.

[50] J. P. Park, A. Morihira, K. Sassa, and S. Asai, "Elimination of Non-Metallic Inclusions Using Electromagnetic Force," *Tetsu-to-hagané,* vol. 80, (1994), 389-394.

[51] J. Barglik and C. Sajdak, "Purification of Liquid Aluminum from Non-Metallic Inclusions in the Electromagnetic Field," *Elektrowärme International,* no. 2, (1985), B77-B80.

[52] G. H. Zhang, K. C. Chou, and F. S. Li, "A New Model for Evaluating the Electrical Conductivity of Nonferrous Slag," *International Journal of Minerals, Metallurgy and Materials,* vol. 16, (2009), 500-504.

[53] N. El-Kaddah, "Apparatus and a Method for Improved Filtration of Inclusions from Molten Metal," *US Patent* 4,909,836, (1990).

[54] D. Shu, J. Wang, H. Chen, and B. Sun, "Multistage Electromagnetic Purification Method for Molten Metal," *US Patent App.* 20,080/216,601, (2005).

[55] A. M. Ampère, *Mémoires Sur L'électromagnétisme Et L'électrodynamique*: Gauthier-Villars, (1921).

[56] M. W. Kennedy, "Magnetic Fields and Induced Power in the Induction Heating of Aluminium Billets," unsubmitted Licentiate Thesis, Materials Science and Engineering, KTH, Stockholm, Sweden, (2012).
[57] L. Lorenz, "Ueber Die Fortpflanzung Der Electricität," *Annalen der Physik,* vol. 243, (1879), 161-193.
[58] H. Nagaoka, "The Inductance Coefficients of Solenoids," *Journal of the College of Science,* vol. 27, (1909), 18-33.
[59] R. S. Weaver, "Practical Considerations in the Calculation of Kelvin Bessel Functions and Complete Elliptic Integrals K and E," October (2009), http://www.g3ynh.info/zdocs/magnetics/appendix/KelvinEllipticCalcs.pdf, [Online], 15 December, 2012.
[60] R. Weaver. http://electronbunker.ca/DL/NumericalExamples01.ods [Online], 15 December, 2012.
[61] H. Wheeler, "Simple Inductance Formulas for Radio Coils," *Proceedings of the IRE,* vol. 16, (1928), 1398-1400.
[62] D. Knight, "*Part 1: Solenoid inductance calculation*", October, 2012, *http://www.g3ynh.info/zdocs/magnetics/Solenoids.pdf* , [Online], 15 December, 2012.
[63] *Copper Wire Tables Circular No. 31*: US Bureau of Standards, (1913).
[64] P. Desai, H. James, and C. Ho, "Electrical Resistivity of Aluminum and Manganese," *Journal of Physical and Chemical Reference Data,* vol. 13, (1984), 1131-1172.
[65] R. Brandt and G. Neuer, "Electrical Resistivity and Thermal Conductivity of Pure Aluminum and Aluminum Alloys up to and above the Melting Temperature," *International Journal of Thermophysics,* vol. 28, (2007), 1429-1446.
[66] J. B. Biot and F. Savart, "Note Sur Le Magnetisme De La Pile De Volta," *Ann. Chim. Phys,* vol. 15, (1820), 222-223.
[67] M. W. Kennedy, S. Akhtar, J. A. Bakken, and J. A. Aune, "Theoretical and Experimental Validation of Magnetic Fields in Induction Heating Coils," *Unpublished,* (2012), 1-11.
[68] H. Dwight and M. Bagai, "Calculations for Coreless Induction Furnaces," *American Institute of Electrical Engineers, Transactions of the,* vol. 54, (1935), 312-315.
[69] J. S. Ames, *The Discovery of Induced Electric Currents,* vol. 2: American book company, (1900).
[70] N. McLachlan, *Bessel Functions for Engineers*, Clarendon Press, Gloucestershire, (1955), 215-230.
[71] V. Korovin, "Motion of a Drop in a Conducting Liquid under the Action of a Variable Electromagnetic Field," *Magnetohydrodynamics (Engl. Transl.);(United States),* vol. 22, (1986), 17-19.
[72] V. Korovin, "Separation of Particles, Suspended in a Conducting Liquid, with the Help of an Alternating Electromagnetic Field," *Magnetohydrodynamics (Engl. Transl.);(United States),* vol. 21, (1986), 321-326.
[73] N. Keegan, W. Schneider, and H. Krug, "Evaluation of the Efficiency of Fine Pore Ceramic Foam Filters," *Light Metals,* (1999), 1031-1041.
[74] E. Moreira, M. Innocentini, and J. Coury, "Permeability of Ceramic Foams to Compressible and Incompressible Flow," *Journal of the European Ceramic Society,* vol. 24, (2004), 3209-3218.
[75] G. Diedericks and J. Du Plessis, "Electrical Conduction and Formation Factor in Isotropic Porous Media," *Advances in Water Resources,* vol. 19, (1996), 225-239.
[76] B. Hübschen, J. Krüger, J. Keegan, and W. Schneider, "A New Approach for the Investigation of the Fluid Flow in Ceramic Foam Filters," *Light Metals,* (2000), 809–815.
[77] P. Forchheimer, "Wasserbewegung Durch Boden," *Z. Ver. Deutsch. Ing,* vol. 45, (1901), 1782-1788.
[78] S. Ergun, "Fluid Flow through Packed Columns," *Chem. Eng. Prog.,* vol. 48, (1952), 89-94.

[79] I. Macdonald, M. El-Sayed, K. Mow, and F. Dullien, "Flow through Porous Media-the Ergun Equation Revisited," *Industrial & Engineering Chemistry Fundamentals,* vol. 18, (1979), 199-208.

[80] J. Richardson, Y. Peng, and D. Remue, "Properties of Ceramic Foam Catalyst Supports: Pressure Drop," *Applied Catalysis A: General,* vol. 204, (2000), 19-32.

[81] B. Dietrich, W. Schabel, M. Kind, and H. Martin, "Pressure Drop Measurements of Ceramic Sponges—Determining the Hydraulic Diameter," *Chemical Engineering Science,* vol. 64, (2009), 3633-3640.

[82] B. Dietrich, "Pressure Drop Correlation for Ceramic and Metal Sponges," *Chemical Engineering Science,* vol. 74, (2012), 192-199.

[83] S. A. Shakiba, R. Ebrahimi, and M. Shams, "Experimental Investigation of Pressure Drop through Ceramic Foams: An Empirical Model for Hot and Cold Flow," *Journal of Fluids Engineering,* vol. 133, (2011), 111105-1-10.

[84] M. W. Kennedy, R. Fritzsch, S. Akhtar, J. A. Bakken, and R. E. Aune, "Apparatus and Method for Priming a Molten Metal Filter," *U.S. Provisional Patent App.*, 6080-0105PUS1, (2012).

[85] J. Große, B. Dietrich, H. Martin, M. Kind, J. Vicente, and E. H. Hardy, "Volume Image Analysis of Ceramic Sponges," *Chemical Engineering & Technology,* vol. 31, (2008), 307-314.

[86] B. Dietrich, G. I. Garrido, P. Habisreuther, N. Zarzalis, H. Martin, M. Kind, and B. Kraushaar-Czarnetzki, "Morphological Characterization of Ceramic Sponges for Applications in Chemical Engineering," *Industrial & Engineering Chemistry Research,* vol. 48, (2009), 10395-10401.

[87] L. F. Moody, "Friction Factors for Pipe Flow," *Trans. Asme,* vol. 66, (1944), 671-684.

[88] M. D. M. Innocentini, L. Lefebvre, R. Meloni, and E. Baril, "Influence of Sample Thickness and Measurement Set-up on the Experimental Evaluation of Permeability of Metallic Foams," *Journal of Porous Materials,* vol. 17, (2010), 491-499.

[89] S. Ergun and A. A. Orning, "Fluid Flow through Randomly Packed Columns and Fluidized Beds," *Industrial & Engineering Chemistry,* vol. 41, (1949), 1179-1184.

[90] T. Lu, H. Stone, and M. Ashby, "Heat Transfer in Open-Cell Metal Foams," *Acta Materialia,* vol. 46, (1998), 3619-3635.

[91] M. Lacroix, P. Nguyen, D. Schweich, C. Pham Huu, S. Savin-Poncet, and D. Edouard, "Pressure Drop Measurements and Modeling on Sic Foams," *Chemical Engineering Science,* vol. 62, (2007), 3259-3267.

[92] T. T. Huu, M. Lacroix, C. Pham Huu, D. Schweich, and D. Edouard, "Towards a More Realistic Modeling of Solid Foam: Use of the Pentagonal Dodecahedron Geometry," *Chemical Engineering Science,* vol. 64, (2009), 5131-5142.

[93] M. V. Twigg and J. T. Richardson, "Fundamentals and Applications of Structured Ceramic Foam Catalysts," *Industrial & Engineering Chemistry Research,* vol. 46, (2007), 4166-4177.

[94] A. Inayat, J. Schwerdtfeger, H. Freund, C. Körner, R. F. Singer, and W. Schwieger, "Periodic Open-Cell Foams: Pressure Drop Measurements and Modeling of an Ideal Tetrakaidecahedra Packing," *Chemical Engineering Science,* (2011), 2758–2763.

[95] R. Fritzsch, "Filtration of Aluminium Melts Using Ceramic Foam Filters (CCF) and Electromagnetic Field," Masters Thesis, Department of Materials Science and Engineering, NTNU, Trondheim, (2011).

[96] S. Ripperger, W. Gösele, and C. Alt, "Filtration, 1. Fundamentals," in *Ullmann's Encyclopedia of Industrial Chemistry*, ed: Wiley-VCH Verlag GmbH & Co. KGaA, (2000), 1-33.

[97] P. Netter and C. Conti, "Efficiency of Industrial Filters for Molten Metal Treatment: Evaluation of a Filtration Process Model," *Light Metals,* (1986), 847-860.

[98] C. Tian and R. I. L. Guthrie, "Direct Simulation of Initial Filtration Phenomena within Highly Porous Media," *Metallurgical and Materials Transactions B,* vol. 26, (1995), 537-546.

[99] S. Bao, "Filtration of Aluminium - Experiments, Wetting, and Modelling," PhD. Thesis, Materials Science and Engineering, NTNU, Trondheim, (2011).

[100] J. Grandfield, D. Irwin, S. Brumale, and C. Simensen, "Mathematical and Physical Modelling of Melt Treatment Processes," *Light Metals,* (1990), 737-746.

[101] P. L. Schaffer and A. K. Dahle, "Settling Behaviour of Different Grain Refiners in Aluminium," *Materials Science and Engineering: A,* vol. 413, (2005), 373-378.

[102] A. Kolsgaard and S. Brusethaug, "Settling of SiC Particles in an AlSi7Mg Melt," *Materials Science and Engineering: A,* vol. 173, (1993), 213-219.

[103] J. Martin, G. Dube, D. Frayce, and R. Guthrie, "Settling Phenomena in Casting Furnaces: A Fundamental and Experimental Investigation," *Light Metals,* (1988), 445-455.

[104] T. Iwasaki, J. Slade, and W. E. Stanley, "Some Notes on Sand Filtration [with Discussion]," *Journal (American Water Works Association),* vol. 29, (1937), 1591-1602.

[105] D. Apelian and R. Mutharasan, "Filtration: A Melt Refining Method," *Journal of Metals,* vol. 9, (1980), 14-19.

[106] F. Acosta G and A. Castillejos E, "A Mathematical Model of Aluminum Depth Filtration with Ceramic Foam Filters: Part II. Application to Long-Term Filtration," *Metallurgical and Materials Transactions B,* vol. 31, (2000), 503-514.

[107] P. Bakke, T. Engh, E. Bathen, D. ymo, and A. Nordmark, "Magnesium Filtration with Ceramic Foam Filters and Subsequent Quantitative Microscopy of the Filters," *Material and Manufacturing Process,* vol. 9, (1994), 111-138.

[108] T. Engh, B. Rasch, E. Bathen, and R. Miller, "Deep Bed Filtration Theory Compared with Experiments," *Light Metals,* (1986), 829-836.

[109] R. Guthrie and M. Li, "In Situ Detection of Inclusions in Liquid Metals: Part II. Metallurgical Applications of LiMCA Systems," *Metallurgical and Materials Transactions B,* vol. 32, (2001), 1081-1093.

[110] J. E. Dore and C. Bickert, "A Practical Guide on How to Optimize Ceramic Foam Filter Performance," *Light Metals,* (1990), 791-796.

[111] E. Laé, H. Duval, C. Rivière, P. Le Brun, and J. Guillot, "Experimental and Numerical Study of Ceramic Foam Filtration," *Light Metals,* (2006), 753-758.

[112] R. Roscoe, "The Viscosity of Suspensions of Rigid Spheres," *British Journal of Applied Physics,* vol. 3, (1952), 267-269.

[113] F. Zenz and N. Weil, "A Theoretical ‐ Empirical Approach to the Mechanism of Particle Entrainment from Fluidized Beds," *AIChE Journal,* vol. 4, (1958), 472-479.

[114] D. Geldart, "Types of Gas Fluidization," *Powder Technology,* vol. 7, (1973), 285-292.

[115] P. Arnold, "Some Observations on the Importance of Particle Size in Bulk Solids Handling," *Powder Handling and Processing,* vol. 13, (2001), 35-40.

[116] R. Fritzsch, B. Mirzaei, M. W. Kennedy, S. Akhtar, J. A. Bakken, and R. E. Aune, "Automated Quantification of SiC-Particles in Solidified A356 Aluminum Using Imagepro® Plus 7.0," Accepted for publication at *Light Metals*, San Antonio, Texas, 3-7 March, (2013).

[117] M. W. Kennedy, C. Harris, and A. MacRae, "Risk Weighted Cash Flow, a Communication Tool for Engineers and Financial Professionals on New Technology Projects," *Journal of the Candian Institute of Mining and Metallurgy,* vol. 3, no. 4, (2012), 1-10.

[118] R. Fritzsch, M.W. Kennedy, S. Akhtar, J.A. Bakken, and R.E. Aune, "Electromagnetic Priming of Ceramic Foam Filters (CFF) for Liquid Aluminium Filtration," Accepted for publication at *Light Metals 2013*, 3-7 March, (2013), San Antonio, Texas.

APPENDIX 1

Apparatus and Method for Priming a Molten Metal Filter

Mark William Kennedy, Shahid Akhtar, Robert Fritzsch, Jon Arne Bakken, Ragnhild Elisabeth Aune

U.S. Provisional Patent Application, 61/639,196, (2012).

APPARATUS AND METHOD FOR PRIMING A MOLTEN METAL FILTER

TECHNICAL FIELD

This invention involves the priming of filters for removal of solid inclusions from liquid metal. Disclosed herein are an apparatus and a method for priming a molten metal filter.

BACKGROUND OF THE INVENTION

Ceramic filters and commonly Ceramic Foam Filters (CFF) are currently available to purify liquid metal, such as disclosed in US Patent Number 3,893,917. Most often this involves the removal of solid inclusions from liquid metal, such as steel and aluminum. These solid inclusions can lead to physical defects in the final metal products if not removed prior to solidification.

In order to most efficiently use the filter media, the open porosity of the filter must be completely filled with liquid metal. Completely filing the filter with liquid metal improves the wetting of the surface of the filter media to facilitate the collection of the solid inclusions. The problem to be solved is that incomplete priming results in locally higher liquid velocities in the active parts of the filter, higher operational pressure drops or lower total liquid metal throughput, combined with lower collection efficiency for the solid inclusions.

A common practice is to place a ceramic foam filter with a gasket material into a filtering device or 'bowl', such that the metal height builds up over the filter and is forced by gravity into and through the filter medium. The inclusions are then removed by either deep or bed filtration mechanisms. The poor wetting characteristics of these ceramic filters and the need to remove the air contained within the pores, often leads to difficulties, particularly at the start of the filtration operation.

The significance of priming in filtration is disclosed in a number of Patents and Patent Applications, such as US Patent Number 4,872,908, where Enright, P.G. et al. describe the definition and role of priming in detail and also give specific efficiency data when removing 20 micron particles (between -13.4 and 54.8%) using LiMCA for 30 PPI filters The large range in filtration efficiency can be partly attributed to the impact of priming on filter performance. US Patent Number 4,081,371, Yarwood, J.C. et al. describe the need to remove gas bubbles from within the ceramic foam filter, and the roles of metallostatic head and filter

angle on priming. Generally speaking higher total pressure (from metallostatic head or other means) improves priming efficiency. In US Patent Application 09/867,144, Quackenbush, M.S., disclose a filter media, without the application of mechanical forces to encourage air bubble release, for the purpose of releasing trapped air bubbles to ensure an easier and more complete priming of the filter media.

In US Patent Number 7,666,248, Belley, L., et al. disclose a method using a vacuum system to generate an additional pressure gradient of about 6 kPa or about 25 cm of liquid aluminum head equivalent for the express purpose of increasing the effective priming pressure to ensure adequate priming for ceramic foam filters with a thickness from 2.5 to 7.6 cm and a low average pore or "window" size of 150-500 microns, which are typical of filters with 60 or more PPI. These filters otherwise require substantial metallostatic heads (vertical distance from trough bottom to filter top) to ensure adequate priming. Belley et al. also disclose that the typical range of priming heads for Ceramic Foam Filters is from about 20-80 cm. Higher values are associated with higher pore density and smaller window sizes, and are often impractical to implement at existing casting operations.

Filters are normally preheated to try to improve the flow of metal into the filter media and, hence, the priming efficiency for a fixed metal height over the filter. Difficulties are often encountered in obtaining uniform heating without localized overheating that can lead to thermal damage of the filter media. This makes it difficult to ensure that the entire filter area will be available to pass liquid metal. In US Patent Number 4,834,876, Walker, N.G. claims a process by which the non-conductive ceramic filter is rendered electrically conductive by the coating of the filter media particles with a conductive substance like nickel or by using an electrically conductive material, such as silicon carbide to construct the filter media. By passing a current through the media or by surrounding the filter with an induction coil to induce eddy currents, the media could be caused to self-heat due to the resistive (I^2R) losses to ensure preheating and complete priming.

A process involving the use of a low frequency induction coil and Ceramic Foam Filter elements has been presented in US Patent 4,837,385 by Calogero, C. et al. In this process a number of different means were presented, whereby a crossed current and magnetic field could be created, which would generate Lorentz forces. Some of these methods involve the use of electrodes and a so-called 'injection current' which is undesirable as the electrodes are

a potential source of contamination to the liquid metal being filtered. The theory behind the process disclosed by Calogero et al. was that the Lorentz forces would act preferentially on the metal and not the inclusions, thus causing migration of the inclusions and interception of the inclusions by the walls of the filter media. The impact of the magnetic field on the priming of the filter media was not disclosed. Furthermore, the mechanism described by Calogero depends on the absence of any significant curl or vorticity in the magnetic and Lorentz force fields. However, as disclosed in US Patent 4,909,836, vorticity is always present in these fields when a normal induction coil with a constant helical pitch is used as the source of crossed current and magnetic field. One aspect of the present invention uses an induction coil in order to avoid direct contact and contamination of the liquid metal. A standard constant pitch induction coil is used. The inventors are well aware of the vorticity in the magnetic and Lorentz forces produced via such an induction coil and have therefore designed the method to make maximum advantageous use of the vorticity, in order to press metal into the filter media to achieve a better degree of priming with a low metallostatic head.

DEFINITIONS

As used herein, the term "priming" refers to the displacement of air contained in the open pore structure of a filter (e.g., a ceramic foam filter) and the improvement of wetting of the filter media by the liquid metal, thus, allowing the maximum volume and internal surface area to be available to pass flow and collect particles.

As used herein, the term "inclusion" refers to any contaminant of the liquid metal having a melting point greater than the metal, and therefore being solid at the processing temperature.

SUMMARY OF THE INVENTION

Various aspects of the present invention relate to: (1) a method of priming, without the use of externally applied vacuum or gas pressure, by applying a low frequency induction coil (1-60 Hz) to ensure complete priming of a non-electrically conductive filter element; (2) a method of priming to improve priming and subsequent operation of ceramic foam filters with small 'window' size, such as those typical of 50-80 PPI commercial Ceramic Foam Filters, in order to operate with higher efficiency and produce a metal product containing fewer inclusions; (3) a method of priming which allows thicker than traditional ceramic foam filters or a stack of traditional filters to be primed; and (4) an apparatus that allows filter media including

previously used filter media, to be maintained hot or reheated, and subsequently reused for more than one casting cycle.

In one embodiment, the apparatus for priming a filter includes a filter element configured to receive a liquid metal flow; an induction coil surrounding the filter element and configured to produce a magnetic field, an axis of the induction coil being substantially aligned with an introduction direction of the liquid metal flow; a gasket configured to provide a secure enclosure to a circumference of the filter element; and a separator accommodating the induction coil and separating the induction coil from the liquid metal flow.

In one embedment, a low frequency induction coil is placed around and in very close proximity to a ceramic filter media, such as a Ceramic Foam Filter element or stack of said filter elements. The presence of a magnetic field allows priming of thicker filters than the conventional industry standard of approximately 50 mm. The total allowable thickness is determined by the installed length of the induction coil.

The orientation the coil and filter elements can be either vertical or horizontal, provided a path is made available for gas to escape during priming.

The electrical conductors of the induction coil can have many different shapes. For example, flat round, tubular, rectangular, or square. Unlike traditional induction furnace coils, the coils of the present invention need not be constructed for low electrical resistance, as they are not being used as part of a device primarily intended for electrically efficient melting. Thus, a higher current density can be advantageously used (e.g. 50 A/mm^2 vs. typical values from 1-10 A/mm^2) resulting in proportionately smaller diameter conductors that can provide more turns in a given height of coil, with a corresponding increase in the magnetic field strength. Single, double or more layers of coils can also be used advantageously to achieve even higher magnetic field strengths over the height of the filter media. Induction coils with more than 3 layers can also be used, but with diminishing benefits of additional magnetic field strength.

In one embodiment, the filter media is substantially horizontal and surrounded by an induction coil. The induction coil is positioned to extend over the upper surface of the filter element, which places the top of the filter within the zone of high longitudinal magnetic flux

density. The flux density of the magnetic field is very strong over the complete height of the coil, but dissipates rapidly after the last turn of the coil.

Another aspect of the invention features metal poured onto the filter to at least as high as the top of the coil. In a preferred embodiment, the metal is substantially higher than the top of the coil to prevent the formation of a significant metal meniscus, and to reduce the potential for oxidation of the metal during priming. The magnetic field of the coil induces eddy currents in the metal sitting on the filter media, which interact with the coil's strong magnetic field, to produce powerful Lorentz forces. The depth at which these forces can be produced is enhanced by the use of a low alternating frequency in the coil excitation current. A filter element with a large width will require the use of a lower frequency to achieve similar results to those of a smaller width filter.

The heating efficiency of the coil increases with frequency. In an aspect of the invention, the frequency of the coil excitation current is preferably between 1 and 60 Hz, and more preferably between 50 to 60 Hz. This frequency range provides an optimal combination of stirring and heating. Higher frequencies can optionally be used if a greater degree of heating is required to re-melt metal frozen in previously used filter media. In a preferred embodiment, the radius of a round filter or the width of a rectangular or square filter is selected, such that the standard electrical line frequency of 50 or 60 Hz can be utilized to provide an optimal beneficial effect.

The coil and filter apparatus can be round, square or rectangular in section without deviating from the purpose of this invention. A rectangular shape has the advantage that the overall filter area can be maximized, while minimizing the width that the magnetic field must be made to penetrate. A rectangular shape can eliminate the need to use frequencies below the line frequency (50 or 60 Hz), where costly solid state power supplies become necessary..

The Lorentz forces are initially produced only in the metal and not in the non-electrically conductive filter media. Therefore, a large initial vorticity exists in the Lorentz force field, which causes rotation of the metal and impingement onto the surface of the filter element. It is the momentum of the impinging metal that forces metal into the filter.

The inventors have found that within the filter media, current flow is inhibited to a surprising degree by the presence of the ceramic matrix. As a result, less current flows within the filter than in the metal over or under the filter, thus reducing the magnitude of the Lorentz forces. The reduced effective electrical conductivity in the filter ensures that a substantial vorticity in the Lorentz forces continues to exist up to and past the point of complete filter priming. The result is that metal is forced into and through the filter media. Higher pore density filters, e.g. 50 and 80 PPI, have increased resistivity, which increases the vorticity in the Lorentz forces and provides the increased driving forces to prime these 'tighter' filter elements.

If the filter media is not preheated, liquid metal will initially freeze on the surface of the filter media. Given that solid metal has a substantially higher electrical conductivity than the liquid metal at the same temperature (approximately a factor of two for aluminum), the solid will preferentially conduct current, while at the same time being impinged upon by fast flowing liquid metal. Being forced to remain stationary and within the height of the inductor, it will experience continuous heating until it liquefies. In a preferred embodiment, the filter element is preheated by conventional means to reduce thermal stresses in order to prevent cracking. However, preheating is not a requirement for priming, even for very tight 80 PPI filter elements.

Once the filter media is substantially filled with metal, the excitation of the coil can be stopped. Thereafter, conventional casting procedures can be used. On completion of the batch casting process, it is typical to dispose of the filter media because it is difficult to reuse in the absence of continuous metal flow.

In another embodiment of the invention, a used filter element can be reused until its capacity to remove inclusions is completely exhausted. A used filter element can be reused by applying a period of inductive heating prior to priming with liquid metal or by maintaining the filter filled with liquid metal between casts by using continuous induction heating. In one aspect, an excitation current higher than 60 Hz is advantageously used. This embodiment utilizes a dual frequency power supply, which could optionally be combined with a second coil specifically designed for the melting operation.

References

3,893,917	7/1975	Pror et al. ……..210/69
4,081,371	3/1978	Yarwood et al. ……..210/69
4,834,876	5/1989	Walker ……...210/185
4,837,385	6/1989	Conti et al. ……210/695
4,872,908	10/1989	Enright et al. ……75/68
7,666,248	2/2010	Belley et al. ……...75/407
09/867,144	12/2002	Quackenbush ……...210/510.1
4,909,836	03/1990	El-Kaddah ……75/10.67

BRIEF DESCRIPTION OF THE DRAWINGS

FIG. **1** is a schematic drawing of one embodiment of the present invention.

FIG. **2** is a Scanning Electron Microscope picture showing the relatively open structure of a new 30 PPI Ceramic Foam Filter.

FIG. **3** is a Scanning Electron Microscope picture showing the relatively closed structure perpendicular to the normal direction of metal flow of a new 80 PPI Ceramic Foam Filter.

FIG. **4** depicts a photograph of a non-limiting example of priming a 30 PPI ceramic filter in accordance with an embodiment of the present invention.

FIG. **5** depicts a photograph of a non-limiting example of priming a 30 PPI ceramic filter in accordance with an embodiment of the present invention.

FIG. **6** depicts a photograph of incomplete priming of a 30 PPI ceramic filter without the presence of an induction coil.

FIG. **7** is a graph showing the data logged data for EXAMPLE **1**.

FIG. **8** is a graph showing the data logged data for EXAMPLE **2**.

FIG. **9** is a graph showing the data logged data for EXAMPLE **3**.

FIG. **10** depicts a photograph of a non-limiting example of priming a 50 PPI CFF in accordance with an embodiment of the present invention.

FIG. **11** depicts a photograph of negligible priming of a 50 PPI CFF without the presence of an induction coil.

FIG. **12** depicts a photograph of a non-limiting example of priming an 80 PPI CFF in accordance with an embodiment of the present invention.

FIG. **13** is a photograph showing negligible priming of an 80 PPI CFF without the presence of an induction coil.

DETAILED DESCRIPTION OF THE INVENTION

For purposes of promoting an understanding of the principles of the invention, reference will now be made to the embodiments illustrated in the drawings. It will nonetheless be understood that no limitation of the scope of the invention is intended by the illustration and description of certain embodiments of the invention. In addition, any alterations and/or modifications of the illustrated and/or described embodiment(s) are contemplated as being within the scope of the present invention. Further, any other applications of the principles of the invention, as illustrated and/or described herein, as would normally occur to one skilled in the art to which the invention pertains, are contemplated as being within the scope of the present invention.

FIG. 1 shows a conventional filter 'bowl' **1** as typically used with Ceramic Foam Filters. FIG. 1 is suitably modified in accordance with the present invention to include an induction coil **2**. A two layer induction coil **2** is shown in FIG. 1. A single, double or more layer coil could also be used without changing the purpose of the invention.

A standard Ceramic Foam Filter element **3** is shown installed within the induction coil **2**. Alternatively, two or more filter elements could be stacked without deviating from the purpose of the present invention, provided that the coil **2** extends above the upper surface of

the top of filter **3** by one coil turn or at least 5% and preferably 10% of the coil radius, as indicated by dotted line **13** in FIG. 1.

The induction coil **2** is preferably placed as close as possible to the edge of filter **3** to achieve the most advantageous results of the magnetic field. Suitable space must be allowed for gasket material **4** to prevent leakage of the liquid metal around the filter **3** and for thermal insulation and refractory material **5**. Sufficient thermal insulation and refractory material must be present to avoid the contact of the hot metal in the upper portion of the bowl **6** or discharge portion of the bowl **7**, with coil **2** or with the coil leads **8**. Those skilled in the art understand that a suitable cooling media (organic or water) must be used in combination with coil leads **8** and coil **2**, to prevent electrical or thermal overheating and damage to the electrical conductors. Contact must be prevented between the conductors **8** and between the layers of the coil **2** to prevent electrical short circuiting of the excitation current.

In order to function as a filtration device, the bowl must be equipped with a suitable liquid metal feed **9** and discharge means **10**. The sides **11** and bottom **12** of the bowl must be designed with adequate refractory to maintain the heat balance of the metal to be filtered. The filter **3** may be preheated by conventional means to prevent excessive thermal shock prior to use.

In a preferred embodiment of the invention, a current is impressed on the induction coil of sufficient magnitude to generate an average magnetic flux density of 0.05-0.25 T, across the width of the un-primed filter. The frequency of the coil excitation current is preferably between 1 and 60 Hz. The frequency of the coil excitation current is preferably in a range where the ratio between the electromagnetic penetration depth (δ) in the liquid metal in the upper portion of the bowl **6** and the average radius or width of the filter **3** is between preferably 0.5 and 3.0, and more preferably between 0.7 and 1.4, in order to achieve both a sufficiently high magnetic penetration and avoid excessive heating.

In one preferred embodiment, liquid metal is added to the upper part of the bowl **6** via inlet **9** with current applied to coil **2**. Alternatively, liquid metal is added first, and then current is applied to coil **2**. In a preferred embodiment, liquid metal fills the upper portion of bowl **6** to a sufficient height over the last turn of coil **2,** such that an electromagnetic meniscus is

prevented from forming. This embodiment also avoids excessive oxidation of the metal during priming.

Electromagnetic priming can be accomplished with minimal liquid metal over the upper surface of the filter. Preferably, a liquid metal height of about 5-10 cm is over the top turn of the coil **2.** Alternatively**,** metallostatic pressures from about 1.1 to 3.6 kPa is preferred to achieve adequate priming of CFF filters between 30 and 80 PPI, while avoiding excessive meniscus formation, and using average magnetic flux densities in the range of 0.1-0.2 T in the air gap between coil and filter.

In one aspect of the invention, current is continued for periods of time from about 30 seconds to about 10 minutes, and even more preferably to about 3-6 minutes. Once adequate priming has been achieved, the excitation current to the coil **2** can be discontinued.

Once a filter element **3** has been used, it can optionally be reused by first using induction coil **2** to re-melt the metal frozen in the pores of the filter **3**. Those skilled in the art understand that a higher frequency is advantageous for melting. A frequency >60 Hz can be applied. A dual frequency power supply may therefore be beneficially used with the present method. A skilled practitioner may specify the frequency, current and time in order to achieve the desired melting in the correct amount of time, without significant overheating and possible damage to the filter elements, while achieving a high electrical efficiency. A second coil can optionally be designed and installed coaxially to coil **2** to achieve even more energy efficient melting.

The present invention can be better understood with reference to specific examples. These examples are illustrative and are not intended to restrict the applicability of the present invention. These examples were conducted using several different coils as indicated in TABLE I. These coils were operated at 50 Hz using applied currents as indicated in the various examples.

TABLE I

Coils:	Coil 1	Coil 2	Coil 3
Number of layers	2	1	2
Inside diameter, mm	126	126	127
Average diameter, mm	140	132	142
Height, mm	107	111	116
Coil copper tube diameter, mm	6	6	6
Coil copper tube thickness, mm	1	1	1
Number of turns	31.0	16.5	31.0
Measured inductance of empty coil, μH	103.3	27.6	101.5

Nominal filter dimensions of 100-105 mm diameter and 50 mm thick where used in these examples. 30, 50 and 80 PPI commercial Ceramic Foam Filter (CFF) elements were used. SEM pictures of 30 and 80 PPI commercial CFF's are shown in FIGS. 2 and 3. It can be clearly seen in these figures that the 30 PPI has a very open structure, while the pore and window size of the 80 PPI is much reduced. The open structure of the 30 PPI allows for very easy priming with low metal head and less preheating, but it also makes for reduced filtration efficiency especially for fine inclusions in the liquid metal. It is more difficult to get metal to penetrate and remove the air from the closed and tight structure of the 80 PPI CFF, thus requiring increased priming metal heights, as is well known to those skilled in the art.

A standard aluminum casting alloy, A356 was used in all examples, to which various levels of contaminants were added. 1.5 wt% (EXAMPLES 4-6) – 3 wt% (EXAMPLES 1-3) SiC was added, using 13-23 micron SiC particles embedded in a matrix of A356 alloy. In EXAMPLES 1-3, oxide particles were also added by the addition of 20% by weight anodized and lacquered aluminum plates.

EXAMPLE 1

A laboratory scale filter bowl was created by cementing a nominal 105 mm diameter, 30 PPI CFF into two sections of 150 mm long by 4" diameter fiber insulating crucibles, such that the midline of Coil 1 was coincident with the bottom of the CFF and approximately a single turn of the coil was over the upper surface of the CFF. The bottom of the bowl was constructed from a dense ceramic plate, ~25 mm thick, in which a 3.2 mm diameter discharge hole had been drilled.

The filter was preheated to a glowing red temperature using a hand held propane burner. An RMS current of 731 A was applied to Coil 1 at 50 Hz. A356 aluminum alloy, containing both SiC and oxide particles and at a nominal initial pouring temperature of 750^{o}C (as measured by immersion thermocouple seconds before pouring) was added to the upper portion of the bowl up to a level of 100 mm over the top of the CFF. This level was maintained until the feeding crucible was emptied after 110 seconds. Power was interrupted after 260 seconds, when aluminum was no longer discharging from the outlet hole. The measured temperature over and under the filter and the discharge rate of the aluminum were data logged as indicated in FIGURE 7. The heating effect of the induction coil is clearly illustrated in FIGURE 13, with the lower temperature rising with time, even as the temperature of the metal over the filter decreases. Average coil current during filtration was 715 A, due to the increased electrical resistance caused by the liquid metal. This effect is present in all examples and well known to those skilled in the art.

The filter was subsequently sectioned using abrasive water cutting, due to the high concentration of extremely hard and abrasive SiC particles. One section is shown as FIG. 4. Areas containing high gas porosity and exhibiting poor metal-ceramic wetting were ablated during the cutting process. In this example where the filter was primed with a 'strong' magnetic field, very little material was ablated and good wetting was observed macroscopically as well as microscopically during subsequent metallographic analysis with a scanning electron microscope.

EXAMPLE 2

An apparatus was constructed using Coil 2, but otherwise identical to EXAMPLE 1. The filter was similarly preheated. An RMS current of 956 A was applied to Coil 2. The same recipe of alloy, SiC and oxide was added, at a nominal pouring temperature of 750^{o}C. The temperature over and under the filter and the discharge rate of the aluminum were again measured as shown in FIG. 8. The feeding crucible was emptied after 110 seconds and the power was interrupted after 215 seconds. This filter element, which had been primed with a 'weak' magnetic field, was again cut using water abrasive cutting and in this case much greater porosity and less wetting of the ceramic was observed as indicated by the loss of ceramic material during cutting shown clearly in FIG. 5.

EXAMPLE 3

An apparatus was constructed without an induction coil, but otherwise identical to EXAMPLES 1 and 2. The filter was preheated till glowing red and again the same feed recipe and target pouring temperatures were used. The level of priming metal was maintained at 100 mm over the filter element for 145 seconds until the feeding crucible was emptied. The temperature over, under and the discharge rate of the aluminum were again measured as shown in FIG. 9. One section of the filter element is pictured in FIG. 6, showing the very high porosity and very poor wetting of the filter element, when compared to FIGS. 4 and 5 from EXAMPLES 1 and 2. The poor priming of the filter is also indicated by the reduced discharge rate of the metal for the same metallostatic head over the filter and the same size of the discharge orifice. Priming results were best with the 'strong' field, less good with the 'weak' field and poorest with no magnetic field.

EXAMPLE 4

An apparatus similar to EXAMPLES 1-3 was constructed, but without a discharge hole in the bottom plate. Coil number 3 was used. A 50 PPI commercial Ceramic Foam Filter (CFF), 100 mm in diameter was placed such that the bottom of the filter was at the same elevation as the midline of the coil and the coil extended approximately one turn above the upper surface of the 50 mm thick filter. A feed consisting of A356 aluminum alloy and 1.5 wt% SiC was used. The filter was not preheated. The upper portion of the filter bowl was filled with the liquid aluminum feed material at a nominal pouring temperature of 750^{o}C, up to a level of 100 mm over the upper surface of the filter element. An excitation current of 738 A was then applied to the coil. Over approximately 20 seconds, metal was drawn into the filter and metal was added to maintain a nearly constant height of 100 mm over the filter (104 mm measured after freezing). Current was maintained for precisely 180 seconds. The power was then stopped and the sample solidified. The filter element was then sectioned using a steel blade. The polished section is shown in FIG. 10, showing very low porosity and complete metal penetration of the filter element.

EXAMPLE 5

An apparatus substantially identical to EXAMPLE 4 was constructed, but without an induction coil. The same feed recipe and filling procedure were used. Again no preheating of the filter element was applied. After filling to 100 mm over the top of the CFF, no decrease in metal height was observed. On disassembly of the apparatus the filter element separated

from the 100 mm of metal, which was frozen over the filter and it was observed that only a very minor amount of metal penetration had occurred (<20 mm) as shown in FIGURE 11. The balance of the filter media was completely devoid of metal and priming had therefore failed. The difference in the results between EXAMPLES 4 and 5 were dramatic, with the only substantial difference in execution being a 'strong' magnetic field in the case of EXAMPLE 4 and no magnetic field in EXAMPLE 5.

EXAMPLE 6

An apparatus substantially identical to EXAMPLES 4 and 5 was constructed, but using an 80 PPI, instead of a 50 PPI CFF. The same procedures and feed recipe from EXAMPLE 4 were used. After filling with liquid alloy to 100 mm over the top of the filter, an excitation current of 747 A was applied to coil 3. Over a period of approximately 30-40 seconds, metal was drawn into the filter element and metal was added over the filter to maintain a level of 100 mm (99 mm measured after freezing). Current was maintained again for precisely 180 seconds. The power was then stopped and the sample solidified. This filter element was then cut using water abrasive cutting. Priming was extremely successful as indicated by the complete metal penetration, low gas porosity and good wetting shown in FIG. 12.

EXAMPLE 7

An apparatus substantially identical to EXAMPLE 6 was constructed, but without an induction coil. The same filling procedures and feed recipe were again used. Liquid aluminum alloy containing the SiC particles was added over the 80 PPI filter element up to a height of approximately 100 mm. No decrease in the metal height was detected. The sample was then solidified. On disassembly, the metal which extended 103 mm over the top of the filter element, separated from the balance of the filter, which was completely free of metal. Approximately 0-5 mm of filter material remained attached to the frozen metal, as shown in FIG. 13. It was concluded that priming had completely failed. Again the only substantive difference between EXAMPLE 6 and 7 was that a 'strong' magnetic field had been used in EXAMPLE 6 and no magnetic field was applied in EXAMPLE 7.

The presence of the strong magnetic field in EXAMPLES 4 and 6 was responsible for the good priming even in the absence of filter preheating. The lack of magnetic fields, combined with no preheating and the low metallostatic height over the filters in EXAMPLES 5 and 7 resulted in a failure to prime.

It should be understood that the examples and embodiments described herein are for illustrative purposes only and that various modifications or changes in light thereof will be suggested to persons skilled in the art and are to be included within the spirit and purview of this application and the scope of the appended claims.

CLAIMS

What is claimed is:

1. A method of priming a non-electrically conductive ceramic filter for removal of solid inclusions from liquid metal, wherein said filter is contained in a filter bowl, and is surrounded by an induction coil whose axis is substantially aligned with the direction of the desired net metal flow, said method comprising:
    a) applying an alternating excitation current to the induction coil;
    b) adding sufficient liquid metal to cover an upstream side of the filter element;
    c) allowing the currents induced in the liquid metal by the coil and the magnetic field of the coil to create Lorentz forces which press upon and stir the liquid metal such that the liquid metal is pressed into the ceramic, hence priming the filter; and
    d) discontinuing the excitation current once a predetermined degree of priming has been obtained.

2. The method according to claim **1,** wherein the design of the coil and magnitude of the applied current generate an average magnetic field strength of at least 0.05T in a space between the coil and ceramic filter.

3. The method according to claim **1**, wherein the average field strength is between 0.05 and 0.25T in a space between the coil and ceramic filter.

4. The method according to claim **1,** wherein the average field strength is between 0.1 and 0.2T in a space between the coil and ceramic filter.

5. The method according to claim **1,** wherein the liquid metal is an aluminum alloy.

6. The method according to claim **1,** wherein the liquid metal is first added to the filter bowl and then current is applied to the induction coil.

7. The method according to claim **1**, wherein the non-electrically conductive ceramic filter is a ceramic foam filter of between 30 and 80 PPI and 25-75 mm of thickness.

8. The method according to claim **1**, wherein 2 or more ceramic foam filters are combined to a total thickness of 50-150 mm.

9. The method according to claim **1**, wherein the coil extends at least one turn and between 5 and 10% of the radius of the coil, but less than half of a total length of the coil, over the upper surface of the top of the filter.

10. The method according to claim **1** or **5**, wherein the metal extends between 5 and 15 cm over the top of the coil.

11. The method according to claim **1**, wherein the frequency applied to the induction coil is between 1-60 Hz.

12. The method according to claim **11**, wherein the frequency of the induction coil is selected to give a ratio of electromagnetic penetration depth between 0.5 and 3.0 and preferably between 0.7 and 1.4.

13. The method according to claims **11** and **12**, wherein local electrical line frequency can be used by adjusting the width or diameter of the filter element to achieve the preferred ratios.

14. The method of reusing a previously used ceramic filter element, comprised of applying an alternating current to the induction coil in claim **1** at a frequency greater than 50 Hz, wherein there is sufficient current to inductively melt the solid aluminum contained in the pores of the filter.

15. The method according to claim **14**, wherein a second coil specifically designed for high efficiency melting is installed co-axially with the mixing coil.

16. An apparatus for priming a filter, comprising:
    a filter element configured to receive a liquid metal flow;

an induction coil surrounding the filter element and configured to produce a magnetic field, an axis of the induction coil being substantially aligned with an introduction direction of the liquid metal flow;

a gasket configured to provide a secure enclosure to a circumference of the filter element; and

a separator accommodating the induction coil and separating the induction coil from the liquid metal flow.

17. The apparatus according to claim 16, wherein the induction coil extends, along the axis, above an upper surface, facing the liquid metal flow, of the filter element.

18. The apparatus according to claim 16, wherein the induction coil is a single layer coil or multi-layer coil.

19. The apparatus according to claim 16, further comprising a liquid metal feed configured to lead the liquid metal feed to the filter element; and a discharge device.

20. The apparatus according to claim 16, further comprising a preheating device configured to preheat the filter element prior to introducing the liquid metal flow.

ABSTRACT

An apparatus and method are described for effectively priming a non-electrically conductive filter for removal of solid inclusions from liquid metal. In one embodiment, the ceramic filter media is surrounded by a low frequency induction coil (1-60 Hz) with its axis aligned in the direction of the net metal flow. The coil is positioned to enhance the heating of any metal frozen onto, or in the pores of, the filter element. In one embodiment, the coil is positioned in order to generate Lorentz forces, which act to cause heated metal to impinge on the upper surface of the filter element, enhancing the priming action. Once a filter equipped with such a coil has been primed, it can be kept hot or reheated, and subsequently reused during several batch tapping sequences.

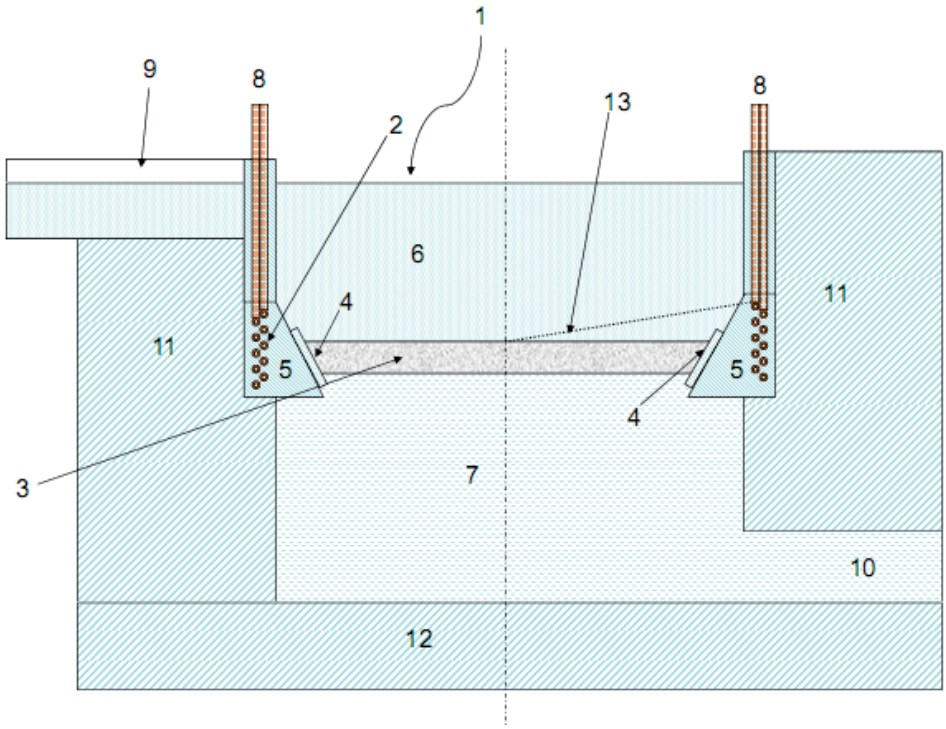

FIG. 1

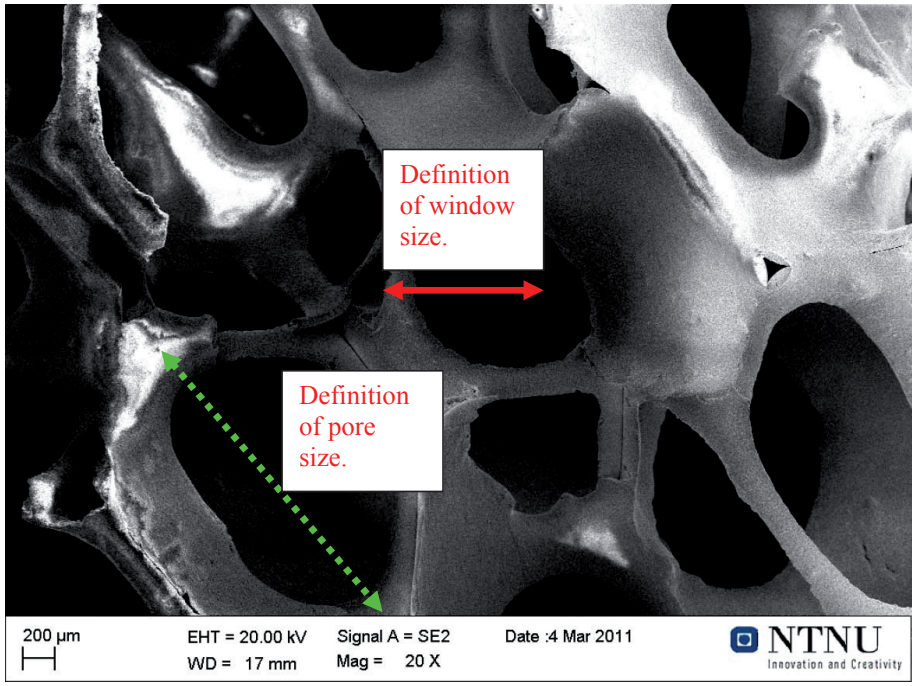
Definition of window size.
Definition of pore size.
200 µm
EHT = 20.00 kV
WD = 17 mm
Signal A = SE2
Mag = 20 X
Date :4 Mar 2011
NTNU
Innovation and Creativity

FIG. 2

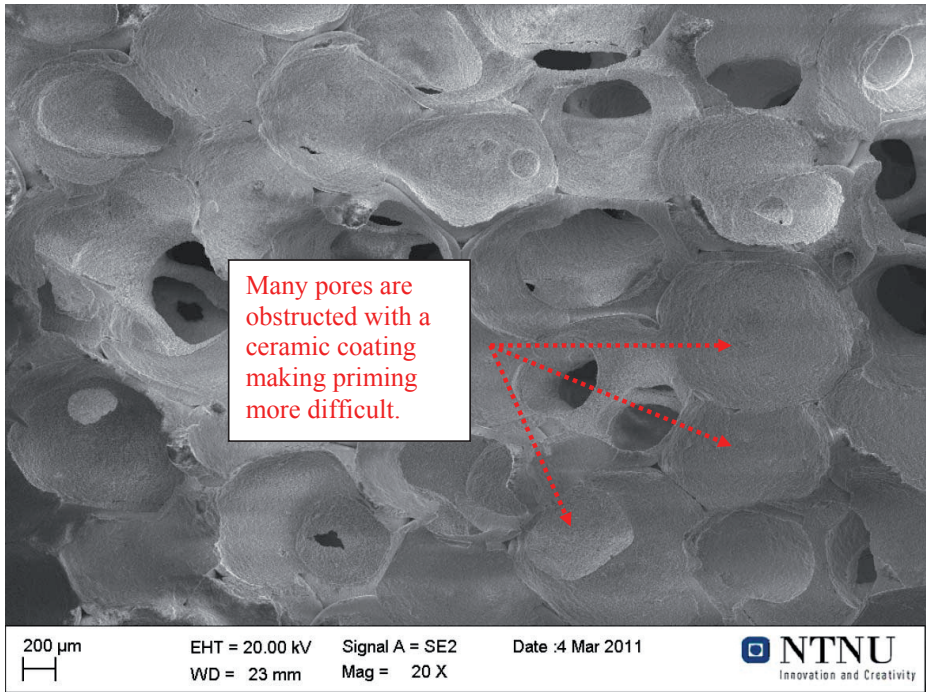
Many pores are obstructed with a ceramic coating making priming more difficult.
200 µm
EHT = 20.00 kV
WD = 23 mm
Signal A = SE2
Mag = 20 X
Date :4 Mar 2011
NTNU
Innovation and Creativity

FIG. 3

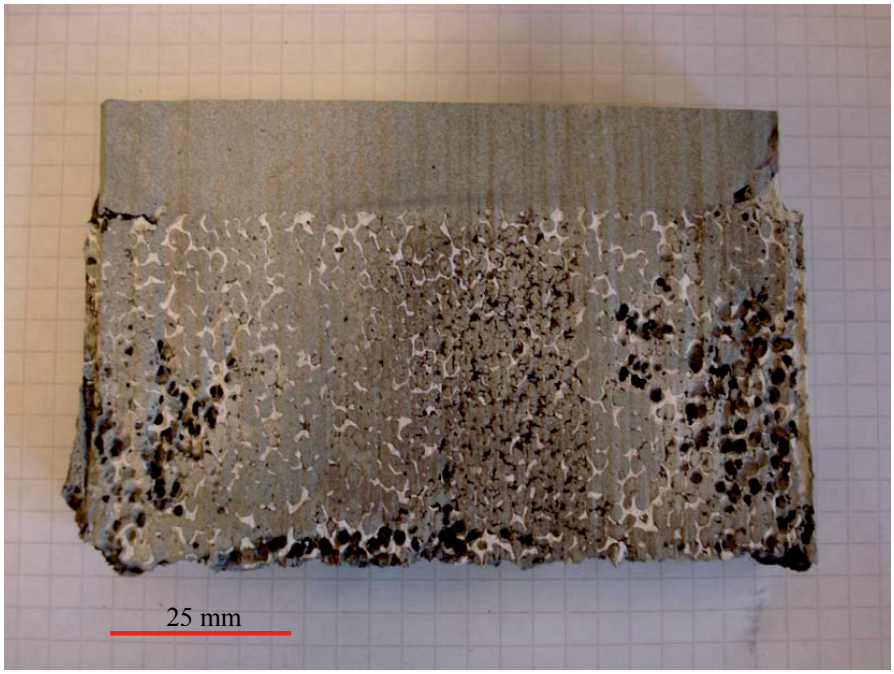

FIG. 4

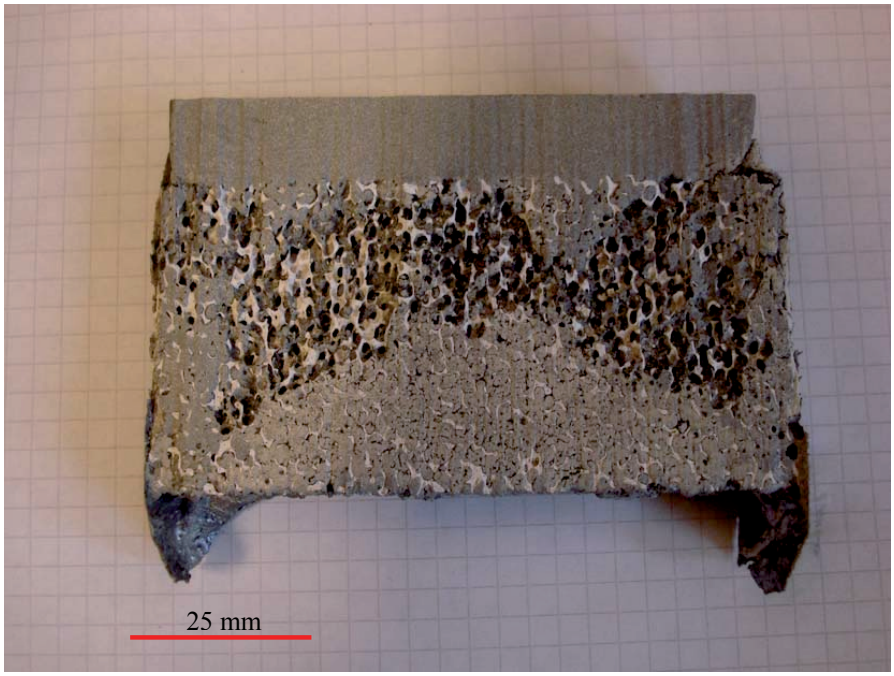

FIG. 5

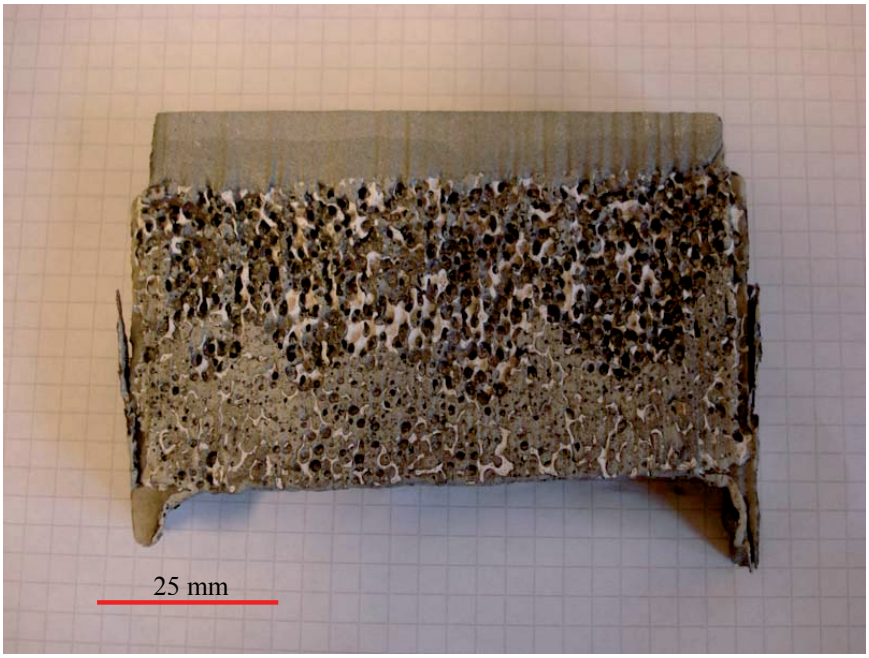
25 mm

FIG. 6

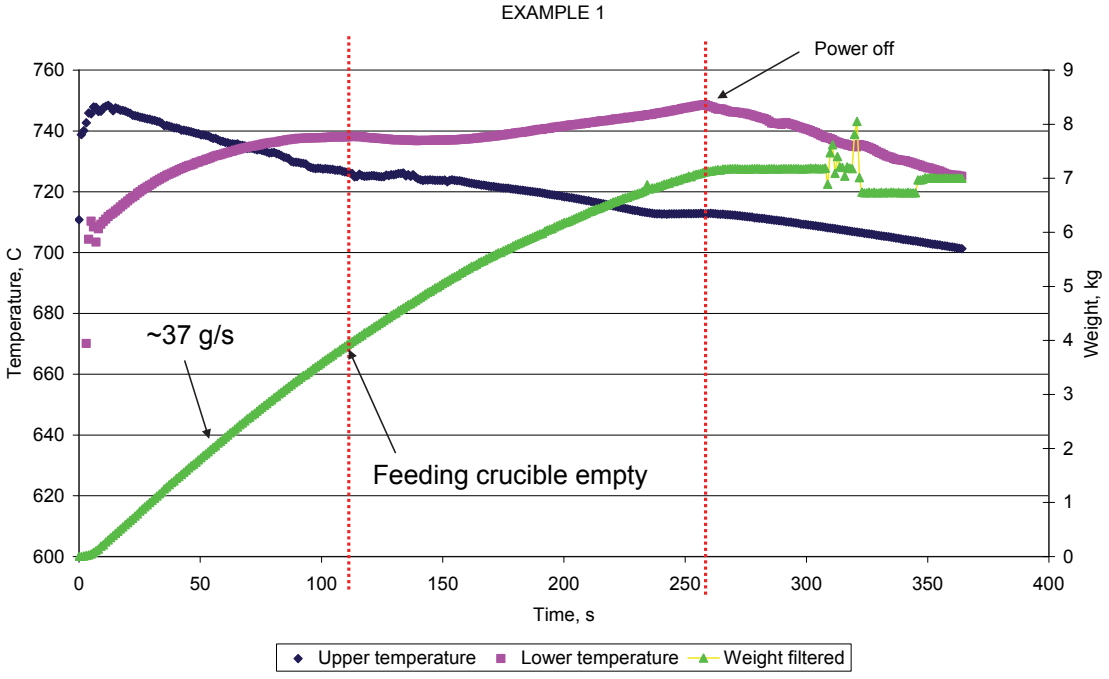
EXAMPLE 1
Power off
~37 g/s
Feeding crucible empty
Temperature, C
Weight, kg
Time, s
760
740
720
700
680
660
640
620
600
9
8
7
6
5
4
3
2
1
0
0
50
100
150
200
250
300
350
400
Upper temperature
Lower temperature
Weight filtered

FIG. 7

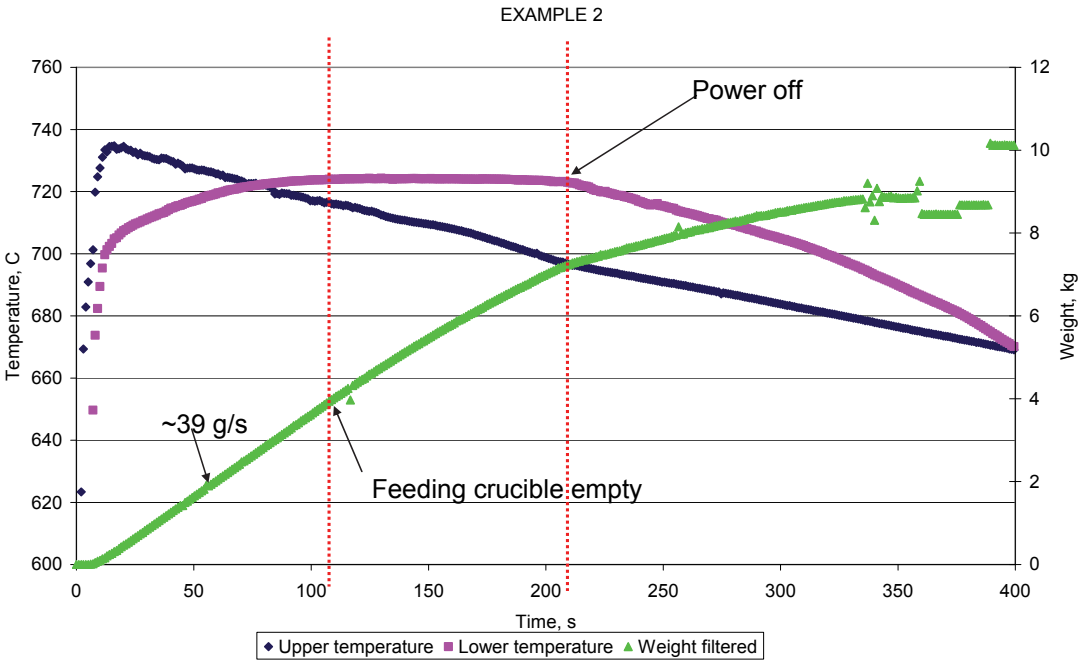
EXAMPLE 2
Power off
~39 g/s
Feeding crucible empty
Temperature, C
Weight, kg
Time, s
Upper temperature
Lower temperature
Weight filtered

FIG. 8

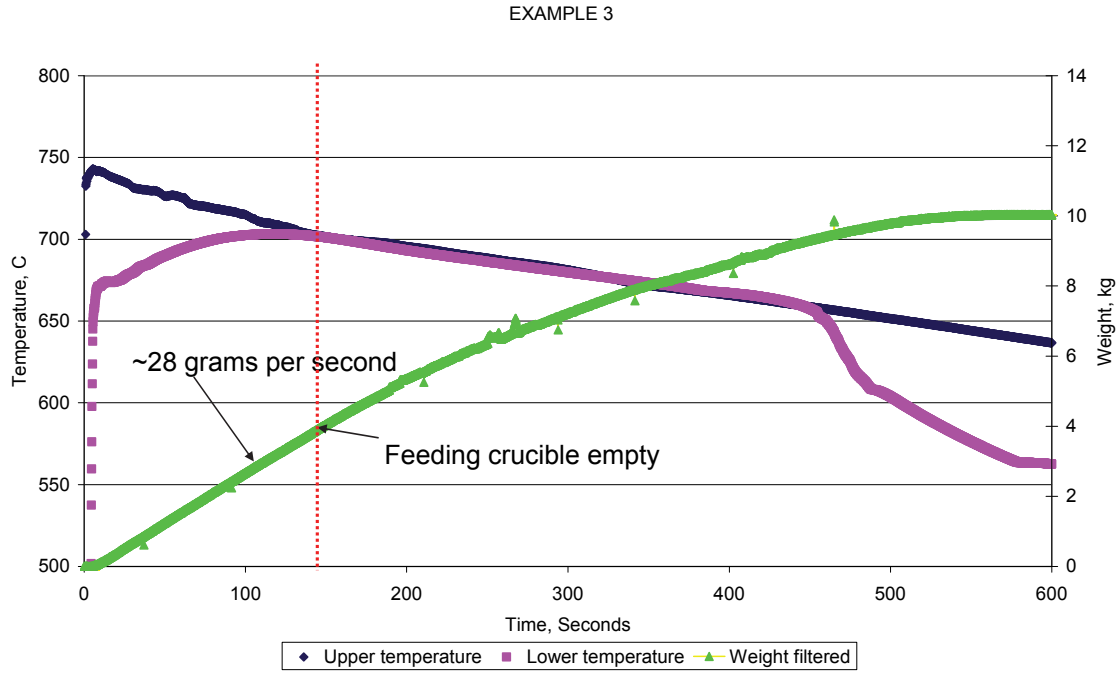
EXAMPLE 3
~28 grams per second
Feeding crucible empty
Temperature, C
Weight, kg
Time, Seconds
Upper temperature
Lower temperature
Weight filtered

FIG. 9

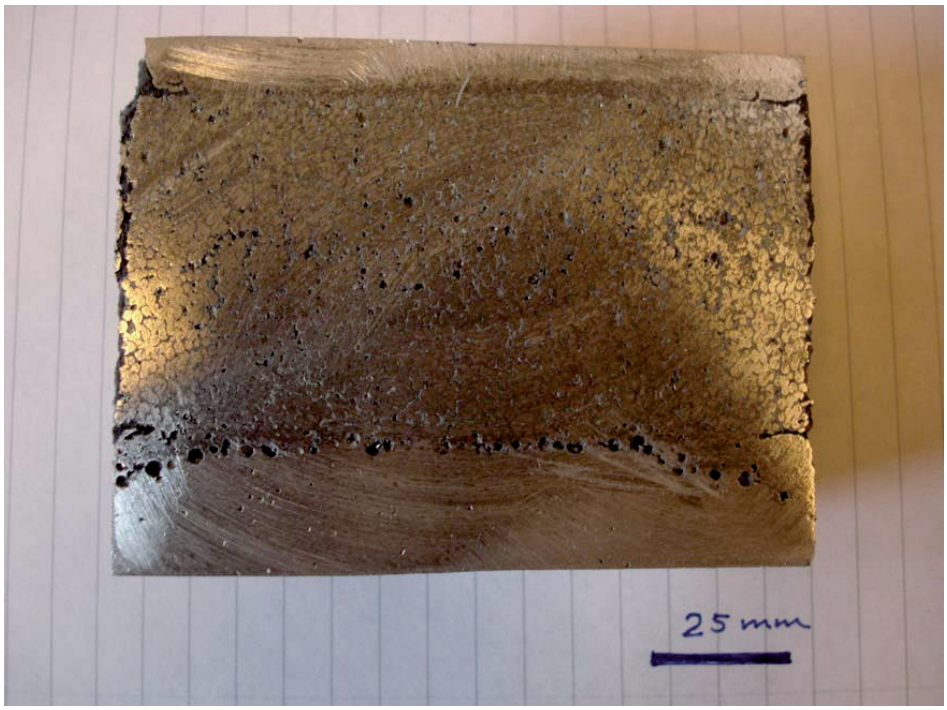

FIG. 10

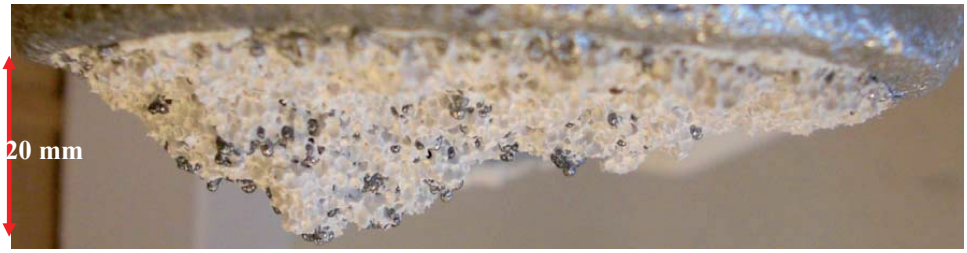

FIG. 11

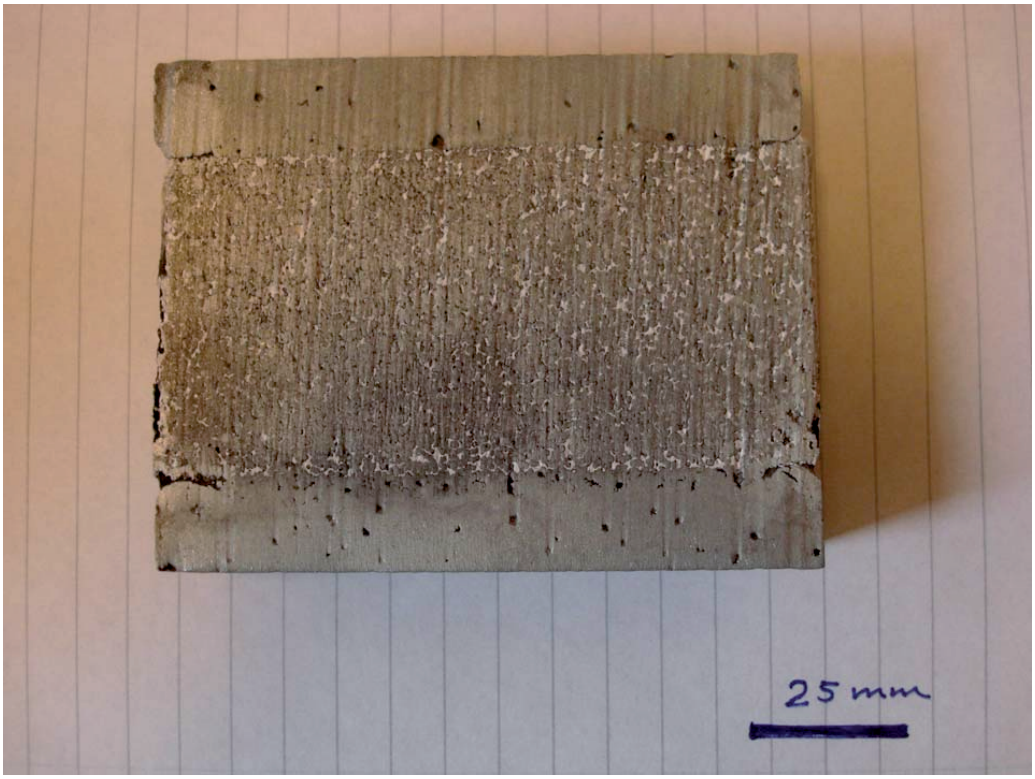

FIG. 12

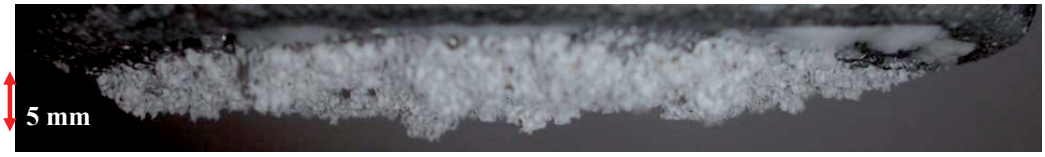

FIG. 13

APPENDIX 2

Glossary of Electrical Units, Symbols and Functions

Appendix 2 Table 1: Glossary of Electrical Units and Symbols

Quantity	Symbol	Scalar Quantity SI Unit	Abbr.
Arbitrary constants	*A, B or C*	undefined	N/A
Coil area	A_c	meter^2	m^2
Magnetic flux density	B	tesla	T
Differential flux density	δB	tesla	T
Water heat capacity	C_p	joules/gram/ kelvin	J/g/K
Differential length	δl	meter	m
Differential area	δs	meter^2	m^2
Insulation depth	d	meter	m
Diameter	D	meter	m
Electric field	E	volt/meter	V/m
Frequency	f	hertz	Hz
Magnetic field	H	ampere/meter	A/m
Current, RMS	I	ampere	A
Square root of -1	j	unitless	-
Current density	J	ampere/meter^2	A/m^2
Heat transfer coefficient	k	watts/meter /kelvin	W/m/k
Nagaoka short coil factor	k_N	unitless	-
Modified Nagaoka factor	k_N^*	unitless	-
Length	l	meter	m
Inductance	L	henry	H
Water flow	m_{water}	gram/second	g/s
Turns	N	unitless	-
Resistive heating	P	Watt, RMS	W
Power factor	$P.F.$	unitless	-
Imaginary or reactive power	Q	VAR, RMS	W
Radius	r	meter	m
Biot-Savart unit vector	$\hat{r}$	meter	m
Resistance	R	ohm	Ω
Northrup's 'coupling factor'	S	unitless	-
Time	t	seconds	s
Temperature	T	kelvin	K
Coil Shape Factor (D_{cs}/l_c)	u	unitless	-
Electric potential	V	volt	V
Dimensionless coil length	x	unitless	-
Reactance	X	ohm	Ω
Temperature coefficient of resistivity	α	kelvin^{-1}	K^{-1}
Electromagnetic penetration depth	δ	meter	m
Delta value (e.g. T_{out}-T_{in})	Δ	-	-
Permeability of vacuum	μ_0	henry/meter	H/m
Relative permeability	μ_r	unitless	-
Dimensionless penetration depth	ξ	unitless	-
Electric conductivity	σ	siemens/meter	S/m
Electric resistivity	ρ	ohm meter	Ω·m
Current-magnetic field cosine of phase shift	φ	unitless	-
Current-magnetic field sine of phase shift	Ψ	unitless	-
Magnetic flux	Φ	weber	Wb
Radial frequency ($2\pi f$)	ω	radians/s	rad/s

Appendix 2 Table 2: Glossary of Subscripts and Functions

Subscripts	Definition
air-gap	Location from the outside of the work piece to the inside diameter of the coil (vertical projection of round tubing).
ambient	Typical room temperature conditions
average Al	Average based measured values
cs	Current sheet
0	Centre line or standard value as in μ_0
c	Coil
calorific	Calorific value based on water
effective	magnitude which results in the correct inductance
electrical	Electrically derived value
loss	A loss to the environment
r	r-component
(r)	Function value at radius r
R	Outer radius of work piece
(R)	Function value at radius R
s	Surface
w	Work piece
with work piece	Work piece inserted in coil
without work piece	No work piece inserted in coil
wool	Values for insulating wool
z	z-component
∞	Designates infinite coil form
w	Work piece
Φ	Φ-component
_	Understroke = complex magnitude
→	Arrow over = vector quantity
*	Complex conjugate
Special Functions	**Definition**
ber	Kelvin function real part
bei	Kelvin function imaginary part
ber′	Derivative of ber
bei′	Derivative of bei
$K(k)$	Complete elliptical integral of the first kind
$E(k)$	Complete elliptical integral of the second kind
I_0	Modified zero order Kelvin Bessel functions of the first kind
K_0	Modified zero order Kelvin Bessel functions of the second kind
J_0	Zero order Bessel function of the first kind

PART I:
ELECTROMAGNETIC PHENOMENA

SUPPLEMENT 1

Review of Classical Design Methods as Applied to Aluminum Billet Heating with Induction Coils

Mark William Kennedy, Shahid Akhtar, Jon Arne Bakken, Ragnhild Elisabeth Aune

EPD Congress 2011:
John Wiley & Sons, ISBN 978-1-1180-3652-5, (2011), 707-722.

REVIEW OF CLASSICAL DESIGN METHODS AS APPLIED TO ALUMINUM BILLET HEATING WITH INDUCTION COILS

Mark William Kennedy[1], Shahid Akhtar[1], Jon Arne Bakken[1], Ragnhild E. Aune[1,2]

[1]Department of Materials Science and Engineering, Norwegian University of Science and Technology, N-7491 Trondheim,
NORWAY
[2]Department of Materials Science and Engineering, Royal Institute of Technology, 100 44 Stockholm,
SWEDEN
Communicating author: ragnhild.aune@ntnu.no

Keywords: Induction, heating, billet, short coil

Abstract

In the present study classical induction design tools are applied to the problem of heating non-magnetic metal billets, using 50 Hz AC. As an example of great practical industrial interest, the induction heating of aluminum billets is addressed specifically. The predicted work piece power is compared with the measured work piece power for a long and a short coil, using well established methods, such as those of Burch and Davis, introduced in 1926/28, Dwight and Bagai in 1935, Baker in 1944/57, Vaughan and Williamson in 1945, and by Tudbury in 1960. A calculation methodology based on a combination of the available tools is also introduced and discussed. The method has proven to give an error of <10% of the actual work piece power. An equation for Tudbury's work piece shortness correction factor is disclosed for the first time.

Introduction

Induction heating of metal billets is a practical problem, with a geometry suitable for solution using analytical methods. This paper will examine solutions related specifically to round work pieces in round coils, although the methods presented can be extended to other regular shapes of work pieces and coils[1]. The methods can also be extended to ferromagnetic materials with slight changes[2-3]. It is assumed that the coil and work piece have a consistent diameter over their entire length and that the work piece is at least as long as the coil. Correction factors can be derived for the cases where the work piece is shorter than the coil.

The study of induction heating by coils began in the late 19th century with theoreticians like Heaviside[4]. The work of Burch and Davis[5-7] in the 1920's greatly improved the theoretical understanding of induction applied to metallurgy. Many investigators in the 1930's-1950's: Dwight and Bagai[8], Baker[1-2, 9], Vaughan and Williamson[3, 10] and others[11-12] added to our understanding with clearer mathematics, solutions for specific applications, semi-empirical modifications and practical design tools. Much of the accumulated knowledge is available in books, such as Tudbury's practical text or Simpson's engineering guide from 1960[13-14]. Perhaps the best description and derivation of the theoretical and semi-empirical solutions can be found in Davies[15].

In coreless induction heating, a work piece is placed within an induction coil as shown in Figure 1. Both the work piece and coil can be of arbitrary shape and length. A cyclically varying voltage is impressed upon the coil, which creates a time varying current in the coil and a strong magnetic field along the axis. This varying magnetic field interacts with the work piece to induce circular voltage gradients and "eddy currents," which circulate around the axis of the coil, but in a direction opposite the coil's current, as shown in Figure 1. The circulation of the eddy currents, J (A/m^2) and the work piece's natural resistivity, ρ (ohm·m), combine to generate heat, P (W/m^3). The relationship between the coil current, the magnetic field strength, the induced voltages and currents, is complex and will be discussed in some detail. Due to the relative simplicity we will begin by discussing an empty or "air core" coil.

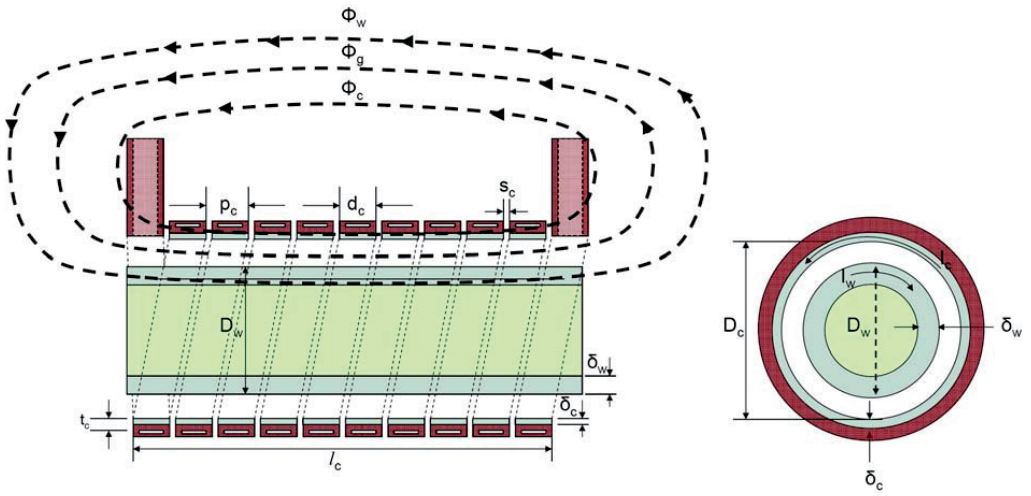

Figure 1. 10 turn induction coil, with billet slightly longer than coil

Derivation of Coil Impedance and Power Formulae

Let us begin by considering the coil shown in Figure 1. It has a length (ℓ_c) that can be measured in two ways: taking the centre-centre distance on the sides of the leads or top-bottom of the coil turns opposite the leads (as shown in Figure 1).

Imagine that the coil was constructed from a solid copper tube of length (ℓ_c). Let the thickness of the copper (t_c) be very small in comparison with the diameter of the cylinder (D_c). (N_c-1) grooves of thickness (s_c) are cut in a helical spiral along the whole length. This forms a long coil or solenoid, with a geometry approaching that of a theoretical "current sheet" with N_c turns as shown in Figure 2.

The coil pitch is equal to:

$$p_c = d_c + s_c \tag{1}$$

The coil space factor is the fraction of the side of the coil occupied by copper:

$$k_r = d_c N_c / \ell_c = d_c N_c / [(N_c - 1) s_c + d_c N_c] \text{ or for large } N_c,\ k_r \sim d_c/p_c \tag{2}$$

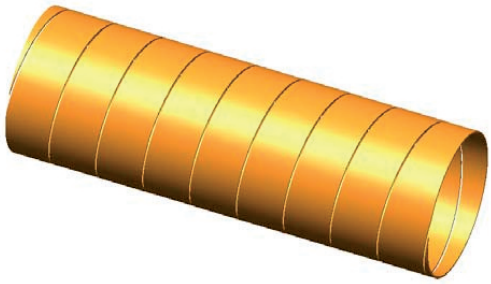

Figure 2. 10 turn helical "current sheet" coil or solenoid

The length of the "wire" in the coil, at the average current depth is:

$$\ell_{wire} = \pi (D_c + \delta_c) N_c \quad (3)$$

The height of each "wire" is:

$$d_c = \ell_c k_r / N_c \quad (4)$$

We now apply an alternating voltage (AC), at a frequency, which has an electromagnetic penetration depth (δ_c) of much less than the thickness of the conductor in the radial dimension, ($\delta_c << t_c$). Where the penetration depth is defined as the depth, which if filled with a homogeneous current (DC current) would yield the same resistance as the AC current distribution over the whole thickness of the conductor. At high frequency, current in a solenoid is biased towards the surface of the wire facing the interior of the coil and attenuates in an exponential manner with each penetration depth into the conductor.

The penetration depth can be calculated from the following commonly accepted formula[16-17]:

$$\delta_c = (2 \rho_c / (\omega \mu_r \mu_o))^{0.5} = (\rho_c / (\pi \mu_r \mu_o f))^{0.5} \quad (5)$$

Where: μ_o is the magnetic permeability of free space, ($4 \pi 10^{-7}$ H/m) and μ_r is the relative permeability for copper and aluminum, which is equal to 1.

The angular frequency is:

$$\omega = 2 \pi f \text{ (radians per second)} \quad (6)$$

Where: f is the frequency (Hz).

A modified penetration depth can be calculated accounting for the presence of the air gaps as derived by Howe[18] and with demonstrated accuracy according to the data of Vaughan and Williamson [10], using the k_r factor from Equation (2):

$$\delta_c = (2 \rho_c / (k_r \omega \mu_r \mu_o))^{0.5} = (\rho_c / (k_r \pi \mu_r \mu_o f))^{0.5} \quad (7)$$

The alternating current resistance of the coil can then be found using the simple formula:

$$R_c = \rho_c \ell_{wire} / a_{current} \quad (8)$$

Where the effective area of the current path for alternating current is:

$$a_{current} = d_c \delta_c = \delta_c \ell_c k_r / N_c \quad (9)$$

The resistivity of the copper is a function of temperature and composition as shown in Figure 3. Phosphorous deoxidized copper (with up to 0.04 wt% residual P) will have an actual conductivity of about 80% IACS (International Annealed Copper Standard of 1913[19]). 100% IACS is equivalent to a resistivity of 1.7241E-8 ohm·m at 20°C, with copper having a temperature coefficient of 0.00393[19-21].

Actual coil copper resistivity can be estimated by:

$$\rho_c = 1.7241E\text{-}8 \text{ ohm·m } (1+0.00393 (T_c - 20^oC)) \ 100 / \%IACS \quad (10)$$

We can now estimate using equations (1-10) the AC resistance of the coil to be:

$$R_c = \pi (D_c + \delta_c) N_c \rho_c / (\delta_c \ell_c / N_c) = \pi (D_c + \delta_c) N_c^2 \rho_c / (\delta_c \ell_c k_r) \quad (11)$$

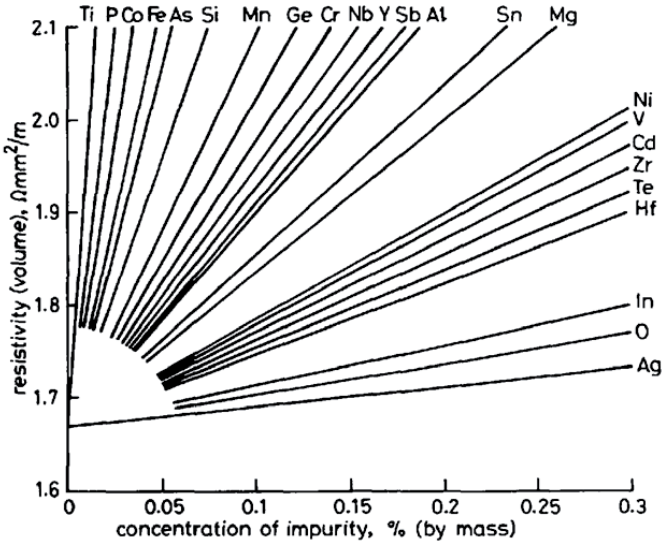

Figure 3. Approximate effect of impurities on the resistivity of copper[20]

Power lost from the coil to the cooling water can then be calculated from $P=I_c^2 R_c$, where I_c is the root mean square (R.M.S.) value:

$$P_c = I_c^2 \pi (D_c + \delta_c) N_c^2 \rho_c / (\delta_c \ell_c k_r) \quad (12)$$

If the electromagnetic penetration depth exceeds more than half the actual conductor thickness, as might occur at low frequency ($t_c > \delta_c > 0.5 t_c$), some small error will be encountered with equations (11-12). If the penetration depth is significantly greater than the thickness ($\delta_c > t_c$), the resistance can be accurately estimated using the total conducting area (equivalent to the DC resistance in this case) in Equation (8). Care must be taken to account for the loss of conducting area due to the cooling channel. In other cases, either an "exact" theoretical solution[18, 22-28] or empirical data[29] must be used. There is a tendency for the "exact" solutions to be in error for very short coils ($\ell_c/D_c < 1$), or

coils with large spaces between the turns (k_r<0.7). It is best if the coil can be designed such that (δ_c<0.5t_c), for low resistive losses and accurate design.

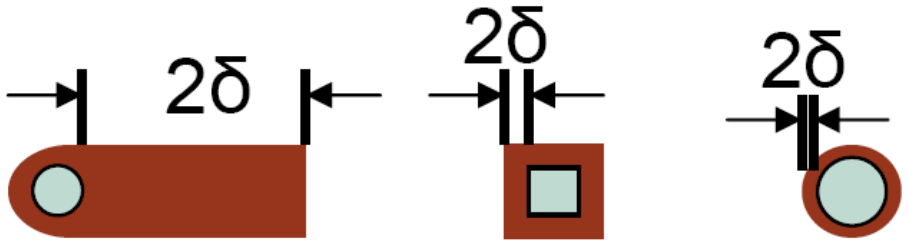

Figure 4. Examples of conductor shapes for mains frequencies (50-60 Hz), medium (500-5000 Hz), and high frequency furnaces, each with the recommended wall thickness of 2δ[30]

It is standard practice in induction furnace coil design to assume that the coil is magnetically thick (δ_c<0.5t_c). It is then assumed that the wire of the coil has an internal reactance equal to the resistance, which is the same as saying that the wire has an internal power factor of 0.707:

$$X_c = R_c \tag{13}$$

This is a dubious assumption except for very high ratios of thickness to penetration depth (δ_c<0.25t_c), but causes little error in the total estimation of reactive power. Errors are smallest at high frequency with thin conductors as shown in Figure 4.

Magnetic Field, Inductance and Impedance for Short and Long "Air Core" Coils

If we imagine that our coil is merely a section of length ℓ_c of an infinitely long coil, the magnetic flux density within the coil is independent of position in the coil. The magnetic flux density can then be estimated using either Amperè's or the Biot-Savart law to be:

$$B_\infty = \mu_o N_c I_c / \ell_c \tag{14}$$

This assumes negligible flux density outside of the coil (no reluctance in the external magnetic circuit), ignores end effects (there are no ends to an infinite coil) and assumes complete linking of all the flux with all the turns of the coil.

The inductance of the empty long coil ("air core" inductor) is then determined from the number of flux linkages per unit current:

$$L_\infty = A_c \mu_o N_c^2 / \ell_c = A_c N_c B_\infty / I_c \tag{15}$$

Where A_c is the area of the coil:

$$A_c = \pi (D_c+\delta_c)^2 / 4 \tag{16}$$

For round tubes or if $\delta_c \geq t_c$, the diameter at the centre line of the conductor should be used.

Induction furnace coils are nearly always "short coils", $\ell_c/(D_c+\delta_c)<8$, and are often very short $\ell_c/(D_c+\delta_c)<1$. There are fundamental differences between long and short coils. In the case of short coils, the assumptions of uniform internal and negligible external flux density are no longer correct. The short coil flux density is now a function of both length and radius [$B_{short}(\ell, r_c)$] and there now exists an external magnetic flux density near the coil, with a finite reluctance. The approximation that all the flux, links all the turns is also questionable.

In the case of short "air core" coils, exact solutions have been calculated for the "end effect" of a "current sheet" and a correction factor (k_N) tabulated by Nagaoka[31-32]. The short coil inductance can then be calculated by:

$$L_0 = k_N A_c \mu_o N^2_c / \ell_c = k_N A_c N_c B_\infty / I_c \quad (17)$$

Equation (17) is the equivalent to saying that the actual flux density (integrated by length and radius) of the short coil in the axial direction is:

$$B_0 = k_N B_\infty = k_N \mu_o H_\infty = k_N \mu_o N_c I_c / \ell_c \quad (18)$$

The Nagaoka factor has been plotted in Figure 5. Alternatively, an empirical equation like that of Wheeler[33], can be used to estimate coil inductance for a short coil. Wheeler's equation has been reformulated by Knight[34] to give the Nagaoka coefficient directly:

$$k_N = 1/[1 + 0.4502 (D_c + \delta_c) / \ell_c)] \quad (20)$$

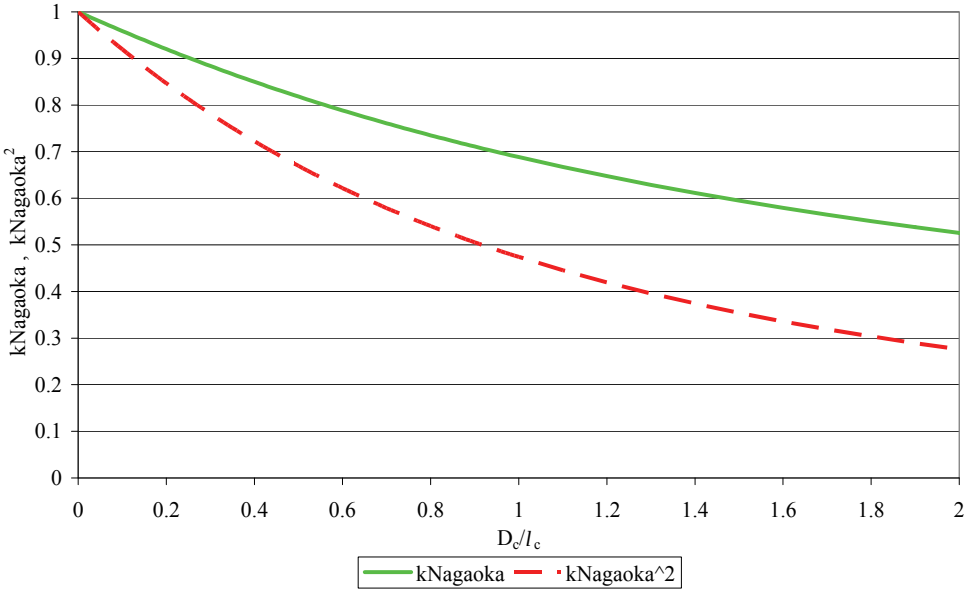

Figure 5. Nagaoka's short coil correction factor

If round tubing is used, it is necessary to apply a round wire correction such as Rosa's[32] to the calculated inductance.

Once the inductance of the short coil has been obtained, it is then simple to estimate the inductive reactance (X_0), the total coil impedance (Z_0) and voltage drop (V_0) for the "air core" coil:

$$X_0 = \omega L_0 = 2 \pi f L_0 \tag{21}$$

$$Z_0 = (R_c^2 + X_0^2)^{0.5} \tag{22}$$

$$V_0 = I_0 Z_0 \tag{23}$$

Impact of the Work Piece on the Magnetic Field

In the presence of a work piece, we can see from Figure 1, that the total magnetic flux can be divided into 3 parts: flux which links only with the coil (Φ_c), flux in the air gap (Φ_g) and the net flux that links the billet (Φ_w). These fluxes in turn produce equivalent inductances and reactive impedances: X_c, X_g and X_w', as indicated in the simplified series circuit diagram, Figure 6.

Several things happen to the magnetic field when a work piece is placed into the coil:

1. The "aperture" of the coil is effectively reduced, making the effective diameter to length ratio look smaller, changing the magnitude of the short coil correction factor k_N and the flux density in the air gap along the axial direction of the coil.
2. Space that was formerly air is occupied by the work piece, reducing the total air gap flux.
3. Eddy currents in the billet produce magnetic fields, which oppose the magnetic field of the coil, reducing the net flux in the space occupied by the billet.

Vaughan and Williamson proposed an empirical modification to the short coil correction factor based on the volumetric fraction of the air-gap occupied by the work piece. Their proposed correction factor is applied to the Nagaoka coefficient to produce an "effective Nagaoka coefficient" for a short coil containing a work piece:

$$k_N^* = k_N (1 - [D_w / D_c]^2) + [D_w / D_c]^2 \tag{24}$$

To be consistent with the previous formulae:

$$k_N^* = k_N (1 - [D_w / (D_c + \delta_c)]^2) + [D_w / (D_c + \delta_c)]^2 \tag{25}$$

The effective magnetic flux density in the air gap of a short coil containing a work piece can then be calculated by:

$$B_0^* = k_N^* \mu_o H_\infty = k_N^* \mu_o N_c I_c / \ell_c \tag{26}$$

It is assumed that this magnetic flux density is constant over the width of the air gap, and that it is this flux density, which induces the eddy currents in the work piece.

The contribution of the air gap to the total inductive impedance of the circuit is:

$$X_g = \omega L_g = 2 \pi f A_g N_c B_0^* / I_c = k_N^* \mu_o N_c^2 \pi^2 (D_c^2 - D_w^2) / 2 \ell_c \tag{27}$$

Derivation of Work Piece Impedance and Power Formulae

It is difficult to make electrical measurement in the work piece. The effect of the work piece on the circuit is normally inferred from electrical changes in the coil, with and without a work piece. As a first approximation it can be assumed that the resistance and reactance of the coil are not affected by the work piece and all measured electrical changes can be attributed to the work piece and changed air gap.

One approach to the mathematics is to consider the magnetic and electrical circuits to be a series circuit as shown in Figure 6, for a "long coil". The picture is similar, but more complex for a "short coil" if the reluctance of the external magnetic circuit is to be accounted for explicitly[1].

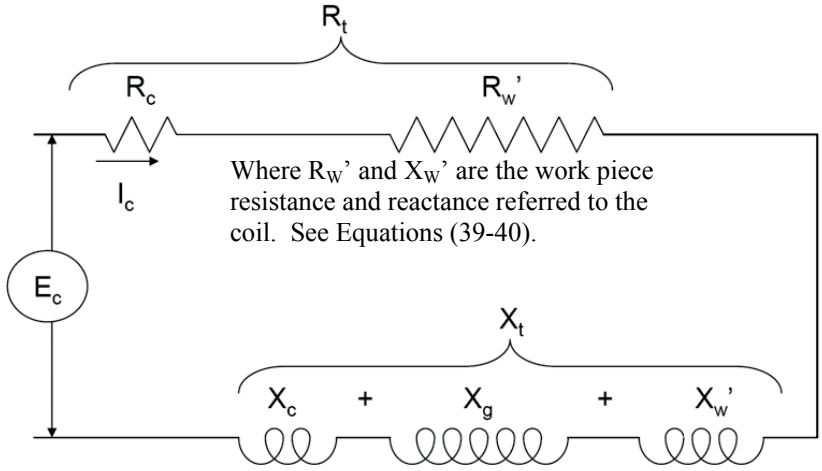

Figure 6. Series equivalent circuit for an induction furnace coil and work piece

When alternating current is applied, the coil and work piece become inductively coupled in a similar way to the windings of a transformer over the length shared by the coil and work piece. The magnetic flux density produced in the air gap by the coil, is the same flux density, which induces eddy currents at the surface of the work piece:

$$B_w = B_0^* = \mu_o \mu_r N_w I_w / \ell_w = k_N^* \mu_o N_c I_c / \ell_c \tag{28}$$

If $\ell_w \geq \ell_c$ take $\ell_w = \ell_c$, i.e. it is assumed that only the length of work piece within the coil interacts with the magnetic field of the coil. In the following derivations we take $\ell_w \geq \ell_c$ and substitute ℓ_c in the place of ℓ_w.

$$N_w I_w = k_N^* N_c I_c (\ell_c / \ell_c) = k_N^* N_c I_c \tag{29}$$

The eddy currents induced in the billet are assumed to make a single turn (N_w=1), while the current in the coil makes N_c turns. It is standard practice to refer conditions in the work piece back to the coil (where we measure the voltage, current, resistance and impedance of the total circuit) via the standard transformer relationship:

$$I_w = k_N^* N_c I_c / 1 = k_N^* N_c I_c \tag{30}$$

By analogy to Equation (11), with N_w=1, k_r=1 (as the work piece has no "air gaps") and the average diameter is **reduced** by the penetration depth:

$$R_w = \pi (D_w - \delta_w) N_w \rho_w / (\delta_w \ell_c / N_w) = \pi (D_w - \delta_w) \rho_w / (\delta_w \ell_c) \quad (31)$$

Where δ_w can be calculated using Equation (5) substituting work piece (w) for coil (c) values.
If the work piece is shorter than the coil, the calculated resistance must be corrected by multiplying by the ratio (ℓ_w / ℓ_c).

Using Equations (30-31), the power in the work piece is then:

$$P_w = I_w^2 R_w = k_N^{*2} (I_c N_c)^2 R_w = k_N^{*2} (I_c N_c)^2 \pi (D_w - \delta_w) \rho_w / (\delta_w \ell_c) \quad (32)$$

Equation (32) is sufficiently accurate (about 1% error) provided that ξ_w>3:

$$\xi_w = D_w / (\delta_w \sqrt{2}) \quad (33)$$

ξ_w as mentioned above is a very important dimensionless parameter in induction heating theory, and can be found in many different forms in various publications.

The actual resistance in the work piece can be "reflected" back onto the coil via:

$$R_w' = R_w N_c^2 \quad (34)$$

and added to the coil resistance, to give the total circuit resistance as indicated in Figure 6:

$$R_t = R_w' + R_c \quad (35)$$

Higher mathematical precision requires the exact solution to the field equations using complex numbers and involves use of (computationally challenging) Bessel functions[4, 6, 8]:

$$R_w' = [\pi N_c^2 D_w \rho_w / (\delta_w \ell_c)] \sqrt{2} (ber\xi_w ber'\xi_w + bei\xi_w bei'\xi_w) / [ber^2(\xi_w) + bei^2(\xi_w)] \quad (36)$$

Substituting Equation (33) in (36):

$$R_w' = (\sqrt{2} \pi N_c^2 \rho_w \xi_w / \ell_c) \sqrt{2} (ber\xi_w ber'\xi_w + bei\xi_w bei'\xi_w) / [ber^2(\xi_w) + bei^2(\xi_w)] \quad (37)$$

Defining $\varphi(\xi_w)$:

$$\varphi(\xi_w) = \sqrt{2} (ber\xi_w ber'\xi_w + bei\xi_w bei'\xi_w) / [ber^2(\xi_w) + bei^2(\xi_w)] \quad (38)$$

Substituting $\varphi(\xi_w)$ in (37):

$$R_w' = \sqrt{2} \pi N_c^2 \rho_w \xi_w \varphi(\xi_w) / \ell_c \quad (39)$$

Similar solutions exist for the inductive reactance of the work piece[4, 6, 8]:

$$X_w' = \sqrt{2} \pi N_c^2 \rho_w \xi_w \psi(\xi_w) / \ell_c \quad (40)$$

Where $\psi(\xi_w)$ is defined as:

$$\psi(\xi_w) = \sqrt{2}\,(\mathrm{ber}\xi_w\ \mathrm{bei}'\xi_w - \mathrm{bei}\xi_w\ \mathrm{ber}'\xi_w) / [\mathrm{ber}^2(\xi_w) + \mathrm{bei}^2(\xi_w)] \quad (41)$$

Substituting Equations (39) and (34) into Equation (32) for the power developed in the work piece:

$$P_w = k_N^{*2}\ \sqrt{2}\,\pi\,(I_c\ N_c)^2\ \rho_w\ \ \xi_w\ \varphi(\xi_w) / \ell_c \quad (42)$$

And similarly for the reactive power of the work piece:

$$Q_w = k_N^{*2}\ \sqrt{2}\,\pi\,(I_c\ N_c)^2\ \rho_w\ \ \xi_w\ \psi(\xi_w) / \ell_c \quad (43)$$

$\varphi(\xi_w)$ and $\psi(\xi_w)$ are plotted in Figure 7 versus ξ_w for use with Equations (42-43). Baker presents the equations in slightly different format, using his functions P and Q, which are similar solutions for the real and imaginary parts of the Bessel functions[1]. Excellent derivations of Baker's P and Q can be found in the literature[14-15].

The power factor of the work piece can be calculated by:

$$\text{P.F.} = \varphi(\xi_w) / [\varphi(\xi_w)^2 + \psi(\xi_w)^2]^{0.5} \quad (44)$$

and becomes close to constant for $\xi_w > 3$, converging slowly towards 0.707 or $\sqrt{2}/2$, for very high ξ_w.

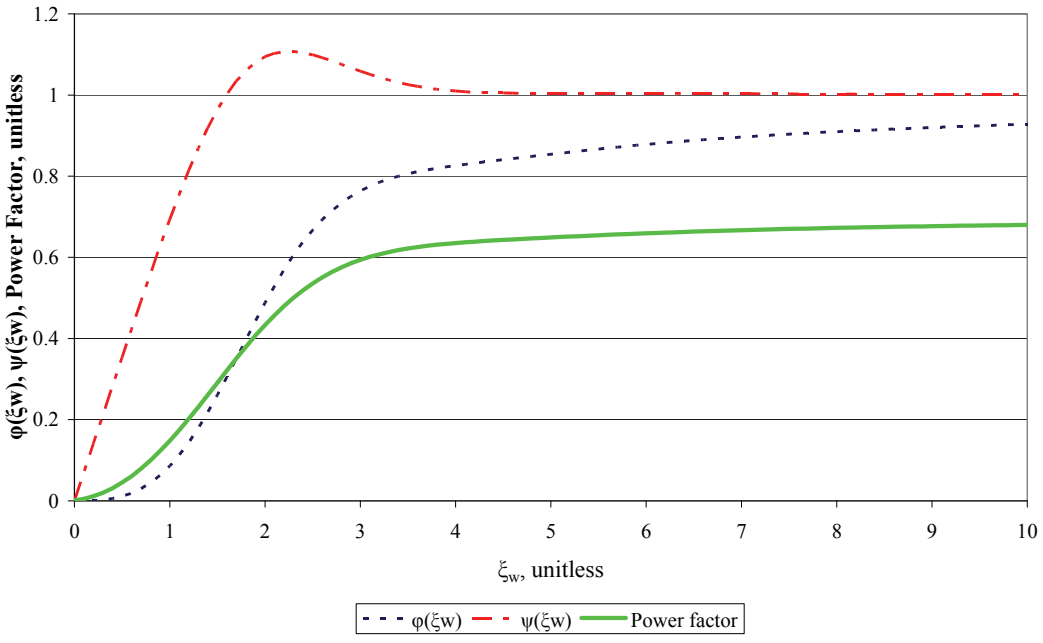

Figure 7. Resistance and Reactive factors for use with Equations (42-43).

Work Piece Shortness Correction Factor

As the length of a coil increases for a fixed diameter, the Nagaoka coefficient and the modified coefficients k_N^* and k_N^{*2} approach unity and the ratio of the coil diameter to length (D_c/ℓ_c) approaches zero at the limit. As the diameter of the work piece is reduced with a constant coil diameter, the coil increasingly looks like an "air core" coil, and at the limit of D_w/D_c going to zero, $k_N^{*2} = k_N^2$.

The modified Nagaoka coefficient squared (k_N^{*2}) of Vaughan and Williamson[10], is plotted in Figure 8. If this figure is compared with the original graph in the book by Tudbury[13], it is clear that they are identical and that the equation fits the logical tests given above. See Figure 5 for the comparison of k_N^2 with the intercepts on Figure 7 (limit of the "air core"). Tudbury's original book must be referenced, as later reproductions are not drawn accurately[35].

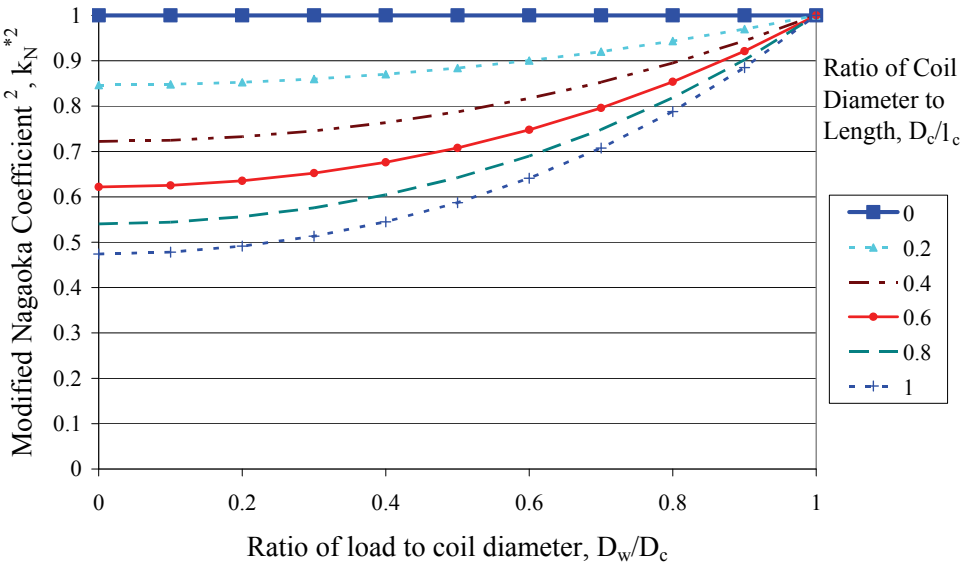

Figure 9. Tudbury's Work Piece Shortness Factor and Vaughan and Williamson's modified Nagaoka Coefficient^2[10, 13]

Results and Discussion

Experiments were conducted using a number of aluminum billets of different sizes and compositions, using two different coils as indicated in Table I. Billet electrical conductivities were estimated by simultaneously minimizing the error from Equation (42) and Baker's method, while ensuring the conductivity fell within the range of published specifications for each alloy. Coils were constructed using thin wall tubing for convenience (as power efficiency was not an issue), where the AC resistance was identical with the DC resistance ($\delta_c > d_c > t_c$). This eliminated the need to have capacitor banks and reduced the impact of harmonics on the measurements. Copper tubing conductivity was ~80% IACS. Measurements were taken with a Fluke 43B Power Quality Analyzer, equipped with a calibrated Fluke i1000s current probe with an accuracy of 1%.

Work pieces were cooled to below room temperature (~10°C) and then readings were taken before they heated beyond 30°C, such that 20°C was a typical temperature to evaluate the resistivity. Ideally the work pieces would have been drilled through, cooled with water to achieve isothermal conditions and the heat input determined calorimetrically; however, in the case of the magnetically thin work pieces (2 and 3) this would have created significant measurement errors. A non-metallic water jacket would be a possible option for cooling without influencing the electromagnetic properties of the work piece.

Table I. Work pieces and coils used in billet heating experiments

Work Pieces:	1	2	3	4	5
Alloy:	A356	6053	6053	6082	7108
Diameter, mm	76.8	38.6	50.5	95.3	95.4
Length, mm	192	356	1078	258	201/340
Resistivity (ohm m) at 20 C:	4.01E-08	4.11E-08	4.11E-08	3.59E-08	3.92E-08
IACS conductivity, %	43	42	42	48	44
Penetration depth (mm) at 50 Hz:	14.25	14.42	14.42	13.49	14.09
ξ_w:	3.810	1.893	2.476	4.996	4.788
$\varphi(\xi_w)$:	0.819	0.397	0.638	0.852	0.846
$\psi(\xi_w)$:	1.014	1.060	1.104	1.004	1.004
Coil 1	X	X	X	X	X
Coil 2			X	X	X

Coils:	Coil 1	Coil 2
Inside diameter, mm	126	118
Average diameter, mm	132	124
Height, mm	111	300
Coil tube diameter, mm	6	6.35
Coil tube thickness, mm	1.00	0.762
Number of turns	16.5	41
"Aircore" inductance, μH	27.6	71.7
Nagaoka coefficient, Equation (20), k_N:	0.653	0.843
Resistance at maximum load, ohms	0.0108	0.0319
Avg. temperature at maximum load, Deg C:	43	62
Modified Nagaoka coefficient for load 1, k_N^*:	0.771	
Modified Nagaoka coefficient for load 2, k_N^*:	0.683	
Modified Nagaoka coefficient for load 3, k_N^*:	0.704	0.869
Modified Nagaoka coefficient for load 4, k_N^*:	0.835	0.935
Modified Nagaoka coefficient for load 5, k_N^*:	0.836	0.935

Table II. Electrical measurements, coils 1 and 2 with work pieces 1-5

Load Number	V	A	kVA	kW	kVAR	Power Factor
1-1	13.14	969	12.7	10.7	7.0	0.84
1-1	14.84	1079	16.0	13.5	8.7	0.84
1-2	13.13	953	12.5	9.8	7.8	0.78
1-2	14.81	1067	15.8	12.5	9.7	0.79
1-3	13.14	954	12.5	10.0	7.6	0.79
1-3	14.81	1067	15.8	12.7	9.5	0.80
1-4	13.13	999	13.1	11.6	6.1	0.88
1-4	14.85	1110	16.5	14.6	7.6	0.89
1-5	13.13	985	13.0	11.4	6.2	0.88
1-5	14.86	1095	16.3	14.4	7.7	0.89
2-3	27.60	703	19.5	16.4	10.5	0.84
2-4	27.58	729	20.1	18.5	7.6	0.93
2-5	27.58	721	19.9	18.5	7.4	0.93

Work piece power has been determined by subtracting the coil power from the power of the work piece and coil and attributing all resistive changes to the work piece. Where multiple readings had been taken, averages are shown in Tables II and III. Measured coil power has been compared to predictions using equations (32) and (42) and against various methods published in the literature[1, 6, 8]. The methods of Vaughan and Williamson[10] and Tudbury[13], utilizing the modified Nagaoka coefficient, will give essentially the same results as Equation (42). Short coil methods of Baker[1] and Burch and Davis[6] and the long coil method of Dwight and Bagai[8], are shown in Table III for comparison.

Table III. Comparison of real and calculated work piece power by various methods

Load Number	Measured Power, W	Equation (32)	Equation (42)	Baker Short Coil	Burch and Davis	Dwight and Bagai
1-1	692	754	759	577	821	1275
1-1	899	936	942	716	1013	1583
1-2	138	224	142	125	271	305
1-2	177	281	178	157	340	382
1-3	325	356	318	266	517	641
1-3	377	445	398	333	647	802
1-4	990	1165	1155	862	945	1656
1-4	1264	1438	1426	1064	1167	2045
1-5	1086	1176	1168	866	962	1673
1-5	1422	1454	1443	1070	1188	2067
2-3	640	674	602	569	740	798
2-4	1553	1533	1520	1591	1402	1738
2-5	1923	1810	1797	1627	1657	2054
Error	+/-~2%	16.6	6.0	14.6	33.0	67.6

It can be seen in Table III, that Equation (42) produces the best results in comparison with the measured data, with a typical error of 6% and a maximum error of 16%. Except for work piece number 2 with $\xi_w<3$, Equation (32) gave comparable results with those of Equation (42).

Coil 1 had a length/diameter ratio of 0.84 using the average diameter. While coil 2 had a ratio of 2.42, i.e. coil 2 was relatively long, while coil 1 was quite short. It can be seen in Table III that the use of the modified Nagaoka coefficient gave an excellent correction for coil shortness, such that the calculation errors are comparable for both coils using equations (32) and (42). Baker's method gives reasonable, but less accurate results for all work pieces and coils. Burch and Davis' short coil correction does not work well for small D_w/D_c (work pieces 2 and 3). Dwight and Bagai's long coil method is of course only suitable for the "long" coil number 2.

Please note that for coil 2, work piece 4 was shorter than the coil and that the suggested correction factor of Baker[1] was applied to all methods, i.e. the calculated resistance of the work piece, e.g. Equation (31), was multiplied by the ratio of the length of the work piece/length of the coil (ℓ_w/ℓ_c). This is a direct consequence of Equation (28).

Conclusions

A method has been described using a modified Nagaoka coefficient, capable of estimating work piece power to better than 10% accuracy, for long and short coils, including cases where the work piece is shorter than the coil. Tudbury's work piece shortness factor has been found to be the square of the modified Nagaoka coefficient as proposed by Vaughan and Williamson in 1945. Given that the presence of a work piece has now been shown to change the magnetic field inside the air gap of a short coil significantly, the assumption that the impedance of the coil does not change due to the presence of the work piece can be questioned. It would be of value to directly measure electrical conditions in the work piece, e.g. circular voltage gradients, in order to separate the effect of the coil on the work piece and the work piece on the coil.

Acknowledgements

The authors wish to express their gratitude to Egil Torsetnes at NTNU, Trondheim, Norway, for helping with the design and construction of the experimental apparatus. Deepest gratitude is also due to Kurt Sandaunet at Sintef, Trondheim, Norway, for the use of the Sintef laboratory and his contribution in the execution of the experiments. Special thanks to Liss Pedersen at Alcoa, Lista, Norway, for the supply of filter materials. The author would also like to acknowledge the funding from the Norwegian Research Council through the RIRA project.

References

1. R. Baker, "Design and calculation of induction heating coils'," *AIEE Trans,* 57, (1957), 31-40.
2. R. Baker, "Induction Heating of Moving Magnetic Strip," *American Institute of Electrical Engineers, Transactions of the,* 64, (1945), 184-189.
3. J. Vaughan and J. Williamson, "Design of Induction Heating Coils for Cylindrical Magnetic Loads," *American Institute of Electrical Engineers, Transactions of the,* 65, (1946), 887-892.
4. O. Heaviside, *Electrical Papers*. (London: Macmillan & Co., 1892), 353-416.
5. C. Burch and N. Davis, "LXX. On the quantitative theory of induction heating," *Philosophical Magazine Series 7,* 1, (1926), 768-783.
6. C. Burch and N. Davis, *An introduction to the theory of eddy-current heating*. (London: E. Benn Limited, 1928).
7. C. Burch and N. Ryland Davis, "Über eisenlose Induktionsöfen," *Electrical Engineering (Archiv fur Elektrotechnik),* 20, (1928), 211-223.
8. H. Dwight and M. Bagai, "Calculations for coreless induction furnaces," *American Institute of Electrical Engineers, Transactions of the,* 54, (1935), 312-315.
9. R. Baker, "Heating of Nonmagnetic Electric Conductors by Magnetic Induction---Longitudinal Flux," *American Institute of Electrical Engineers, Transactions of the,* 63, (1944), 273-278.
10. J. Vaughan and J. Williamson, "Design of Induction-Heating Coils for Cylindrical Nonmagnetic Loads," *American Institute of Electrical Engineers, Transactions of the,* 64, (1945), 587-592.
11. H. Storm, "Surface Heating by Induction," *American Institute of Electrical Engineers, Transactions of the,* 63, (1944), 749-755.
12. N. Stansel, "Induction Heating---Selection of Frequency," *American Institute of Electrical Engineers, Transactions of the,* 63, (1944), 755-759.
13. C. Tudbury, *Basics of Induction Heating Vol. 1*, (New York: John F. Rider, 1960).
14. P. Simpson, *Induction heating: coil and system design*. (New York, Toronto, London: McGraw-Hill, 1960).
15. E. J. Davies, *Conduction and induction heating*. (London: Peter Peregrinus on behalf of the Institution of Electrical Engineers, 1990).
16. L. Kelvin, *Mathematical Papers, Vol. 3*,(London: Cambridge University Press, 1890), 484-515.
17. O. Heaviside, *Electrical Papers*, *Vol. 2*, (London: Macmillan & Co., 1892), 396-424.
18. G. Howe, "The high-frequency resistance of wires and coils," *Electrical Engineers, Journal of the Institution of,* 58, (1920), 152-162.
19. *Copper Wire Tables Circular No. 31*: US Bureau of Standards, 1913).
20. V. Callcut, "Coppers for electrical purposes," *IEE Proceedings A Physical Science, Measurement and Instrumentation, Management and Education, Reviews,* 133, (1986), 174-201.
21. H. Coppers, "Copper Development Association," Orchard House, Mutton Lane, Potters Bar, Herts EN6 3AP, (1990).
22. C. Hickman, "Alternating-Current Resistance and Inductance of Single Layer Coils," *Scientific Papers of the Bureau of Standards*, *No. 472*, (1923), 73-105.
23. S. Butterworth, "Eddy-current losses in cylindrical conductors, with special applications to the alternating current resistances of short coils," *Philosophical Transactions of the Royal Society of London. Series A, Containing Papers of a Mathematical or Physical Character,* 222, (1922), 57-100.
24. S. Butterworth, "Note on the Alternating Current Resistance of Single Layer Coils," *Physical Review,* 23, (1924), 752-755.
25. S. Butterworth, "On the alternating current resistance of solenoidal coils," *Proceedings of the Royal Society of London. Series A,* 107, (1925), 693.
26. A. Arnold, "The resistance of round-wire single-layer inductance coils," *Proceedings of the IEE-Part IV: Institution Monographs,* 98, (1951), 94-100.

27. A. Reatti and M. Kazimierczuk, "Comparison of various methods for calculating the AC resistance ofinductors," *IEEE Transactions on Magnetics,* 38, (2002), 1512-1518.
28. E. Fraga*, et al.*, "Practical model and calculation of AC resistance of long solenoids," *IEEE Transactions on Magnetics,* 34, (1998), 205-212.
29. R. Medhurst, "High Frequency Resistance and Self-Capacitance of Single-Layer Solenoids," ed. Wireless Engineer: February, (1947), 35-43.
30. O. Todnem, "Induksjonsoppvarming, Industriell Elektrovarme," ed: NTNU, 1992, 1-60.
31. H. Nagaoka, "The inductance coefficients of solenoids," *Journal of the College of Science,* 27, (1909), 18-33.
32. E. B. Rosa and F. Grover, "Formulas and Tables for the Calculation of Mutual and Self Induction," *Scientific Papers of the Bureau of Standards,* No. 169., (1916), 5-231.
33. H. Wheeler, "Simple inductance formulas for radio coils," *Proceedings of the IRE,* 16, (1928), 1398-1400.
34. D. Knight. (2010, August 25). *3.1. Solenoids: Part 1.*, http://www.g3ynh.info/zdocs/magnetics/part_1.html
35. S. Zinn and S. Semiatin, *Elements of induction heating: design, control, and applications*: Asm Intl, 1988), 22.

SUPPLEMENT 2

Analytical and Experimental Validation of Electromagnetic Simulations Using COMSOL®, re Inductance, Induction Heating and Magnetic Fields

Mark William Kennedy, Shahid Akhtar, Jon Arne Bakken, Ragnhild Elisabeth Aune

COMSOL Conference 2011 - Proceedings CD:
COMSOL, Burlington, MA, USA, ISBN 978-0-9839688-0-1, (2011), 1-9.

Analytical and Experimental Validation of Electromagnetic Simulations Using COMSOL®, re Inductance, Induction Heating and Magnetic Fields

Mark W. Kennedy[1], Shahid Akhtar[1], Jon Arne Bakken[1] and Ragnhild E. Aune[1,2]
[1]Dept. of Materials Science and Engineering, Norwegian University of Science and Technology (NTNU),
N-7491 Trondheim, NORWAY
[2]Dept. of Materials Science and Engineering, Royal Institute of Technology (KTH),
S-100 44 Stockholm, SWEDEN

Communicating author: mark.kennedy@ntnu.material.no

Abstract: COMSOL® is a powerful numerical modelling tool for electromagnetic calculations. The present paper examines the numerical agreement between COMSOL® 2D axial symmetric models, classical analytical solutions and experimental data. Comparison is made between the analytical solution for the inductance of an empty 'current sheet' inductor and the numerical results of COMSOL® Version 4.2, as a benchmark of the fundamental accuracy of the software. The effect of the size of the computational space or 'magnetic domain' on the calculated total inductance is also examined.

COMSOL®'s single and multi-turn domains are used to model an induction coil, and the simulations of induction heating are made at a range of frequencies from 50 Hz to 500 kHz. Results are compared with the predictions of a 1D analytical model at each frequency and a representative experimental value at 50 Hz. The obtained COMSOL® predictions of the magnetic flux density are compared with experimental values measured using Hall probes at 50 Hz, for both an empty coil and for a coil containing a work piece. The numerical magnetic field results obtained in the present study are in excellent agreement with the analytical solution for the 'air core' coil.

Based on the present results analytical criteria are presented as guidelines for when to use COMSOL®'s single or multi-turn domains, and for the minimum mesh size to be used to achieve accurate high frequency simulations of induction processes.

Keywords: Induction, inductance, heating, magnetic field.

1. Introduction

Re-heating of aluminium billets before forging or extrusion is a common application of induction heating technology. The process is driven by the magnetic flux created by a time varying current flowing in the induction coil, i.e. the magneto-motive force.

Coils used for induction heating are generally very short, and the magnetic fields which they produce are much weaker than what would be expected from the following equation for a long coil (the mathematical terms used in this paper are listed in Appendix 1: Table 1):

$$\left|\overrightarrow{B_\infty}\right| = \frac{\mu_o \mu_r N_c I_c}{l_c} \qquad (1)$$

The magnetic field on the centre line of a short coil can; however, be found by solving the Biot-Savart law, as presented in Figure 1 for 'air core' coils [1]:

$$\partial \vec{B} = \frac{\mu_o}{4\pi} \frac{I \vec{\partial l} \times \hat{r}}{r^2} \qquad (2)$$

In Figure (1) the integral of equation (2), B_o, is plotted as a ratio of B_∞ from Equation (1) versus a dimensionless coil length. Figure 1 indicates that to achieve the magnetic flux density predicted by Equation (1) anywhere in the coil, the coil must be extremely long, e.g. a length of 10 times its diameter. This is much longer than a typical induction coil, and it can therefore be concluded that induction coils are in general, 'short'.

Based on the results presented in Figure 1, the following observations are made which counter some of the commonly accepted assumptions made regarding short coils:

1. A short coil does not have a homogeneous internal magnetic field in either the axial or radial direction (not indicated in Figure 1), or equivalently a negligible external magnetic field.
2. The magnetic flux density at either end of the coil is not half the value at the middle.
3. The magnetic flux density in the middle of the coil is not equal to that of an equivalent length of an infinite coil (i.e. one having the same number of turns per unit length).

In the present study the effect of the non-infinite nature of short coils will be examined by comparing inductance, induction and magnetic field strength estimated by various analytical equations, to experimentally measured data, as well as the numerical results of COMSOL®.

2. Governing Equations of the COMSOL® Model and Modelling Approach

In classical induction furnace theory the solutions are derived starting from the magnetic field intensity created by the coil [2]; however, they can also be derived beginning with the magnetic vector potential, $\vec{A}$, as given by Equation (3), and solved using the quasi-static approach ($\nabla \cdot \vec{J} = 0$) as presented in Equations (3)-(8) for zero velocity and ignoring the displacement current. Equations (8) and (9) are equivalent for sinusoidal currents:

$$\vec{B} = \nabla \times \vec{A} \tag{3}$$

$$\vec{B} = \mu_o \mu_r \vec{H} \tag{4}$$

$$\nabla \times \vec{H} = \vec{J} \tag{5}$$

$$\vec{J} = \sigma \vec{E} + \vec{J^e} \tag{6}$$

$$\vec{E} = \nabla V - \frac{\partial \vec{A}}{\partial t} \tag{7}$$

$$j\omega\sigma \vec{A_\phi} + \nabla \times \vec{H} = \vec{J^e} \tag{8}$$

$$\frac{\partial^2 \vec{A_\phi}}{\partial r^2} + \frac{1}{r}\frac{\partial A_\phi}{\partial r} + \frac{\partial^2 \vec{A_\phi}}{\partial z^2} - \frac{\vec{A_\phi}}{r^2} = \mu_o \mu_r \sigma \frac{\partial \vec{A_\phi}}{\partial t} \tag{9}$$

Considering the approximately cylindrical geometry of both the coil and the work piece, a cylindrical co-ordinate system was used in the present study, and the equations solved using 2D axial symmetric models. It should be noted that the errors obtained in estimating magnetic flux density introduced by modelling helical coils as a series of stacked loops, are generally very small (e.g. one part per thousand), and strongly depend on the spacing and angle of the coil turns [3]. All solutions reported have been calculated using current driven coils, which ensure that the correct magneto-motive force is present. The voltage and impedance in the coil domains may then be in error without causing any impact on estimated induction in the work piece.

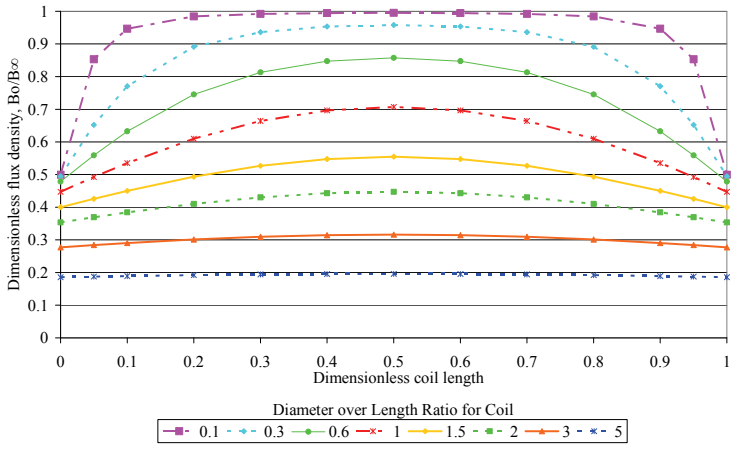

Figure 1. Dimensionless Flux Density (z-component) on the Centre Line of a Short 'Air core' Coil as a Function of Dimensionless Coil Length [1].

3. Inductance of a Short Coil

The inductance of a short coil, which is determined by the flux linkages per unit current, can be calculated using the method of Lorenz [4]. A more convenient method uses a tabulated correction factor, first published by Nagaoka [5] to six significant figures, which contains the solutions to the double elliptical integrals of Lorenz:

$$L_o = \frac{k_N A_c N_c \left|\overrightarrow{B_\infty}\right|}{I_c} \tag{10}$$

For induction coils, k_N can also be estimated by the method of Knight [6] to approximately three significant figures:

$$k_N = \frac{1}{1 + 0.4502\left(\frac{D_c + \delta_c}{l_c}\right)} \tag{11}$$

In the present study, the analytical solutions for k_N were estimated using numerical software available online, to more than 12 significant figures [7]. In evaluating k_N, the centre line of the round coil tubing was found to be the optimum reference diameter (least overall error), over the full range of frequencies from 50 Hz to 500 kHz.

As an example for inductance, an 'air core' 16 turn 'current sheet' coil is considered. This 'coil' was modelled using COMSOL® 4.2, and the results compared against the theoretical solution, i.e. Equation (10), in order to benchmark the accuracy of the COMSOL® software. A theoretical current sheet consists of one infinitely thin turn, with the current increased to $N_c I_c$ in order to represent the number of revolutions the current would make in a real helical coil. Using COMSOL®, the current sheet was modelled as a single 0.1 mm thick by 105.8 mm high copper sleeve, using the single-turn domain. The Nagaoka coefficient for this coil (k_N) is 0.639413 and from Equation (10), its inductance is 26.4051 μH. The measured value for a real tubular coil of the same overall dimensions was found to be 26.902 μH including lead effects.

The single turn inductance of the current sheet calculated by COMSOL® was adjusted to the value of the equivalent helical 16 turn coil, using the factor N_c^2 to account for the number of magnetic flux linkages and the true current per turn. Results were calculated as a function of the relative size of the 'magnetic domain' to the size of the coil. This was done in order to estimate the error introduced by the change of the external magnetic reluctance, on the flux density of the coil. The results obtained are presented in Table 1. More details of the models used in this paper can be found in Appendix 1: Table 2.

Table 1: Comparison between COMSOL® and Equation (10)

Ratio of Magnetic Domain Dimensions to Coil Dimensions	COMSOL Calculated Inductance (μH)	COMSOL - Analytical Solution Difference (%)
2.00	22.7563	-13.82
4.00	25.9502	-1.72
6.00	26.2783	-0.48
10.00	26.3870	-0.07
14.00	26.4057	0.00
20.00	26.4129	0.03

A ratio of 14, between the size of the coil and the size of the computational space, was selected as numerically sufficient to represent an infinite external volume with a negligible error in the coil's average internal magnetic flux density.

4. Induced Heating of a Cylindrical Work Piece

When circular eddy currents are induced in a work piece, heat is generated due to resistive heating by the portion of the current that is in phase with the voltage. The amount of heat generated is affected by the size and electrical conductivity of the work piece, the frequency and amount of the applied current, the number of turns in the coil, etc. The present authors have reviewed the classical approach for the computation of heat generation in a cylindrical work piece [2], and the equations can be summarized as follows:

$$P_w = k_N^{*2}\sqrt{2}\pi(I_c N_c)^2 \rho_w \xi_w \varphi(\xi_w)/l_c \tag{12}$$

$$k_N^* = k_N\left(1 - \left(\frac{D_w - \delta_w}{D_c + \delta_c}\right)^2\right) + \left(\frac{D_w - \delta_w}{D_c + \delta_c}\right)^2 \tag{13}$$

$$\xi_w = \frac{D_w}{\delta_w\sqrt{2}} \tag{14}$$

$$\varphi(\xi_w) = \frac{\sqrt{2}(ber\xi_w ber'\xi_w + bei\xi_w bei'\xi_w)}{ber^2(\xi_w) + bei^2(\xi_w)} \tag{15}$$

$$\delta_w = \left(\frac{\rho_w}{\pi\mu_r\mu_o f}\right)^{0.5} \tag{16}$$

Equation (13) calculates the modified Nagaoka short coil correction factor first developed by Vaughan and Williamson [8] in 1945. This equation, which only accounts for the fraction of the volume of the coil occupied by the work piece and its effect on the magnetic flux density in the air-gap, is essential for obtaining accurate calculations for short coils. Appropriate frequency correction validated using COMSOL® has therefore been added to Vaughan and Williamson's original equation to account for the electromagnetic penetration into both the coil and the work piece. For tubular coils over the large range of frequencies examined in the present study, a good correlation was achieved by fixing the effective current sheet diameter to the average coil diameter in accordance with the classical approach for calculating coil inductance, i.e. $D_c+\delta_c= D_c$ measured at the tube centre-line.

Model simulations were performed using the input data summarized in Appendix 1: Table 2, for frequencies from 50 Hz to 500 kHz. The initial mesh (Mesh 1) is presented in Figure 2 (with the work piece indicated by a white outline). The heating results are summarized in Table 2 and compared to the values calculated using Equations (12) to (16).

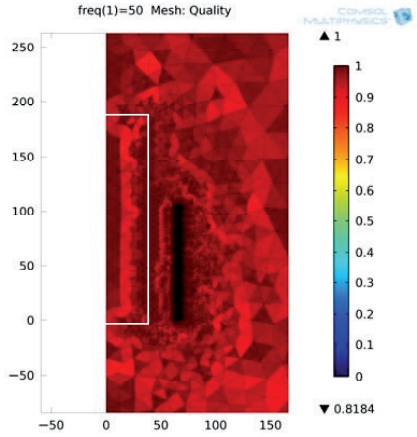

Figure 2. Mesh Quality for Mesh 1.

The electrical conductivity of the aluminium work piece was measured using an AutoSigma 3000 conductivity analyser (General Electric Inspection Technologies, UK) to within ±0.5%, calibrated against aluminium standards accurate to ±0.01% IACS. The electrical conductivity was not used as a fitting parameter. Actual power measurements were taken as described in detail elsewhere [2], using a Fluke 43B power quality analyser (Fluke, USA) and an i1000S inductive current probe (Fluke, USA), with a reproducibility of ~±6%. The resistive heating in the work piece at 50 Hz, for a coil excitation of 988.5 A, was determined to be 696 W, based on 2 readings.

Table 2: Comparison of Experimental, Analytical and COMSOL® Results for Mesh 1

Frequency (Hz)	Experimental Power (W)	Analytical Power (W)	Mesh 1 Power (W)	Mesh 1-Analytical Difference (%)	δ (mm)
50	696	691	650	-6.0	14.50
500	N/A	2768	2604	-5.9	4.59
5000	N/A	9549	10280	7.7	1.45
50000	N/A	29697	24211	-18.5	0.46
500000	N/A	94123	25728	-72.7	0.14
	Mesh 1spacing at work piece interface =				5.10

The results presented in Table 2, clearly reveal that the accuracy of the COMSOL® results dramatically decreases as the mesh at the work piece/air-gap interface becomes coarser than the electromagnetic penetration depth; however, if the mesh is improved by the use of boundary elements, then accurate results can be obtained at very high frequency as presented in Table 3. It should be noted that with the electrical measuring technique presently used, it is not possible to determine if COMSOL® has any significant error in determination of the heat generation in the work piece. In future studies direct calorific measurements of the heat generation in the work piece will be performed.

Table 3: Comparison of Experimental, Analytical and COMSOL® Results for Mesh 2

Frequency (Hz)	Experimental Power (W)	Analytical Power (W)	Mesh 2 Power (W)	Mesh 2-Analytical Difference (%)	δ (mm)
50	696	691	650	-6.0	14.5
500	N/A	2768	2597	-6.2	4.59
5000	N/A	9549	8834	-7.5	1.45
50000	N/A	29697	28305	-4.7	0.46
500000	N/A	94123	90029	-4.3	0.14
	Mesh 2 spacing at work piece interface =				0.02

It is possible to use the COMSOL® multi-turn domain with high frequency simulations of induction processes, but only if work piece data is the sole desired output. The work piece remains surrounded by the same magneto-motive force, and hence the induced power remains virtually constant (less than 1% change), regardless of frequency.

If information regarding the impedance of the coil is important, it is **essential to use the COMSOL® single-turn domain** when the electromagnetic penetration depth into the coil is less than the thickness for a square conductor or the tube diameter for a circular conductor, i.e. if $\delta_c < t_c$.

If the electromagnetic penetration depth is smaller than the tube diameter, the current distribution will not be homogeneous over the volume of the tube. As the frequency increases the current will first be biased to the side of the conductors facing the coil centre line and subsequently be redistributed over the whole outer surface of the conductors, as presented in Figure 3. With a tubing diameter of 6 mm, a single-turn domain must be used above 168 Hz.

To use the COMSOL® single-turn domain, each turn must be modelled as a separate domain. Failure to do so will result in a non-physical vertical redistribution of the current as COMSOL® attempts to achieve the lowest possible coil impedance.

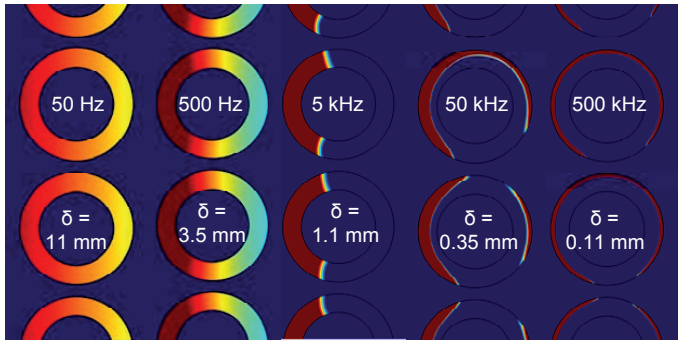

Figure 3. COMSOL® Results Showing Relative Current Distribution for Frequencies Ranging from 50 Hz to 500 kHz, (The Coil Centre Line is on the Left Side of the Conductors).

It is also necessary to insert boundary elements into the coil domains at high frequencies to accurately estimate: the current distribution, the inductance and most importantly the coil resistance. The same electromagnetic penetration depth criterion applies, i.e. the thickness of the boundary elements must be less than the electromagnetic penetration depth into the copper in the coil. Errors in estimating the coil resistance at high frequency using the multi-turn domain are given in Table 4.

Table 4: Comparison between Experimental, Analytical, Single and Multi-turn Estimates for Coil Resistance as a Function of Frequency

Frequency (Hz)	Experimental Coil Resistance (mΩ)	Mesh 2 Single-Turn Coil Resistance (mΩ)	Mesh 1 Single-Turn Coil Resistance (mΩ)	Multi-Turn Coil Resistance (mΩ)	Multi-Mesh 2 Single Difference (%)	δ (mm)
50	10.14	10.02	10.68	10.02	0.0	10.98
500	As above	10.56	13.26	10.02	-5.1	3.47
5000	25.70	24.57	33.91	10.02	-59.2	1.10
50000	91.40	81.78	97.90	10.02	-87.7	0.35
500000	300.30	289.89	325.50	10.02	-96.5	0.11
Yellow = analytical solution			Mesh 2 spacing at coil interface =			0.02

Based on the results presented in Table 4, it is clear that significant errors occur in the coil resistance estimates calculated using the multi-turn domain at frequencies for which the electromagnetic penetration depth is less than the coil tubing diameter, i.e. when the skin depth, coiling and proximity effects begin to have a major impact on the current distribution and therefore impedance [9-13].

5. Magnetic Field of an 'Air Core' Coil

A short 'air core' coil does not have a homogeneous magnetic field in either the axial or radial directions as explained in Section 1 and shown axially in Figure 1. Analytical solutions to determine the off-axis magnetic field strength of a coil do exist [14-17], but experimental values are reported in this study for physical validation. The direct measurements of the magnetic flux density of a real short coil in the present study were taken using a F.W. Bell model 6010 Gauss meter (Pacific Scientific OECO, USA). Standardized axial and radial Hall probes, with a measuring error of less than ±1% for AC magnetic fields were used. Accuracy was confirmed using

axial standards of 0.05 and 0.2 T, and a transverse standard of 0.05 T, prior to use.

In Figure 4, axial experimental data for the air-core coil are plotted together with the solution to Equation (2) for a coil diameter to length ratio of 1.24. The measurements were taken with a 6 mm diameter probe, and results plotted allowing for the average 3 mm off-set. As can be seen from Figure 4, there is excellent agreement between the experiment and analytical results, as well as the COMSOL® calculations. The small discrepancies near the coil wall are likely due to minor geometric imperfections in the stacking of the coil turns.

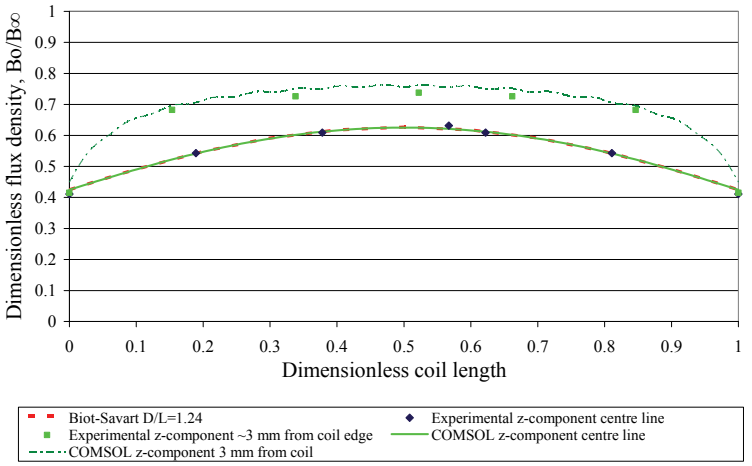

Figure 4. Dimensionless Magnetic Flux Density for a 16 Turn Induction Coil at 50 Hz, without a Work Piece.

6. Magnetic Field of a Coil Containing an A356 Aluminium Alloy Work Piece

The presence of the work piece will increase the magnetic flux density in the air gap of the coil as predicted by Equation (13), and indicated in Figure 5. The increase in the magnetic field strength is apparent by the difference between the Biot-Savart solution for an empty coil (dotted red line), the blue dots representing the measured values, and the green lines representing the COMSOL® calculated values 3 mm from the work piece and coil, respectively. The agreement between the actual measured and COMSOL® estimated values were typically ±1.5% with or without a work piece, except near the coil wall. Physical errors in the probe position (±0.5 mm), and the angle of alignment are the most likely source of discrepancies.

7. Conclusions and Future Work

Based on the present study the following conclusions and suggestions for future work are proposed:

- Comparison of the COMSOL® predictions against analytical models of known accuracy, proved critical in determining when the numerical model had achieved an acceptable level of precision.
- A magnetic domain 14 times as large as the dimensions of an induction coil is sufficiently large to accurately calculate the correct average magnetic flux density in the air-gap of the coil in the current model.
- Single-turn domains must be used if the frequency in the simulation is such that the electromagnetic penetration depth is less than the diameter of the coil tubing.
- Each turn of the coil must be modelled separately to prevent COMSOL® from redistributing the current in a non-physical manner.
- Meshing at the interface of both the work piece and the coil must be finer than the electromagnetic penetration depth in order to achieve accurate results when working at high frequencies.

- With proper experimental validation, meshing and selection of domains, it is believed that COMSOL® is capable of calculating electromagnetic phenomena as accurately as can be reasonably measured in the laboratory.
- Based on the accurate modelling of the power, i.e. induced current, as well as the magnetic flux density at the surface of the work piece, it is assumed that COMSOL® should predict electromagnetic Lorentz forces in the work piece with high accuracy.

The Lorentz forces and the resulting flow patterns developed in liquid aluminium will be explored in a future publication in relation to magneto-hydrodynamic modelling.

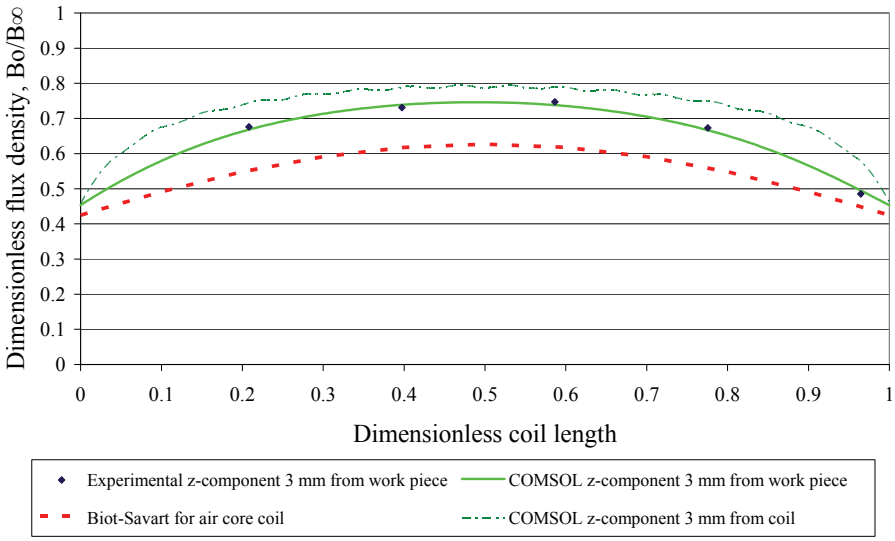

Figure 5. Dimensionless Magnetic Flux Density for a 16 Turn Induction Coil with 76.8 mm Diameter, with A356 Work Piece at 50 Hz.

8. Acknowledgements

This research was carried out as part of the Norwegian Research Council (NRC) funded BIP Project (No. 179947/I40) RIRA (Remelting and Inclusion Refining of Aluminium). The project partners are as follows: Hydro Aluminium AS, SAPA Heat Transfer AB, Alcoa Norway ANS, Norwegian University of Science and Technology (NTNU) and SINTEF Materials and Chemistry. Funding by the industrial partners and NRC is gratefully acknowledged.

The authors also wish to express their gratitude to Egil Torsetnes at NTNU, Trondheim, Norway, for helping with the design and construction of the experimental apparatus. Sincere gratitude is also due to Kurt Sandaunet at SINTEF, Trondheim, Norway, for his support and help, as well as for the use of the SINTEF laboratory.

9. Appendix 1

Table 1: Glossary of Units and Symbols

Quantity	Symbol	Scalar Quantity SI Unit	Abbr.
Magnetic potential (vector)	A	weber/meter	Wb/m
Area	A_c	meter^2	m^2
Magnetic flux density (vector)	B	tesla	T
Differential flux density (vector)	∂B	tesla	T
Differential length (vector)	$\partial \ell$	meter	m
Diameter	D	meter	m
Electric field (vector)	E	volt/meter	V/m
Frequency	f	hertz	Hz
Magnetic field (vector)	H	ampere/meter	A/m
Current, RMS	I	ampere	A
Current density (vector)	J	ampere/meter^2	A/m^2
Nagaoka short coil correction factor	k_N	unitless	-
Modified Nagaoka factor	k_N^*	unitless	-
Length	ℓ	meter	m
Inductance	L	henry	H
Turns	N	unitless	-
Resistive heating, RMS	P	watt	W
Radius	r	meter	m
Biot-Savart unit (vector)	$\hat{r}$	meter	m
Resistance	R	ohm	Ω
Tube diameter	t_c	meter	m
Time	t	seconds	s
Electric potential	V	volt	V
Electromagnetic penetration depth	δ	meter	m
Permeability of vacuum	μ_o	henry/meter	H/m
Relative permeability	μ_r	unitless	-
Dimensionless penetration depth	ξ	unitless	-
Electric conductivity	σ	siemens/meter	S/m
Electric resistivity	ρ	ohm meter	Ω m
Induction effectiveness factor	φ	unitless	-
Magnetic flux	Φ	weber	Wb
e	External		
o	Used for short coil form		
∞	Designates infinite coil form		
c	Coil		
w	Work piece		
ber	Kelvin function real part		
bei	Kelvin function imaginary part		
ber'	Derivative of ber		
bei'	Derivative of bei		

Table 2: Model Parameters

Model Parameter	Value	Unit
Work piece diameter	76.8	mm
Work piece height	192	mm
Work piece alloy	A356	-
Work piece conductivity	48%	IACS
Work piece conductivity	2.41E+07	S/m
Work piece temperature	54	C
Work piece relative magnetic permeability μ_r	1	-
Copper tubing diameter	6.0	mm
Copper tubing thickness	1.0	mm
Copper tubing conductivity	80%	IACS
Copper tubing conductivity	4.20E+07	S/m
Copper tubing temperature	43	C
Coil diameter average	131.5	mm
Coil height	105.8	mm
Coil current	988.5	A
Coil turns	16	-
Mesh 1 cells	12159	-
Mesh 1 quality	0.8184	Average
Mesh 2 cells	33713	-
Mesh 2 quality	0.7813	Average

10. References

1. M. W. Kennedy, S. Akhtar, J. A. Bakken, and R. E. Aune, "Electromagnetically Enhanced Filtration of Aluminum Melts," 2011 TMS Annual Meeting & Exhibition, Proceedings: Light Metals 2011 - Cast Shop for Aluminum Production, Ed. G. Brooks and J. Grandfield, San Diego, USA, February 27 - March 3, 2011.
2. M. W. Kennedy, S. Akhtar, J. A. Bakken, and R. E. Aune, "Review of Classical Design Methods as Applied to Aluminum Billet Heating with Induction Coils," 2011 TMS Annual Meeting & Exhibition, Proceedings EPD Congress 2011: Materials Processing Fundamentals, Ed. P. Anyalebechi and S. Bontha, San Diego, USA, February 27 - March 3, 2011.
3. C. Snow, "Formula for the inductance of a helix made with wire of any section," Ed: US Govt. Print. Off., 1926, p. 91.
4. L. Lorenz, "Ueber die Fortpflanzung der Electricität," *Annalen der Physik,* vol. 243, pp. 161-193, 1879.
5. H. Nagaoka, "The inductance coefficients of solenoids," *Journal of the College of Science,* vol. 27, pp. 18-33, 1909.
6. D. Knight, (2010, August 25), *3.1. Solenoids: Part 1.,* http://www.g3ynh.info [Online].
7. R. Weaver, (2011, July 26), http://electronbunker.sasktelwebsite.net/DL/NumericalExamples01.ods [Online]
8. J. Vaughan and J. Williamson, "Design of Induction-Heating Coils for Cylindrical Nonmagnetic Loads," *American Institute of Electrical Engineers, Transactions of the,* vol. 64, pp. 587-592, 1945.
9. R. Medhurst, "High Frequency Resistance and Self-Capacitance of Single-Layer Solenoids," *Wireless Engineer,* pp. 80-92, 1947.
10. E. Fraga, C. Prados, and D. Chen, "Practical model and calculation of AC resistance of long solenoids," *IEEE Transactions on Magnetics,* vol. 34, p. 205, 1998.
11. C. Hickman, "Alternating-Current Resistance and Inductance of Single Layer Coils," 1922.
12. S. Butterworth, "Eddy-current losses in cylindrical conductors, with special applications to the alternating current resistances of short coils," *Philosophical Transactions of the Royal Society of London. Series A, Containing Papers of a Mathematical or Physical Character,* vol. 222, pp. 57-100, 1922.
13. S. Butterworth, "Note on the Alternating Current Resistance of Single Layer Coils," *Physical Review,* vol. 23, pp. 752-755, 1924.
14. R. H. Jackson, "Off-axis expansion solution of Laplace's equation: Application to accurate and rapid calculation of coil magnetic fields," *Electron Devices, IEEE Transactions on,* vol. 46, pp. 1050-1062, 1999.
15. V. Labinac, N. Erceg, and D. Kotnik-Karuza, "Magnetic field of a cylindrical coil," *American journal of physics,* vol. 74, p. 621, 2006.
16. D. B. Montgomery and J. Terrell, Some useful information for the design of air-core solenoids: National Magnet Laboratory, Massachusetts Institute of Technology, 1961.
17. S. R. Muniz, M. Bhattacharya, and V. S. Bagnato, "Simple analysis of off-axis solenoid fields using the scalar magnetostatic potential: application to a Zeeman-slower for cold atoms," *Arxiv preprint arXiv:1003.3720,* 2010.

PART II:
CERAMIC FOAM FILTERS, CHARACTERIZATION AND HYDRODYNAMICS

SUPPLEMENT 3

Characterization of Ceramic Foam Filters used for Liquid Metal Filtration

Mark William Kennedy, Kexu Zhang, Robert Fritzch, Shahid Akhtar, Jon Arne Bakken, Ragnhild Elisabeth Aune

Metallurgical and Material Transactions B
DOI 10.1007/s11663-013-9799-7
ISSN 1073-5615
Published On-line February 9, 2013, 1-20.

Characterization of Ceramic Foam Filters Used for Liquid Metal Filtration

MARK WILLIAM KENNEDY, KEXU ZHANG, ROBERT FRITZSCH, SHAHID AKHTAR, JON ARNE BAKKEN, and RAGNHILD E. AUNE

In the current study, the morphology including tortuosity, and the permeability of 50-mm thick commercially available 30, 40, 50, and 80 pores per inch (PPI) alumina ceramic foam filters (CFFs) have been investigated. Measurements have been taken of cell (pore), window, and strut sizes, porosity, tortuosity, and liquid permeability. Water velocities from ~0.015 to 0.77 m/s have been used to derive both first-order (Darcy) and second-order (Non-Darcy) terms for being used with the Forchheimer equation. Measurements were made using 49-mm "straight through" and 101-mm diameter "expanding flow field" designs. Results from the two designs are compared with calculations made using COMSOL 4.2a® 2D axial symmetric finite element modeling (FEM), as a function of velocity and filter PPI. Permeability results are correlated using directly measurable parameters and compared with the previously published results. Development of improved wall sealing (49 mm) and elimination of wall effects (101 mm) have led to a high level of agreement between experimental, analytic, and FEM methods (±0 to 7 pct on predicted pressure drop) for both types of experiments. Tortuosity has been determined by two inductive methods, one using cold-solidified samples at 60 kHz and the other using liquid metal at 50 Hz, giving comparable results.

DOI: 10.1007/s11663-013-9799-7

I. INTRODUCTION

CERAMIC foam filters (CFFs) have been used commercially in the aluminum foundry industry for more than four decades.[1] CFFs are industrially applied to remove small (<50 μm) solid inclusions (*e.g.*, oxides—Al_2O_3, spinels—$MgO{\cdot}Al_2O_3$, or carbides—SiC, Al_4C_3) and large oxide films, primarily for the production of premium quality aluminum products.

A research effort has been recently undertaken with the objective of using electromagnetic fields to achieve improved purification of liquid aluminum using commercial CFFs (30–80 PPI).[2,3] It was found in the current study that the vertical gradient in the Lorentz forces ($\vec{J} \times \vec{B}$) induced strong movements in the liquid metal. Based on preliminary finite element magneto-hydrodynamic (MHD) modeling and experimental observation of liquid movement within the equipment, velocities of up to 0.2 m/s are anticipated to exist within the filter elements. This velocity is approximately one order of magnitude higher than typical casting velocity for these types of commercial filters[4] and indicates that MHD dominates the flow field development. The modified filtration process can therefore not be understood, without first comprehending the impact of the Lorentz "driving" forces interacting with the resistance to flow produced by the permeability of the porous media, at these unusually high velocities.

The transition of pressure drop from first- to second-order behaviors for 65 and 80 PPI CFFs using water has been reported to be in the range from 0.01 to 0.015 m/s and to be beyond 0.015 m/s for 40 and 50 PPI filters.[5] In order to model MHD more accurately using finite element modeling (FEM) at high velocity of liquid, it was necessary to obtain both first-order (Darcy) and second-order (Non-Darcy) terms for use with the Forchheimer equation[6]:

$$\frac{\Delta P}{L} = \frac{\mu}{k_1} V_s + \frac{\rho}{k_2} V_s^2 \qquad [1]$$

where ΔP is pressure drop (Pa), L is the filter thickness (m), V_s is the fluid superficial velocity (m/s), μ is the fluid dynamic viscosity (Pa s), ρ is the fluid density (kg/m^3), and k_1 (m^2) and k_2 (m) are the empirical constants called the Darcian and non-Darcian permeability coefficients, respectively. Equation [1] represents the sum of viscous (first term) and kinetic energy losses (second term).

MARK WILLIAM KENNEDY, Ph.D. Candidate, is with the Department of Material Science and Engineering, Norwegian University of Science and Technology (NTNU), 7491, Trondheim, Norway and is now Chief Technology Officer, with the Proval Partners S.A., 1004, Lausanne, Switz. Contact e-mail: m.kennedy@provalp.com KEXU ZHANG, formerly Masters Student, Department of Material Science and Engineering, Norwegian University of Science and Technology (NTNU), and is now Product Engineer, with the Wartsila Norway A.S., 5420, Rubbestadneset, Norway. ROBERT FRITZSCH, Ph.D. Candidate, and JON ARNE BAKKEN, Professor Emeritus, are with the Department of Material Science and Engineering, Norwegian University of Science and Technology (NTNU). SHAHID AKHTAR, Technical Manager (Quality), is with the Wire Rod Cast House, Hydro Aluminium, Karmøy, N-4265 Håvik, Norway. RAGNHILD E. AUNE, Professor, is with the Department of Material Science and Engineering, Norwegian University of Science and Technology (NTNU) and also with the Department of Material Science and Engineering, Royal Institute of Technology (KTH), 10044, Stockholm, Sweden.

Manuscript submitted December 9, 2012.

Published online: 09 February 2013

Permeability experiments were therefore conducted using water with commercial alumina CFFs of 30, 40, 50, and 80 PPI. In order to understand and correlate the obtained results, it was necessary to simultaneously study the morphology of the filters including cell (pore), window and strut sizes, porosity, and tortuosity.

II. THEORY

Permeability is an important parameter for the characterization of CFFs, since it is required to predict the flow rate obtainable for an imposed pressure gradient (*e.g.*, the casting rate for a given metal head and filter area) or to be able to predict the pressure drop (and therefore the required head or elevation change) necessary to achieve a specific flow rate for a fixed filter area (as in the design of a casting line and filter bowl). The correlation between flow and pressure drops can be obtained empirically by fitting experimental data as per Eq. [1] or by prediction using "easily" the measured physical properties such as porosity, ε (unitless), characteristic porous media dimensions, and the known liquid properties. The Ergun equation is often applied to predict the pressure drop in beds of solids[7]:

$$\frac{\Delta P}{L} = 150\frac{(1-\varepsilon)^2}{\varepsilon^3}\frac{\mu V_s}{d_p^2} + 1.75\frac{(1-\varepsilon)}{\varepsilon^3}\frac{\rho V_s^2}{d_p} \qquad [2]$$

where d_p is the "equivalent" spherical particle diameter (m). Even "improved" versions of Eq. [2] are known to have deviations in the range of ±50 pct, relative to actual measured packed bed pressure drops.[8]

Given that a porous solid is not a packed bed and has no clearly definable particle diameter, d_p, it is possible to apply the Ergun formula using alternately the diameters of the cell, d_c (m), window, d_w (m), or strut, d_s (m). These diameters are indicated in Figures 1 and 2(a) through (d), for the 30 through 80 PPI filters used in this study. One would expect that the estimation errors would exceed the ±50 pct typical of the Ergun equation, unless an appropriate "diameter" could be defined.

Ergun defined the "equivalent" particle diameter of a non-spherical solid, d_p, as the diameter of the sphere having the same "outer" specific surface area per unit solid volume, S_v (m^2/m^3) of the actual material in question (internal porosity, and small projections or cavities were ignored)[7]:

$$d_p = \frac{6}{S_v} \qquad [3]$$

In Eq. [3], the nomenclature of Ergun is maintained. Some confusion may ensue when referring to the recent literature, where S_v is sometimes used to represent the surface area of solid per unit bed volume, *i.e.*, S_B. Equation [2] can be re-written using Eq. [3] as

$$\frac{\Delta P}{L} = \alpha\frac{S_v^2(1-\varepsilon)^2\mu V_s}{\varepsilon^3} + \beta\frac{S_v(1-\varepsilon)\rho V_s^2}{\varepsilon^3} \qquad [4]$$

where α and β are unitless empirical constants found by Ergun to be approximately 4.17 and 0.292, respectively.[9]

Richardson *et al.*[9] explored the relationship between S_v and d_w for porous ceramics and suggested applying the

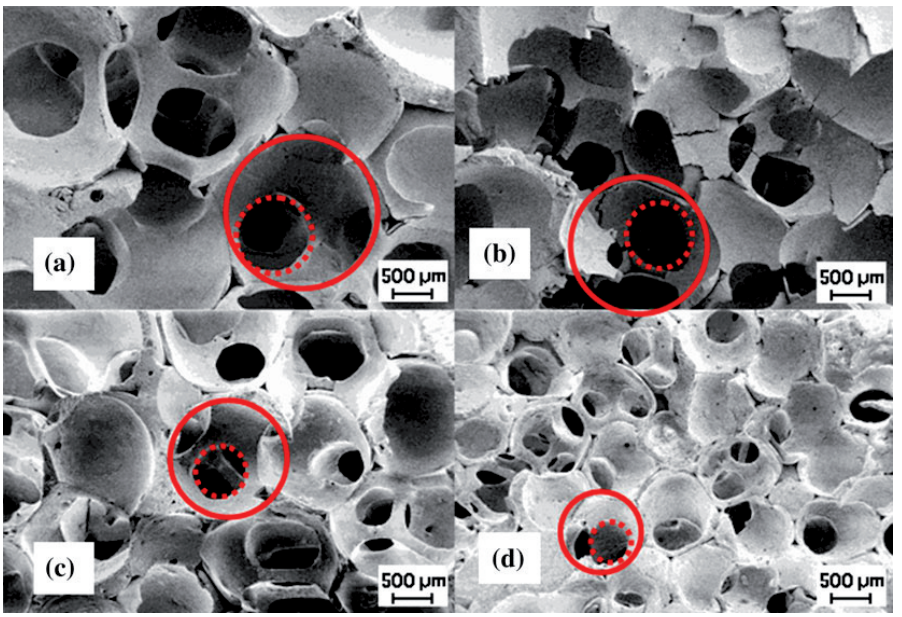

Fig. 1—Representative SEM micrographs of 30 (*a*), 40 (*b*), 50 (*c*), and 80 (*d*) PPI commercial alumina ceramic foam filters. Cell or pore sizes (d_c) are indicated by solid circles and window sizes (d_w) are indicated by dotted circles.

hydraulic diameter, d_h (m), concept. They equated the hydraulic diameter to the measured window diameter:

$$d_w = d_h = 4\frac{\text{wetted area}}{\text{wetted perimeter}} \quad [5]$$

Assuming idealized regular pores, *i.e.*, all with the same hydraulic diameter, a simple geometric analysis yields

$$S_v = \frac{4\varepsilon}{d_w(1-\varepsilon)} \quad [6]$$

Substituting Eq. [6] into Eq. [4] yields

$$\frac{\Delta P}{L} = 66.7\frac{\mu V_s}{\varepsilon d_w^2} + 1.17\frac{\rho V_s^2}{\varepsilon^2 d_w} \quad [7]$$

Recently, Dietrich *et al.*[10,11] proposed the following equation after correlating 2500 separate experimental values from 20 authors:

$$\frac{\Delta P}{L} = 110\frac{\mu V_s}{\varepsilon d_h^2} + 1.45\frac{\rho V_s^2}{\varepsilon^2 d_h} \quad [8]$$

The similarity between Eqs. [7] and [8] is obvious. If the hydraulic diameter is assumed equal to the window diameter in Eq. [8], then Eq. [8] will yield 40 through 50 pct higher pressure drops than Eq. [7].[10] As both empirical constants in Eq. [8] are larger than those in Eq. [7], it will yield higher estimated pressure drops for any velocity. Equation [8] has recently been independently shown to give excellent results using the optically determined hydraulic diameter, *i.e.*, the equivalent circular window diameter, d_w.[12]

It should be noted that the total, ε, and open porosity, ε_o, are of very similar magnitudes, as shown in Figure 3 for an electromagnetically primed[13] 50 PPI filter filled with an A356 aluminum alloy. Some small areas of closed porosity are shown in dotted circles as typical examples of closed porosity created by the substrate used in the filter fabrication process. Grosse *et al.* have described the morphological characterization of CFFs

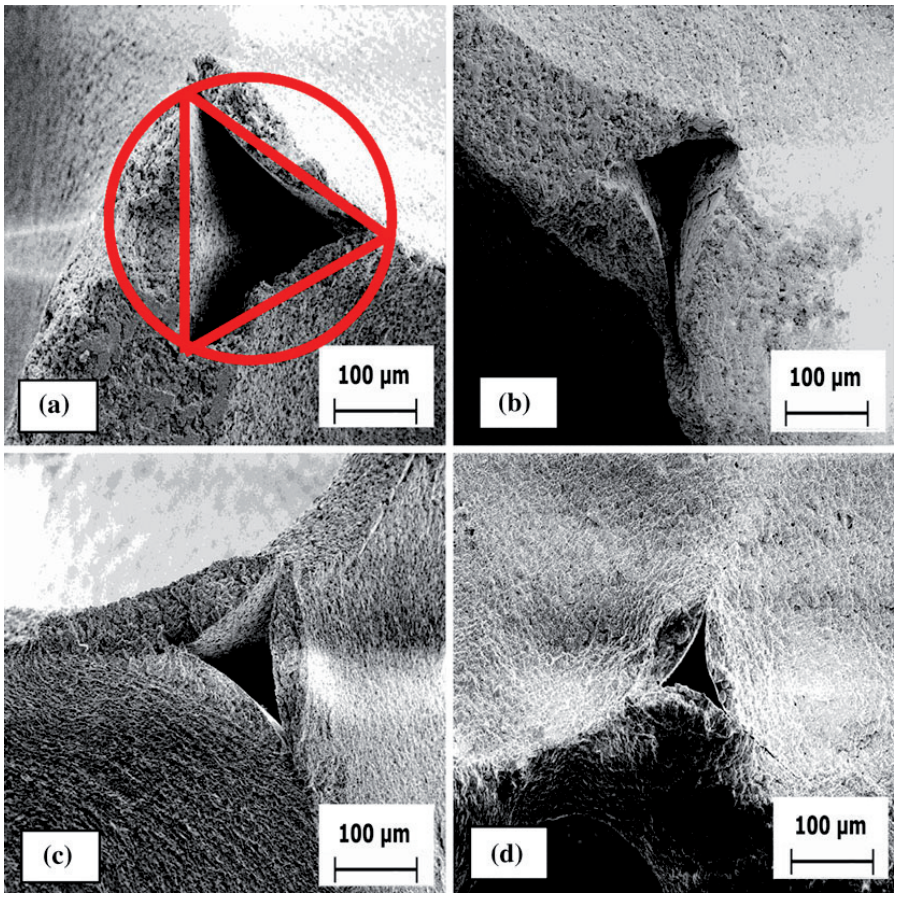

Fig. 2—Representative SEM micrographs of 30 (*a*), 40 (*b*), 50 (*c*), and 80 (*d*) PPI commercial alumina ceramic foam filters. Cell strut diameter (d_s) is indicated for the 30 PPI filter as the solid circle. The internal porosity left by the removal of the substrate is indicated as a triangle.

in detail, including the steps required to correctly determine total and open porosity (*e.g.*, using mercury at up to 4000 bar).[14,15] Grosse *et al.* found that the difference between the total and the open porosity is <5 pct of the measured value. The convention of Dietrich, *i.e.*, equality between the total and open porosities has therefore been followed in the current study.

Total porosity, ε, can be determined using the true particle density, ρ_p (kg/m^3), found using pycnometry and the measured filter mass, m_f (kg) for a known filter volume V_f (m^3), *i.e.*, the filter density, ρ_f (kg/m^3):

$$\varepsilon = 1 - \frac{m_f}{\rho_p V_f} = 1 - \frac{\rho_f}{\rho_p} \quad [9]$$

Tortuosity, τ (unitless), is here defined as the ratio between the actual length traversed by the liquid flow, L_a (m), and the linear thickness of the filter, L (m):

$$\tau = \frac{L_a}{L} \quad [10]$$

Tortuosity can be determined by electromagnetic induction experiments using alloys of known electrical conductivity, σ_m (Ω^{-1} m^{-1}). The actual resistance of a filter element filled with metal, as shown in Figure 3, can be compared with the known resistance of an equivalent path length of metal either liquid or solid and the tortuosity determined. The conductivity is related to the path length, area, and resistance by

$$\sigma_m = \frac{l}{aR_m} \quad [11]$$

where σ_m is the conductivity of the metal (Ω^{-1} m^{-1}) at the measurement temperature, l is the length of the conducting path (m), a is the area of the conducting path (m^2), and R_m is the resistance of the metal along the conducting path (Ω).

Within the filter, the available conducting area is reduced by the presence of non-conducting obstructions (*e.g.*, trapped gas or solid and filter media), and the conducting path length is increased because of the tortuosity. Assuming that the filter media is the only significant obstruction, the reduced apparent electrical conductivity can be estimated as follows:

$$\sigma_f = \frac{\sigma_m \varepsilon}{\tau} \quad [12]$$

where σ_f is the apparent electrical conductivity of the metal-impregnated filter (Ω^{-1} m^{-1}).

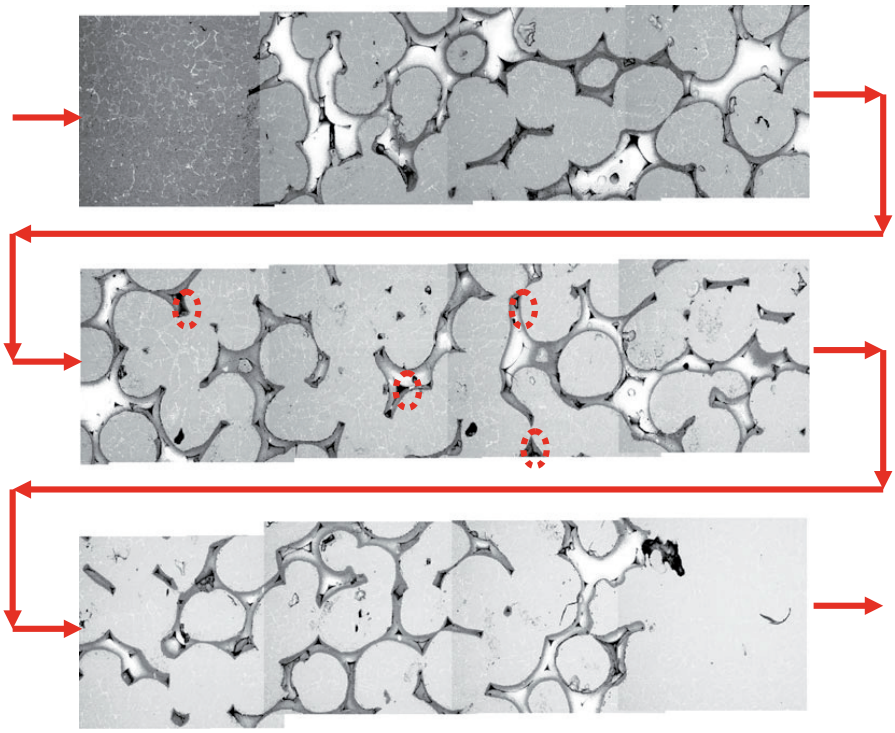

Fig. 3—Representative SEM micrographs showing a full 50-mm thickness vertical profile through a well-primed 50 PPI commercial alumina ceramic foam filter. Areas of "closed" porosity can be seen in black, some of which are highlighted by dotted circles as examples. Visual inspection confirms that nearly the entire porosity is filled with metal, *i.e.*, substantive agreement between total, ε and open porosity, ε_o.

Rearranging Eq. [12] to solve for the tortuosity yields

$$\tau = \varepsilon \frac{\sigma_m}{\sigma_f} \quad [13]$$

III. EXPERIMENTAL

A. *Filter Characterization*

Commercial filters of 30, 40, 50, and 80 PPI where examined by a combination of light microscopy, optical scanning, and scanning electron microscope (SEM) to determine cell, d_c, window, d_w and strut, d_s dimensions. 200 counts were made for each cell and window determination, on the original, uncut surface of the 50-mm-thick alumina CFFs. 40 counts were made of the strut dimensions, which were measured at their thinnest point.

Porosities of the 101-mm filter sections used in these experiments were determined using Eq. [9] by precise measurement of the filter dimensions, calculation of the total volume, and weighing on an analytic balance. Overall precision was estimated to be ±0.2 pct porosity. The 49-mm-diameter filters used during testing were cut from the center of the 101-mm filters, and the porosities were assumed as constant. For the 30, 50, and 80 PPI filters, porosity measurements were also taken for all the commercially sized filter elements for comparison (23″, 20″, and 23″ square).

The electrical conductivity of the solid aluminum and sectioned metal-impregnated filter elements were measured using an AutoSigma 3000 inductive conductivity analyzer (General Electric Inspection Technologies, UK) to an accuracy of ±0.5 pct using a 12.7-mm-diameter 47P001 probe. The instrument was calibrated before use against certified aluminum standards of 8.64 and 60.37 pct IACS (International Annealed Copper Standard). For reference: 100 pct IACS conductivity is 58.0 MS/m,[16] and typical electrical grade aluminum (*i.e.*, "commercially" pure) has a nominal conductivity of ~61 pct IACS. Measurements were taken on metal frozen over and under the filter elements, and on both vertical and horizontal cuts through the filters. A frequency of 60 kHz was used, which resulted in electromagnetic penetration depths from ~0.3 to 0.5 mm, depending on the alloy's conductivity and filter's tortuosity. An arithmetic average on 20 through 30 readings was used to estimate the room temperature conductivity of the metal-impregnated filter. Circular induced currents (*i.e.*, eddy currents) were generated by the probe, and these represent current flow in either the r–phi axes (horizontal cut) or the r–z axes (vertical cut). It was therefore expected that readings could be different, if any anisotropy existed in the filter morphology.

The effective electrical conductivities of the filters were also determined from liquid metal electromagnetic induction experiments, using procedures described in detail elsewhere.[2,3,17] A schematic of the apparatus used is shown in Figure 4(a), and a photograph is shown in Figure 4(b). The power induced in a tight stack of three 50-mm-thick, and ~100-mm-diameter filters of 30, 40, 50, or 80 PPI was determined electrically at a known temperature (and therefore metal electrical conductivity), while being filled with "commercially pure" aluminum alloys with initial electrical conductivity from 61 to 62 pct IACS. Temperatures were logged every 100 ms by type K thermocouples located under and over the 150-mm stack of filters.

An average temperature was used to estimate the liquid metal conductivity within the filter elements, starting with the literature conductivity data for ultra pure metal, and correcting for the actual measured room temperature conductivity of the clean metal after experimentation[18]:

$$\sigma_m = \frac{IACS_m^{293K}}{24.77 \times 10^{-8} \left(1 + 0.000571 \left[T_m - 933.2\right]\right) 65} \quad [14]$$

where $IACS_m^{293K}$ is the average room temperature conductivity of the solidified metal used during the experiment (pct IACS), and T_m is the temperature of the liquid alloy under experimental conditions (K).

A 50-Hz electromagnetic field was applied along the long (z) axis of the stack of filters. This time-varying magnetic field induced circular currents along the phi-axis, through the metal-impregnated interstitial spaces of the filter elements. The induced power was determined electrically, using high accuracy instrumentation measuring changes in coil power. Power measurements were taken using a Fluke 43B power analyzer (Fluke, USA), with a resolution of 100 W. Coil current measurements were made with an i1000S inductive current probe (Fluke, USA), with an accuracy of ±1 pct and a resolution of 1A.

The effective electrical conductivity of the filter elements where then determined from the equipment geometry, the experimentally measured power (W), and the applied coil current (A), with 2D axial symmetric FEM modeling, using the commercial COMSOL 4.2a® software. Details of the validation of the modeling methods can be found elsewhere.[19,20] The FEM model had been previously shown to have ~±2 pct uncertainty in power estimation, compared with direct calorific measurements taken in solid billet heating experiments.[20] The effective conductivity was determined by adjusting the model conductivity, until the model's induced power precisely matched the measured induced power, for the given applied current. The tortuosity along the phi-axis could then be determined using Eq. [13].

The uncertainty in the tortuosity estimates then represents the sum of the uncertainty in the model (±2 pct), measured workpiece power (~±10 pct), and any error in the solid (±0.5 pct) and liquid (±5 to 10 pct) estimates of the metal conductivity. Variation of up to ±20 pct should therefore be expected on a single reading of tortuosity. Five through eight individual power readings taken once every minute were averaged to produce 1 power/tortuosity measurement. Three through eight sets of measurements (depending on the degree of thermal and electrical stability) were then

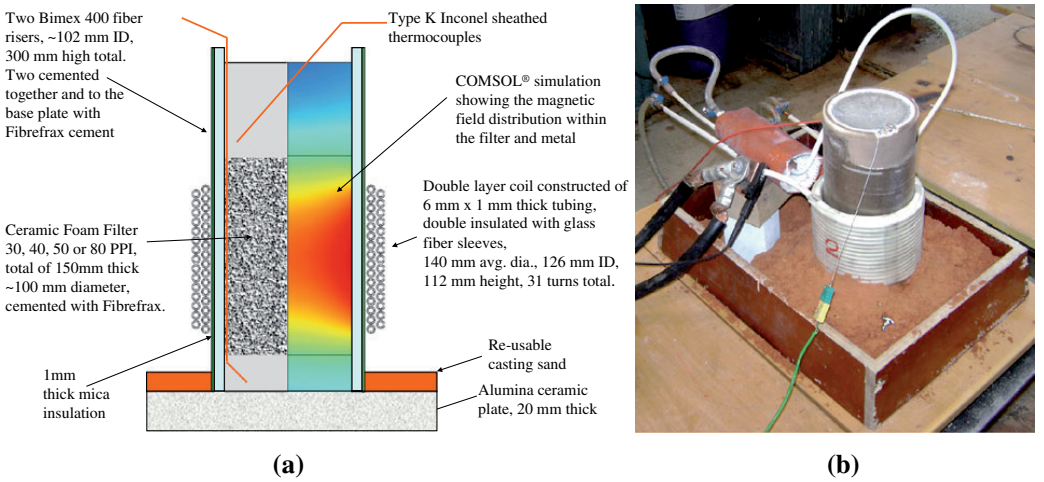

Fig. 4—Schematic of the filter tortuosity apparatus (*a*) and photograph (*b*), showing a two-layer, 31-turn (total) induction coil, operated from 371 to 734 A, using line frequency 50-Hz AC power.

individually modeled using FEM and averaged to produce the final estimate of tortuosity for each filter type.

The resulting tortuosity measurements are representative of the entire cross section of the filter, as the electromagnetic penetration depth exceeded the filter radius (50 mm), because of the low electrical conductivity of the molten metal (~10 pct of the room temperature solid metal electrical conductivity), combined with the low frequency of operation (50 Hz).

B. *Liquid Permeability: Experimental Conditions and Procedures*

The liquid permeability of 50-mm-thick commercial ceramic foam filters (CFFs) with 30, 40, 50, and 80 PPI were measured using water as the working fluid, in a temperature range from 278 K to 281 K (5 °C to 8 °C) (typical ρ_w = 999.9 kg/m^3, and μ_w = 1.3775 10^{-3} Pa s). Mass flows from about 0.05 to 2 kg/s of water were circulated through 46.4-mm ID smooth plastic piping, representing Reynolds numbers from ~1200 to 39000 and moving from laminar flow, into transitional and partially turbulent pipe flow in the inlet pipe.[21]

Eight through ten different experimental velocities were used to measure pressure drop for each filter. 101-mm nominal diameter elements were cut from the full size (20″ or 23″ square) commercial filters using diamond bores. The 49-mm diameter filter elements were cut from the center of the 101-mm filter elements. The true diameter and thickness of each filter element were measured using a micrometer, and the averages of six readings were used in the subsequent experimental analysis.

The main Plexiglas filter apparatus used in the permeability experiments is shown in Figures 5(a) and (b). The use of a transparent housing ensured that all air was completely eliminated from the system before recording any pressure readings. Two apparatus designs where used: one for the 101-mm diameter filters, shown in Figure 5(a); and the second, for 49-mm filters, shown in Figure 5(b). The sealing arrangements were of critical importance in the design of the filter housings. In order to prevent wall effects from significantly affecting the results, it is of paramount importance to prevent the flow from bypassing the filter and moving along the walls. Therefore, in the final experimental procedure, high-viscosity silicone grease was used to smoothen the outer surface of each filter (fill the outer-most broken or cut cells), which were then wrapped in paper and pressed tightly into the holder. Upon making contact with water, swelling of the cellulose fibers provided a seal of negligible permeability. It is necessary to seal the entire side surface of the filter, as normal O-rings are unable to stop the flow from bypassing along the wall.

In the 101-mm diameter design, the impacts of "wall effects" are essentially eliminated by allowing the flow field to expand within the filter element and making the outer wall a "stagnant" region. FEM is then required to elucidate the flow field and calculate an "effective" flow diameter for use with Eq. [1], which assumes a single representative diameter. It was necessary to use soft rubber gasket materials to press into the top and bottom faces of the filter elements, to prevent horizontal flow at the inlet or outlet and provide a clearly defined "entrance/exit diameter" of 49 mm for later CFD analysis.

The pressure transducer used was a DF-2 (AEP Transducers, Italy), with measuring range from 0 to 1 bar, and equipped with an output range from 4 to 20 mA. The transducer was factory calibrated and certified to an error of $<\pm 0.04$ pct of reading, over the full scale from 0 to 1 bar, using a six-point calibration. During the experiments, the current produced by the transducer at zero liquid flow velocity was determined

manually using a FLUKE 26 III, True RMS Multimeter (Fluke, USA) to a precision of 0.001 mA (6.25 Pa), using the lowest available current scale. Currents during the flow measuring periods were computer data logged at 100-mS intervals by conversion to signal range from 0 to 5 V, with a resolution of 0.001 V or 0.004 mA (*i.e.*, 25 Pa resolution). At greater than 4.1 mA, no bias could be detected between the manual and automated current readings, at the available 0.01 mA resolution (the FLUKE meter switched to a lower resolution at greater than 4.099 mA). The length between the pressure taps was 160 mm (varying ~±1 mm). One tap was located at 1.5 L/Ds up-stream and the other 0.75 L/Ds down-stream of the filter element.

The required inlet lengths to fully develop the flow regime are

Laminar[22]:

$$\frac{L_{\text{inlet}}}{d_{\text{pipe}}} \approx 0.03 Re_{\text{pipe}} \quad [15]$$

Turbulent[23]:

$$\frac{L_{\text{inlet}}}{d_{\text{pipe}}} \approx 4.4 Re_{\text{pipe}}^{1/6} \quad [16]$$

where L_{inlet} is the required inlet length (m) to fully develop the flow profile (*e.g.*, 99 pct centerline approach), d_{pipe} is the inside diameter of the pipe (m), and Re_{pipe} is the pipe Reynolds number (unitless).

The filter holders were used in a piping circuit containing ten 90 deg bends, with five being located before and five after the filter holder apparatus. There was a total of 8.3 m of piping in the standard "short" inlet configuration and 12.3 m in the "long" inlet configuration. In the "short" configuration, there were 22 L/Ds of straight sections of pipe before the filter housing, and in the "long" configuration, there were 65 L/Ds.

From Table I, it can be seen that except at very low or very high velocity, the "short" inlet should be adequate to achieve fully developed flow (*i.e.*, "99 pct approach"), while the "long" inlet should be adequate at all Reynolds numbers. The impact of back-to-back and out-of-phase 90° bends on the flow will be to promote turbulence even at low Reynolds numbers. Owing to the difficulty of simulating such a complex flow path (originating at a centrifugal pump), 3D fluid flow modeling was not deemed to be warranted. Various biased flow inlet conditions were tested for the "long" and "short" inlet lengths using 2D axial symmetry FEM and were found to have only second-order effects at the most. For FEM modeling, an extremely simplistic uniform inlet velocity was therefore assumed at the entrance to the pressure apparatus shown in Figures 5(a) and (b); the reasonableness of this assumption then is subject to empirical verification.

The pressure in the system was produced by a 1000 W, 0.8 bar maximum submersible pump, which was located at the bottom of a 70-cm-tall holding tank of 100-L capacity. The water flow rate was regulated using a DN 25 ball valve, located immediately at the outlet of the

Table I. Required Inlet Length to Fully Develop Flow as a Function of Pipe Reynolds Number

Velocity (m/s)	Pipe Re	L/D Inlet Laminar	L/D Inlet Turbulent	Estimated L/D Inlet
0.03	1010	30.3	N/A	30.3
0.05	1684	50.5	15.2	32.8
0.1	3368	N/A	17.0	17.0
0.2	6736	N/A	19.1	19.1
0.4	13472	N/A	21.5	21.5
0.8	26945	N/A	24.1	24.1
1	33681	N/A	25.0	25.0
1.2	40417	N/A	25.8	25.8

d_{pipe} = 0.0464 m, ρ_w = 999.9 kg/m^3, and μ_w = 1.3775 × 10^{-3} Pa s.

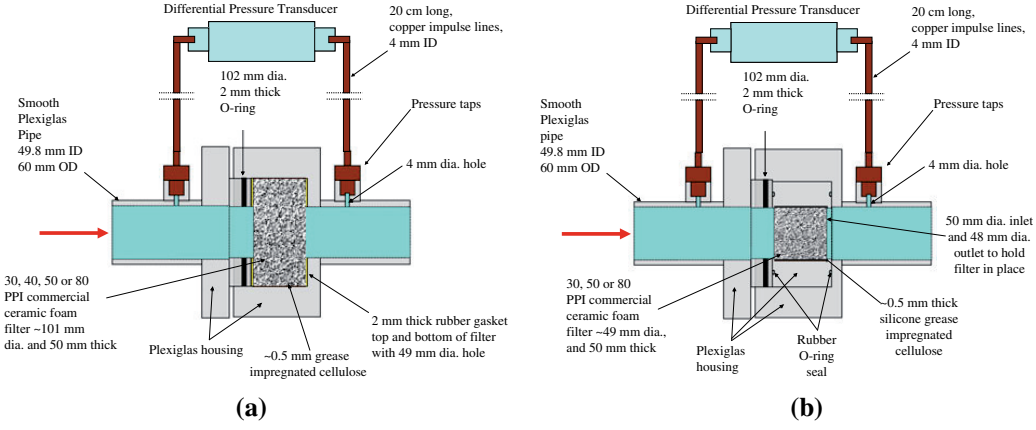

Fig. 5—Apparatus used for the 101-mm (*a*) and the 49-mm (*b*) diameters, 50-mm-thick filter experiments, both drawn approximately to scale. Fluid flow was from right to left.

pump. The flow rate was determined by accumulating mass over the measuring period in a second 100-L tank, located on a digital balance, equipped with an output range from 4 to 20 mA. The scale had a resolution of 10 g and a maximum reading of 100 kg. The zero and span of the scale were verified for accuracy at the 10-g resolution using test weights to 50 pct of full scale before use. The rate of mass gain of the measuring tank was computer data logged at 100 ms intervals. Depending on the required mass flow, from 10 to 50 kg of water was accumulated. "Sloshing" of the water in the tank (mainly at very high flows) produced noise on the weight signal that was smoothened by taking a 1-s rolling average (rolling average of 10 readings), which resulted in a maximum flow rate uncertainty of ~±0.5 pct of reading. The flow rate was found from the slope of the accumulation of mass with time and determined using least squares regression over the whole measuring period (typical $R^2 = 0.9985$). Temperatures were measured using a 1-mm-diameter Inconel-sheathed Type K thermocouple located in the holding tank, and the temperature data were also computer logged.

Eq. [1] was used with the measured pressure gradients and superficial velocities to determine the Forchheimer terms k_1 and k_2. Each estimate used the appropriate water temperature, and therefore density and viscosity, representative of the individual mass flow reading. Superficial velocity was determined using the actual measured filter diameter for the 49-mm filter elements or using the "effective" flow field diameter for the 101-mm filter elements (to be described in more detail later). Final k_1 and k_2 values are the arithmetic average of the 8 through 10 values determined for each filter element.

IV. RESULTS

A. *Filter Characterization*

SEM micrographs indicating the physical structures ranging from 30 to 80 PPI alumina ceramic foam filters used in this study are shown in Figures 1 and 2. The filter porosity and key dimensions are summarized in Table II. Sample porosity was calculated using Eq. [9] from the measured particle density of 3.48 ± 0.02 g/cm^3 (average of 3 readings). Overall filter porosity indicated in Table II is the average result of 2 through 4 readings on industrial 20″ or 23″ filters.

Histograms have been made of the 200 counts of window diameter, d_w as can be seen in Figures 6(a) through (d) for the 30 to 80 PPI filter types. Median values are indicated by dotted lines. Average cell diameter, d_c, has been plotted *vs*. the average window diameter, d_w in Figure 7, and the results correlated according to the following equation:

$$d_c = 1.79 d_w, \; R^2 = 0.988 \qquad [17]$$

The linear relationship between cell and window diameters implies a simple geometric relationship, likely originating with the original substrate used during the filter fabrication process. There is an excellent agreement between the current findings and the literature values for both cell and window sizes for similar alumina CFFs.[24]

B. *Filter Tortuosity Measurements*

Filter tortuosity has been determined for metal-impregnated 30, 40, 50, and 80 PPI filters. Measurements have been obtained with the metal in both liquid and solid states. The metal used was "commercially" pure electrical grade aluminum, which was determined to have 61.7 ± 0.1 pct IACS conductivity (average of 10 readings) before melting. After melting, the solidified metal samples were found to have conductivities of 59.7 pct (30 PPI), 54.0 pct (40 PPI), 60.0 pct (50 PPI), and 61.0 pct (80 PPI). The hot metal experiments were conducted using the apparatus already shown in Figure 4, and detailed results can be found in Appendix Table I.

Hot liquid metal (FEM estimate) and cold-solidified filter section measurements (average, vertical, and horizontal cuts) and calculated tortuosity results (using the hot metal data) are summarized in Table III, for all four filter types. Experimental data have also been plotted in Figure 8.

Results show reasonable agreement between hot and average cold conductivity ratios, given the different equipments, temperatures, and frequencies involved in these two sets of measurements. The conductivity ratio between the metal and metal-impregnated filters for the liquid metal experiments was correlated according to the following equation:

$$\frac{\sigma_m}{\sigma_f} = 5.10 - 3.8 \times 10^3 d_w, \; R^2 = 0.981 \qquad [18]$$

The variation in conductivity ratios between the horizontal or vertical cuts appeared to be random in nature. The observed variations may be the result of the

Table II. Summary of Basic Filter Physical Properties

Filter Type (PPI)	Filter Porosity (Eq. [9])	Full Filter Porosity (Eq. [9])	Cell Diameter, d_c (μm)	Window Diameter, d_w (μm)	Strut Diameter, d_s (μm)
30	0.892	0.890 ± 0.0002	1668 ± 417	961 ± 190	185 ± 41
40	0.900	N/A	1306 ± 251	698 ± 151	211 ± 46
50	0.863	0.864 ± 0.004	1132 ± 130	623 ± 120	190 ± 36
80	0.865	0.860 ± 0.004	683 ± 87	383 ± 87	119 ± 20

One standard deviation is indicated by the ranges.

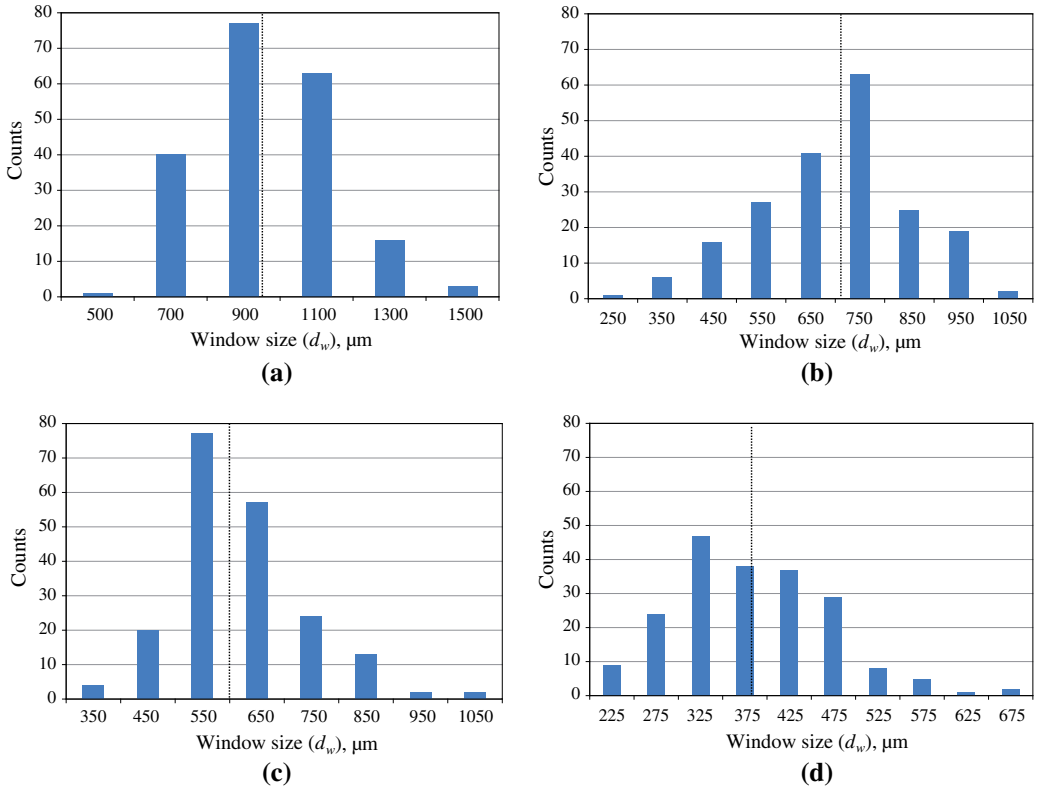

Fig. 6—Histograms of (*a*) 30, (*b*) 40, (*c*) 50, and (*d*) 80 PPI window sizes, d_w (μm). Median values are marked with dotted lines.

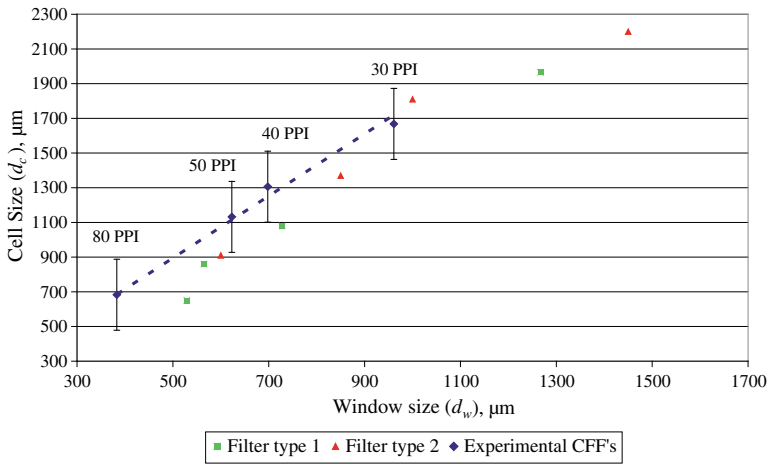

Fig. 7—Commercial ceramic foam filter cell size, d_c *vs.* window size, d_w (μm), and comparison with the literature data.[24] One "standard error" is indicated by the error bars.

random location of the sections through the pore structure of the filter elements and the low electromagnetic penetration depth of the high-frequency cold method, which is less than one cell diameter.

Relatively very few measured values have been published previously for ceramic foam tortuosities. Moreia *et al.* measured tortuosity values using an ionic conduction method equivalent to the induction method

described here. Their values for ceramic foams of 8, 20, and 45 PPI were 1.68, 1.71, and 1.84, respectively.[25] Diedericks *et al.* have theoretically studied tortuosity in some detail, proposing a value of ~1.45 at $\varepsilon = 0.88$, for "foam-like" materials.[26] Methods, using water and ionic solutes, will likely underestimate the true filter tortuosity, because of penetration of the water and ions into the micro and nano-porosity of the filter structure itself. Liquid metal

Table III. Summary of Key Tortuosity Experimental Results

Filter Type (PPI)	Filter Porosity (Eq. [9])	Filter Tortuosity (Eq. [13])	FEM Estimate of Conductivity Ratio (σ_m/σ_f)	Cold Average Conductivity Ratio (σ_m/σ_f)	Cold Vertical Conductivity Ratio (σ_m/σ_f)	Cold Horizontal Conductivity Ratio (σ_m/σ_f)
30	0.892	1.30	1.46 ± 0.06	1.70	1.64	1.77
40	0.900	2.29	2.54 ± 0.18	2.15	2.27	2.02
50	0.863	2.19	2.54 ± 0.12	2.70	2.34	3.05
80	0.865	3.20	3.70 ± 0.06	2.79	2.91	2.66

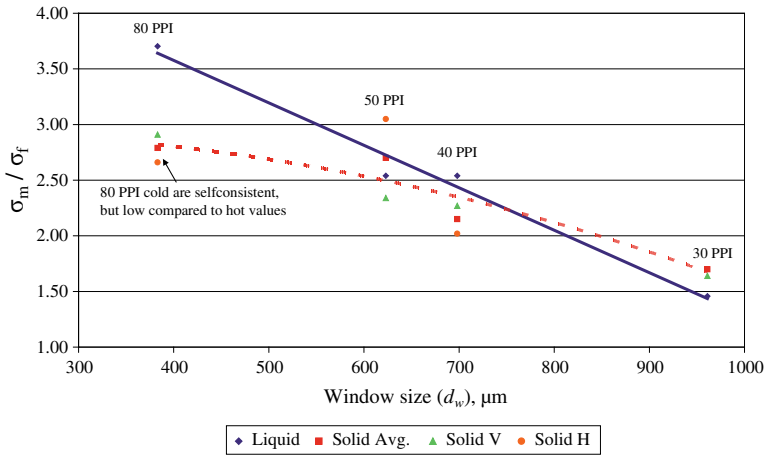

Fig. 8—Conductivity ratio of metal, σ_m and metal-impregnated filter, σ_f *vs.* window size, d_w (μm). Comparison between liquid metal values fitted to experimental data using FEM and average, vertical, and horizontally cut solid filter sections (cold readings).

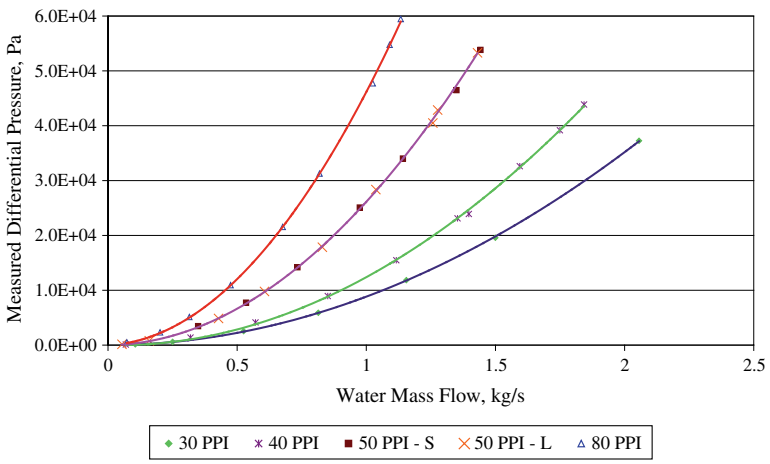

Fig. 9—Ceramic foam filter pressure drop measurements (Pa) as a function of water mass flow (kg/s) for the 101-mm "expanding flow field" filter design.

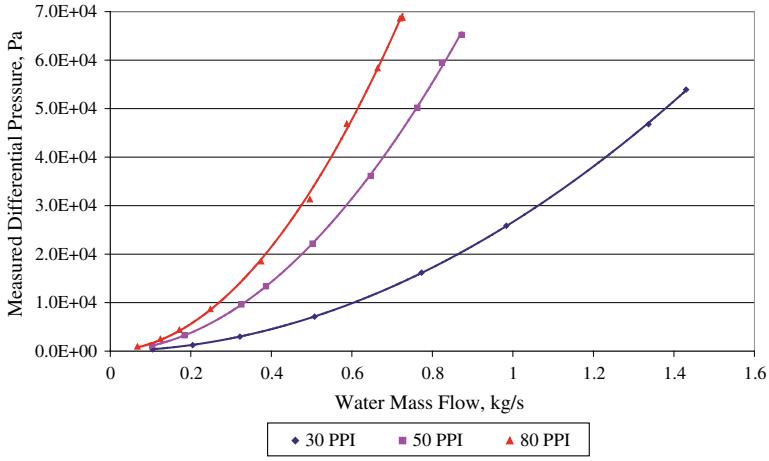

Fig. 10—Ceramic foam filter pressure drop measurements (Pa) as a function of water mass flow (kg/s) for the 49-mm "straight through" filter design.

Table IV. Empirical Coefficients for Eq. [19]

Filter Type (PPI)	Filter Diameter (mm)	A (Eq. [19])	B (Eq. [19])	R^2 (Eq. [19])
30	101	8754	83.2	0.9999
40	101	13362	−974.4	0.9996
50	101	25703	428.6	0.9997
80	101	44142	2017.1	0.9998
30	49	25480	1131.9	1.0000
50	49	83965	1771.7	0.9998
80	49	129032	1960.1	0.9994

poorly wets the surface of the ceramic, and in the absence of intense pressure (*e.g.*, 4000 bar for mercury) will not penetrate the micro porosity.

C. *Filter Permeability Measurements, Analytic and FEM Modeling*

Permeability measurements were performed using 101- and 49-mm-diameter filters as shown in Figures 5(a) and (b). Results for these experiments are summarized in Figures 9 and 10. Results are nearly perfectly described by second-order empirical equations of the following form:

$$\text{Filter Pressure Drop (Pa)} = A\dot{m}^2 + B\dot{m} \qquad [19]$$

where A and B are empirical constants, and $\dot{m}$ is the measured mass flow rate of water (kg/s). Values for the coefficients A and B are summarized in Table IV.

The experiments conducted using the 101-mm filters allowed the flow field within the filter element to expand, virtually negating wall effects; however, these experiments did not have a defined flow area, and therefore had no definable velocity for use with Eq. [1]. In order to determine the Forchheimer k_1 and k_2 terms using the 101-mm filters, it was necessary to use computational fluid dynamics (CFD) to solve for the flow field. An iterative procedure was applied as described in Figure 11. An "effective" flow field diameter was initially assumed for use with Eq. [1], the resulting k_1 and k_2 terms were then used with the CFD model, and the pressure gradients determined. If the results were in error, then a new "effective" diameter was assumed, and the procedure repeated until convergence was achieved. Example flow fields for the 101- and 49-mm diameter filter apparatus at 280 K (7 °C) and 0.5 m/s inlet water velocity are shown in Figures 12(a) and (b), respectively.

Results for the Forchheimer k_1 and k_2 terms for the 49- and 101-mm filters are summarized in Table V. More detailed results are given in Appendix Table II. The FEM-estimated k_1 and k_2 parameters for the "expanding flow field" 101-mm diameter experiments do not deviate by more than 16 pct from the directly measured "straight through" results for either k_1 or k_2.

Excellent agreement was found between the measured pressure gradients and those predicted using 2D axial symmetric FEM or analytic Eq. [1]. Deviations were in the range of ±0 to 7 pct, as plotted in Figures 13 and 14, against the 1:1 diagonal. This level of agreement can be taken as empirical confirmation of the adequateness of the uniform inlet velocity profile assumed in the FEM modeling and the use of the "effective" diameter for the analytic modeling using Eq. [1] of the "expanding flow field" 101-mm filters.

Important confirmation is also evidenced by the lack of variation of the measured pressure gradient between experiments conducted using 50 PPI, 101-mm diameter filters with the "long" and "short" inlet length configurations and the equivalent 49-mm filter, with the "short" inlet configuration, as shown in Figure 15. This figure verifies that inlet length and variation of the inlet

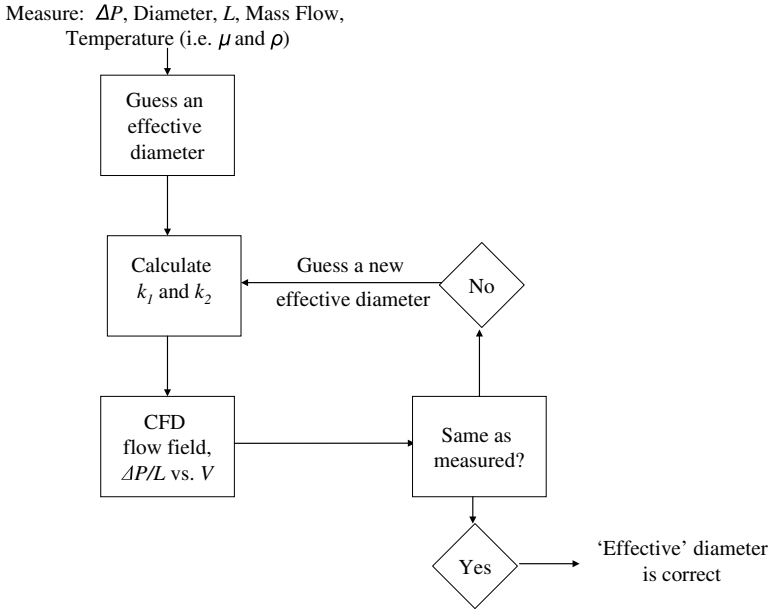

Fig. 11—FEM CFD procedure applied to the 101-mm experimental results to determine the Forchheimer, Eq. [1], parameters k_1 and k_2.

condition from laminar to turbulent pipe flow over the range of flow conditions should not have resulted in significant (*i.e.*, measurable) biases to the results.

V. DISCUSSION ON PERMEABILITY MEASUREMENTS

A. *Forchheimer Eq. [1] Coefficients, k_1 and k_2*

Using the apparatus in this study, the pressure resolution during flow was better than 62.5 Pa, *i.e.*, the 0.01 mA manual verification of automated readings (which had a theoretical resolution of 25 Pa), or a gradient uncertainty of ~±625 Pa/m depending on the sample. 625 Pa/m represented >5 pct uncertainty at flow rates in the range from 0.03 to 0.08 m/s, depending on the filter PPI. It has previously been reported that the transition to second-order behavior occurs at <0.02 m/s for 65 and 80 PPI filters similar to those used in these experiments.[5] With the limitations of the apparatus, it was therefore necessary to determine both k_1 and k_2 from flow conditions, where both terms were simultaneously significant, *i.e.*, it was not possible to operate in a purely "Darcy" regime.

In order to derive the Forchheimer coefficients in Table V, three procedures were explored:

(a) An "automated" second-order regression, with a zero intercept, using Excel 2003/2010.
(b) Ergun *et al.*'s procedure of dividing Eq. [1] by the velocity and performing a linear regression.[27]
(c) An iterative procedure to first guess k_1 and then correlate the remainder for k_2 using an exponential regression.

It should be noted that the values for the coefficients A and B summarized in Table IV for Excel 2nd-order correlations of the data can be converted to the Forchheimer coefficients through simple mathematical manipulation. This clearly makes the negative coefficient (B) for the 40 PPI physically meaningless, even when $R^2 = 0.9996$.

No physically meaningful correlations could be performed on the values of k_1 and k_2 found using Excel, *e.g.*, comparison with total porosity or window size. Better results were obtained following the recommended method of Ergun. The most physically meaningful results (*i.e.*, those with a clear trend) were obtained following the third procedure, where k_1 was initially guessed, the first-order component of Eq. [1] subtracted from the total and an exponential regression performed on the remainder. When the exponent on the velocity became 2.00000, the procedure was deemed converged. These are the values of k_1 and k_2, previously presented in Table V. k_1 and k_2 obtained by all the three methods are summarized in Appendix Table II for reference.

The third procedure appeared to prevent experimental variance from appearing disproportionately in the first-order k_1 term. Very small percentage errors in measured pressure at high velocity, represent very large errors when compared with the magnitude of pressure measured at low velocity, given the two orders change in magnitude with velocity, *i.e.*, "small" errors at high velocity can produce large changes in the estimated values for k_1.

The k_1 and k_2 values from Table V have been plotted in Figure 16 as functions of the window diameter d_w, and more specifically the window area, $\frac{\pi d_w^2}{4}$. Empirical correlations have been developed for k_1 (m^2) and k_2 (m) as functions of the window diameter d_w (m):

$$k_1 = \frac{6.71 \times 10^{-2} \pi d_w^2}{4}, \; R^2 = 0.974 \qquad [20]$$

$$k_2 = \frac{7.27 \times 10^{2} \pi d_w^2}{4}, \; R^2 = 0.960 \qquad [21]$$

From Figure 16 and Eqs. [20] and [21], it is concluded that from 30 to 80 PPI filters tested in these experiments behave much more like a series of "orifices," than they do a series of struts as is assumed in simple cubic cell[28,29] or more complex dodecahedron[30] and tetrakaidecahedron[9,31,32] models. An examination of Figure 1 would seem to support the concept of "orifices," given the high percentage of closed windows, particularly at higher PPIs. A simple strut model would not appear to be valid for the ceramic foam filters used in this study.

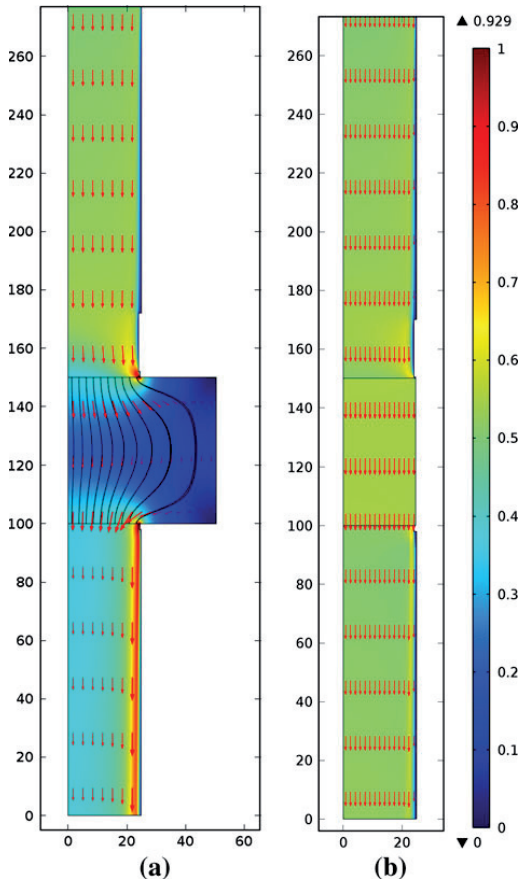

Fig. 12—Comparison of calculated flow fields for 50 PPI filters for the 101-mm "expanding flow field" (*a*) and 49-mm "straight through" (*b*) designs, both for 0.5 m/s uniform inlet velocity, and 280 K (7 °C) water temperature, shown with a common 0–1 m/s color scale. Pressure gradients of 501.1 and 1612.4 kPa/m were calculated for these two cases with the "short" inlet k_1 and k_2 parameters as shown in Table V.

B. *Development of the Experimental Method*

Concern with regard to bypassing of the flow around the filters and down the wall of the apparatus was the primary consideration in the design of the filter holder apparatus, as explained in the experimental section. The previous literature provided little guidance on the detailed design of the filter holder or how to produce functional wall sealing arrangements.

A series of incremental improvements were therefore necessary to arrive at the final procedure. The initial "expanding flow field" 101-mm apparatus was operated without wall sealing, and this was found relatively adequate, except at the highest velocity/pressure drops and the "tightest" 80 PPI filters. High flow and tight filters created large driving forces for bypassing.

The use of the "straight through" 49-mm apparatus necessitated the development of adequate wall sealing. High viscosity silicone was initially used alone, but visual observation through the Plexiglas housing showed that the sealant was forced out of the channel at the wall for 50 and 80 PPI filters, particularly during operation at high velocity and high pressure. The loss of seal was verified experimentally by repeating measurements and comparing with the previously "well-sealed" results as

Table V. Forchheimer Empirical Coefficients for Eq. [1]

Filter Type (PPI)	Actual Filter Diameter (m)	Filter Thickness L (m)	Water Temperature (K)	Water Density ρ (kg/m^3)	Water Viscosity μ (Pa·s)	Eq. [1] Forchheimer k_1 (m^2)	Eq. [1] Forchheimer k_2 (m)	Inlet Length (m)
30	48.7	50.7	281.4	999.9	1.330E−03	5.08E−08	5.46E−04	1.0
30	101	50.7	280.2	999.9	1.374E−03	5.57E−08	5.25E−04	1.0
40	101	47.7	279.1	999.9	1.422E−03	3.10E−08	3.38E−04	1.0
50	49.2	49.6	280.1	999.9	1.378E−03	1.57E−08	1.66E−04	1.0
50	101	49.6	278.9	999.9	1.426E−03	1.71E−08	1.69E−04	1.0
50	101	49.6	280.0	999.9	1.382E−03	1.52E−08	1.71E−04	3.0
80	49.1	50.3	279.3	999.9	1.413E−03	6.52E−09	1.15E−04	1.0
80	101	50.3	280.8	999.9	1.351E−03	5.44E−09	9.96E−05	1.0

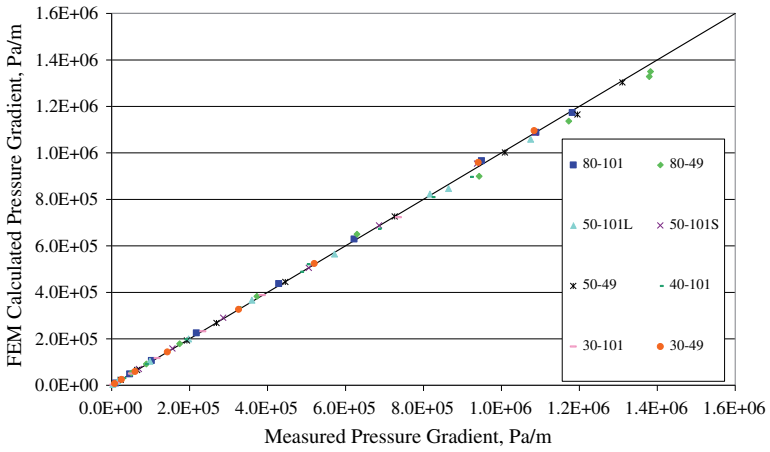

Fig. 13—FEM CFD results for 30 through 80 PPI filters of 101- and 49-mm nominal filter diameters, L = "long" (3 m) and S = "short" (1 m) inlet lengths, compared against the experimental pressure gradients (Pa/m).

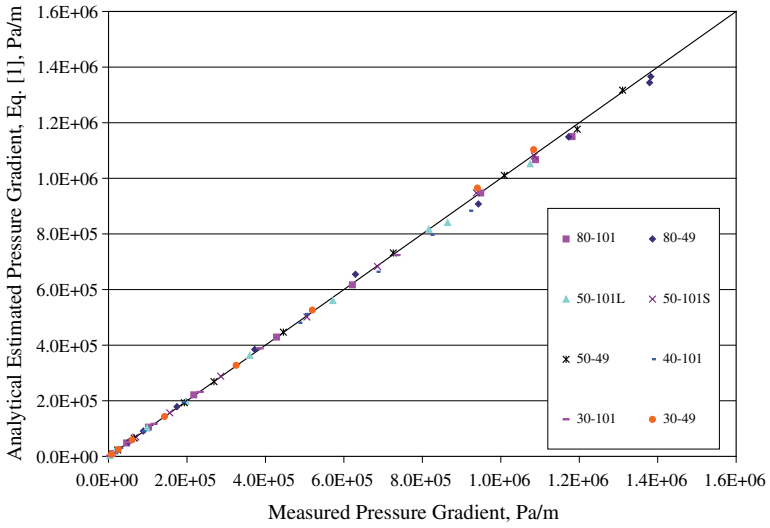

Fig. 14—Eq. [1] results for 30 through 80 PPI filters of 101- and 49-mm nominal filter diameters, L = "long" (3 m) and S = "short" (1 m) inlet lengths, compared with the experimental pressure gradients (Pa/m).

shown in Figure 17 for experiments conducted using the 80 PPI, 49-mm diameter filter.

The final experimental design used water-swollen cellulose and silicone to provide a very low permeability seal, which was not subject to physical removal at pressures of up to 0.8 bar. This was verified both visually and by repeated measurements over the whole pressure range with test filters. Results for the 80 PPI filter using this final procedure, are also presented in Figure 17. It is worth noting that all deviations in the experiments resulted in lower measured pressure gradients, *i.e.*, the highest measured pressure drop and the lowest permeability value for a given filter are most probably the correct values.

Recently, Innocentini *et al.*[33] discussed the impact of bypassing and flow field expansion on measured pressure drops in metal foam. Examination of the change in pressure drop with filter thickness indicated that wall bypassing reduced the pressure drop and that the measured pressure drop did not increase linearly with larger thickness. It must therefore be assumed that the equipment was operating partially as an "annular orifice" along the wall. The flow field expansion in Innocentini's alternate apparatus design was not

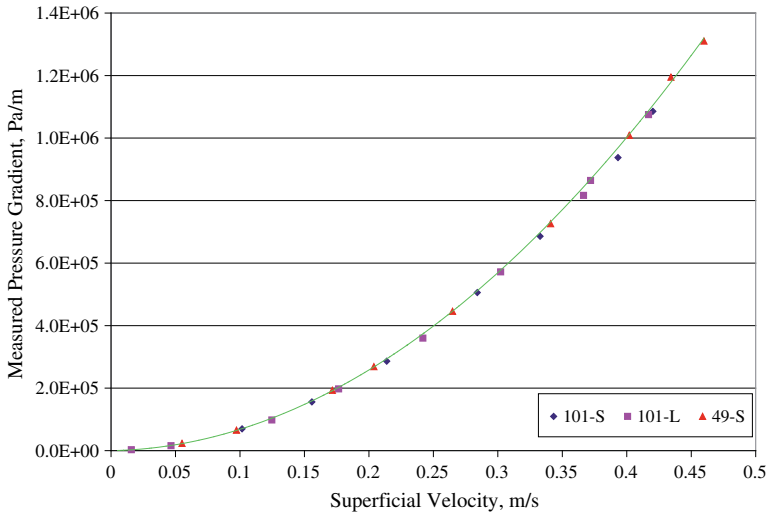

Fig. 15—Comparison between the L = "long" (3 m) and S = "short" (1 m) inlet length for the 101-mm and comparison with the 49-mm diameter filter results. Velocities are calculated using an "effective" flow diameter of 66.1 mm, determined by FEM/CFD for the 101-mm diameter filters.

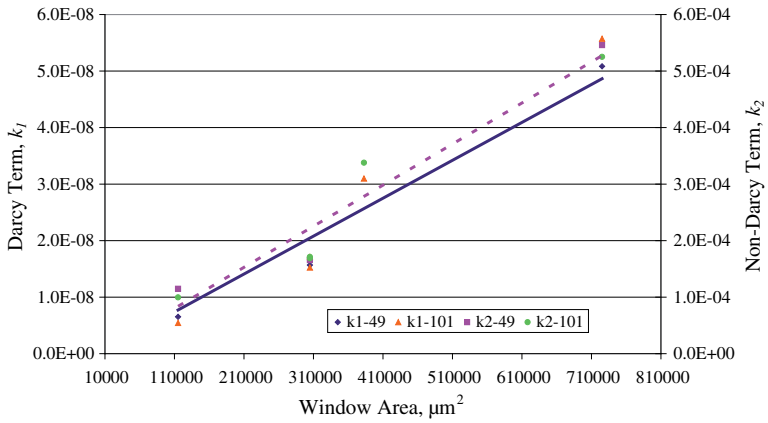

Fig. 16—Correlation of Darcy term, k_1 (m^2) and Non-Darcy term, k_2 (m) with window area $\frac{\pi d_w^2}{4}$. k_1 is correlated by the solid line and k_2 by the dotted line.

analyzed using CFD, and in both cases, no sealing was indicated at the walls.[33]

C. *Correlation of Results, and Comparison with Dietrich and Ergun*

Extensive efforts have been made to correlate the obtained results and compare with previously published equations. Of the previously published equations, only the equation of Dietrich, Eq. [8], was found to adequately describe the data. This comparison is made for the 30, 50, and 80 PPI, "straight through" 49-mm results shown in Figure 18. Agreement is considered as adequate being typically within ±50 pct (except at low velocity), *i.e.*, it achieves a similar accuracy for foams, as the original Ergun equation achieves for packed beds.

Other equations were found to underestimate dramatically the measured pressure drops obtained using the final and "well-sealed" experimental procedure. Most previously published equations did describe the obtained results for the "straight through" experiments in the absence of a wall seal or the "expanding flow field" results in the absence of area correction. No firm conclusions can be drawn from these facts, as details on the sealing arrangements and analysis techniques used in previous studies are generally lacking.

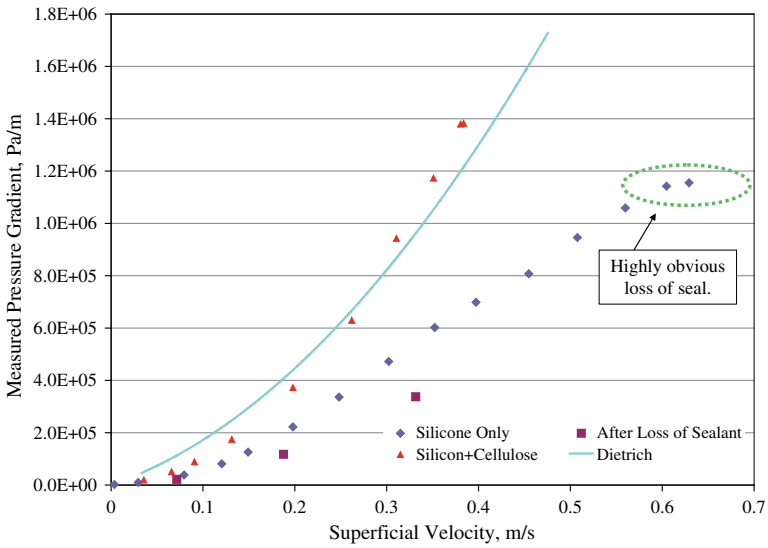

Fig. 17—Impact of sealing method and loss of seal on measured pressure gradients for 49-mm diameter "straight through" design using an 80 PPI filter element as a function of water superficial velocity. Comparison is made with Dietrich's equation [8].[10,11]

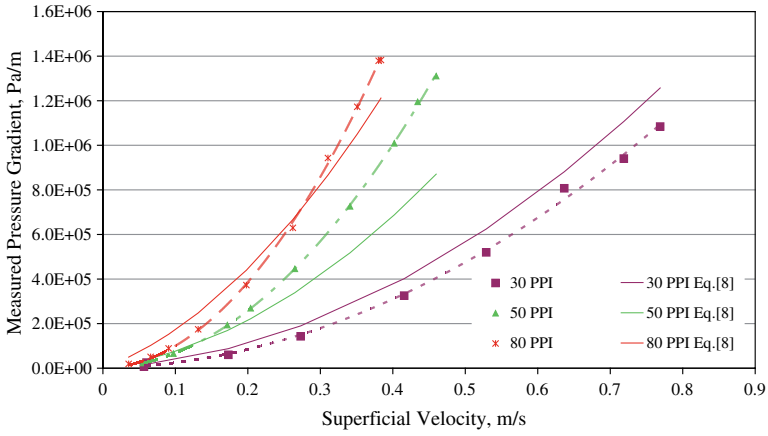

Fig. 18—Comparison between Dietrich's Eq. [8][10,11] and measured data for the 49-mm diameter "straight through" 30, 50, and 80 PPI filters' measured data. Experimental data are plotted with dotted lines and symbols, Dietrich's predictions are plotted as solid lines.

The best empirical correlation obtained was a slightly modified version of Ergun's equation.[7]

$$\frac{\Delta P}{L} = 8.385\left(150\frac{(1-\varepsilon)^2}{\varepsilon^3}\frac{\mu V}{D_w^2} + 1.75\frac{(1-\varepsilon)}{\varepsilon^3}\frac{\rho V^2}{D_w}\right), R^2 = 0.95 \quad [22]$$

Equation [22] is plotted in Figure 19, along with the +30 and −30 pct lines.

Equation [22] is equivalent to using 23.4 and 2.00 (based on an average $\varepsilon = 0.88$), as the empirical constants, instead of the values 110 and 1.45 in Dietrich's Eq. [8] or the Ergun equivalent values of 66.7 and 1.17 from Eq. [7]:

$$\frac{\Delta P}{L} = 23.4\frac{\mu V_s}{\varepsilon d_h^2} + 2.00\frac{\rho V_s^2}{\varepsilon^2 d_h} \quad [23]$$

Applying Eq. [23] to the obtained data indicates a significant reduction in error compared with the original Eq. [8], particularly at low velocity and pressure and an overall reduction in average error from ~40 pct to

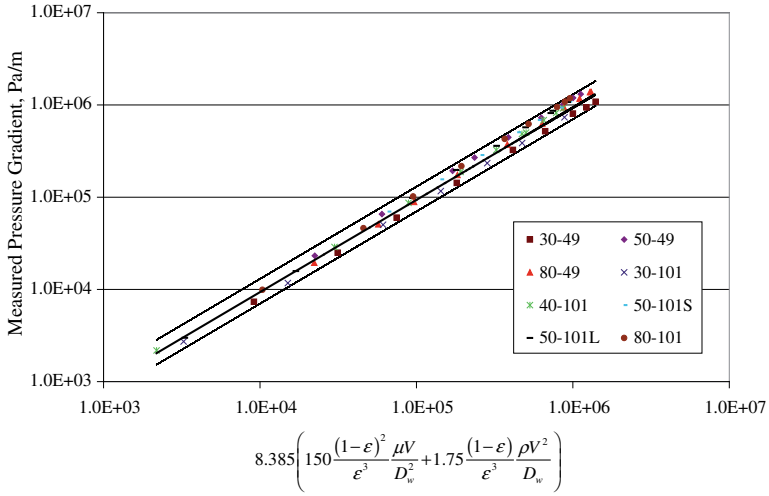

Fig. 19—Overall correlation Eq. [22], comparison with the measured pressure gradients ranging from 30 to 80 PPI filter elements. 49-mm diameter measurements were not available for the 40 PPI filters, as the filter exhibited poor mechanical properties and disintegrated on cutting. The upper and lower lines in the figure indicate a range of ±30 pct.

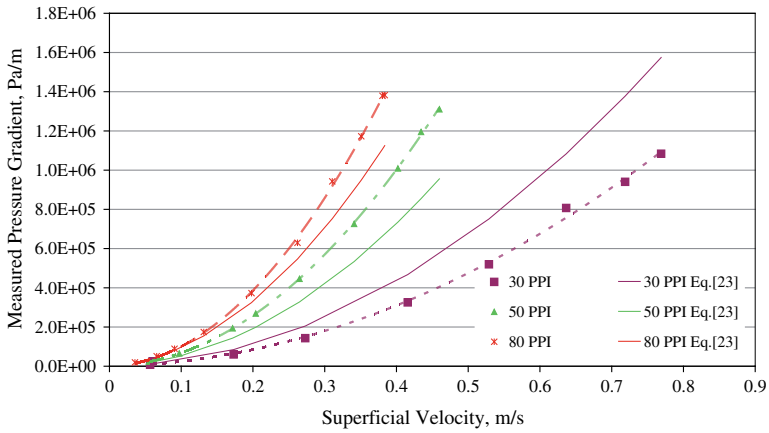

Fig. 20—Comparison of the modified Dietrich Eq. [23] with experimental data for the 49-mm diameter "straight through" experimental results from the 30, 50, and 80 PPI filters.

~30 pct. Equation [23] is plotted against the 30, 50, and 80 PPI, "straight through" 49-mm results in Figure 20.

Attempts were made to use cell diameter, d_c, strut diameter, d_s, and tortuosity, τ, in various correlations; however, no improvement could be made over the accuracy of Eqs. [23], [22], or [8].

D. *Comments Regarding CFD Modeling*

The CFD models presented here are discussed in more detail elsewhere.[34] Some pertinent points to achieving adequate agreement between FEM, analytic models and measured values are as follows:

(a) Iteration between high-quality measurements and FEM to ensure validity of assumptions and accuracy of final models.
(b) Correct and validated boundary conditions, *e.g.*, no-slip walls, contiguous velocity fields between liquid and porous media domains, and the inlet velocity profile.
(c) Use of the low Reynolds number k-ε, and Reynolds Averaged Navier–Stokes (RANS) model for turbulence ($k_0 = 0.005\ m^2/s^2$ and $\varepsilon_0 = 0.005\ m^2/s^3$), to adequately cover the difficult range of velocities in the inlet region.
(d) Use of dense meshes in regions of high velocity gradients (*e.g.*, boundary mesh at the "no-slip" walls).

(e) Precise measurement and exact geometric reproduction of the actual apparatus.

It is important to note that if significant bypassing had occurred during these experiments, it would not have been possible to achieve agreement between the CFD model and the experimental data for the 49-mm filter design. The agreement between the CFD results and the 49-mm and, subsequently that between the 49-mm and the 101-mm designs, are taken as confirmation that the wall-sealing arrangements in fact were of negligible permeability.

VI. CONCLUSIONS

Pressure gradients in CFFs have been found to correlate against velocity with high precision at both low and high velocities, using the Forchheimer equation, Eq. [1]. Forchheimer first-order k_1 and second-order k_2 terms were both found to correlate directly with the measured mean window area for each filter type (30, 40, 50, and 80 PPI).

The obtained pressure drops in this study could be best estimated using the measured total porosity ε, the optically determined window size d_w, and either Dietrich's original equation, Eq. [8], a modified version of Dietrich's equation, Eq. [23], or a slightly modified Ergun equation [22].

Bypassing along the wall must be prevented if accurate permeabilities of CFFs are to be measured using water flow experiments.

If the diameter of the filter is larger than the diameter of the pipe, then CFD must be used to analyze the impact of the expansion of the flow field on the measured pressure drop, *i.e.*, to determine the effective flow field diameter for use with Eq. [1].

Care must be taken while determining how results are mathematically correlated to prevent small percentage errors with the large pressure drops at high velocity from producing too much "noise" in the determination of first-order empirical coefficients for use with the Forchheimer equation, Eq. [1].

VII. FUTURE STUDY

Experiments should be conducted to elucidate the change of filter pressure drop with filter thickness. This would provide further validation that wall bypassing has been prevented by the current experimental procedures and/or determine the impact of bypassing on measured filter permeabilities.

Additional experiments should be conducted with filters produced from different suppliers and with other filter pore densities, to attempt to improve upon the Dietrich/modified Dietrich equations presented above.

Additional experiments could be conducted with a low range, from 0 to 0.1 bar pressure transducer, at low velocity (0 to 0.05 m/s), to study the Darcy and transitional regions in greater detail.

The conductivity of metals is best known and can be most easily measured at room temperature. It is recommended that for future tortuosity measurements, impregnate and then cool and solidify the sample. Solid samples can then be machined to precise tolerances, and inductive heating experiments can then be conducted at room temperature and low frequency to determine the tortuosity. Water cooling can even be applied to directly measure the quantity of heat produced and allow operation at steady-state thermal conditions, as has been applied elsewhere.[35]

ACKNOWLEDGMENTS

The current study was carried out as part of the RIRA (Remelting and Inclusion Refining of Aluminium) project funded by the Norwegian Research Council (NRC)—BIP Project No. 179947/I40. The industrial partners involved in the project are Hydro Aluminium AS, SAPA Heat Transfer AB, Alcoa Norway ANS, Norwegian University of Science and Technology (NTNU), and SINTEF Materials and Chemistry. The funds granted by the industrial partners and the NRC are gratefully acknowledged. The authors wish to express their gratitude to Egil Torsetnes at NTNU for helping with the design and construction of the experimental apparatus. Sincere gratitude is also due to Kurt Sandaunet at SINTEF for his support and help, as well as for the use of the SINTEF laboratory.

APPENDIX

See Appendix Tables I and II.

Appendix Table I. Tortuosity Experimental Data and FEM Calculated Conductivity Ratios

Filter Type (PPI)	Average Metal Temperature (K)	Estimated Hot Metal Conductivity Using Eq. [14] $(\text{ohm m})^{-1}$	Experimental Current (A)	Experimental Power (W)	FEM Estimate of Conductivity Ratio (σ_m/σ_f)
30	947	3.70E+06	716.9	1462	1.50
30	1000	3.58E+06	728.0	1469	1.51
30	1048	3.50E+06	517.7	764	1.42
30	995	3.60E+06	371.2	404	1.40
Room temperature final metal conductivity: 60.0 pct IACS, ±0.2 pct, 6 counts					1.46
40	940	3.34E+06	628.5	790	2.75
40	1026	3.09E+06	628.7	836	2.42
40	1033	3.17E+06	629.0	827	2.45
Room temperature final metal conductivity: 54.0 pct IACS, ±0.8 pct, 48 counts					2.54
Likely Fe or Si Al alloy contamination from melting crucible or metal skimming tool					
50	933	3.78E+06	728.3	1078	2.67
50	957	3.73E+06	727.8	1105	2.54
50	983	3.68E+06	728.0	1059	2.65
50	1021	3.60E+06	728.2	1053	2.61
50	1044	3.56E+06	729.2	1039	2.63
50	1052	3.54E+06	632.7	840	2.38
50	1044	3.56E+06	632.7	854	2.34
50	1032	3.58E+06	634.0	820	2.50
Room temperature final metal conductivity: 61.0 pct IACS, ±0.5 pct, 66 counts					2.54
80	948	3.68E+06	732.4	831	3.75
80	954	3.66E+06	732.9	832	3.74
80	963	3.65E+06	733.6	852	3.60
80	972	3.62E+06	733.4	814	3.80
80	979	3.61E+06	733.1	823	3.72
80	985	3.60E+06	733.1	823	3.71
80	991	3.59E+06	732.9	832	3.63
80	994	3.58E+06	732.9	817	3.72
80	997	3.58E+06	733.0	827	3.66
Room temperature final metal conductivity: 59.7 pct IACS, ±0.4 pct, 37 counts					3.70

Appendix Table II. Detailed Permeability Experimental Results

Filter Type (PPI)	Effective Filter Diameter (m)	Filter Thickness (m)	Water Temperature (K)	Water Density (kg/m^3)	Water Viscosity (Pa s)	Excel 2003 Forchheimer k_1 (m^2)	Excel 2003 Forchheimer k_2 (m)	Ergun Method Forchheimer k_1 (m^2)	Ergun Method Forchheimer k_2 (m)	Method 3 Forchheimer k_1 (m^2)	Method 3 Forchheimer k_2 (m)	Inlet Length (m)
30	48.7	50.7	281.4	999.9	1.330E−03	2.14E−08	5.83E−04	4.58E−08	5.48E−04	5.08E−08	5.46E−04	1.0
30	65.5	50.7	280.2	999.9	1.374E−03	2.46E−07	5.10E−04	7.19E−08	5.18E−04	5.57E−08	5.25E−04	1.0
40	66.0	47.7	279.1	999.9	1.422E−03	−2.03E−08	3.05E−04	1.09E−07	3.24E−04	3.10E−08	3.38E−04	1.0
50	49.2	49.6	280.1	999.9	1.378E−03	1.84E−08	1.65E−04	1.63E−08	1.65E−04	1.57E−08	1.66E−04	1.0
50	66.1	49.6	278.9	999.9	1.426E−03	1.63E−08	1.69E−04	1.24E−08	1.72E−04	1.71E−08	1.69E−04	1.0
50	66.1	49.6	280.0	999.9	1.382E−03	4.67E−08	1.64E−04	2.17E−08	1.67E−04	1.52E−08	1.71E−04	3.0
80	49.1	50.3	279.3	999.9	1.413E−03	1.90E−08	1.08E−04	8.68E−09	1.11E−04	6.52E−09	1.15E−04	1.0
80	66.5	50.3	280.8	999.9	1.351E−03	9.69E−09	9.45E−05	6.58E−09	9.68E−05	5.44E−09	9.96E−05	1.0

REFERENCES

1. M. J. Pryor: US Patent 3,893,917, 1975.
2. M.W. Kennedy, S. Akhtar, J.A. Bakken, and R.E. Aune: *Metall. Mater. Trans. B*, in press.
3. M.W. Kennedy, S. Akhtar, J.A. Bakken, and R.E. Aune: *Light Metals*, San Diego, CA, 27 February to 3 March, 2011, pp. 763–68.
4. Sivex® Application Guidelines, Jan-10-E4-565.
5. B. Hübschen, J. Krüger, J. Keegan, and W. Schneider, *Light Metals,* 2000, pp. 809–15.
6. P. Forchheimer: *Z. Ver. Deutsch. Ing*, 1901, vol. 45, pp. 1782–88.
7. S. Ergun: *Chem. Eng. Prog.*, 1952, vol. 48, pp. 89–94.
8. I. Macdonald, M. El-Sayed, K. Mow, and F. Dullien: *Ind. Eng. Chem. Fundam.*, 1979, vol. 18, pp. 199–208.
9. J. Richardson, Y. Peng, and D. Remue: *Appl. Catal. A*, 2000, vol. 204, pp. 19–32.
10. B. Dietrich, W. Schabel, M. Kind, and H. Martin: *Chem. Eng. Sci.*, 2009, vol. 64, pp. 3633–40.
11. B. Dietrich: *Chem. Eng. Sci.*, 2012, vol. 74, pp. 192–99.
12. S.A. Shakiba, R. Ebrahimi, and M. Shams: *J. Fluids Eng.*, 2011, vol. 133, pp. 111105-1–10.
13. M.W. Kennedy, R. Fritzsch, S. Akhtar, J.A. Bakken, and R.E. Aune: U.S. Provisional Patent Application 61/639,196, 2012.
14. J. Große, B. Dietrich, H. Martin, M. Kind, J. Vicente, and E.H. Hardy: *Chem. Eng. Technol.*, 2008, vol. 31, pp. 307–14.
15. B. Dietrich, G.I. Garrido, P. Habisreuther, N. Zarzalis, H. Martin, M. Kind, and B. Kraushaar-Czarnetzki: *Ind. Eng. Chem. Res.*, 2009, vol. 48, pp. 10395–401.
16. Copper Wire Tables Circular No. 31: US Bureau of Standards, 1913, pp. 1–76.
17. R. Fritzsch, M.W. Kennedy, S. Akhtar, J.A. Bakken, and R.E. Aune, *Electromagnetic Processing of Materials*, 23–25 October, Beijing, China, 2012, pp. 1–4.
18. P. Desai, H. James, and C. Ho: *J. Phys. Chem. Ref. Data*, 1984, vol. 13, pp. 1131–72.
19. M.W. Kennedy, S. Akhtar, J.A. Bakken, and R.E. Aune, *COMSOL Users Conference*, 26–28 October, Stuttgart, Germany, 2011, pp. 1–9.
20. M.W. Kennedy, S. Akhtar, J.A. Bakken, and R.E. Aune, *Light Metals*, Orlando, Florida, 3–7 March, 2012, pp. 269–75.
21. L.F. Moody: *Trans. ASME*, 1944, vol. 66, pp. 671–84.
22. W. Zhi-qing: *Appl. Math. Mecha.*, 1982, vol. 3, pp. 433–46.
23. F.M. White, *Fluid Mechanics*, 4th ed., McGraw Hill, Boston, 1999, pp 331–32.
24. N. Keegan, W. Schneider, and H. Krug, *Light Metals,* 1999, pp. 1031–41.
25. E. Moreira, M. Innocentini, and J. Coury: *J. Eur. Ceram. Soc.*, 2004, vol. 24, pp. 3209–18.
26. G. Diedericks and J.Du. Plessis: *Adv. Water Resour.*, 1996, vol. 19, pp. 225–39.
27. S. Ergun and A.A. Orning: *Ind. Eng. Chem.*, 1949, vol. 41, pp. 1179–84.
28. T. Lu, H. Stone, and M. Ashby: *Acta Mater.*, 1998, vol. 46, pp. 3619–35.
29. M. Lacroix, P. Nguyen, D. Schweich, C.Pham. Huu, S. Savin-Poncet, and D. Edouard: *Chem. Eng. Sci.*, 2007, vol. 62, pp. 3259–67.
30. T.T. Huu, M. Lacroix, C.Pham. Huu, D. Schweich, and D. Edouard: *Chem. Eng. Sci.*, 2009, vol. 64, pp. 5131–42.
31. M.V. Twigg and J.T. Richardson: *Ind. Eng. Chem. Res.*, 2007, vol. 46, pp. 4166–77.
32. A. Inayat, J. Schwerdtfeger, H. Freund, C. Körner, R.F. Singer, and W. Schwieger, *Chem. Eng. Sci.*, 2011, vol. 66 (12), pp. 2758–63.
33. M.D.M. Innocentini, L. Lefebvre, R. Meloni, and E. Baril: *J. Porous Mater.*, 2010, vol. 17, pp. 491–99.
34. M.W. Kennedy, R. Fritzsch, J.A. Bakken, and R.E. Aune: *Presented at COMSOL® User's Conference*, Milan, Italy, 10–12 October, 2012, pp. 1–7.
35. M.W. Kennedy, S. Akhtar, J.A. Bakken, and R.E. Aune, *3rd International Symposium on High Temperature Processing*, Orlando, Florida, 3–7 March, 2012, pp. 373–82.

SUPPLEMENT 4

Determination and Verification of the Forchheimer Coefficients for Ceramic Foam Filters Using COMSOL CFD Modelling

Mark William Kennedy, Kexu Zhang, Jon Arne Bakken, Ragnhild Elisabeth Aune

COMSOL Conference 2012 - Proceedings CD:
COMSOL, Burlington, MA, USA, ISBN 978-0-9839688-0-1 (2012), 1-7.

Determination and Verification of the Forchheimer Coefficients for Ceramic Foam Filters Using COMSOL CFD Modelling

Mark W. Kennedy*[1], Kexu Zhang[1], Jon Arne Bakken[1] and Ragnhild E. Aune[1,2]
[1]Dept. of Mat. Sci. and Eng., Norwegian University of Science and Tech. (NTNU), Norway
[2]Dept. of Materials Science and Engineering, Royal Institute of Technology (KTH), Sweden
*Communicating author: mark.kennedy@material.ntnu.no, mark.kennedy@metallurgy.no

Abstract: Experiments have been conducted with water at velocities from ~0.015-0.77 m/s to determine the permeability of 50 mm thick commercially available 30, 40, 50 and 80 Pores Per Inch (PPI) alumina Ceramic Foam Filters (CFF) used for liquid metal filtration.

Measurements were made using two different experimental setups, i.e. the 49 mm diameter 'straight through' and 101 mm diameter 'expanding flow field' designs. Difficulties were encountered in regards to sealing the 'straight through' design to prevent flow bypassing, as well as defining an effective diameter for the 'expanding flow field' design for use with the Forchheimer equation.

2D axial symmetric CFD modelling, using COMSOL® 4.2a, has been performed to show that the two experimental designs delivered equivalent permeability data. Based on the obtained outcome from the modelling it has been shown that COMSOL can give results with <7% error by including the Forchheimer second order term in the model for the porous media. This was also the case for flows at high pore Reynolds numbers.

Keywords: Ceramic Foam Filter, CFF, Permeability, Forchheimer, CFD

1. Introduction

Inclusions in liquid aluminium can have serious detrimental effects on the properties of the metal as well as on the performance of products produced from such metal [1-6]. Typical particle sizes cover a large range from 0.1 to 50 μm [7]. Ceramic Foam Filters (CFFs) have since the 1990's been used to filter inclusions from more than 50% of the aluminium produced world wide [4]. A typical CFF with 30 Pores Per Inch (PPI) is presented in Figure 1. CFFs are normally capable of removing particulate inclusions larger then 20 μm with an efficiency exceeding 50% [8]. Commercial CFFs are typically 50 mm thick and operate in a filter bowl with a gravity metal head producing the driving force needed for obtaining a flow through the filter. In this regard, filter permeability is a key property which determines the required metal head to produce any given flow velocity during casting operations.

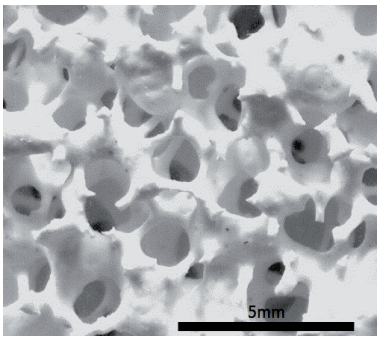

Figure 1. Image of a 30 PPI alumina CFF used for the filtration of liquid metal.

The permeability of new and clean CFFs can be conveniently determined under cold conditions using water. Water is a reasonable analogue for liquid aluminium, having the same dynamic viscosity at 20°C, as aluminium at normal casting temperatures of ~700°C. With aluminium being a light metal, the kinematic viscosity is only different by a factor of 2.4. It should, however, be pointed out that measurements made with clean water can only be directly compared with new filters. Aluminium filtration with CFFs is normally performed in deep mode, which limits the increase of pressure with time. In most cases, CFFs are changed before entering cake filtration mode, except in the case of 80 PPI filters and/or highly contaminated metal. The initial drop in the pressure over the filter does therefore dominate the hydrodynamic behaviour of the CFFs in operation.

2. Theory

Typical superficial flow velocities during casting are low, i.e. on the order of 0.2-1.5 cm/s [7]. It is often assumed that only the viscous first order Darcy term is required to predict pressure drop at such low velocity. The transition velocity to second order inertial behaviour has, however, been shown to be as low as 1 cm/s for CFFs [9]. Due to this it is therefore necessary to know both the Darcy and the non-Darcy terms of the Forchheimer equation [10]:

$$\frac{\Delta P}{L} = \frac{\mu}{k_1} V_s + \frac{\rho}{k_2} V_s^2 \qquad (1)$$

where ΔP is the pressure drop across the CFF [Pa], L the filter thickness [m], μ the fluid viscosity (which for water at 280 K is 1.382×10^{-3} [Pa·s]), V_s the fluid superficial velocity [m/s], k_1 the first order Darcy coefficient [m^2], ρ the fluid density (which for water at 280 K is ~1000 [kg/m^3]), and k_2 the non-Darcy coefficient [m].

Equation (1) represents the sum of the viscous (first term) and the kinetic energy losses (second term). Implicit in Equation (1) is that there is flow in only the axis defined by the direction of L, e.g. the z-axis, and that a constant area or 'effective diameter' can represent the extent of the flow field. This was approximately true for the 'straight through' flow design used in the current experiments, see Figure 2 (a), but not true for the 'expanding flow field' design, see Figure 2 (b).

In order to apply Equation (1) to the 101 mm diameter experimental filters it was necessary to solve the Reynolds-Averaged Navier-Stokes (RANS) equation for flow in porous media using 2D axial symmetry. This was done to be able to account for the expansion and contraction of the flow field in the radial direction as the flow entered and exited the apparatus through the attached Plexiglas® pipes.

3. Experimental

The liquid permeability of 50 mm thick commercial CFFs with 30, 40, 50 and 80 PPI, were measured using water. Mass flows from about 0.05 to 2 kg/s of water were circulated through 46.4 mm ID smooth plastic piping, representing Reynolds numbers from ~1200-39000, and moving from laminar flow into transitional and partially turbulent pipe flow in the inlet pipe [12].

8-10 different velocities (~0.015-0.77 m/s) were used to measure the pressure drop for each filter. The 101 mm nominal diameter elements were cut from full size commercial filters using diamond bores. The 49 mm diameter filter elements were cut from the centre of the 101 mm filter elements, and thus should possess the same porosity and permeability. From the 30 to the 80 PPI CFFs the porosity varied from 89.2% to 86.5% in a roughly linear fashion [11].

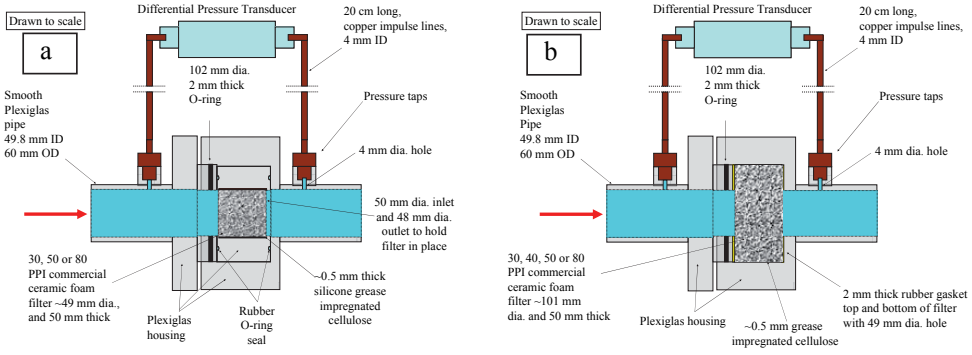

Figure 2. (a) the experimental setup used for the 50 mm thick 49 mm diameter 'straight through', and (b) the 101 mm diameter 'expanding flow field' filter experiments (both drawn approximately to scale). The flow is from left to right. For further equipment details, see reference [11].

The sealing arrangements were of critical importance in the design of the filter housings. It was necessary to prevent flow from bypassing the filters along the wall of the housing (particularly in the case of the 49 mm diameter filters), and that horizontal flow should be prevented from occurring in the case of the 101 mm filters. The various seals and gaskets used are presented in Figures 2 (a) and (b). In the final experimental setup, high viscosity silicone grease was used to smoothen the outer surface of each filter, i.e. to fill the outer-most broken or cut cells, before being wrapped in paper and pressed tightly into the holder. Upon contact with water, swelling of the cellulose fibres provided an extra seal of negligible permeability. It was necessary to seal the entire side surface of the filter, as normal O-rings would be unable to stop the flow from bypassing along the wall.

The pressure transducer used during the experiments was a DF-2 (AEP transducers, Italy) with a 0-1 bar measuring range equipped with a 4-20 mA output. The transducer was factory calibrated and certified to an error of ±0.04% over the full scale from 0-1 bar, using a 6 point calibration. The zero flow current was established to a precision of 0.001 mA (6.25 Pa), and the current during the flow measuring periods were computer data logged at 100 ms intervals by conversion to a 0-5 V signal with a resolution of 0.001V or 0.004 mA, i.e. 25 Pa resolution. The flow rate was determined from the slope of the gain-in-weight with time plot of a water receiving tank placed on a 100 kg scale having a resolution of 0.01 kg. The obtained flow rate had an error of <0.5%.

4. Use of COMSOL

In the 101 mm diameter experimental apparatus no predefined diameter existed to calculate the superficial velocity to be used with Equation (1). It was therefore necessary to iteratively solve the equation for the effective flow field diameter using a COMSOL 4.2a® 2D axially symmetric model, by adopting the procedure presented in Figure 3. This was done in order to correctly determine the Forchheimer coefficients to be used with Equation (1). For the 49 mm diameter experimental apparatus, the Forchheimer coefficients were determined directly from Equation (1) and the measured pressure gradients. The Forchheimer terms where then used with COMSOL to determine if the same pressure gradients could be calculated numerically, to ensure that no fluid leakage was occurring along the walls of the 49 mm diameter experimental apparatus.

Models were created using the ”Free and Porous Media Flow” module, with an added second order Forchheimer term, as well as the “Turbulent Flow, k-ε” module with the low Reynolds number and incompressible options. A uniform inlet velocity and non-slip walls were assumed. Variation of the inlet conditions were experimentally tested by using L/D ratios from 22 to 65, and were found to have no influence on the obtained pressure gradients. The system pressure was defined by setting one point at the apparatus outlet as being at zero Pa gauge pressure. Velocity fields were used to define the boundary conditions between the two turbulent flow domains and the porous media domain.

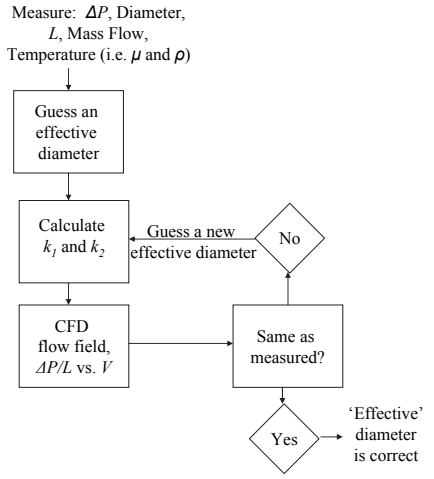

Figure 3. The FEM CFD procedure applied to the 101 mm experimental results to determine the Forchheimer parameters k_1 and k_2 [11].

The geometry used was a representation of the apparatus shown in Figure 2, using measurements with a precision of 0.1 mm. Boundary meshes (5 layers) were inserted along the outer walls where high velocity gradients were anticipated. “Normal” fluid mechanical controlled triangular mesh was used elsewhere. Tighter meshes were tested and found to result in increased computational time and to have negligible influence on the reported results.

The pressure gradient was determined in the z-axis, by using the COMSOL 'probe' function, to establish the local pressure at the precise locations of the side wall pressure taps, see Figure 2.

5. Results

The obtained experimental pressure gradients for the 101 mm diameter filters, with long (3 m) and short inlet (1 m) lengths, are presented in Figure 4. The results for the 49 mm diameter filters are similar in appearance and have been published elsewhere [11].

The summary of the obtained Forchheimer coefficients for the 49 mm and 101 mm diameter filter elements are given in Table 1. Excellent agreement is shown between the values directly calculated from Equation (1), i.e. from the 49 mm results and those obtained by using the procedure shown previously in Figure 3, and the 101 mm filters.

A sample calculation at 0.5 m/s inlet velocity has been performed using both the FEM models for the 101 mm and 49 mm diameter filter elements. The effect of the expansion of the flow on the velocity field for the 101 mm filter element is clearly indicated in Figure 5 (a). The resulting decrease in velocity reduced the pressure gradient for the 101 mm filter element to 501 kPa/m, when compared with the 49 mm filter element with 1612 kPa/m, both at an inlet velocity of 0.5 m/s.

Table 1: Empirically Calculated (49 mm) and Numerically Derived (101 mm) Forchheimer Coefficients for Equation (1) [11].

Filter Type (PPI)	Actual Filter Diameter (m)	FEM Effective Flow Field Diameter (m)	Eq. 1 Forchheimer k_1 (m^2)	Eq. 1 Forchheimer k_2 (m)	Inlet Length (m)
30	48.7	N/A	5.08E-08	5.46E-04	1.0
30	101	65.5	5.57E-08	5.25E-04	1.0
40	101	66.0	3.10E-08	3.38E-04	1.0
50	49.2	N/A	1.57E-08	1.66E-04	1.0
50	101	66.1	1.71E-08	1.69E-04	1.0
50	101	66.1	1.52E-08	1.71E-04	3.0
80	49.1	N/A	6.52E-09	1.15E-04	1.0
80	101	66.5	5.44E-09	9.96E-05	1.0

In Figure 6 comparison is made between FEM calculated and measured results for all experimental velocities, showing individual errors between 0% and 7%, as well as average errors between 0.6% and 4% for each filter type.

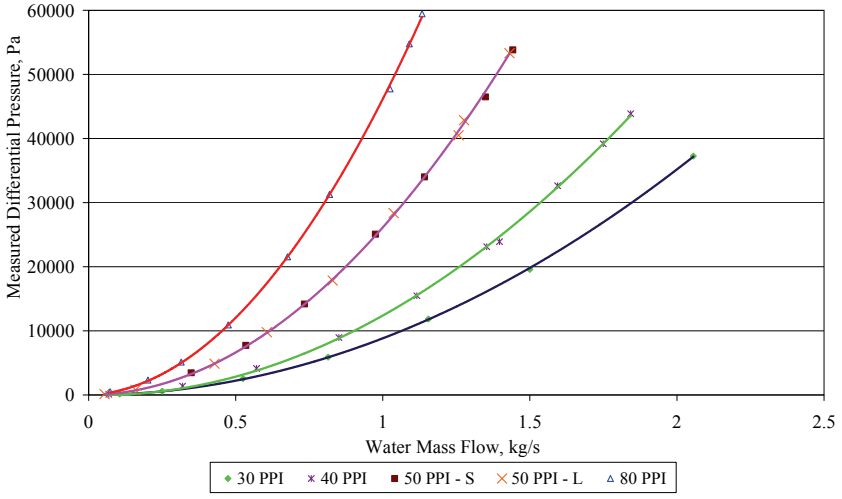

Figure 4. Experimentally measured pressure gradients for the 101 mm 'expanding flow field' design [11].

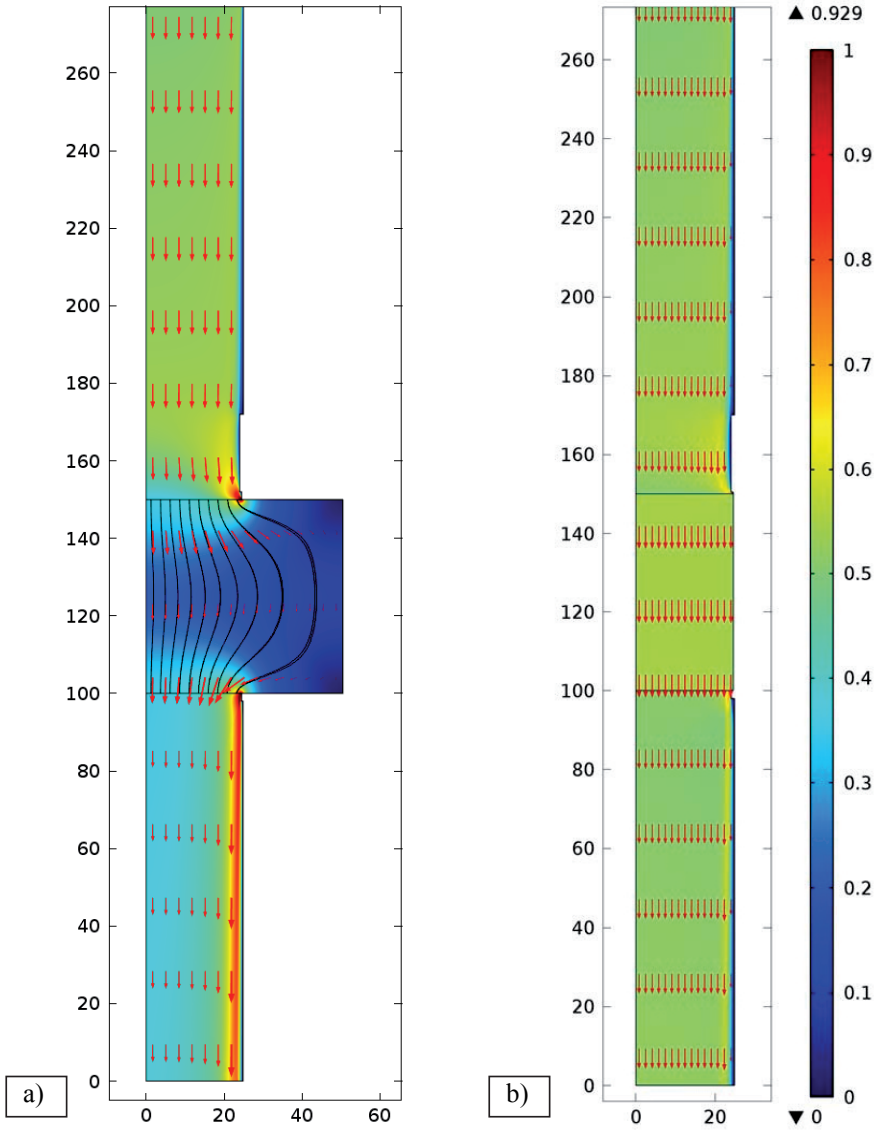

Figure 5. Comparison of calculated flow fields for 50 PPI CFF, i.e. for (a) the 101 mm 'expanding flow field' and (b) the 49 mm 'straight through' designs, both at a 0.5 m/s uniform inlet velocity and for 280 K water temperature. The results are shown with a common 0-1 m/s colour scale.

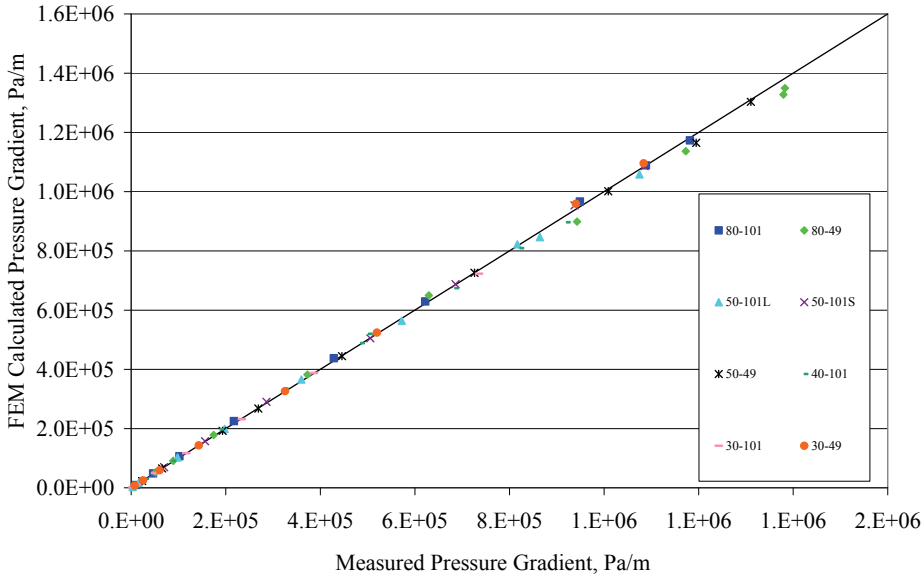

Figure 6. Comparison of FEM calculated and measured pressure gradients, indicating typical errors of <4% for each filter type. S is for a short inlet (1 m) and L is for a long inlet (3 m), as shown previously in Table 1 [11].

6. Discussion

The use of boundary meshes proved critical to achieve an acceptable agreement between model and experimental data, particularly for the 'straight through' 49 mm diameter experimental apparatus. For example, if the results shown in Figure 5 are recalculated without boundary meshes, an error of -18% is obtained for the 49 mm diameter experimental apparatus, and -8.2% for the 101 mm case. Smaller errors of ~±1% can be generated by using inappropriate slip wall boundary criteria, or by using significantly biased inlet flow conditions, rather than the assumed uniform inlet velocity.

Discrepancies between the k_1 and k_2 derived with the help of numerical methods (expanding flow field), and those directly determined experimentally (straight through), were on average within 5%, with no individual difference exceeding 17%. Deviations were such that they were compensated, i.e. a high k_1 value was compensated by a lower k_2 value, resulting in nearly identical total pressure drop for each superficial velocity.

It proved critical to avoid using the automatic second order correlation function built into Excel, as it resulted in errors being concentrated into the first order term k_1, and produced physically meaningless results, e.g. negative k_1 values. Dividing the measured pressure gradient by velocity, and using a linear regression gave improved results. The best results, i.e. those shown in Table 1, were obtained by (i) guessing k_1, (ii) subtracting the first order term from the total gradient, (iii) performing an exponential regression, and (iv) iterating until the desired exponent of 2.00000 was obtained for the second order term [11].

7. Conclusions

A high level of agreement was achieved between the experimental and the 2D axial symmetric CFD FEM results for both the 49 mm diameter 'straight through' design and the 101 mm diameter 'expanding flow field' design. Errors in the range of ±0-7% on predicted pressure drop for individual readings were obtained in both cases.

The agreement obtained between the FEM model of the 49 mm filter apparatus, using the analytically derived Forchheimer coefficients and the experimental data, indicated that there was negligible bypassing of the filter media by the water during the experiments.

The agreement obtained between the analytical 49 mm and the 'numerical' 101 mm Forchheimer coefficients indicated the success of the iterative procedure applied in the present study to deduce the effect of the expanding flow field on the resulting pressure gradients of the 101 mm filter media.

It has been demonstrated that COMSOL can perform CFD calculations under demanding circumstances with a high level of precision, i.e. under high variation in Reynolds numbers, as well as when using both normal fluid flow and porous media.

8. References

1. D. E. Groteke, "The Reduction of Inclusions in Aluminum by Filtration," *Modern Casting,* vol. 73, (1983), 25-27.
2. H. Duval, C. Rivière, É. Laé, P. Le Brun, and J. Guillot, "Pilot-Scale Investigation of Liquid Aluminum Filtration through Ceramic Foam Filters: Comparison between Coulter Counter Measurements and Metallographic Analysis of Spent Filters," *Metallurgical and Materials Transactions B,* vol. 40, (2009), 233-246.
3. S. Instone, M. Badowski, and W. Schneider, "Development of Molten Metal Filtration Technology for Aluminium," *Light Metals,* (2005), 933-938.
4. K. Butcher and D. Rogers, "Update on the Filtration of Aluminum Alloys with Fine Pore Ceramic Foam," *Light Metals,* (1990), 797-803.
5. A. Engelbrecht, "Removal of Solid Inclusions from Molten Aluminium through Ceramic Foam Filtration," *Light Metals,* (2010), 779-784.
6. F. Frisvold, "Filtration of Aluminium: Theory, Mechanisms, and Experiments," PhD. Thesis, Norwegian University of Science and Technology, (1990).
7. C. Conti and P. Netter, "Deep Filtration of Liquid Metals: Application of a Simplified Model Based on the Limiting Trajectory Method," *Separations Technology,* vol. 2, (1992), 46-56.
8. S. Ray, B. Milligan, and N. Keegan, "Measurement of Filtration Performance, Filtration Theory and Practical Applications of Ceramic Foam Filters," *Aluminium Cast House Technology,* (2005), 1-12.
9. B. Hübschen, J. Krüger, J. Keegan, and W. Schneider, "A New Approach for the Investigation of the Fluid Flow in Ceramic Foam Filters," *Light Metals,* (2000), 809–815.
10.P. Forchheimer, "Wasserbewegung Durch Boden," *Z. Ver. Deutsch. Ing,* vol. 45, (1901), 1788.
11. M. W. Kennedy, K. Zhang, R. Fritzsch, S. Akhtar, J. A. Bakken, and R. E. Aune, "Characterization of Ceramic Foam Filters Used for Liquid Metal Filtration," *To be submitted to Metallurgical Transactions B,* (2012), 1-46.
12. L. F. Moody, "Friction Factors for Pipe Flow," *Trans. Asme,* vol. 66, (1944), 671-684.

9. Acknowledgements

The present research was carried out as part of the Norwegian Research Council (NRC) funded BIP Project (No. 179947/I40) RIRA (Remelting and Inclusion Refining of Aluminium). The project partners are as follows: Hydro Aluminium AS, SAPA Heat Transfer AB, Alcoa Norway ANS, Norwegian University of Science and Technology (NTNU) and SINTEF Materials and Chemistry. Funding by the industrial partners and NRC is gratefully acknowledged.

The authors also wish to express their gratitude to Egil Torsetnes at NTNU, Trondheim, Norway, for helping with the design and construction of the experimental apparatus. Sincere gratitude is also due to Kurt Sandaunet at SINTEF, Trondheim, Norway, for his support and help, as well as for the use of the SINTEF laboratory. The assistance of Robert Fritzsch in the SEM and optical analysis of the CFFs is greatly appreciated.

PART III: ELECTROMAGNETICALLY MODIFIED FILTRATION, INCLUDING GRAVITY REFERENCE EXPERIMENTS, AND PRIMING

SUPPLEMENT 5

Electromagnetically Enhanced Filtration of Aluminum Melts

Mark William Kennedy, Shahid Akhtar, Jon Arne Bakken, Ragnhild Elisabeth Aune

Light Metals 2011: Wiley-Blackwell, ISBN 9781118029350, (2011), 763-768.

ELECTROMAGNETICALLY ENHANCED FILTRATION OF ALUMINUM MELTS

Mark William Kennedy[1], Shahid Akhtar[1], Jon Arne Bakken[1], Ragnhild E. Aune[1,2]

[1]Department of Materials Science and Engineering, Norwegian University of Science and Technology, N-7491 Trondheim NORWAY
[2]Department of Materials Science and Engineering, Royal Institute of Technology, 100 44 Stockholm, SWEDEN
Communicating author: ragnhild.aune@ntnu.no

Keywords: Aluminum, Ceramic Foam Filters, Magnetic Field, Meniscus, Coil

Abstract

The major drawback of the use of Ceramic Foam Filters (CFF) for purification of aluminum is their low efficiency for particles in the range of 10-30 μm. The application of electromagnetic force from an induction coil in combination with a filter can cause back mixing and recirculation through the filter media. In the present work an experimental set-up has been designed, built and verified by studying the meniscus behavior of molten aluminum under varying magnetic field strength. Batch type filtration experiments with 30 ppi CFF were also conducted with and without a magnetic field using an A356 aluminum alloy containing 20% anodized and lacquered plates, as well as 20% composite material (A356 base and 15% SiC particles with size range 10-50 μm). The presence of a magnetic field has proven to have both an effect on the build up of the filter cake, as well as on the re-distribution of particles within the filter.

Introduction

Due to increased demand for clean high-performance aluminum products, it has become an increasingly important task to reduce the level of impurities, and especially inclusions, in aluminum melts. It is a well known fact that non-metallic inclusions not only form porosity, but also result in stress concentration, which in turn may affect the static and dynamic properties of aluminum alloy products[1-2]. Traditional processes such as gravity sedimentation/flotation, degassing, flux refining and filtration, have difficulty meeting the cleanliness levels demanded in many applications, due to their low efficiency in removing micrometer-sized inclusions[3].

El-Kaddah *et.al*[4] presented the concept of combining electromagnetic separation with filtration to enhance the inclusion removal efficiency. They did, however, not provide sufficient experimental verification of the idea.

In the present work an experimental set-up including several different induction coils has been designed and verified with respect to the generation of magnetic pressure and hence flow using a 50 Hz AC field. The molten metal meniscus behavior has also been studied as a way of directly evaluating the influence of the magnetic field on the molten metal sample. Different coil designs and a number of different currents were used. It was hoped to qualitatively observe mixing, the size of the meniscus and how great a magnetic pressure that could be developed, without damaging the apparatus or excessive overheating the molten aluminum. In order to demonstrate the effect of back mixing of the fluid through the filter media, batch filtration tests have been conducted with and without a magnetic field.

Theory

The use of electromagnetic fields is an emerging technology for the production of high-quality aluminum alloys with increased melt cleanliness[5]. Electromagnetic fields provide a means of influencing separation processes, without physical contact and added risk of contamination. The liquid metal will be acted upon by the electromagnetic Lorentz force $\vec{F}$ (N/m^3) inducing motion:

$$\vec{F} = \vec{J} \times \vec{B} \qquad (1)$$

where $\vec{J}$ is the induced current density (A/m^2), and $\vec{B}$ the magnetic flux density (also simply referred to as the magnetic field (T)). In addition to generating motion the electromagnetic field will also heat the metal.

The convective flow induced in the liquid metal by the axial variation of the electromagnetic field of a short coil, may adversely affect the separation process[6]. In Figure 1, the variation of the axial magnetic field along the coil length for various coil diameters to length ratios, evaluated using the Biot-Savart Law for an empty coil, are presented. It can be seen in Figure 1, that longer coils give a more powerful magnetic field, which can be very homogenous over much of their length, but with significant end effects. Shorter coils give less axial variation and overall weaker fields, as well as more radial variation of the magnetic field strength (not shown). The possible impact this has on the separation process is not clear; however, it could be expect that a very short coil behaves differently from a very long coil.

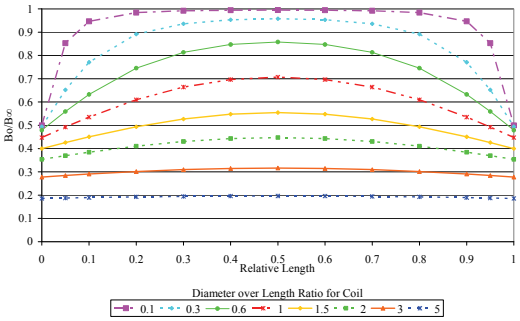

Figure 1. Relative (short coil/equivalent length of infinite coil) axial magnetic flux density for an empty coil is plotted against the shape at constant current and turns per unit length.

In a short coil, the presence of the work piece alters the strength of the axial component of the magnetic field in the air gap, due to the reduced coil aperture. Kennedy *et. al.*[7] have successfully used Equation (2) to estimate the strength of the axial magnetic flux density in a short coil, accounting for the length of the coil and the presence of the work piece:

$$B_0^* = k_N^* B_\infty = k_N^* \mu_o H_\infty = k_N^* \mu_o N_c I_c / l_c \qquad (2)$$

where B_0^* is the axial magnetic flux density in the air gap of a short coil containing a work piece (T), B_∞ the magnetic flux density of an equivalent length of infinite coil without a work peice (T), k_N^* a modified shortness correction factor for a loaded coil, μ_o is the magnetic permiability of free space = 4 π 10^{-7} H/m, N_c is the number of coil turns, I_c is the coil current (A) and l_c is the length of the coil (m).

Vaughan and Williamson[8] developed an equation for a modified short coil correction factor, to account for the presence of the work piece:

$$k_N^* = k_N (1 - [D_w / D_c]^2) + [D_w / D_c]^2 \qquad (3)$$

where k_N is the Nagaoka coefficient, D_w the diameter of the work piece (m), and D_c the diameter of the coil (m). The Nagaoka coefficient is a theoretical factor, which accounts for the reduced strength of the magnetic field in an empty short coil and it has been tabulated elsewhere [9-10].

For the dimensions of typical induction coils, the Nagaoka coefficient can be conveniently estimated by the Wheeler formula[11] as reformulated by Knight[12]:

$$kN = 1/[1 + 0.4502 (Dc + \delta c) / lc)] \qquad (4)$$

where δ_c is the electromagnetic penetration depth in the coil (m).

The magnetic flux density in the air gap is extremely important as it directly relates to the magnitude of the electromagnetic pressure P_m (Pascals) that can be developed as follows:

$$Pm = B0^* 2 / (2 \mu o \mu r) \qquad (5)$$

One problem associated with the electromagnetic separation techniques is the difficulty in generating large Lorentz forces deep within a highly conductive metal. This is especially true for AC fields at high frequencies, due to the skin effect:

$$\delta = (\rho/[\pi f \mu_o \mu_r])^{0.5} \qquad (6)$$

where ρ is the electrical resistivity (ohm m), f the frequency (Hz) and μ_r is the relative permeability of the metal (1 for aluminum).

The electromagnetic penetration depth (δ) is reduced in proportion to the square root of the frequency ($1/\sqrt{f}$), as presented in Figure 2 and Equation (6). As can be seen from Figure 2, the penetration depth becomes very small at high frequency, e.g. ~1 mm for pure liquid aluminum at 100 kHz, while at mains frequencies of 50 or 60 Hz, it is ~35 mm. For magnetically thick samples (*Radius/δ>3*) the magnetic flux density declines nearly exponentially with each penetration depth, resulting in that only a negligible flux remains after about 3 penetration depths. As a result of this, it is therefore not possible to produce significant Lorentz forces deep within a thick work piece of a high conductivity metal at high frequency.

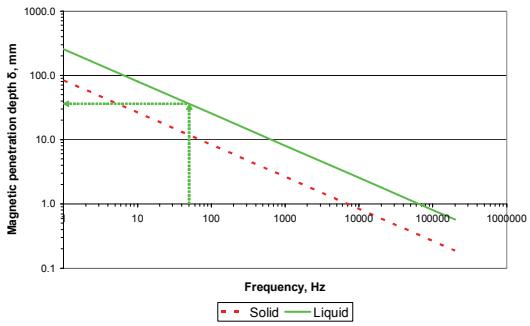

Figure 2. The electromagnetic penetration depth is plotted against the frequency for solid and liquid aluminum.

The use of high frequency does, however, improve the efficiency of induction heating by increasing the ratio of (*Radius/δ*) for a fixed work piece radius. Overheating of the work piece will then limit the amount of current and hence the magnitude of the magnetic field that can be effectively used.

Conducting experiments at mains frequencies, i.e. 50 or 60 Hz, have therefore the following significant advantages:

- deep electromagnetic penetration, and
- powerful magnetic fields without overheating of the work piece.

Experimental

Set Up

Two separate coil designs were produced for use with the meniscus and batch experiments. One coil was a traditional "long" coil (Coil 1), and the other an unusual multi-layer "short" coil (Coil 2), as pictured in Figures 3 a) and b). The multi-layer coil was specifically designed to produce the most powerful magnetic field possible over the desired length of the sample, using the available power supply. The specifications for the coils are given in Table I.

Table I. Specifications for the long (Coil 1) and multi-layer coil (Coil 2).

Coils:	Coil 1 Expt 2	Coil 2 2-1	Coil 2 2-2	Coil 2 2-3	Coil 2 2-1 + 2-2	Coil 2 2-2 + 2-3
Inside diameter, mm	118	126	140	153	126	140
Average diameter, mm	124	132	146	159	132	146
Height, mm	300	104	105	105	107	108
Coil copper tube diameter, mm	6.35	6	6	6	6	6
Coil copper tube thickness, mm	0.762	1	1	1	1	1
Number of turns	41.0	15.5	15.5	15.5	31.0	31.0
Measured inductance of empty coil, μH	71.7	25.1	29.0	33.2	103.3	119.9
Measured resistance at maximum load, ohms	0.0319	0.00928	0.01018	0.01126	0.01962	0.02193
Avg. Coil temperature at maximum load, Deg C	62	23	23	25	23	27

The various sub-coils in Coil 2 could be placed in series or parallel to achieve the most advantageous configuration. The strongest magnetic fields (~0.2 T), as well as the most stable thermal operation, were achieved when the two inner coils were electrically connected in series and operated at the maximum available voltage (~28 V) with the water cooling in parallel and flowing counter currently. A cooling water flow of approximately 3-4 m/s was obtained at 4-6 Bar line pressure.

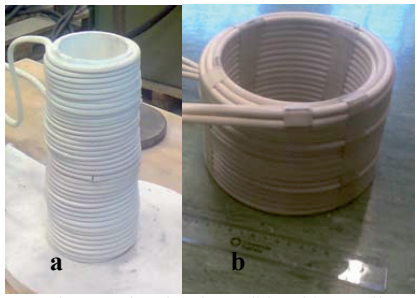

Figure 3. Photographs of a) the traditional long coil (Coil 1), and b) the multi-layer coil (Coil 2).

The transformer used as the power supply was limited to a nominal voltage of 30 V and a maximum of 1500 A. Due to the high resistance of the coils, it was not necessary to compensate the power factor on the secondary side using a capacitor bank. Electrical measurements were conducted using a Fluke 43B Power Quality Analyzer. In Experiments 1 and 2, a 500 A Fluke current probe was used. This probe was however, replaced with a Fluke i1000s AC current probe, with an accuracy of 1% and a precision of 1 A, on all subsequent experiments. The amount of energy entering the liquid metal was determined by subtracting the power lost in the coil (measured empty) from the total power of the system while operating with liquid metal. Electrical values were qualitatively verified using batch calorimetric measurements, which agreed within the accuracy of ~ 5%. For Experiment 2, the obtained values for the current, as well as the power are only indicative as the current probe was used outside of its linear range (readings were later adjusted by calibration against the i1000s probe).

The experimental apparatus were constructed using two lengths of BIMEX 400 fiber riser supplied by Intermet Refractory Products Ltd., with a nominal inside diameter of 102 mm, an outside diameter of 120 mm, and a length of 150 mm. The two lengths were joined together using Fibrefrax moldable cement. The bottom portion of the apparatus was imbedded in a sand mold to provide a leak free bottom.

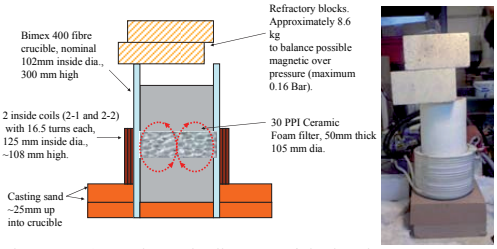

Figure 4. a) A schematic diagram of the batch test apparatus, and b) a photograph of the same.

In the meniscus experiments the coil was positioned in such a way that the bottom of the coil was in level with the top of the sand inside the fiber risers. In the batch filtration experiments, a CFF was cemented in at the junction of the two risers, as shown in Figure 4a). The coil was positioned in such a way that the mid-line of the coil (and the strongest point in the magnetic field) was in level with the bottom of the filter.

Alloy

A standard non-grain refined A356 alloy was used for the study of the meniscus behavior. The chemical composition of the alloy is given in Table II.

Table II. The chemical composition of the A356 alloy in wt. %.

Alloy type	Si	Mg	Fe	Mn	Zn	Ti	Al
A356	7.03	0.41	0.091	0.008	0.005	0.11	Bal

For the batch filtration tests a feed recipe was prepared containing: 60% A356 alloy, 20% anodized and lacquered plates, and 20% A356 composite material containing SiC particles with a size range 10-50 µm. For the meniscus tests, as well as the filtration tests, the alloy was melted in an induction oven at 750 ^{o}C.

Two filtration tests were conducted with 30 ppi CFF, i.e. one test with and one without a magnetic field, in the set-up shown in Figures 4a) and b). Maximum voltage was applied to the coil i.e. ~28 V, for ten minutes after pouring the molten metal. The power was then stopped and the sample solidified.

Results and Discussion

Meniscus tests

Four meniscus experiments and one batch filter test using magnetic field were conducted as summarized in Table III.

Table III. Summary of experimental results

Experiments	Coil	Voltage (V)	Current (A)	Total Power (W)	Load Power (W)	Magnetic Flux Density (T)	Theoretical Magnetic Pressure (Bar)	Liquid Metal Depth (mm)	Meniscus (mm)	Average Temperature (oC)
1	1	14.21	364	4140	260	0.06	0.016	105	10	N/A
2	1 thicker insulatio	27.96	684	16536	680	0.11	0.047	125	58	808
3	2 (1+2 in series)	28.15	730	11900	1270	0.20	0.16	108	70	774
4 meniscus	2 (1+2 in series)	14.40	373	3155	460	0.11	0.049	114	44	650
4 batch filter	2 (1+2 in series)	28.23	723	12200	1930	0.20	0.15	100 over and 100 under the filter	N/A	709

The aluminum was, as previously mentioned, heated to 750^{o}C and added to the unheated crucible where it cooled to ~710^{o}C. Coil 1, the traditional long coil, was used initially. In the first experiment the lowest available voltage (14 V) was used, and in the second experiment the highest (28 V). It was not known at the time if sufficient heating could be produced to hold the sample temperature at either voltage. The meniscuses produced in the first and second experiments are presented in Figure 5a) and b).

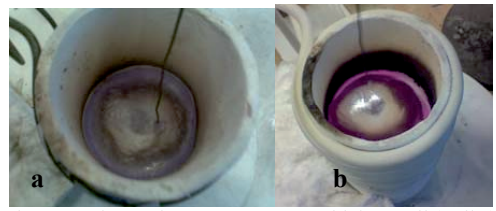

Figure 5. The meniscus measurement with long coil (Coil 1) with a magnetic flux density equal to a) ~0.06 T, and b) ~0.11 T.

It was established that the long coil (Coil 1) was just capable of compensating for heat losses at the lowest voltage, i.e. 14 V, with 260 W delivered for heating the sample. No temperature control was, however, possible. At the highest voltage, i.e. 28 V, 680 W was produced heating the sample to over 850^{o}C within about 10 minutes. The power was

periodically interrupted during the experiment to avoid excessive overheating.

Between experiments 1 and 2, it was found necessary to improve the electrical insulation of the coil, by the addition of a glass fiber sleeve. This caused the length of the coil to change slightly from 275 to 300 mm, and the inside diameter from 120 to 118 mm.

Based on the first experiments, it was realized that a more powerful magnetic field could be produced if the coil was shortened, and if a multi-layer coil was used (giving similar total conductor length and impedance). Fabricating a coil in segments gave more electrical flexibility, and better cooling could be achieved as the length of each segment was shorter and more cooling water could be supplied at the available line pressure.

The inner two layers of the multi-layer coil arrangement (Coil 2) were used in Experiments 3 and 4, first at the highest voltage and subsequently at the lowest. The meniscus formed at the highest magnetic field strength was reduced in diameter and increased in height as presented in Figures 6a) and b). Its motion was extremely dynamic, and it had a tendency to fall onto the side of the coil missing ½ of a turn.

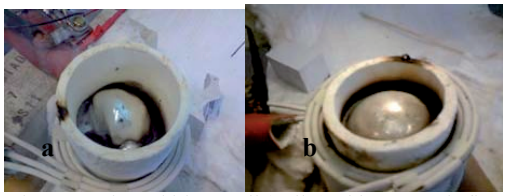

Figure 6. The multi-layer coil (Coil 2) with a magnetic flux density of a) ~0.20 T, and b) ~0.12 T.

The experimental data obtained from Experiment 3 and 4 are summarized in Table III. The meniscus heights as a function of the estimated magnetic flux density in the air gap between the coil and the work piece are plotted in Figure 7.

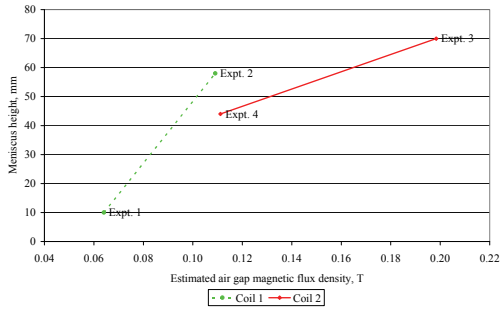

Figure 7. The obtained meniscus height (+/- 5mm) is plotted against the magnetic flux density estimated using Equation (2) for the long coil (Coil 1) and the multi-layer coil (Coil 2).

For the long coil (Coil 1) a greater meniscus height was created for a given magnetic flux density as the coil, and therefore the axial magnetic field, extended well beyond the aluminum pool. With the multi-layer coil (Coil 2), the aluminum was pushed up and partly out of the coil by the magnetic pressure. The observed meniscus height with the multi-layer coil, at the maximum transformer voltage, was sufficient to create back mixing through a filter depth of ~ 50 mm thickness.

Most of the Lorentz forces generated due to Equation (1) are dissipated due to viscous forces (flow) and this results in much less than the theoretically possible height increase in the liquid metal, as indicated in Table III (~10-30% of theoretical was observed).

Batch tests

In order to observe the largest possible difference between the gravity and the magnetic batch tests, the highest available voltage (~28 V) was applied to the coil to create the most powerful magnetic field possible. By adopting Equation (2), the magnetic flux density in the air gap between the coil and the work piece was estimated to be ~0.2 T.

The filter element was positioned in such a way that the bottom of the filter was located in the position of the highest magnetic flux density, as shown in Figure 1. It was believed that this would cause a maximum upwards flow through the filter element.

In the batch filtration tests it was found necessary to pre-heat the filter before starting the experiment to avoid an initial blockage under gravity conditions. Under the influence of the magnetic field preheating was, however, not required due to the resulting conditions caused by the field. The experimental data collected during the magnetic filtration experiment are also summarized in Table III.

During the batch test it was established, that with a sufficient metal height over the filter it was possible to avoid the formation of an excessive meniscus when under the influence of a stronger magnetic field. This experimental condition could be used to reduce the degree of oxidation and dross formation caused by the melt circulation. The degree of melt circulation was established to be so intense, that some of the sand from the bottom of the crucible was drawn from the sand base of the experimental set-up and dispersed into the liquid metal phase located beneath the filter, see Figure 4. Sand particulates were in fact lifted and pushed into the bottom of the filter element giving proof that intense back mixing was taking place during the experiment. The sand base at the bottom of the crucible remained, however, intact during the gravity filtration experiment. The cross section of the bottom part of the ingot with and without the influence of a magnetic field is presented in Figures 8a) and b).

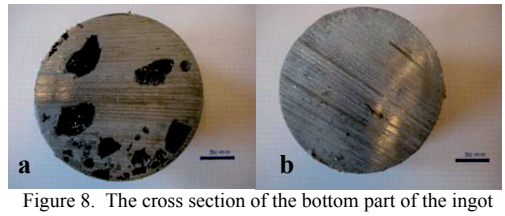

Figure 8. The cross section of the bottom part of the ingot obtained from the batch filtration tests a) with a magnetic field, and b) without a magnetic field.

The cross section of the filter media obtained from the experiments with and without a magnetic field is presented in Figures 9a) and b). In the sample influenced by the magnetic field it was established that the center part of the filter media at the top had been worn down as a result of the strong upward melt circulation through the filter. The filter media with the gravity pouring conditions showed, however no sign of degradation.

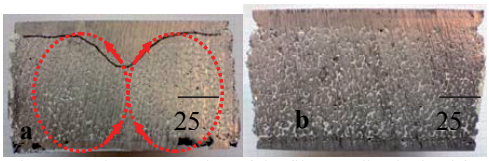

Figure 9. The cross section of the filter media obtained from the batch tests a) with a magnetic field, and b) without a magnetic field.

Representative Scanning Electron Microscope (SEM) micrographs of the filter cake with and without the influence of a magnetic field are presented in Figures 10 a) and b). It can be seen from the figure, that there are more SiC particles present in the filter cake in the sample poured under gravity conditions, while the SiC particle density is less in the sample poured and stirred with the magnetic field. It is assumed that the SiC particles, in this case, were more evenly dispersed due to the upward flow of the aluminum caused by the magnetic back mixing.

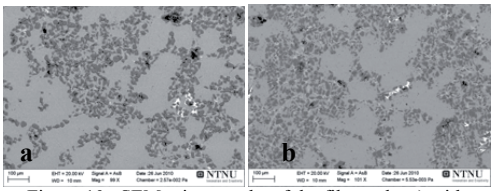

Figure 10. SEM micrographs of the filter cake a) with a magnetic field, and b) without a magnetic field (magnification X 100).

Conclusions

An experimental set-up has been designed and verified for the fluid re-circulation under different transformer voltages and coil designs. The largest meniscus height was observed using a multi-layer coil arrangement and a maximum transformer voltage of 28 V. Melt circulation under the influence of a magnetic field has proven to be effective in distribution of SiC particles.

Future Work

In industrial casting operations, a bulk flow field is produced in the filter by the gravity flow of metal, passing though the filter at a velocity of ~1 cm/s[13]. An example from the literature[14] is presented in Figure 11, indicating that a magnetic field should be capable of generating an internal flow velocity an order of magnitude greater than the normal industrial flow velocity range. Additional parametric studies will be conducted to explore the influence of the magnetic field on aluminum and inclusions flowing through a filter element.

Acknowledgements

The authors wish to express their gratitude to Egil Torsetnes at NTNU, Trondheim, Norway, for helping with the design and construction of the experimental apparatus. Deepest gratitude is also due to Kurt Sandaunet at Sintef, Trondheim, Norway, for the use of the Sintef laboratory and his contribution in the execution of the experiments. Special thanks to Liss Pedersen at Alcoa, Lista, Norway, for the supply of filter materials. The author would also like to acknowledge the funding from the Norwegian Research Council through the RIRA project.

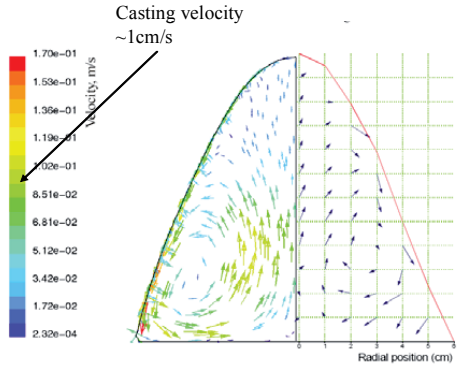

Figure 11. A simulation of the flow velocity and magnetic head produced in cold crucible experiments [14].

References

1. O. Majidi, S.G. Shabestari, and M.R. Aboutalebi, "Study of Fluxing Temperature in Molten Aluminum Refining Process", *Journal of Mat Pro Tech*, 182 (2007), 450–455.
2. B.W. Zhang, Z.M. Ren, and J.X. Wu, "Continuous Electromagnetic Separation of Inclusion from Aluminum Melt Using Alternating Current", *Trans Nonferrous Met SOC China,* 16(2006), 33-38.
3. K. Li, J. Wang, D. Shu, T.X. Li, B.D. Sun, and Y.H. Zhou, "Theoretical and Experimental Investigation of Aluminum Melt Cleaning Using Alternating Electromagnetic Field", *Materials Letters*, 56 (2002), 215– 220.
4. N. El-Kaddah, A.D. Patel, and T.T Natarajan, "The Electromagnetic Filtration of Molten Aluminum Using an Induced-Current Separator", *Journal of Materials*, 46 (1995).
5. Z.T. Zhang, Q.T. Guo, F.Y. Yu, J. Li, J. Zhang and T.J. Li, "Motion Behavior of Non-Metallic Particles Under High Frequency Magnetic Field", *Trans. Nonferrous Met SOC China*, 19 (2009), 674-680.
6. D. Shu , B. Sun, K. Li, and Y. Zhou, "Particle Trajectories in Aluminium Melt Flowing in a Square Channel Under an Alternating Magnetic Field Generated by a Solenoid", *Scripta Materialia*, 48 (2003), 1385–1390.
7. M.W. Kennedy, S. Akhtar, J.A. Bakken, and R.E. Aune, "Review of Classical Design Methods as Applied to Aluminum Billet Heating with Induction Coils", submitted to EPD Congress 2011, TMS.
8. J. Vaughan and J. Williamson, "Design of Induction-Heating Coils for Cylindrical Nonmagnetic Loads," *American Institute of Electrical Engineers, Transactions of the*, 64, (1945), 587-592.
9. H. Nagaoka, "The Inductance Coefficients of Solenoids," *Journal of the College of Science,* 27, (1909), 18-33.
10. E. B. Rosa and F. Grover, "Formulas and Tables for the Calculation of Mutual and Self Induction," *Scientific Papers of the Bureau of Standards,* No. 169., (1916), 5-231.
11. H. Wheeler, "Simple Inductance Formulas for Radio Coils," *Proceedings of the IRE,* 16, (1928), 1398-1400.

12. D. Knight. (2010, August 25). *3.1. Solenoids: Part 1.* http://www.g3ynh.info/zdocs/magnetics/part_1.html
13. C. Dupuis, G. Béland, J.P., "Filtration Efficiency of Ceramic Foam Filters for Production of High Quality Molten Aluminum Alloys," (Paper presented at the 32nd Annual Canadian Conference of Metallurgists, 29th August – 2nd September), 1993.

14. E. Baake, A. Umbrashko, B. Nacke, A. Jakovics, and A. Bojarevics, "Experimental Investigations and LES Modeling of the Turbulent Melt Flow and Temperature Distribution in the Cold Crucible Induction Furnace", (Paper presented at the 4th International Conference on Electromagnetic Processing of Materials, Lyon, France, 14-17 October, 2003).

SUPPLEMENT 6

Electromagnetically Modified Filtration of Liquid Aluminium with a Ceramic Foam Filter

Robert Fritzsch, Mark William Kennedy, Shahid Akhtar,
Jon Arne Bakken, Ragnhild Elisabeth Aune

Accepted for publication by Journal of Iron and Steel Research, International, (2012), 1-4.

Electromagnetically Modified Filtration of Liquid Aluminium with a Ceramic Foam Filter

R. Fritzsch[1], M.W. Kennedy[1], S. Akhtar[2], J.A. Bakken[1], R.E. Aune[1,3]

[1]Dept. of Materials Science and Engineering, Norwegian University of Science and Technology, 7491 Trondheim, NORWAY
[2] Hydro Aluminium Karmøy, 4265 Håvik, NORWAY
[3]Dept. of Materials Science and Engineering, Royal Institute of Technology, 100 44 Stockholm, SWEDEN

Abstract: Conventional Ceramic Foam Filter (CFF) technology has some difficulties in removing fine particulates (*e.g.* < 20 µm) from liquid aluminium. In the present work the filtration behaviour of 30, 50 and 80 ppi CFF filters have been studied in the presence of magnetic fields in the range of 0.06-0.2T, produced by induction coils operated at 50 Hz. A feed recipe containing 90 wt. % of the aluminium alloy A356 doped with 10 wt. % A356 composite, containing 15 wt. % SiC particles with a particle size ranging from 13 to 23 µm, was used. When the results obtained for the experiments conducted under the influence of a magnetic field where compared with similar reference gravity filtration experiments profound changes were observed in the distribution of particulates within, over and below the filter. Significant improvements in the wetting behaviour of the liquid metal to the CFF surface were also observed. It is believed that a successful change in filtration mechanisms is obtained as a result of the presence of the Lorentz forces and the metal recirculation produced by the magnetic field. The magnitude of the Lorentz forces, *i.e.* the magnetic pressure, are in the present work discussed in relation to the filtration results, and quantified based on experimental data and validated 2D axial symmetric Finite Element Modelling (FEM).
Keywords: electromagnetic, filtration, Ceramic Foam Filter, CFF

1. Introduction

Premium quality aluminium castings require a high level of metal cleanliness, and are crucial for critical structural components. The development of more efficient filtration methods for liquid aluminium is therefore essential in order to produce very clean aluminium, *i.e.* have conditions that allows for particulates down to 10 µm to be removed. As a result, the particulate removal efficiency of CFF's has become a subject of interest.
The generation of a magnetic field by an induction coil in combination with a CFF causes recirculation of the melt through the filter media, modifying the inclusion separation. Applying an alternating magnetic field produced by a solenoid has clearly several advantages, *i.e.* (i) avoidance of contamination by physical contact with the stirring device, (ii) no sub-cooling during filtration, (iii) better priming of the filter element with a lower metallic head, and (iv) subsequently higher casting rates for high pores per inch (ppi) filter grades [1].
In the present study the influence of the magnetic field on the priming and wetting ability that the aluminium alloy A356 has on the ceramic surface of the CFF will be studied, as well as the possible impact it may have on the filtration mechanisms inside the ceramic filters by analysing the distribution of the 13-23 µm SiC particles. 2-D axial symmetric COMSOL® (Version 4.2) models and analytical modelling will be performed to estimate the heat and Lorentz forces produced, as well as to study the flow pattern induced in the melt inside of the filter elements.

2. Materials and Experimental Methods

In the present experimental set-up the time varying magnetic field induces currents in the molten metal that is contained in the apparatus. The cross product of the induced current and the magnetic field generates in turn a magnetic pressure, and the gradient of the flux density along the axis of the coil creates a pressure gradient. The pressure gradient results in a curl which then induces a bulk flow in the metal. The curl of the Lorentz force is highly dependent on the conductivity of the metal and the effective conductivity of the metal within the CFF, which is reduced due to the tortuosity and porosity of the filter. The induced liquid metal velocity within the CFF can be determined by using the fluid permeability of the filter media. Due to the high induced velocity within the filter both the Darcian and Non-Darcian permeability terms are required to be solved for the resulting flow field using a Finite Element Model (FEM). A review of the pertinent theory [2], the experimental development [1], and the validation [3-4] of the COMSOL® induction heating/magnetic field model [5] have already been published earlier by members of the present research group. The details of the model computations are beyond the scope of the present paper and can be found elsewhere [3-5].

Bach filtration experiments were conducted using ~5000 g of molten charge, *i.e.* 90 wt. % of the aluminium alloy A356 doped with 10 wt. % A356 composites, containing 15 wt. % SiC particles with a particle size ranging from

13 to 23 µm. The melt was heated to ~750°C in a high frequency induction furnace, *i.e.* one separate melt for each batch filtration experiment. The experimental filtration set-up was energized at 50 Hz, and the molten metal was poured into the apparatus until a metallic head of ~100 mm above the filter was reached. For each filter grade, experiments were conducted at 3 and 10 minutes treatment times. Gravity reference experiments were also performed for each filter grade. Special trials to investigate the required gravity priming height of the different grade CFF's studied were also executed. For the metallographic evaluation of the obtained results 12 samples were extracted from each of the filter elements. Scanning Electron Microscopy (SEM) was used to analyse the samples using the Back Scattered Electron (BSE) mode. The magnetic field density was estimated using FEM by integrating from the bottom to the top of the innermost coil along the surface of the work piece, and the average Lorentz force along the surface of the filter integrated from the bottom to the top of the filter. The Lorentz force obtained under the filter was, however, integrated from the bottom of the liquid metal to the bottom of the filter.

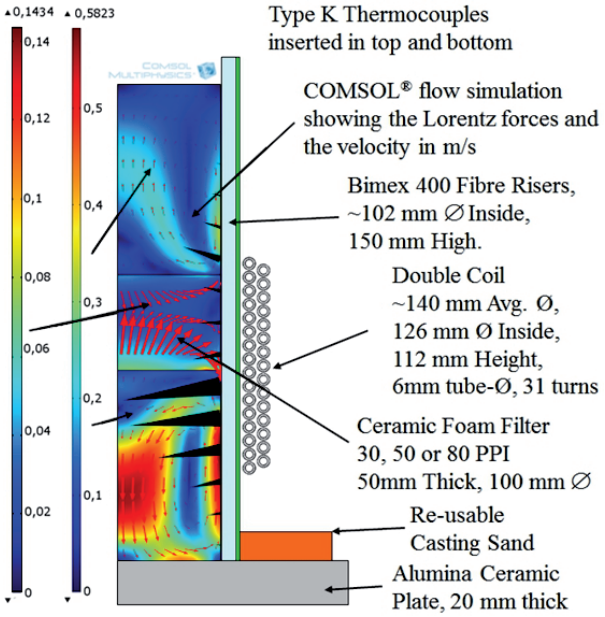

Figure 1: Presently adopted experimental setup with COMSOL® FEM simulation of the flow field (arrows and shading), as well as the Lorentz forces (cones), for a 50 ppi CFF. The applied conditions are summarised in Table 1. A detailed description of the coil design has been presented in earlier papers by members of the present research group [2-5].

In Figure 1 the experimental apparatus used (i) for the 50 and 80 ppi experiments, (ii) for the FEM calculated flow field for a 50 ppi CFF, and (iii) for the FEM calculated induced Lorentz forces on the outer surface of the work piece is presented. It should be mentioned that due to the effect of the Lorentz forces, the flow velocity inside the filter is estimated to be one order of magnitude higher compared to normal industrial casting conditions (as indicated in Figure 1). Typical experimental data and FEM model results are summarised in Table 1.

Table 1: Summary of experimental and modelling data obtained using a magnetic field and various CFF grades. The apparent porosity has been calculated from the total filter density (*e.g.* 0.47 g/cm^3) and the density of the ceramic particles (*i.e.* 3.48 g/cm^3).

CFF (ppi)	Temp. (°C)	Apparent Porosity (%)	Metal Conductivity (MS/m)[5]	Amps (A)	FEM Magnetic Field (T)	FEM Calculated Power (kW)	Effective Resistivity of Filter (R_f/R_m)	Average Surface Lorentz Force Filter/Under-Filter (10^4 N/m^3)
30	727	89.3	3.22	715	0.166	1.70	1.5	10.8 / 10.9
50	765	86.3	3.16	719	0.156	1.54	2.5	5.48 / 11.0
80	705	86.5	3.26	718	0.157	1.44	3.7	2.51 / 11.4

3. Results and Discussion

3.1 Priming and wetting

CFF's are normally operated in a "filter bowl" and are primed using a gravity head of liquid metal with a recommended pre-heating procedure. In other words, the gravity head forces the metal into and through the CFF, displacing much of the entrapped air. The poor wetting characteristics of alumina by aluminium [7], and the need to remove the trapped air, can lead to difficulties at the start of the filtration process (particularly with high pore density filters). The typical heights of industrial priming heads are, for different grades of commercial filters, plotted in Figure 2. As can be seen from the figure, the presence of an electromagnetic field secures a significant reduction in the required metal head during priming.

In Figures 3 a) and b) metallographic pictures of the 50 and 80 ppi CFF's after a gravity priming experiment with 100 mm metal head above the filter element is presented. As can be seen from the figures the experiments failed and the molten metal solidified over the filter elements with nearly complete lack of penetration of metal into the filters. This was, however, expected based on the industrial priming data presented in Figure 2.

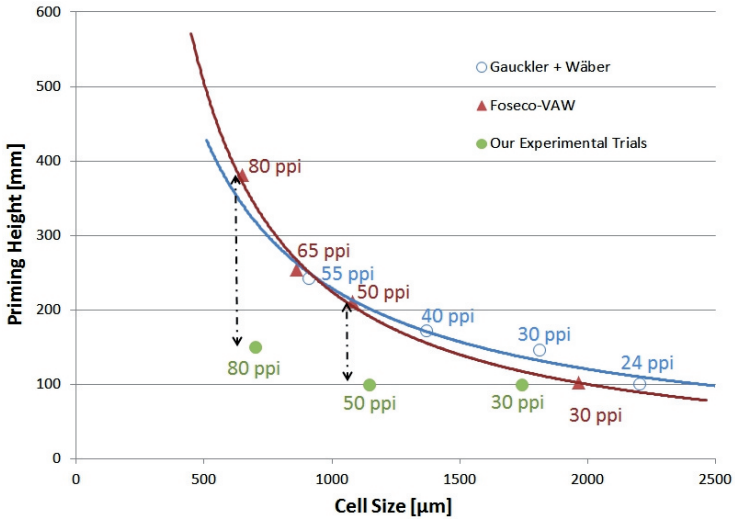

Figure 2: The presently measured priming height from the electromagnetic field experiments are plotted as a function of the filter cell size. The measured priming height from earlier publications has been included as a comparison [8].

When applying a magnetic field of ~0.16 T, the filters studied were nearly perfectly primed and wetted using the same 100 mm of metal head, see Figures 3 c) and d) representing the results obtained for 3 and 10 minutes treatment time. The SEM micrographs obtained shows a greatly improved wetting, as well as successful removal of gas with an increased electromagnetic stirring time. The electromagnetic priming phenomena are now the subject of an US patent application filed by the present authors [9].

3.2 Particle redistribution

For gravity filtration it is common to observe a dense filter cake above the CFF, as well as bridging and clogging in the upper part of the filter. Profound changes in the distribution of particles, both inside and below the filter

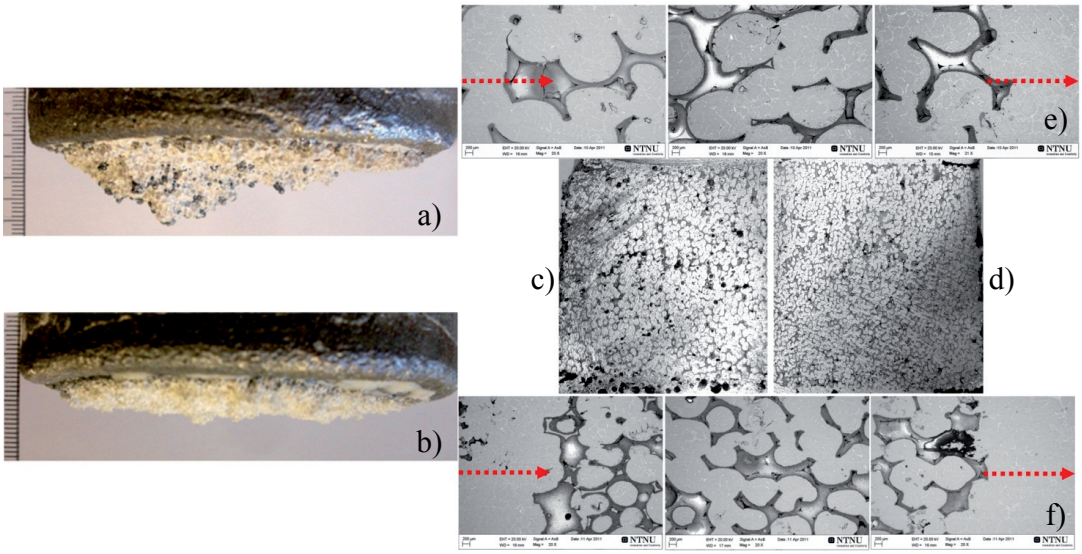

Figure 3: Unsuccessful gravity experiments with (a) 50 ppi CFF's and (b) 80 ppi CFF's. Fully primed and well wetted filters were obtained after 3 minutes of electromagnetic stirring, for (c) 50 ppi CFF's, and for (d) 80 ppi CFF's shown as half filter sections. Complete gas removal was obtained after 10 minutes of electromagnetic stirring for 80 ppi CFF's. The arrows represent the flow direction of the melt.

media have, however, been observed in the present work due to the influence of the electromagnetic field, see Figure 4. As can be seen from the figure, when using electromagnetic forces the highest particle density obtained was observed in Area 2. In addition, the backflow of the melt caused by the curl in the Lorentz forces has resulted in Area 3 also having a higher concentration of particles. Area 4, however, was nearly particle free due to that clean metal re-enters the filter from below.

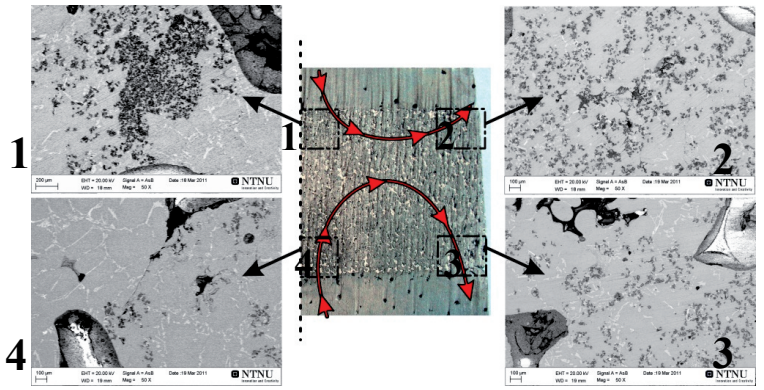

Figure 4: Observed distribution of particles in a 30 ppi half filter section and the FEM estimated flow field (arrow) inside the filter media. The numbers mark the areas clockwise starting at the centre on the top (Area 1) and ending in the centre below the filter (Area 4). In Area 2 the highest density of particles was observed, followed by Area 3 and Area 1 with a more or less equal distribution of particles. Nearly no particles were observed in Area 4. The original gravity feed of metal was from the top to the bottom.

4. Conclusion

The present study has proven that by applying an electromagnetic field a substantial improvement of the wetting between alumina and liquid aluminium in 30, 50 and 80 ppi CFF's can be obtained with a significant reduction of the required metal head. Nearly perfect priming of high pore density filters was demonstrated. A redistribution of particles inside the CFF was also observed. Based on this it is clear that the electromagnetically induced bulk flow secures that the filter media do not clog, and changes the filtration mode from cake-filtration to deep-bed and in-bed-cake-filtration for the high pore density filters.

5. Acknowledgements

The present study was carried out as part of the RIRA (Remelting and Inclusion Refining of Aluminium) project funded by the Norwegian Research Council (NRC) - BIP Project No. 179947/I40. The authors wish to express their gratitude to Egil Torsetnes (NTNU, Trondheim, Norway) for helping with design and construction of the experimental apparatus. Deepest gratitude is also due to Kurt Sandaunet (SINTEF, Trondheim, Norway) for the use of the SINTEF laboratory and his contribution in the execution of the experiments. Also, a special thanks to Liss Pedersen (Alcoa, Lista, Norway) for the supply of filter materials, and Kexu Zhang (M.Sc. student at NTNU, Trondheim, Norway) for providing the CFF permeability data.

6. References

[1] KENNEDY M W, AKHTAR S, BAKKEN J A, AUNE R E, Electromagnetically Enhanced Filtration of Aluminium Melts. Light Metals, 2011, 763-768.
[2] KENNEDY M W, AKHTAR S, BAKKEN J A, AUNE R E, Review of Classical Design Methods as Applied to Aluminium Billet Heating with Induction Coils. EPD Congress, 2011, 707-722.
[3] KENNEDY M W, AKHTAR S, BAKKEN J A, AUNE R E, Analytical and Experimental Validation of Electromagnetic Simulations Using COMSOL®, re Inductance, Induction Heating and Magnetic Fields presented at the COMSOL User Conference, Stuttgart, Germany, 2012, 1-9.
[4] KENNEDY M W, AKHTAR S, BAKKEN J A, AUNE R E, Analytical and FEM Modelling of Aluminium Billets Induction Heating with Experimental Verification. Light Metals, 2012, 269-275.
[5] KENNEDY M W, AKHTAR S, BAKKEN J A, AUNE R E, Improved Short Coil Correction Factor for Induction Heating of Billets. 3rd International Symposium on High-Temperature Metallurgical Processing, 2012, 373-382.
[6] BRANDT R, NEUER G, Electrical Resistivity and Thermal Conductivity of Pure Aluminium and Aluminium Alloys up to and above the Melting Temperature. International Journal of Thermophysics, 2007, 1429-1446.
[7] FREUND H, ZEISER T, SCHWEIGER W, INAYAT A, Determining the Specific Surface Area of Ceramic Foams: The Tetrakaidecahedra Model Revisited. Chemical Engineering Science, 2011, 1179-1188.
[8] KEEGAN N J, SCHNEIDER W, KRUG H P, Evaluation of the Efficiency of Fine Pore Ceramic Foam Filters. Light Metals, 1999, 1031-1041.
[9] KENNEDY M W, FRITZSCH R, AKTHAR S, BAKKEN J A, AUNE R E, U.S. Patent Application 61/639,196, Apparatus and Method for Priming a Molten Metal Filter, May, 2012.

SUPPLEMENT 7

Electromagnetically Modified Filtration of Aluminum Melts Part I: Electromagnetic Theory and 30 PPI Ceramic Foam Filter Experimental Results

Mark William Kennedy, Shahid Akhtar, Jon Arne Bakken, Ragnhild Elisabeth Aune

Metallurgical and Material Transactions B
DOI 10.1007/s11663-013-9798-8
ISSN 1073-5615
Published On-line February 6, 2013, 1-15.

Electromagnetically Modified Filtration of Aluminum Melts—Part I: Electromagnetic Theory and 30 PPI Ceramic Foam Filter Experimental Results

MARK WILLIAM KENNEDY, SHAHID AKHTAR, JON ARNE BAKKEN, and RAGNHILD E. AUNE

In the present work, laboratory-scale continuous filtration tests of liquid A356 aluminum alloy have been performed. The tests were conducted using standard 30 PPI (pores per inch) ceramic foam filters combined with magnetic flux densities (~0.1 and 0.2 T), produced using two different induction coils operated at 50 Hz AC. A reference filtration test was also carried out under gravity conditions, *i.e.*, without an applied magnetic field. The obtained results clearly prove that the magnetic field has a significant affect on the distribution of SiC particles. The influence of the electromagnetic Lorentz forces and induced bulk metal flow on the obtained filtration efficiencies and on the wetting behavior of the filter media by liquid aluminum is discussed. The magnitudes of the Lorentz forces produced by the induction coils are quantified based on analytical and COMSOL 4.2® finite element modeling.

DOI: 10.1007/s11663-013-9798-8

I. INTRODUCTION

A typical aluminum melt normally contains a large number of small non-metallic inclusion particulates, less than or equal to 50 μm in size. These include particles of oxides (Al_2O_3), spinels ($MgO{\cdot}Al_2O_3$), and carbides (SiC, Al_4C_3), with a higher melting point than the host metal. The presence of these inclusions in the aluminum melt not only reduces the static and dynamic mechanical properties of the material but also decreases the corrosion resistance and has detrimental effects on the surface finish of the end product. Non-metallic inclusions can also act as nucleation sites for hydrogen porosity.[1] Remelting of post-consumed and process aluminum scrap also reveals new challenges not only in relation to environmental issues but also with respect to the metal yield and quality.

Removal of inclusions from liquid aluminum alloys is today an important melt treatment process. The increasing demand for high purity aluminum components to be used in the automotive and aviation industry, as well as for construction and electrical purposes, has put a strain on the manufacturers to produce cleaner aluminum. Attention is therefore being given to finding new or improved processes and/or process routes for the removal of non-metallic inclusions from aluminum melts.[2]

Many different methods for the removal of inclusions from molten aluminum already exist, *i.e.*, (i) settling, (ii) flotation, (iii) degassing, and (iv) liquid metal filtration. Each of these methods is capable of removing a size range of inclusions, but the methods are generally ineffective at removing inclusions of <10 μm and each have unique process limitations.[3]

The filtration process has a complex mechanism influenced by hydrodynamic factors such as fluid flow, turbulence, surface and body forces, as well as chemical and metallurgical interactions between the inclusions, the filter media, and the liquid metal. These filtration mechanisms are not thoroughly understood and deeper theoretic and experimental analyses are needed to explore the potential for improving the cleaning efficiency of the filter media.[4] In the aluminum filtration process, the most frequently used filter media are ceramic foam filters (CFFs).

The principle of electromagnetic separation by Lorentz forces ($\mathbf{J} \times \mathbf{B}$) was described mathematically in 1954 by Leenov and Kolin.[5] A schematic representation of the Lorentz forces and the reaction forces acting on a non-conducting particle in a curl-free magnetic field is presented in Figure 1. Figure 1 does not represent the geometry used in the current work, but is meant to be illustrative of the electromagnetic principles applied. In this concept, non-conductive particles migrate through the melt in a direction opposite to the Lorentz forces produced by the cross product of a homogeneous magnetic field and a uniform current distribution. The non-conductive particles present in the fluid will expe-

MARK WILLIAM KENNEDY, PhD Candidate, is with the Department of Material Science and Engineering, Norwegian University of Science and Technology (NTNU), 7491 Trondheim, Norway and Chief Technology Officer, Proval Partners S.A., 1004 Lausanne, Switzerland. Contact e-mail: m.kennedy@provalp.com SHAHID AKHTAR, Technical Manager, is with the Hydro Aluminium, Karmøy, 4265 Håvik, Norway. JON ARNE BAKKEN, Professor Emeritus, is with the Department of Material Science and Engineering, Norwegian University of Science and Technology (NTNU). RAGNHILD E. AUNE, Professor, is with the Department of Material Science and Engineering, Norwegian University of Science and Technology (NTNU) and also with the Department of Material Science and Engineering, Royal Institute of Technology (KTH), 100 44 Stockholm, Sweden.

Manuscript submitted December 2, 2011.

Published online: 06 February 2013

rience a pressure gradient created by the Lorentz forces, but not the Lorentz forces themselves. This will cause the particles to migrate in a direction counter to the Lorentz forces. An early example of the application of this technique was reported in 1968 by Vilinskas and Schiltz,[6] *i.e.*, the removal of zirconium oxide spheres from liquid sodium. Various methods of applying this principle in metallurgical processing were patented by Conti *et al.* in 1989.[7]

There are several studies reported in the literature illustrating the migration of oxide and SiC inclusions under the influence of electromagnetic fields.[8–12] Based on metallographic examinations, it has been established that in the presence of an electromagnetic field, the particles are collected into the stagnant hydrodynamic boundary layers. While the potential of this innovative method has been demonstrated in small batch tests, its implementation in industrial application under continuous flow conditions has not been reported for aluminum. A significant problem at present is that powerful and curl-free Lorentz forces are difficult to achieve in industrial practice.[13]

In 1990, El-Kaddah *et al.*[14,15] presented the concept of combining electromagnetic separation with filtration to control secondary mixing effects and to enhance the inclusion removal efficiency. Sufficient experimental verification of this concept was, however, not provided at that time. A more recent patent application on the use of flow modifying devices of a high collection area has been filed by other researchers.[16]

The current authors have recently shown that the melt circulation through the filter media is driven by the strong curl present in the Lorentz forces.[17] A figure indicating the electromagnetic field and Lorentz forces present in the filtration apparatus used in these experiments (as modeled with the commercial finite element code COMSOL 4.2®) is shown in Figure 2. If a standard induction coil of constant pitch is used in such an experiment, a large curl is always present in the Lorentz forces due to strong coil end effects (*i.e.*, practical coils are not infinite in length). The magnitude of the curl in the experimental apparatus is increased by the reduced effective electrical conductivity of the filter element itself.

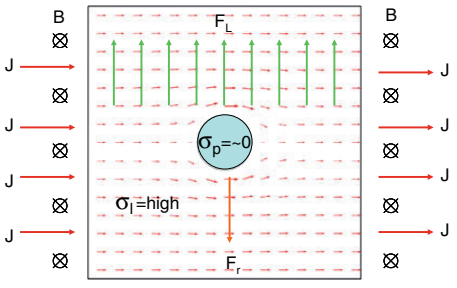

Fig. 1—The Lorentz forces (F_L) and the reaction forces (F_r) acting on a non-conducting particle in a curl-free magnetic field. Note the impact of the particulate on the current distribution (J = current density (A/m^2); B = magnetic flux density (T); σ_l = liquid phase electrical conductivity (S/m); σ_p = particulate electrical conductivity (S/m)).

For the 30 PPI filters used in these experiments, there is ~50 pct higher electrical resistance or 33 pct lower effective electrical conductivity inside of the filter due to the obstructions (tortuosity) and reduced conducting area (porosity), as has recently been reported elsewhere.[18] In Figure 2, the impact of the variable "effective" electrical conductivity between the metal and filter regions is very clearly indicated by the shape and intensity of the electromagnetic field and the resulting magnitude of the Lorentz forces produced, as indicated by the length of the arrows. The resulting curl is figuratively illustrated by the rotating dotted circle.

With strong melt flow driven by the Lorentz forces, it was expected that the melt recirculation and not the *Leenov-Kolin "pinch" effect* would dominate the distribution of the particles over, within, and under the filters used in these experiments. Only at the outer wall, where velocities are low (*i.e.*, in the hydrodynamic boundary layer) and the Lorentz forces are maximized, is it reasonable to assume that magnetic particle migration may occur under the influence of the "pinch" effect.

In the present study, an experimental setup was designed for laboratory-scale continuous filtration flow testing. The tests were conducted with standard 30 PPI CFFs under the influence of a magnetic flux density of ~0.1 and 0.2 T. One reference gravity flow test was also conducted for comparison. A new analytical expression of the time average Lorentz forces will be presented and

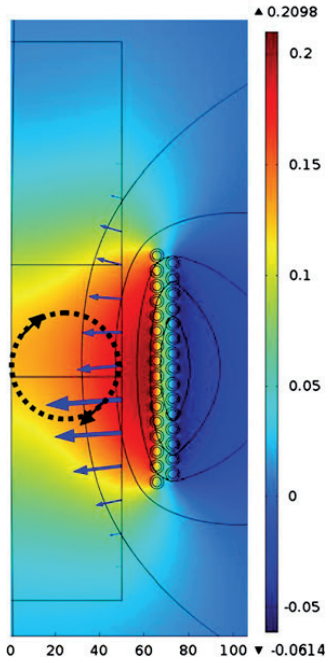

Fig. 2—Actual experimental geometry showing a COMSOL 4.2® simulation of the RMS magnetic flux density (T) as well as the relative magnitude of the Lorentz forces acting on the surface of the test samples (solid arrows) for Coil #2. The direction of the expected bulk aluminum circulation is marked as a dotted circle with arrows.

compared with finite element modeling using COMSOL 4.2®. The filter elements used in the filtration flow tests were characterized using standard metallographic techniques. Overall quantitative filtration efficiency and efficiency as a function of particle size are reported for gravity reference and high field strength conditions using a computerized macro-automated photographic particle analysis technique.

II. THEORY

Leenov and Kolin[5] derived the following equation describing the reaction force acting on a low conductivity particle present in a high conductivity fluid when subjected to a curl-free Lorentz force field:

$$\mathbf{F}_r = -\frac{3}{2}\frac{\sigma_l - \sigma_p}{2\sigma_l + \sigma_p}\frac{\pi d_p^3}{6}\mathbf{F}_L \quad [1]$$

where $\mathbf{F}_r$ is the reaction force experienced by the particulate (N), $\mathbf{F}_L$ is the Lorentz force acting on the fluid (N/m^3), σ_l is the electrical conductivity of the liquid phase (S/m), σ_p is the particle electrical conductivity (S/m), and d_p is the particle diameter (m). For non-conducting particles, Eq. [1] can be reduced to the following:

$$\mathbf{F}_r = -\frac{\pi d_p^3}{8}\mathbf{F}_L \quad [2]$$

where

$$\mathbf{F}_L = \mathbf{J} \times \mathbf{B} \quad [3]$$

assuming that

$$\nabla \times \mathbf{F}_L = 0 \quad [4]$$

It is a well-known fact that a curl-free Lorentz force field can be effectively produced by combining a homogenous direct current and a non-varying magnetic field working at 90 deg as figuratively illustrated in Figure 1. However, if a curl exists in the Lorentz force field, it will produce electromagnetic or magneto-hydrodynamic (MHD) stirring. This is referred to as the secondary mixing effect, as observed by several investigators.[13,14] These mixing effects result in particles being rapidly transported from the bulk of the melt to the crucible walls (in crucible batch experiments) where the stagnant hydrodynamic boundary layers exist. The particles can then be collected into the boundary layers through the reaction force presented in Eq. [1] or [2]. A limited volume, however, exists within which to accumulate particles and the ability of the particles to resist re-entrainment can be questioned.

In the present study, two different induction coil designs have been used to simultaneously produce (i) a magnetic field, (ii) induce eddy currents to produce resistive heating, and (iii) produce Lorentz forces through the interaction of the magnetic flux density and the induced currents. The eddy current density (**J**) is related to the curl of the magnetic field intensity ($\nabla \times \mathbf{H}$) and the magnetic flux density (**B**) as presented in the following equation:

$$\mathbf{J} = \nabla \times \mathbf{H} = \frac{\nabla \times \mathbf{B}}{\mu} \quad [5]$$

where **J** is the eddy current density (A/m^2), **H** is the magnetic field intensity (A(-turns)/m), **B** is the magnetic flux density (T), and μ is the electromagnetic permeability of the conductive fluid, which is equal to $4\pi \times 10^{-7}$ for aluminum (H/m). Further details related to the magnetic fields produced by "short" solenoidal coils and induction heating can be found elsewhere.[19,20]

Most coils used for induction heating are "short,"[19–21] and have a significant radial and axial variation in their magnetic flux density. This is axially evaluated using the Biot-Savart law[20] and presented in Figure 3 in a dimensionless form. As indicated in Figure 3, a large variation in the magnetic flux density does exist for "short" coils along their z-axis when the diameter to length ratio of the coil (D_c/l_c) lies between 0.3 and 2.0, which are typical values for induction coils.

It is the time-varying value of the local magnetic flux density in the z-direction which induces the current in the liquid metal in the phi direction. It should be pointed out that this is in accordance with Eq. [5]. The variation in the local flux density will result in a similar variation in the local current density. In other words, an axial variation in **H** and **B** will produce a similar variation in **J**. These local variations will then combine to produce a powerful curl in the z-direction of the Lorentz forces, resulting in strong MHD mixing.

Lorentz forces orders of magnitude stronger than the gravity forces can easily be generated using "short" induction coils. This will in turn result in MHD mixing, which will dominate the hydrodynamic flow and cause robust recirculation. The investigation of the curl in the Lorentz forces, and the resulting recirculation of the melt, is the main focus of the present study.

It is important to point out that in Eq. [3], **J** and **B** are both vectors and phasors (time-varying functions) that can be represented by complex vector quantities, *i.e.*, by $\underline{\mathbf{J}}$ and $\underline{\mathbf{B}}$. The phase shift between $\underline{\mathbf{J}}$ and $\underline{\mathbf{B}}$ changes with the penetration depth into the workpiece, making the

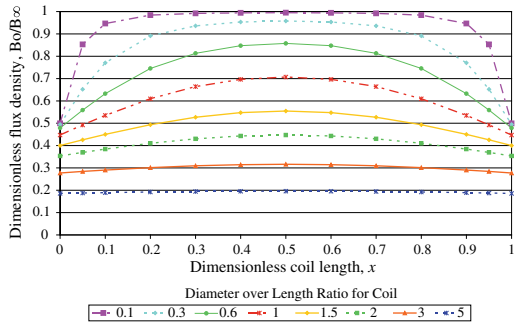

Fig. 3—The dimensionless flux density B_0/B_∞ (z-component) for different coil diameter to length ratios (D_c/l_c) as a function of the dimensionless coil length (x).[20]

solution for the Lorentz forces challenging. The following formula is proposed for the time-averaged values, *i.e.*, the real part of $\underline{\mathbf{J}} \times \underline{\mathbf{B}}$:

$$|\mathbf{F}_{\mathrm{L}}| = \mathrm{Re}\{\underline{\mathbf{J}}^* \times \underline{\mathbf{B}}\} \qquad [6]$$

where $\mathbf{J}^*$ is the complex conjugate of the root mean square (RMS) current density (scalar values of $\mathrm{A/m^2}$) and $\underline{\mathbf{B}}$ is the RMS complex magnetic flux density (scalar values of T). From the definition of the vector cross product and the right hand rule, the time average force is known to be in the negative r-direction. The Lorentz component in the z-direction is in the present study assumed to be negligible.

Inserting the relevant phi and axial components of $\mathbf{J}$ and $\mathbf{B}$ in accordance with Eq. [3] into Eq. [6] and applying the modified zero order Kelvin Bessel functions will result in the following expression for the time-averaged Lorentz forces:

$$F_{\mathrm{RMS}} = -\frac{\mu_{\mathrm{r}}\mu_0}{\delta_{\mathrm{l}}}\left(\frac{k_{\mathrm{N}}^* N_{\mathrm{c}} I_{\mathrm{c}}}{l_{\mathrm{c}}}\right)^2 \varphi(R,r) = -\frac{\mu_{\mathrm{r}}\mu_0}{\delta_{\mathrm{l}}}\, H_{\mathrm{s}}^2 \varphi(R,r) \qquad [7]$$

where μ_{r} is the relative magnetic permeability with a suggested value of 1.0000 for air, copper, and aluminum (unitless), μ_0 is the magnetic permeability of free space 4×10^{-7} (H/m), k_{N}^* is the modified short coil correction factor (unitless), N_{c} is the number of coil turns, I_{c} is the coil RMS current (A), l_{c} is the length of the coil (m), φ is a dimensionless correction factor accounting for the magnitude and phase shift of $\underline{\mathbf{J}}$ and $\underline{\mathbf{B}}$ at depth r, δ_{l} is the electromagnetic penetration depth in the liquid metal (m), and H_{s} is the average z-component of the surface magnetic field intensity (A(-turn)/m). The negative sign in Eq. [7] indicates an orientation in the negative radial direction. The dimensionless correction factor $\varphi(R,r)$ can be expressed as follows:

$$\varphi(R,r) = \frac{\sqrt{2}(\mathrm{ber}\xi_{\mathrm{r}}\mathrm{ber}'\xi_r + \mathrm{bei}\xi_{\mathrm{r}}\mathrm{bei}'\xi_{\mathrm{r}})}{\mathrm{ber}^2(\xi_{\mathrm{R}}) + \mathrm{bei}^2(\xi_{\mathrm{R}})} \qquad [8]$$

where ξ_{r} is the dimensionless reference depth where the Lorentz force is to be evaluated and ξ_{R} is the dimensionless reference depth at the surface. Ber, ber′, bei, and bei′ are the real and imaginary parts of the zero order modified Kelvin Bessel functions and their derivatives, the solutions to which can be found using numerical solvers[22] or lookup tables.[23] The following is valid for the dimensionless reference depths:

$$\xi_{\mathrm{R}} = \frac{\sqrt{2}R}{\delta_{\mathrm{l}}}, \quad \xi_{\mathrm{r}} = \frac{\sqrt{2}r}{\delta_{\mathrm{l}}} \qquad [9]$$

where R is the outer radius (m) and r is the radius at which the Lorentz forces are to be evaluated (m).

For the electromagnetic penetration depth, the following is valid:

$$\delta_{\mathrm{l}} = \left(\frac{\rho_{\mathrm{l}}}{\pi\mu_{\mathrm{r}}\mu_0 f}\right)^{1/2} \qquad [10]$$

where ρ_{l} is the resistivity of the liquid metal (Ω m) and f is the frequency (Hz).

Equations [7] through [10] are similar to the equations previously published by Korovin[24,25]; however, the real and imaginary parts have been separated in Eq. [8]. In the English translations of Korovin's work,[24,25] the real and imaginary parts of his equations were confounded by the accidental omission of the $\sqrt{-1}$ and the resulting equation cannot be used for any practical purpose. The present authors have also modified Eq. [7] to include the frequency adjusted "short" coil correction factor,[20] without which it is not possible to analytically estimate the Lorentz forces with less than about a factor of two errors, *i.e.*,

$$k_{\mathrm{N}}^* = k_{\mathrm{N}}\left(1 - \left(\frac{D_{\mathrm{l}} - \delta_{\mathrm{l}}}{D_{\mathrm{c}} + \delta_{\mathrm{c}}}\right)^2\right) + \left(\frac{D_{\mathrm{l}} - \delta_{\mathrm{l}}}{D_{\mathrm{c}} + \delta_{\mathrm{c}}}\right)^2 \qquad [11]$$

where k_{N} is the "air-core" "short" coil correction factor of Nagaoka,[26] D_{l} is the outside diameter of the liquid metal (m), D_{c} is the inside diameter of the coil (m), and δ_{c} is the electromagnetic penetration depth into the coil (m).

The empirical formula proposed by Knight[27]

$$k_{\mathrm{N}} = \frac{1}{1 + 0.4502\left(\frac{(D_{\mathrm{c}} + \delta_{\mathrm{c}})}{l_{\mathrm{c}}}\right)} \qquad [12]$$

conveniently estimates the "air-core" "short" coil correction factor to ~3 significant digits. It should be pointed out that Eqs. [11] and [12] are one-dimensional correction factors. To compare the analytical results with 2D axial symmetric finite element modeling, a line integral must be calculated at each radial position of interest, *i.e.*, a line taken from the top to the bottom of the coil.

To evaluate Eqs. [7] through [12], it is necessary to estimate the electrical resistivity of the liquid aluminum as a function of temperature. The data of Brandt and Neuer[28] have in the present study been selected for the calculation of the electrical resistivity of the liquid metal. Their data for metal containing 7 wt pct Si and 0.6 wt pct Mg can be represented as follows

$$\rho_{\mathrm{l}} = \rho_0(1 + \alpha_{894}\,[T - 894\ \mathrm{K}]) \qquad [13]$$

where ρ_0 is the resistivity of the liquid metal at the reference temperature T (Ω m), α_{894} is the temperature coefficient of resistivity ($\mathrm{K^{-1}}$), and T is the reference temperature [894 K (621 °C)]. The following values are recommended: $\rho_0 = 2.883 \times 10^{-7}\ \Omega$ m, $\alpha_{894} = 5.59 \times 10^{-4}\ \mathrm{K^{-1}}$.[28]

The conductivity of the experimental alloy with additions of SiC and oxide particles can be estimated by dividing Eq. [13] by the fraction of the molten metal excluding the additions of particles. It should be noted that Eq. [13] only gives the resistivity of the metal and cannot be used to estimate the effective resistivity within the filter media. The "effective" resistivity of the filters must be found experimentally due to the reduction in the conducting area produced by the non-conducting

ceramic filter and the increased tortuosity. Values for 30 to 80 PPI filters have been found to be 1.5 for 30 PPI, 2.5 for 40 PPI, 2.5 for 50 PPI, and 3.7 for 80 PPI, expressed as a ratio to the metal resistivity.[29]

In Figure 4, the correction factor, φ, calculated from Eq. [8], is plotted for different values of the dimensionless radius, r/R, as a function of the dimensionless reference depth at the surface, ξ_R. As can be seen from the figure, at larger values of ξ_R, a higher value is obtained for the correction factor, φ, at the surface. It can also be seen that the correction factor φ decreases rapidly with the penetration into the liquid metal.

For a fixed outer radius, R, a large dimensionless reference depth, ξ_R, corresponds to a low electromagnetic penetration depth, δ_l, and thus a high frequency, f. At high frequencies, the magnitude of Eq. [7] becomes very large at the surface (due to the low electromagnetic penetration depth obtained in the denominator as well as the high value of the correction factor, φ), and the obtained electromagnetic force becomes very powerful, but confined to a thin layer, *i.e.*, the Lorentz force boundary layer. This effect is clearly seen in Figure 5 where the time average Lorentz forces, F_{RMS}, are plotted against the dimensionless radius, r/R, for different values of the dimensionless reference depth at the surface, ξ_R, equivalent to frequencies from 16 Hz to 14.4 kHz.

III. EXPERIMENTAL

A. *Coil Specifications and Electrical Measurements*

Experiments were conducted using a flow test apparatus with two different coil designs for high and low magnetic flux densities (~0.1 and 0.2 T). For comparison, one gravity experiment was also performed in the same apparatus. Each of the coils used in the present experiments was constructed from copper tubing with 6 mm inner diameter and 1 mm wall thickness. The coils were electrically insulated using a 0.7-mm-thick high temperature glass fiber sleeve and wrapped with glass fiber tape to prevent vibration. Detailed information on the coils is summarized in Table I.

Electrical measurements (kW, kVA, V, A, and cos φ) were taken using a power analyzer from Fluke, USA (Fluke 43B), with a resolution of 0.1 kW. Current measurements were made with an inductive current probe from Fluke, USA (i1000S), with an accuracy of ± 1 pct and a resolution of 1 A. The coil resistance was determined first without the liquid metal present, when operating at steady state conditions. The electrical parameters were then measured under actual test conditions with the presence of liquid metal. The net power input to the liquid metal was further determined using the measured current and the obtained change in the measured resistance.

B. *Setup*

The experimental apparatus was constructed using three lengths of BIMEX 400 fiber riser supplied by Intermet Refractory Products Ltd., U.K., with a nominal inner diameter of 102 mm, an outer diameter of ~125 mm, and a length of 150 mm. The three lengths of riser tubes were joined together using Fibrefrax® moldable cement.

In the continuous flow filtration experiments, a 30 PPI CFF was cemented into the junction of the two bottom risers, as shown in Figure 6. The coil was positioned in such a way that the mid-line of the coil and the strongest point in the magnetic field were in line with the bottom of the filter, as shown in Figures 6 and 7. The bottom section of the apparatus was glued to a 20-mm-thick ceramic alumina plate, in which a 3.2-mm hole was drilled to provide a flow control orifice. Casting sand was placed around the coil and the fiber riser tubes to ensure proper insulation of the equipment assembly and further to avoid the risk of any molten metal leakage during testing.

The temperature over and under the filter was measured using Inconel-sheathed K type thermocouples. The liquid metal flow through the filter per unit

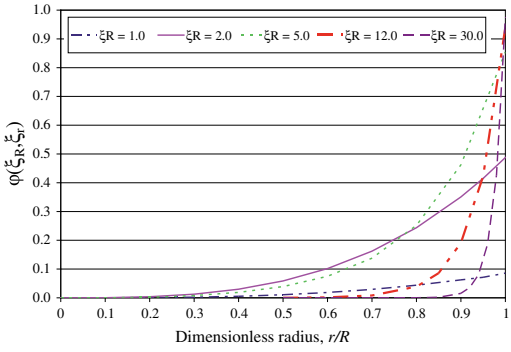

Fig. 4—The solution to Eq. [8] as a function of the dimensionless radius (r/R) for different values of the dimensionless reference depth at the surface (ξ_R).

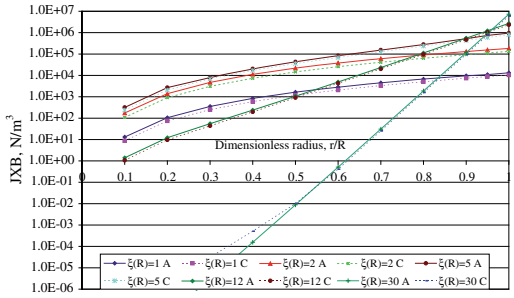

Fig. 5—Comparison of the time-averaged Lorentz force estimates from Eq. [7] and from COMSOL 4.2®. The calculations were performed for 100 mm in diameter of liquid A356 alloy (with 4 pct non-conductive solids) at 980 K (707 °C) using 932 A in a "short" coil (Coil #1).

Table I. Summary of Data for Single and Double Layer Coils

Coils	Coil #1 Single Coil	Coil #2 Double Coil
Inside diameter (mm)	126	126
Average diameter (mm)	132	140
Height (mm)	111	107
Diameter to height ratio	1.18	1.31
Coil copper tube diameter (mm)	6	6
Coil copper tube thickness (mm)	1	1
Number of turns	16.5	31.0
Measured inductance of empty coil (μH)	27.6	103.3
Measured resistance at maximum load (Ω)	0.01082	0.01962
Avg. coil temperature at maximum load [K (°C)]	316 (43)	296 (23)

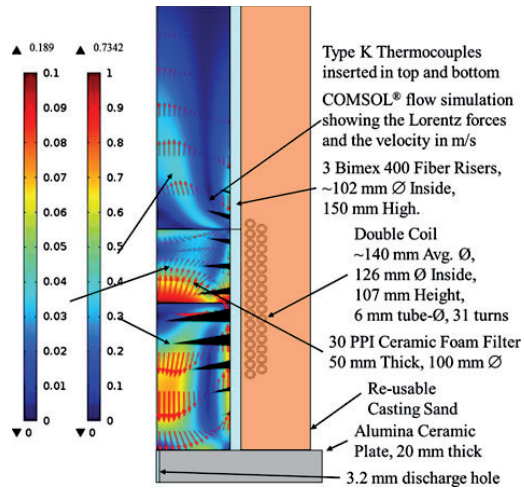

Fig. 6—A schematic drawing of the flow test apparatus with COMSOL® FEM simulation of the flow field (arrows and shading), as well as the Lorentz forces (cones), for a 30 PPI CFF in the absence of bulk flow, *i.e.*, in "batch" mode.

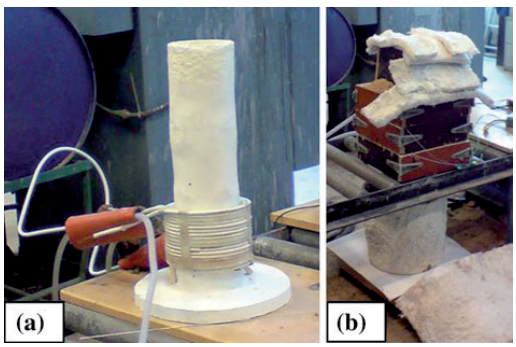

Fig. 7—Photographs of the flow test apparatus: (*a*) the double coil and fiber crucibles with alumina base plate and (*b*) the apparatus fully assembled.

time was determined by measuring the weight change as a function of time on a 100-kg scale with an accuracy of 0.01 kg. The temperature and weight values were recorded using a digital logger system.

During the experiments, metal was continuously added to maintain 250 mm of metal head over the filter. This was continued until the supply crucible (which had a capacity of 18 kg) was empty. The tests were terminated when the metal ceased to flow from the bottom orifice of the apparatus.

C. *Materials and Sample Analysis*

A standard non-grain refined A356 alloy was used for all the continuous filtration flow tests. The chemical composition of the alloy is given in Table II.

For the flow filtration tests, a feed recipe was prepared containing 60 pct A356 alloy, 20 pct anodized and lacquered plates, and 20 pct A356 composite material containing 15 wt pct SiC particles with a reported size range of 13 to 23 μm. The feed recipe alloy was melted in an induction furnace at a target temperature of 1023 K (750 °C). The melt was skimmed to remove the dross formed on the surface of the melt prior to pouring into the flow test apparatus. The dross consisted mainly of thick oxide films originating from the added anodized and lacquered plates.

For the filter element metallographic investigations, the filter media were cut into five slices using a high speed water jet. After cutting, the specimens were mounted in a cold mounted resin and further sanded using SiC-based papers (P80-P4000 Grit) to a surface finish of 5 μm. After sanding, the samples were polished using diamond suspensions with nominal grain sizes of 3 and 1 μm, each for 2 minutes with the lowest possible force on a polishing disk. Ethanol was used as a lubricant during the polishing, until a mirror-like surface finish was obtained. The hard SiC particles and soft aluminum matrix made developing a successful polishing method challenging.

The quantitative filtration efficiency for both gravity and electromagnetic field operation was determined in a second round of experiments, using 90 pct by weight A356 alloy and 10 pct by weight of the same A356 composite material containing SiC particles as used previously. A large batch of 150 kg of melt was produced in a graphite mixer-agitated resistance heated furnace for use with several experiments. The anodized

Table II. Chemical Composition of the A356 Alloy in Weight Percentage

Alloy Type	Si	Mg	Fe	Mn	Zn	Ti	Al
A356	7.03	0.41	0.091	0.008	0.005	0.11	bal

plates were eliminated due to the quantity of dross they produced and the significant loss of SiC particles that resulted. The initial quantity of SiC was reduced by 50 pct for these experiments.

Rapidly solidified metallographic samples were analyzed from before (eight samples averaged) and during the flow filtration trials (two each for gravity and electromagnetic field operation averaged, taken during the initial constant flow velocity phase). Quantitative filtration efficiency as a function of particle size has been determined using a series of digital images taken from the rapidly solidified samples. The samples were machined flat, polished to a mirror-like finish using the same procedure as for the filter sections, and optically analyzed using an LEICA MEF4M white light microscope, equipped with a Jenoptic ProgRes-C10 Plus, 10 MP digital camera. 40 pictures at 10 times magnification were taken of each sample and computer analyzed using Image-Pro® Plus Version 7.0 macro-automated image processing and analysis software. The software ran a macro to load and analyze all the pictures for each sample as a batch to determine the number and area of each individual particle and the fraction of the total area of the sample occupied by particulates.

Overall efficiency (E_{total}) could be determined by comparing the normalized count of particles (*i.e.*, particles per total area) before and after filtration.

$$E_{\text{total}} = \frac{\text{Normalized Count In} - \text{Normalized Count Out}}{\text{Normalized Count In}} \quad [14]$$

Efficiency by size ($E_{\text{size fraction } x}$) was determined using the equivalent spherical particle diameters in the ranges from 2 to 5, 5 to 10, 10 to 15, 15 to 20, and 20 to 25 μm and comparing the particle counts before and after filtration for identical photographic areas.

$$E_{\text{size fraction } x} = \frac{\text{Normalized Count In}_{\text{size fraction } x} - \text{Normalized Count Out}_{\text{size fraction } x}}{\text{Normalized Count In}_{\text{size fraction } x}} \quad [15]$$

The equivalent spherical particle diameter is the spherical particle with the same area as the observed particle, correcting for the fact that the observed particle has been cut at a random "latitude" by the machining and polishing. The stereoscopic effects have been corrected by multiplying the obtained particle diameters by the average correction factor of $\sqrt{1.5}$ appropriate for spherical particles cut at a random location.[30]

Particles less than 2 μm could not be counted by this automated method with any precision for the 10 times magnification used. Below 2 μm, "objects" like dendrites and scratches began to be counted in addition to particles.

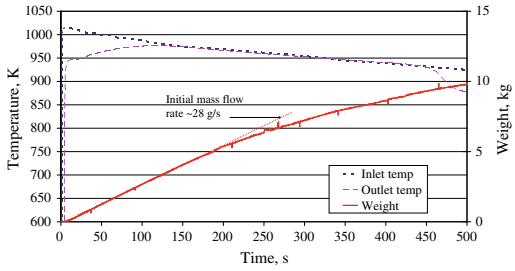

Fig. 8—Gravity test experimental data.

IV. RESULTS AND DISCUSSION

The obtained results from the gravity experiment are plotted in Figure 8 and the obtained results from the experiment using the highest magnetic flux density, *i.e.*, Coil #2 at ~0.2 T, are plotted in Figure 9. As can be seen from the figures, a decrease in the feed metal temperature with time was obtained. In the case of Coil #2, however, the outlet temperature remained stable due to the resulting induction heating effects. In the case of the gravity experiment, the outlet temperature proves to have equalized with the inlet temperature, which also declined throughout the experiment. It can also be seen from Figures 8 and 9 that the discharge rates were slightly higher in the experiments performed under the influence of a magnetic field. This is believed to be due to thermal/viscosity effects or the magnetic pressure produced by the Lorentz forces.

All the experimental values logged during the present study are summarized in Table III. It should be pointed out that the resistivity values presented in Table III are for the metal alone and that the electromagnetic penetration depth in the metal phase has been adjusted to allow for 96 pct of the theoretic conducting area, *i.e.*, the presence of non-conducting particulates. The metal-free space velocity over the filter area was 15 mm/s in

the case of the gravity discharge and 20 mm/s in the case of the coil operation.

In Table IV, the magnitude of the Lorentz force is analytically estimated by using Eqs. [7] through [13]. The obtained results are compared to the data generated from the finite element modeling using COMSOL 4.2®. Both solutions indicate that the Lorentz forces are approximately one order of magnitude greater than the gravity forces. As a result, the Lorentz forces can be assumed to dominate the hydrodynamics of the process.

It should be pointed out that as the COMSOL 4.2® model is 2D axial symmetric, there is no exact correspondence between the geometry in the experimental setup and the model. A 17 turn coil (Coil #1) was used to model the experimental coil of 16.5 turns. In the case of the two-layered coil (Coil #2), one 16 turn layer and one 15 turn coil layer were used to model the two 15.5 turn layers of the experimental coil. For Coil #2, Eqs. [7] through [13] were numerically solved taking the average coil diameter located between the two coil layers into consideration. These equations are only valid for a single layer coil; however, this procedure has even proven to give good agreement between the calculated and measured power input (discrepancies of ±10 to 20 pct).

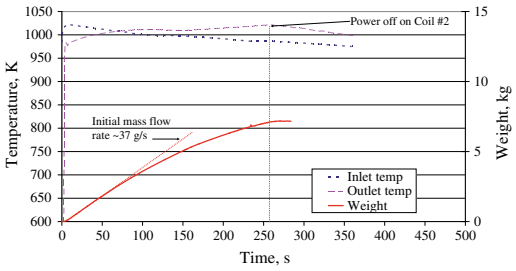

Fig. 9—High magnetic field experimental data obtained for Coil #2 at ~0.2 T, *i.e.*, the highest magnetic flux density.

In the absence of the "short" coil correction factor, *i.e.*, the result of Eq. [11], errors of more than a factor of two would be experienced in the estimated Lorentz forces using Eq. [7]. It should be noted that the Lorenz forces estimated using both COMSOL 4.2® and Eq. [7] are evaluated only at the surface, *i.e.*, radius = R, and represent an averaged or integrated value over the full height of the coil. In this comparison, the effect of the filter was excluded as Eq. [7] does not allow for variable electrical conductivity, *i.e.*, metal was assumed along the full coil height.

A representative magneto-hydrodynamic (MHD) simulation has been performed for Coil #2 using COMSOL 4.2® and is included as part of Figure 6. The flow field was calculated for the physical parameters presented in Table V. A separate article describes the careful measurement of pressure drop, Forchheimer equation[31] parameter derivations, and the filter physical characterization (porosity and effective electrical conductivity measurements) required to ensure the validity of the simulation.[29]

In Figure 6, the flow field resulting from the curl in the Lorentz forces can now be clearly seen from the arrows in the liquid metal and filter domains. The velocities in the two domains are shown by the two scale bars, indicating a maximum velocity in the liquid metal of 0.73 and 0.19 m/s in the filter media. The filter velocity is approximately one order of magnitude larger than normal velocities encountered in the gravity filtration of aluminum by CFFs, showing the dominating influence of the electromagnetic Lorentz forces on the resulting flow field.

A. *Filter Cross Sections*

In Figures 10(a) through (c), representative cross sections of the filters used during the flow tests are presented. In the case of the filtration tests performed under gravity conditions, almost no wetting is obtained in the top section of the filter, while some wetted grains

Table III. Summary of Experimental Data

Experimental Case	Voltage (V)	Current (A)	Power (kW)	Net Power (kW)	Average Temperature [K (°C)]	Equation [13] Estimated Metal Resistivity (Ω m)	Equation [10] Feed Recipe 8 (mm)
Coil #1	13.30	932	10.0	0.8	980 (707)	3.02E−07	39.9
Coil #2	28.58	715	12.7	1.8	1005 (732)	3.06E−07	40.2
Gravity	N/A	N/A	0	0	959 (686)	N/A	N/A

Table IV. Comparison of Calculated Lorentz Force Estimates from Analytical Equations and COMSOL 4.2®

Experimental Case	Equation [11] Short Coil Correction Factor (unitless)	Calculated Average Air-Gap Flux Density (T)	Equation [9] ξ_R and ξ_r at Surface (Unitless)	Equation [8] φ (Unitless)	Equation [7] Lorentz Forces at Surface (kN/m^3)	COMSOL Estimate of Lorentz Force (kN/m^3)
Coil #1	0.725	0.126	1.77	0.351	−111	−93
Coil #2	0.697	0.181	1.76	0.351	−229	−182
Gravity	N/A	0	N/A	N/A	0	0

Table V. Summary of Data Used in FEM Flow Field Simulation

Model Criteria	Value	Units	References
Forchheimer Darcy term, k_1	5.08	10^{-8} m^2	[29]
Forchheimer non-Darcy term, k_2	5.46	10^{-4} m	[29]
Filter total porosity, ε	0.892	Unitless	[29]
Liquid metal density, ρ	2390	kg/m^3	[46]
Liquid metal viscosity, μ	1.0	mPa S	[47]
σ_{metal}-containing particles	3.14	MS/m	[28]
Filter resistance ratio, $\sigma_{filter}/\sigma_{metal}$	1.5	Unitless	[18]
Current, I	715	A	—
Frequency, f	50	Hz	—
Coil	#2	—	—

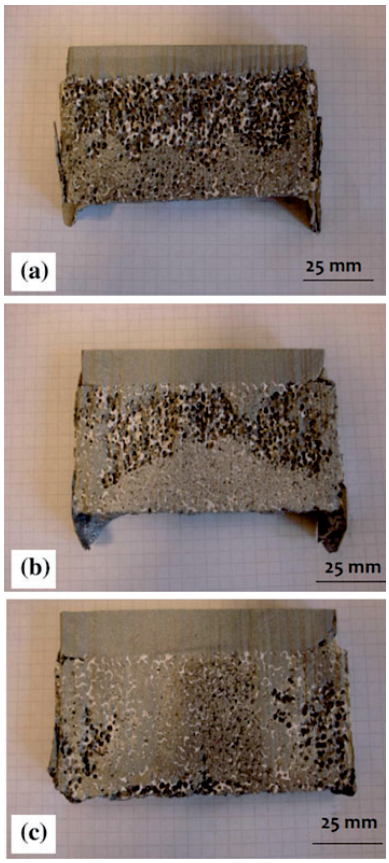

Fig. 10—Filter cross sections from flow tests performed under different experimental conditions, *i.e.*, (*a*) gravity, (*b*) low magnetic flux density (Coil #1), and (*c*) high magnetic flux density (Coil #2).

are observed at the bottom section, see Figure 10(a). Even from the filtration tests performed with low magnetic flux density (Coil #1 at ~0.1 T), non-wetted grains are obtained at the top section of the filter, but complete wetting is observed at the bottom section, see Figure 10(b). Filter grains are completely wetted by the molten metal when performing the filtration tests with high magnetic flux density (Coil #2 at ~0.2 T), see Figure 10(c). The presented cross sections clearly demonstrate the effect that the magnetic field strength has on the molten metal when filtered through a conventional non-conductive filter media.

B. *Particle Distribution Inside the Filter*

In Figures 11 to 14(a) through (c), representative optical micrographs resulting from gravity flow tests and high magnetic flux density tests, using Coil #2 at ~0.2 T, are presented. As can be seen from Figures 11(a) and 12(a), the filter cake is intact and dense in the case of the gravity filtration test, while the cake is disrupted and less dense in the case of filtration under the influence of a electromagnetic field. It can also be seen from the figures that there are more SiC particles present on top of the filter in the sample poured under gravity conditions, while the SiC particle density is less in the sample poured and stirred with the electromagnetic field. Under gravity conditions, there is clearly no wetting of the filter grains in the central regions of the filter, while complete wetting is obtained in the case of filtration combined with a "strong" electromagnetic field. Another observation is that more particulates are found at the bottom of the gravity filtration sample, see Figure 11(c), compared with the bottom of the electromagnetically stirred sample, see Figure 12(c). This is believed to be due to the "strong" upward flow located in the central part of the filter, as shown in Figure 6.

C. *Filter Side Wall*

In Figures 13 and 14(a) through (c), the comparison between the SiC particle distributions inside the filter media and along the filter side walls for the gravity flow test, as well as the high magnetic flux density test with Coil #2 at ~0.2 T, is presented. As can be seen from the micrographs, the wetting conditions are visibly improved by the application of the electromagnetic field during filtration. It is, however, qualitatively observed that the number of particles collected along the filter side wall in the gravity filtration experiment is less than in the case of the filtration combined with the electromagnetic forces. It is believed that particles are transported and

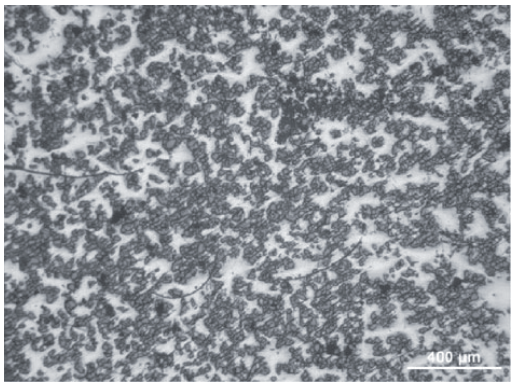

(a) Top

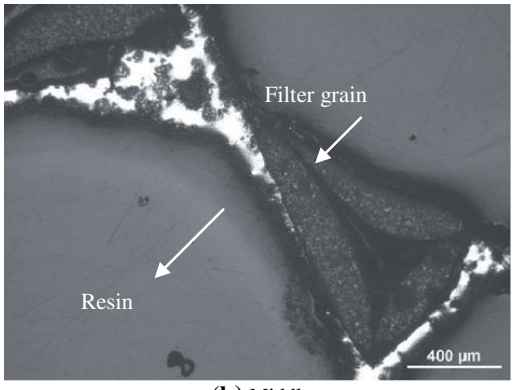

(b) Middle

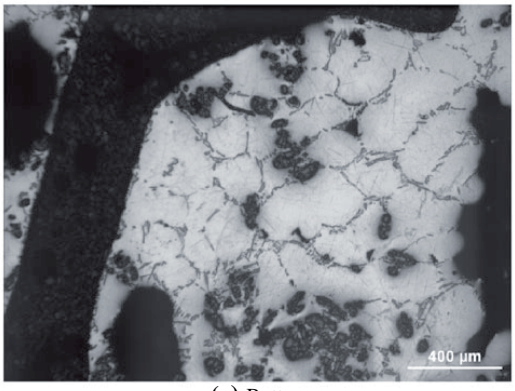

(c) Bottom

Fig. 11—The SiC particle distribution, inside the filter media along the filter center line, resulting from the gravity flow tests. The overall direction of flow is from the top to the bottom of the figure. The magnification for each of the micrographs is 50 times.

collected at the filter side wall as a direct result of the strong upward fluid circulation through the filter center and the downward circulation along the side wall, caused by the strong curl present in the Lorentz forces, as shown in Figure 6.

D. *Quantitative Filtration Efficiency*

The Image-Pro® Plus Version 7.0 software successfully counted the areas of >93 pct (when compared against a meticulous manually controlled count) of the individual particles from each micrograph for sizes >2 μm. Representative initial and final micrographs are shown in Figures 15(a) through (c). The adjusted equivalent spherical particle diameters have been measured for each sample and assembled into histograms of particle count in and out for both the gravity and the electromagnetic experiment using Coil #2, as shown in Figures 16(a) and (b).

The overall filtration efficiencies for both the gravity (0.844) and the electromagnetic filtration experiment (0.472) have been calculated using Eq. [14], and the results have been plotted against "typical" results for the same type of 30 PPI commercial filters in Figure 17. The obtained overall filtration efficiencies are found to both be within the wide range of expected performance for this type of commercial filter. The gravity result is located very near the maximum and the electromagnetic result is toward the average of the "typical" values. Given that both are within the normal range, it is difficult to reach a firm conclusion, although the preliminary data appear to indicate a decrease in the overall filtration efficiency for the electromagnetic experiment.

Empirical models of filtration proposed for this type of CFF are of the following form[32]:

$$E_{\text{size fraction } x} = 1 - e\left(\frac{-K_0 L}{V_f}\right) \qquad [16]$$

where $E_{\text{size fraction } x}$ is the fractional collection efficiency of size fraction, x, based on observed particle counts in and out using Eq. [15]; K_0 is an empirical constant (1/s) for each range of sizes, having reported values of[32] 0.205 for 15 to 20 μm, 0.250 for 20 to 25 μm, and 0.283 for 25 to 30 μm particles; L is the filter thickness (mm); and V_f is the interstitial velocity of the melt within the filter (mm/s). Typically, K_0 is determined from LiMCA data in and out and such data are not available for sizes <15 μm due to limitations in the measuring principle applied.

Based on Eq. [16], it would be expected that individual and overall filtration efficiency will vary inversely proportionally to the aluminum "casting" rate in the range of typical velocities from 3 to 19 mm/s.[32] The high efficiency found for the gravity filtration experiment is likely explained by the fact that a low interstitial velocity on the order of 2 mm/s was used when compared with typical filtration velocities.

The low efficiency of the electromagnetic experiment could also be expected in light of Eq. [16] and the extremely high flow velocities induced by the curl in the electromagnetic Lorentz forces inside the filter region, *i.e.*, 10 to 189 mm/s, as shown previously in Figure 6. The higher melt velocities may have broken internal "bridges," which typically form during deep filtration in CFFs as shown in Figure 18,[32] or re-entrained material collected at the walls and hence elutriated previously collected particles from the filter.

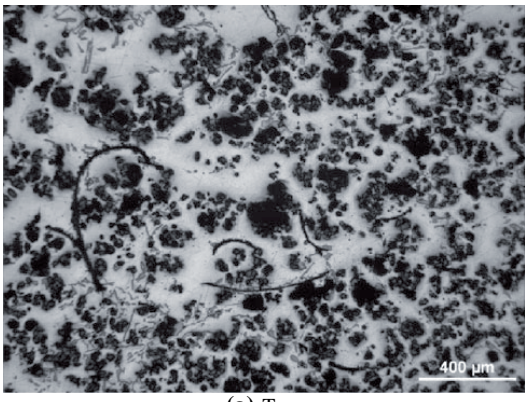

(a) Top

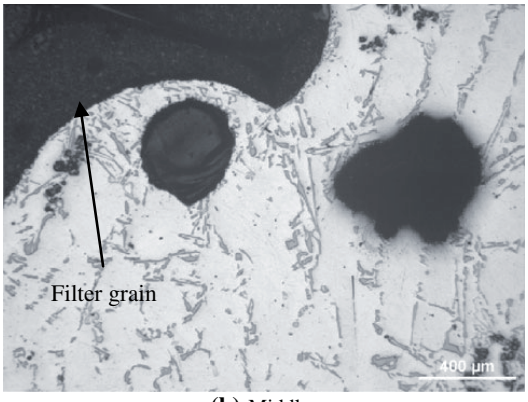

(b) Middle

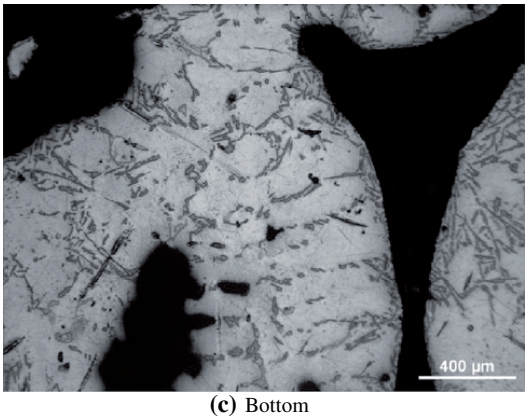

(c) Bottom

Fig. 12—The SiC particle distribution, inside the filter media along the filter center line, resulting from a high magnetic flux density test (Coil #2 at 0.2 T). The overall direction of flow is from the top to the bottom of the figure. The magnification for each of the micrographs is 50 times.

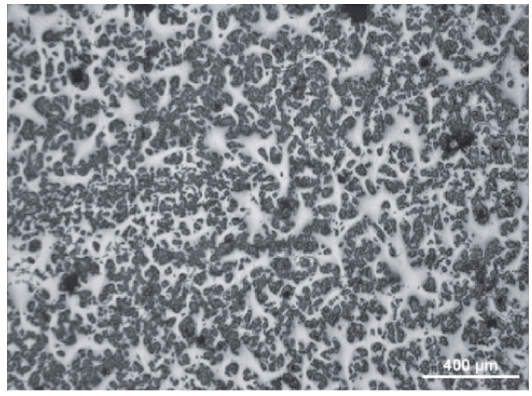

(a) Top

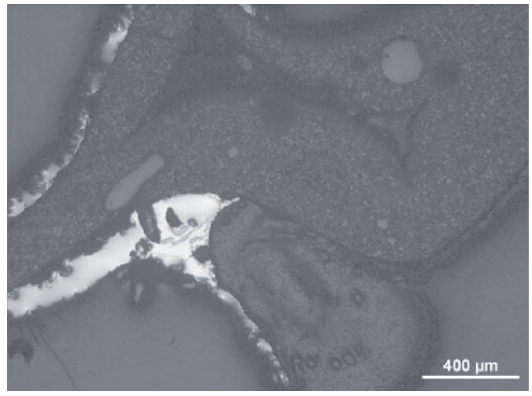

(b) Middle

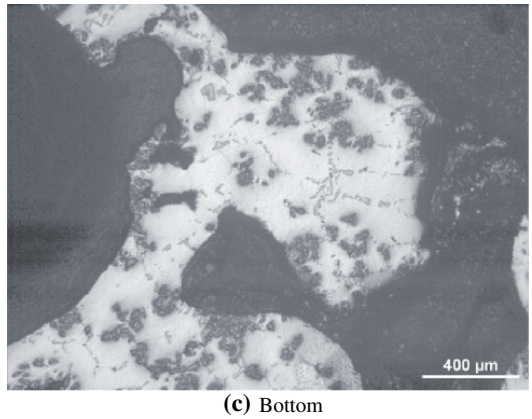

(c) Bottom

Fig. 13—The SiC particle distribution, inside the filter media along the filter side wall, resulting from gravity flow tests. The overall direction of flow is from the top to the bottom of the figure. The magnification for each of the micrographs is 50 times.

If the fine nature of the particles used in this experiment is taken into account, Eq. [16] would indicate that the overall observed electromagnetic filtration efficiency (0.472) is representative of a bulk velocity of about 12 mm/s. Given that the actual range of velocities induced by the Lorentz forces was up to 15 times higher,

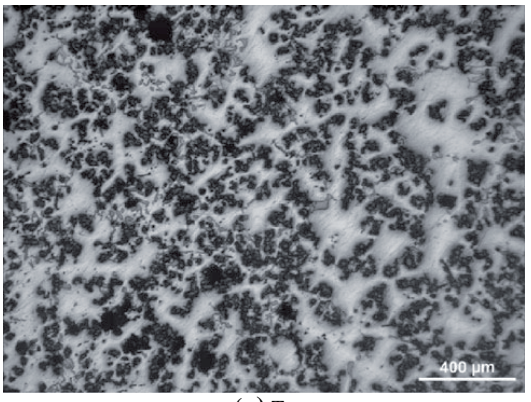

(a) Top

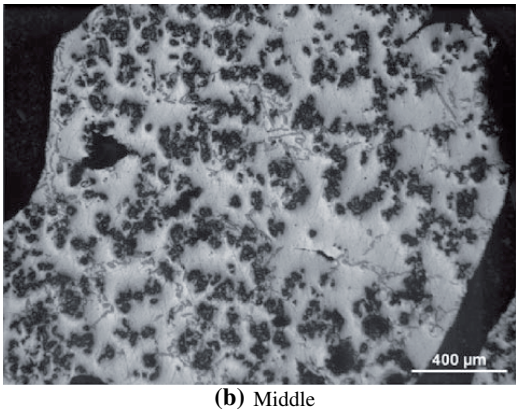

(b) Middle

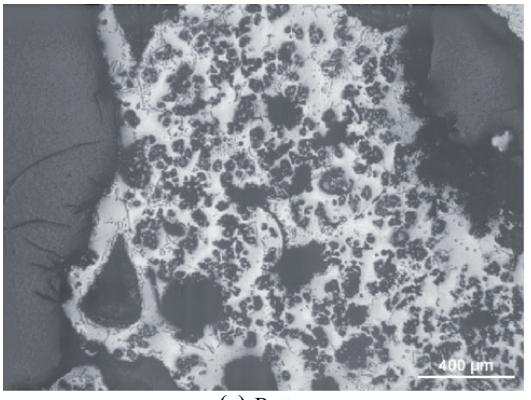

(c) Bottom

Fig. 14—The SiC particle distribution, inside the filter media along the filter side wall, resulting from the high magnetic flux density test (Coil #2 at 0.2 T). The overall direction of flow is from the top to the bottom of the figure. The magnification for each of the micrographs is 50 times.

this could indicate that bulk recirculation of the melt driven by the Lorentz forces or "enhanced" removal by the *Leenov-Kolin "pinch" effect* in the hydrodynamic boundary layer at the sides of the filter may have had a compensating effect. More optimized results might be experienced by testing alternate filters with different permeability, utilizing a different magnetic flux density or alternate coil configurations (*e.g.*, variable pitch), producing different magnitudes and curls of the Lorentz forces.

Particle efficiency by size has been calculated for both the gravity and the electromagnetic filtration experiments using Eq. [15] and plotted in Figure 19. Results indicate that each experiment has both different overall efficiencies and also substantially different variation of efficiency as a function of particle size. In the case of gravity filtration, the efficiency is relatively constant, increasing slightly with particle size in the size range of 2 to 25 μm. In the case of the electromagnetic experiment, the filtration efficiency decreases monotonously with increasing particle size. An examination of the micrographs presented in Figures 11 through 15 indicates a high degree of agglomeration of individual particles. It may be that particle agglomerates are formed (during the master alloy solidification or during remelting) and can be subsequently collected, with some common efficiency, rather than as individual particles being collected with differing efficiencies. In Figure 20, a typical "cluster" or agglomerate from the "cleaned" side of the electromagnetic filtration experiment is shown. Expanded bifilms are often observed decorated with numerous particles over, inside, and under the filters.[33] Bifilms appear to play a role as a "scaffold," building bridges across the open windows within the filter porosity and may play a role in the overall filtration efficiency, as has been described in previous investigations.[34]

The decrease of efficiency with increasing size in the case of the electromagnetic filtration may be due either to greater re-entrainment at the high velocities induced by the electromagnetic Lorentz forces or more likely due to rapid settling of the largest particles once they have made their "first pass" through the filter, *i.e.*, large particles and agglomerates are more likely to settle once below the filter and not have a second or third chance at "re-filtration" due to bulk fluid recirculation as shown in Figure 6. The decrease in efficiency with increased particle size is a strong indication that bulk recirculation and not the *Leenov-Kolin effect* is "maintaining" the overall efficiency at these high interstitial velocities during the electromagnetic filtration.

Clustering or agglomeration effects with SiC[35,36] as well as other particles, such as intermetallics[37] and TiB_2,[38] have been reported many times in the literature. These clustering effects lead to rapid settling of particulates in liquid aluminum, at rates about an order of magnitude higher than would be expected from the Stokes law. Stokes law is only valid for freely falling individual particles. This rapid particle settling was also observed during batch testing conducted as part of this study.[33] It is hypothesized that these clustering effects dominate the filtration efficiency of particles in the size ranges used in this study, which would invalidate models based on single particle efficiency and negate the value of so-called "particle tracking" using MHD-FEM.

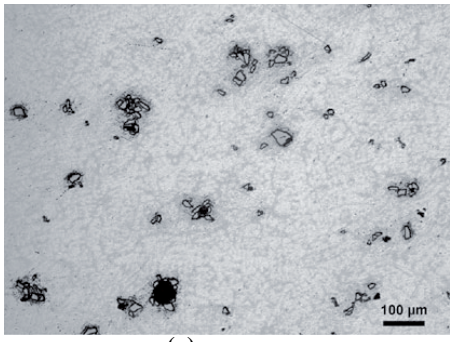

(a) before filtration

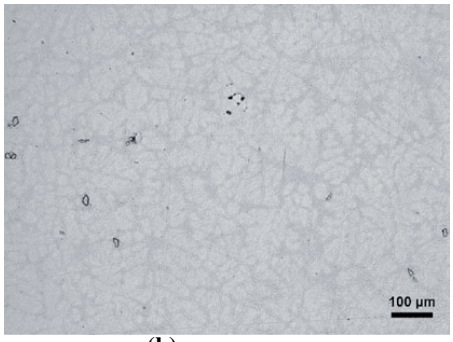

(b) after gravity filtration

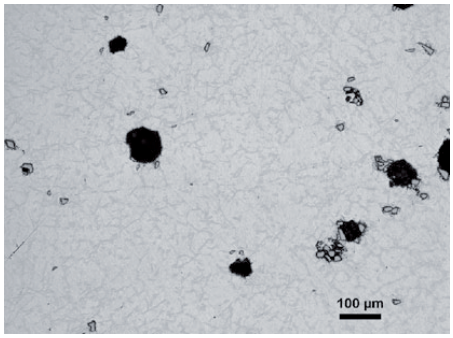

(c) after electromagnetic filtration

Fig. 15—Representative micrograph (*a*) before and (*b*) after gravity and (*c*) electromagnetic filtration at ~0.2 T, taken at 10 times magnification with a light microscope.

Cluster effects emerge in processes when the particle density becomes high enough (highly likely just over or inside of a filter), or the level of turbulence becomes large enough, for particles to have a high probability of "encountering" and interacting with one another, for example to minimize their net surface energy. These "particles" can be liquid organic media in solvent extraction mixer-settlers, liquid metal prills in molten slag containing furnaces, or even solid particles in gas-particle cyclones. These effects have become better known within particle-gas physics for highly loaded cyclones, where particles at and below 1 μm can be

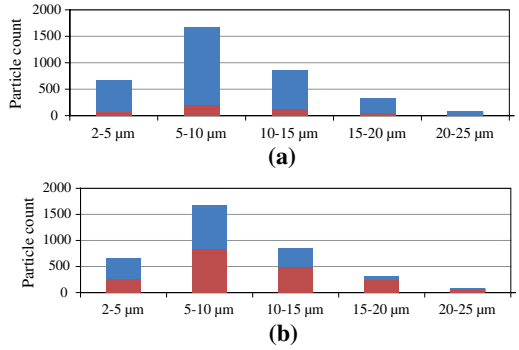

Fig. 16—Particle counts in and out for (*a*) 30 PPI gravity and (*b*) electromagnetic filtration experiments as functions of size ranges from 2 to 25 μm, at ~0.2 T.

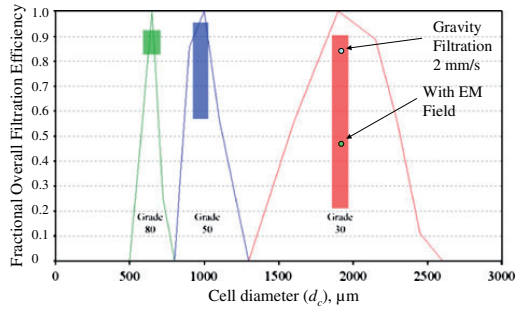

Fig. 17—Overall filtration efficiency for 30 PPI gravity and electromagnetic experiments, plotted *vs* "typical" industrial filter performance, for the same type of commercial filters.[42]

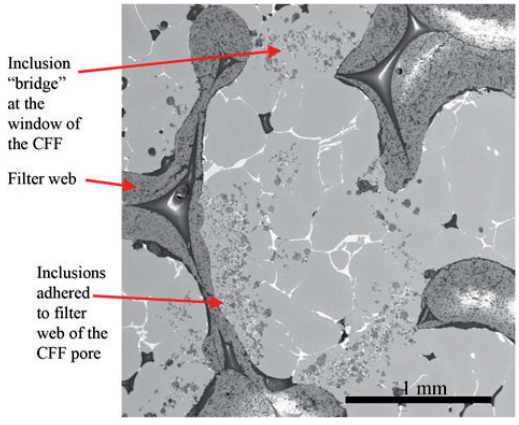

Fig. 18—Particle bridges formed during filtration of aluminum.[32]

collected with extremely high efficiency when cyclones are operated with high inlet loadings due to clustering.[39] These solid "clusters" are not broken up in such cyclones, even with many gs of gravity force, so it is further hypothesized that the clusters encountered in the

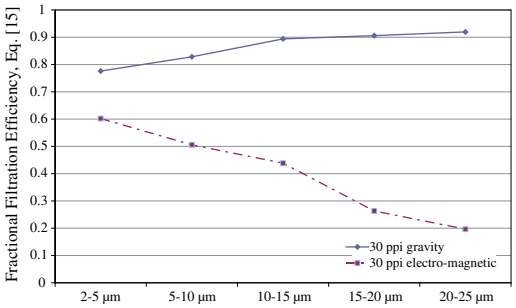

Fig. 19—Filtration efficiency as a function of particle size range from 2 to 25 μm for 30 PPI gravity and electromagnetic experiments at ~0.2 T.

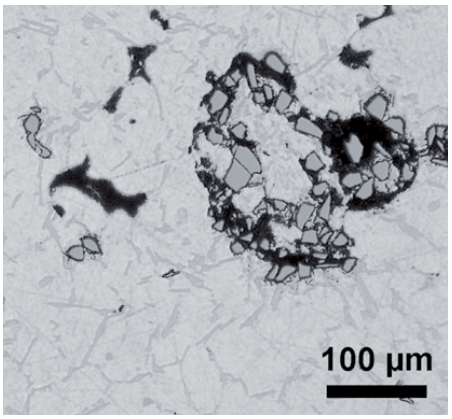

Fig. 20—SiC Agglomerates found in the "cleaned" metal taken from the outlet of the 30 PPI electromagnetic filtration apparatus.

current experiment will not be deagglomerated by the mixing effects induced by the curl of the Lorentz forces.

Previous publications could not be found giving filtration efficiency by size in aluminum for the range of particles used in this study, as the industry standard LiMCA equipment has difficulty to accurately detect particles below 20 μm.[34,40–42] The macro-automated computerized optical analysis technique used in this study may offer a reasonable way to explore the efficiency of filtration for very fine particles in molten metal processes.

V. CONCLUSIONS

The powerful mixing caused by the curl in the Lorentz force fields (produced by "short" induction coils) has a profound impact on the wetting behavior and resulting distribution of SiC particles during filtration of liquid aluminum using CFFs. In the case of electromagnetic stirring, fewer particles have been found on top of the filter, and more particles were located close to the side walls of the crucible. The higher velocities induced inside the filter by the influence of the Lorentz forces appear to have resulted in a reduction in the overall filtration efficiency from 0.844 to 0.472, for the 30 PPI commercial CFFs used in this study, and a significant change in the variation of the particle filtration efficiency with size.

The filtration efficiencies have been reported as a function of size using a macro-automated computerized optical analytical procedure suitable for very fine particulates from 2 to 25 μm. The observed efficiency of filtration for the very fine particulates used in these experiments was higher than expected (*e.g.*, 0.844 for gravity) and did not appear to vary substantially as a function of particle size under gravity filtration conditions. Clustering effects appear to create agglomerates of fine particles, which are subsequently collected with high and nearly uniform filtration efficiency. This would not be possible to measure using industrial measuring devices of the LiMCA type as agglomerates would be counted as individual "large" particles.

A new analytical expression for the time-averaged Lorentz forces has been proposed, incorporating a frequency modified "short" coil correction factor which shows good agreement with estimates found using finite element modeling (COMSOL 4.2®).

VI. FURTHER WORK

In order to better understand and optimize the electromagnetically modified filtration process, the physical (permeability at high velocity and porosity) and electrical conductivity properties of CFFs must be combined into a MHD model of the type shown in Figure 6. The physical and electrical properties of CFFs from 30 to 80 PPI have been measured, modeled analytically and using CFD, and reported in a separate article.[29]

The obtained efficiency for gravity and electromagnetic filtration, using 30 to 80 PPI filters at both low and high bulk filtration velocities, has been measured and will be reported in a future publication.[43] Results are compared with flow fields computed with MHD modeling using validated filter properties and with representative micrographs.

Practical implications of the current research on the design and operation of cast house filter equipment and a detailed description of the optical analysis technique are to be published in future articles.[44,45]

ACKNOWLEDGMENTS

The present study was carried out as part of the RIRA (Remelting and Inclusion Refining of Aluminium) project funded by the Norwegian Research Council (NRC)—BIP Project No. 179947/I40. The industrial partners involved in the project are Hydro Aluminium AS, SAPA Heat Transfer AB, Alcoa Norway ANS, the Norwegian University of Science and Technology (NTNU), and SINTEF Materials and Chemistry. The funding granted by the industrial partners and the

NRC is gratefully acknowledged. The authors wish to express their gratitude to Egil Torsetnes at the NTNU for helping with the design and construction of the experimental apparatus. Sincere gratitude is also due to Kurt Sandaunet at SINTEF for his support and help as well as for the use of the SINTEF laboratory. The high quality metallographic work of Robert Fritzsch and Behzad Mirzaei was also invaluable.

REFERENCES

1. S. Makarov, R. Ludwig, and D. Apelian: *Meas. Sci. Technol.*, 1999, vol. 10, pp. 1047–53.
2. Z. Xu, T. Li, and Y. Zhou: *Metall. Mater. Trans. A*, 2007, vol. 38A, pp. 1104–10.
3. T. Li, Z. Xu, B. Sun, D. Shu, and Y. Zhou: *Acta Metall. Sinica Engl. Lett.*, 2000, vol. 13, pp. 1068–74.
4. L. Damoah and L. Zhang: *Metall. Mater. Trans. B*, 2010, vol. 41B, pp. 886–907.
5. D. Leenov and A. Kolin: *J. Chem. Phys.*, 1954, vol. 22, pp. 683–88.
6. P. Vilinskas and R. Schiltz: *Nucl. Appl.*, 1969, vol. 6 (2), p. 176.
7. C. Conti, J. Meyer, J. Riquet, and P. Netter: Patent Number EP 290360 A(00290360/EP-A), 1988.
8. D. Shu, T. Li, B. Sun, J. Wang, and Y. Zhou: *Metall. Mater. Trans. A*, 1999, vol. 30A, pp. 2979–88.
9. K. Takahashi and S. Taniguchi: *ISIJ Int.*, 2003, vol. 43, pp. 820–27.
10. J.P. Park, A. Morihira, K. Sassa, and S. Asai: *Tetsu-to-Hagané*, 1994, vol. 80, p. 389.
11. S. Taniguchi and J. Brimacombe: *ISIJ Int.*, 1994, vol. 34, pp. 722–31.
12. J. Barglik and C. Sajdak: *Elektrowärme Int.*, (2), 1985, pp. B77–B80.
13. D. Shu, B. Sun, K. Li, J. Wang, and Y. Zhou: *ISIJ Int.*, 2002, vol. 42, pp. 1241–50.
14. N. El-Kaddah, A. Patel, and T. Natarajan: *JOM*, 1995, vol. 47, pp. 46–49.
15. N. El-Kaddah: US Patent 4,909,836, 1990.
16. D. Shu, J. Wang, H. Chen, and B. Sun: US Patent Application 20,080/216,601, 2005.
17. M.W. Kennedy, S. Akhtar, J.A. Bakken, and R.E. Aune: *Light Metals*, San Diego, California, 27 February–3 March, 2011, pp. 763–68.
18. R. Fritzsch, M.W. Kennedy, S. Akhtar, J.A. Bakken, and R.E. Aune: *Electromagnetic Processing of Materials*, Beijing, China, 23–25 October, 2012, pp. 1–4.
19. M.W. Kennedy, S. Akhtar, J.A. Bakken, and R.E. Aune: *EPD Congress*, San Diego, California, 27 February–3 March, 2011, pp. 707–22.
20. M.W. Kennedy, S. Akhtar, J.A. Bakken, and R.E. Aune: *COMSOL Users Conference*, Stuttgart, Germany, 26–28 October, 2011, pp. 1–9.
21. M.W. Kennedy, S. Akhtar, J.A. Bakken, and R.E. Aune: *Light Metals*, Orlando, FL, 11–15 March, 2012, pp. 269–75.
22. R. Weaver: http://electronbunker.ca/DL/NumericalExamples01.ods, accessed 15 December 2012.
23. N. McLachlan: *Bessel Functions for Engineers*, Clarendon Press, Gloucestershire, 1955, pp. 215–30.
24. V. Korovin: *Magnetohydrodynamics (Engl. Transl.)*, 1986, vol. 22, pp. 17–19.
25. V. Korovin: *Magnetohydrodynamics (Engl. Transl.)*, 1986, vol. 21, pp. 321–26.
26. H. Nagaoka: *J. Coll. Sci.*, 1909, vol. 27, pp. 18–33.
27. D. Knight: *Part 1: Solenoid Inductance Calculation*, October, 2012, http://www.g3ynh.info/zdocs/magnetics/Solenoids.pdf, accessed 15 December 2012.
28. R. Brandt and G. Neuer: *Int. J. Thermophys.*, 2007, vol. 28, pp. 1429–46.
29. M.W. Kennedy, K. Zhang, R. Fritzsch, S. Akhtar, J.A. Bakken, and R.E. Aune: *Metall. Trans. B*, 2012 (accepted).
30. A. Çiftja: PhD Thesis, Department of Materials Science and Engineering, NTNU, Trondheim, 2009.
31. P. Forchheimer: *Z. Ver. Deutsch. Ing.*, 1901, vol. 45, pp. 1782–88.
32. S. Ray, B. Milligan, and N. Keegan: *Aluminium Cast House Technology 2005*, 9th Australasian Conference and Exhibition, Melbourne, Australia, 12–15 September, 2005, pp. 1–12.
33. R. Fritzsch: Masters Thesis, Department of Materials Science and Engineering, NTNU, Trondheim, 2011.
34. H. Duval, C. Rivière, É. Laé, P. Le Brun, and J. Guillot: *Metall. Mater. Trans. B*, 2009, vol. 40B, pp. 233–46.
35. A. Kolsgaard and S. Brusethaug: *Mater. Sci. Eng. A*, 1993, vol. 173, pp. 213–19.
36. A. Ourdjini, K. Chew, and B. Khoo: *J. Mater. Process. Technol.*, 2001, vol. 116, pp. 72–76.
37. S. Shabestari and J. Gruzleski: *Metall. Mater. Trans. A*, 1995, vol. 26A, pp. 999–1006.
38. P.L. Schaffer and A.K. Dahle: *Mater. Sci. Eng. A*, 2005, vol. 413, pp. 373–78.
39. A. Hoffmann, H. Arends, and H. Sie: *Filtr. Sep.*, 1991, vol. 28, pp. 188–93.
40. D. Chesonis, D. DeYoung, D. Lake, N. Ridler, G. Alcoa Manufacturing, L.W. Works, and W.S.A.I. Swansea: *Light Metals*, Seattle, 17–21 February, 2002, pp. 937–44.
41. N. Keegan, W. Schneider, and H. Krug: *Light Metals*, San Diego, California, 28 February–4 March, 1999, pp. 1031–41.
42. N.J. Keegan and S.F. Ray: in *Alcastek*, Mumbai, India, Dr. Nilmanied, ed., 2002, pp. 1–10.
43. M.W. Kennedy, R. Fritzsch, S. Akhtar, J.A. Bakken, and R.E. Aune: *Metall. Trans. B*, 2012 (in press).
44. R. Fritzsch, M.W. Kennedy, J.A. Bakken, and R.E. Aune: *Light Metals*, San Antonio, 3–7 March, 2013 (in press).
45. R. Fritzsch, B. Mirzaei, M.W. Kennedy, J.A. Bakken, and R.E. Aune: *Light Metals*, San Antonio, 3–7 March, 2013 (in press).
46. K. Yeum and D. Poirier: *Light Metals*, 1988, pp. 469–76.
47. D. Wang and R. Overfelt: *Int. J. Thermophys.*, 2002, vol. 23, pp. 1063–76.

SUPPLEMENT 8

Electromagnetically Modified Filtration of Aluminum Melts Part II: Filtration Theory and Experimental Filtration Efficiency with and without Electromagnetic Priming for 30, 50 and 80 PPI Ceramic Foam Filters

Mark William Kennedy, R. Fritzsch, Shahid Akhtar, Jon Arne Bakken, Ragnhild Elisabeth Aune

Submitted to Metallurgical Transactions B, (2012), 1-69.

Is not included due to copyright